ENHANCED SHRINKAGE CHARACTERIZATION OF CLAYEY SOILS

by

RAJU ACHARYA

Presented to the Faculty of the Graduate School of

The University of Texas at Arlington in Partial Fulfillment

of the Requirements

for the Degree of

DOCTOR OF PHILOSOPHY

THE UNIVERSITY OF TEXAS AT ARLINGTON

DECEMBER 2015

Acknowledgements

First of all, I would like to express my deepest gratitude to my research advisor, Dr. Anand J. Puppala, for offering me the opportunity to complete my Ph.D. at the University of Texas at Arlington under his esteemed patronage and valuable direction. Without his excellent guidance, continuous support and motivation, advanced research facilities, and the friendly working environment, this work would not be possible. I am indebted to him forever for all the help extended to me throughout my stay at UTA. I also appreciate the time he afforded to improve not only the research but also my future career.

I am also grateful to Dr. Laureano Hoyos, Dr. Xinbao Yu, and Dr. Shih-Ho Chao for their willingness to serve on my examination committee. Their valuable comments and suggestions during the research and in the completion of this dissertation are truly appreciated.

In addition, I would like to thank the Department of Civil Engineering for their financial support through EGTA fellowships and graduate assistantships. My special thanks are due to Dr. Aravind Pedarla for providing me with the soils for this research. I truly appreciate his guidance and help with SWCC, chemical, and mineralogical tests. I would like to thank Dr. Bhaskar Chittoori and Dr. Thornchaya Wejrungsikul for guiding me in the shrinkage induced pressure test. I also like to thank Dr. Minh Le for his help with direct shear and torsional ring shear tests. In addition, very special thanks goes to Venkatesh Kaka and

Mohammad Reza Zarrinpour for their valuable help with the digital image correlation technique.

My extended thanks go to my colleagues Dr. Tiwari, Dr. Pradhan, Dr. Bheemasetti, Dr. Ruttanaporamakul, Dr. Patil, Dr. Nan, Alejandro, Santiago, Aritra, Minh Hai, Gaily, Haifeng, Book, Sadikshya, Spoorthi, Rathna, Minh Tran, Kalesiha, and Rudy for their help during the field monitoring visits and during laboratory tests.

I would like to express my heartfelt gratitude to my first teachers and parents, Narayan Prasad Acharya and Kamala Devi Acharya, for their love and inspiration all along. My sincere thanks are also extended to my sisters, and brother for their moral support throughout my stay in USA. Last, but not the least, I would like to thank my beloved wife Shrijana for her endless love, care, understanding, and continuous support in my life.

October 27, 2015

Abstract

ENHANCED SHRINKAGE CHARACTERIZATION OF CLAYEY SOILS

Raju Acharya, PhD

The University of Texas at Arlington, 2015

Supervising Professor: Anand J. Puppala

Surficial slope failure is a common problem experienced by most of the compacted earth dams in Texas and several other southern states in USA as a result of desiccation or shrinkage induced cracking of the surficial soils. Cracking of the soil occurs when the tensile stress exceeds the tensile strength during drying process. Tensile stress increases with an increase in shrinkage strain and thus soil chemical admixtures can reduce the tensile stress by reducing the shrinkage potential of soil. Inclusion of such admixtures invariably affects the tensile strength. Yet there are not many test methods that could be utilized for shrinkage characterization of the expansive soils and hence there is a major need to develop a method to perform better shrinkage characterization of soils. This has been the main objective of the present dissertation research.

A test method presented as a shrinkage induced pressure (SIP) test was further refined to study the shrinkage potential, tensile strength, and desiccation

cracking of soils. As a part of this study, several expansive soils were utilized and studied with the refined characterization method.

A statistical tool was also developed to predict the SIP based on different soil variables. Also, three dimensional unsaturated slope stability analysis of the dam slope was conducted using the finite difference program FLAC3D to study the effects of seasonal moisture content fluctuations, formation of desiccation cracks and how these impact surficial slope stability.

Also, a new treatment method that utilizes biopolymer to amend the soil to reduce desiccation cracking was evaluated using the developed characterization method. The moderate increase in the shear strength of the biopolymer treated soil compared to the untreated soil may work well in natural slope conditions of dam and highway embankments. This dissertation uses same characterization tool in the assessment of biopolymer treatment of expansive soils in reducing their shrinkage behavior. Future research directions are also presented in this field.

Table of Contents

List of Illustrations

List of Tables

Chapter 1

Introduction

1.1 Background

Desiccation cracking in soil has been a challenging issue in geotechnical engineering for decades. Soils tend to shrink when they lose moisture content during seasonal fluctuations during summer periods. In particular, clayey soils are susceptible to shrinkage, subsequent volume changes, and will undergo cracking. Desiccation cracking adversely affects the mechanical, hydrological, physico-chemical and thermal properties of soil masses (Kodikara and Costa, 2013). It eventually reduces the overall stability and bearing capacity of soil masses. As a result the stability and integrity of the structures associated with these compacted soils will always pose major concerns.

The mechanism of desiccation cracking of shrinking soil explained in many research studies (George, 1969; Towner, 1987; Morris et al., 1992; Fang, 1994; Omidi et al., 1996; Albrecht and Benson, 2001; Puppala et al., 2006; Costa et al., 2008; Puppala et al., 2011, Puppala et al., 2012; Kodikara and Costa, 2013) based on the unsaturated soil mechanics theory can be summarized as follows: during the drying process, soil loses moisture content and consequently the matric suction of the soil increases. The increase in matric suction increases the net effective stress, and the decrease in water content also increases the tensile strength of the drying soil. The increase in effective stress causes volumetric

shrinkage of the soil. Consequently, tensile stresses are developed within the soil mass either due to the restrained boundary condition or due to moisture gradient along the soil profile or combination of both. As the drying process continues, the tensile stress developed within the soil mass can exceed the tensile strength of the soil at some point thereby causing the cracking of the soil.

The problematic expansive soils are found in different geological formations around the globe. These soils are also present in different parts of the Unites States. High plasticity clay soils are also prevalent in North Central Texas as a result of weathering of products of limestone material and alluvial deposits. Formations of expansive clay shale are also present in this region (Le, 2013). Construction of several rolled earthfill embankment dams in the area, including Grapevine, and Joe Pool dams, utilized on-site soils as borrow materials, which invariably included the high plasticity clays and clay shale materials. Repeated weathering (wetting-drying) cycles have produced desiccation cracking within high plasticity fill materials in these dam slopes. Moreover, the infiltration of rainwater into the desiccation cracks saturates the top soil surface and increases the pore water pressure thereby causing surficial slope failure (Dronamraju, 2008; Le, 2013).

Previous research studies conducted at the University of Texas at Arlington (UTA) have investigated the advantages of utilizing lime-treated fill and lime-fiber treated fill as admixtures to mitigate surficial slope failures

(McCleskey, 2005; Dronamraju, 2008; Le, 2013). The long term slope movement data collected from Grapevine and Joe Pool dams demonstrated that the aforementioned soil treatment methods considerably reduced the deformation of slope resulting from desiccation cracking compared to the untreated. The improvements were reported based on the shear strength parameters measured on the lab as well as the filed monitoring of the slope movement in the treated sections. The shrinkage studies conducted on the treated soils were mainly based on linear shrinkage bar test and volumetric shrinkage test.

1.2 Problem Statement

According to Abou Najm et al. (2009), interaction among the soil particles and the pore fluids is the key factors behind internal stresses in soils. Lu and Likos (2006) highlighted that the Van der Waals forces, capillary forces, electrical double layer forces and cementation between particles are the governing factors for the internal stresses in soils. Measurement of the evolution of internal stresses during drying is very important to understand the desiccation cracking in the soil. There have been some developments in measuring the internal stresses of a drying soil. For example, Kodikara and Choi (2006) and Abou Najm et al. (2009) presented the analytical and experimental techniques to determine the internal stresses of drying soil based on linear shrinkage bar test and restrained ring test respectively. However, existing experimental procedures and analytical solutions for internal stress evolution are too specific and/or complex for routine lab

experiment. Also, there is lack of empirical solutions that can link the soil properties to the internal stresses.

The previous studies conducted in the UTA suggested lime, and lime+fiber treatments as the effective means of mitigating the surficial slope failures (Dronamraju, 2008; Le, 2013). These methods of soil improvements are not environment friendly and also inhibit the growth of vegetation on the slopes. The application of biopolymers in soil improvement has been explored in recent years. Soils amended with biopolymers have been shown to reduce hydraulic conductivity and slope erosion, and increase shear strength, drought resistance and slope stability due to enhanced establishment of vegetative cover (Kavazanjian et al., 2009; Nugent et al., 2010; Larson et al., 2013). However, the biopolymer treated soils are yet to be characterized for shrinkage and desiccation cracking. This sustainable soil treatment method has not been investigated in mitigating the surficial slope failures of the Grapevine and Joe Pool dams. The possible benefits of the biopolymer amended soils in reducing desiccation cracking can be utilized in mitigating surficial failure of the engineered slopes.

Slope stability analysis has been commonly conducted by using finite element or limit equilibrium methods in two dimensions (2D). Two dimensional modeling cannot effectively represent the actual field conditions, especially when cracks are present. Although it is possible to model the presence of cracks in 2D, the extent of the crack length, crack network and its effects cannot be studied

accurately. A current version of a commercially available finite difference program FLAC3D makes it possible to model the slope in three dimensions and also conduct the slope stability analysis on the slope using strength reduction method. This capability of the program has made it possible to study the effect of desiccation cracks and how these impact surficial slope stability.

The advent of new shrinkage characterization method for desiccation cracking, lack of studies on the potential advantageous application of biopolymer treated soil in mitigating surficial slope failures resulting from desiccation cracking, and limitation of traditional 2D slope analysis method to accurately capture the effects of cracks in slope stability have been the motivation factors for the present dissertation research.

1.3 Research Objectives

The main objective of this research is to refine and develop the shrinkage characterization of different soils with a major focus on shrinkage induced pressures and shrinkage cracking in soils. Another objective is to use this methodology to address biopolymer treatment to reduce shrinkage cracking and thereby control surficial slope failures. As a part of the first objective, this research aims at establishing a relationship between the SIP and tensile strength of the soil determined from indirect tensile strength test. In addressing these objectives, digital image correlation technique is also focused in understanding the shrinkage cracking patterns and mechanisms of natural and stabilized soils

with. Another objective is to investigate three dimensional (3D) slope stability analysis of two dams namely, Grapevine and the Joe Pool Dam embankment slopes. This objective focuses on both the effects of seasonal moisture content fluctuations, and extent of desiccation cracks on slope stability issues.

1.4 Research Methodology

First of all a detailed literature review was carried out. This is followed by a selection of ten (10) different clayey soils from different geological formations around the United States of America (USA). The research methodology further includes shrinkage characterization of the soils using shrinkage induced pressure (SIP) test, indirect tensile strength (IDT) test, linear shrinkage bar tests, determination of soil water characteristics curve, and digital image correlation technique to study the soil behavior during drying shrinkage and cracking. In addition, laboratory tests were also conducted to determine the basic soil properties, engineering properties, and chemical and mineralogical composition of the soils. Figure 1-1 provides a schematic of various tasks outlined in this research. Three different treatment methods, lime, lime+fiber, and biopolymer treatments, were analyzed to study changes in the shrinkage behavior of the soil and their influence in reducing the desiccation cracking problem. The test methods used in the shrinkage characterization of the untreated soils were repeated to compare the changes brought in by the introduction of soil additives. Furthermore, a multiple linear regression model was developed to predict the peak

SIP using soil properties. Finally, 3D unsaturated slope stability analysis of the dam slopes is conducted using a finite difference program, FLAC3D.

1.5 Organization of the Dissertation

The dissertation is divided in 7 chapters. The quantities are expressed in SI units along with English units wherever possible. Some of the graphs and figures that are cited from previous researchers include English units and are presented without any revision.

Chapter 1 presents an introduction, background, problem statements, research objectives and the methodology of the research, and organization of the dissertation to provide a framework of the current research.

Chapter 2 presents the literature review on desiccation cracking, its effect in slope stability, modeling of desiccation cracking. Different factors responsible for the shrinkage and desiccation cracking are presented in detail. This chapter also comprises of a review of the previous research in the areas of amendment of soils, determination of SWCC curve, influence of soil suction on slope stability, conventional slope stability methodologies, and unsaturated slope stability.

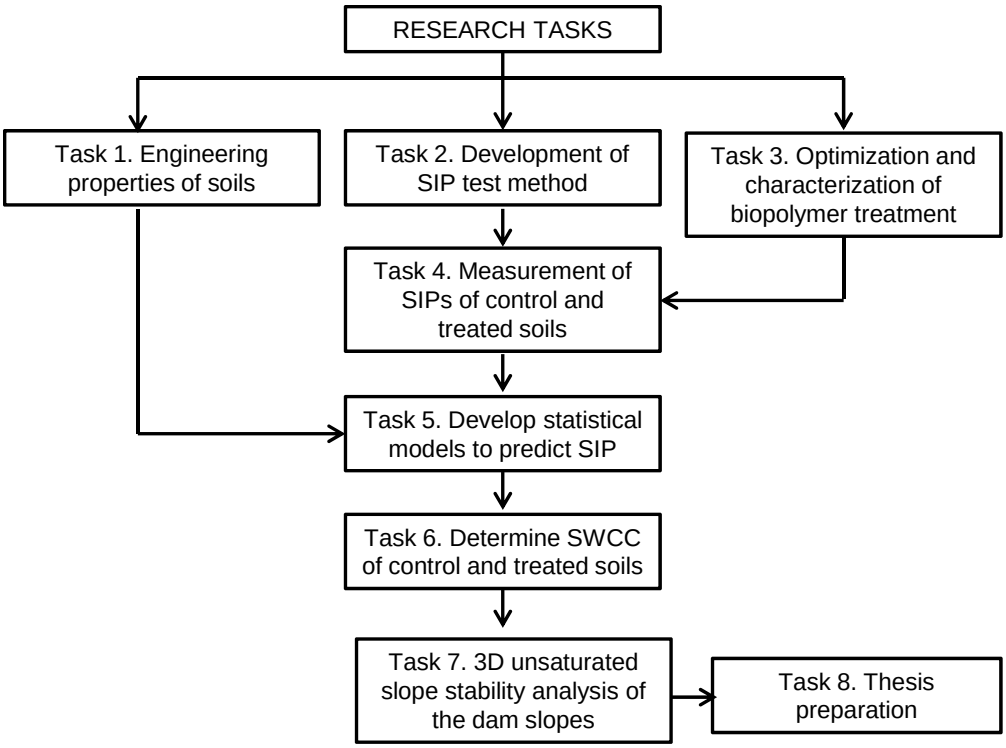

Figure 1-1 Schematic of the research tasks outlined in this study

Chapter 3 covers the selection of the soils and their basic classification. Entire experimental program conducted on the test soils and soils treated with different additives are also presented in this chapter. A new SIP test method as well as linear shrinkage bar test, indirect tensile strength test, determination of SWCC, and digital image correlation is also explained in this chapter for shrinkage characterization of the soil.

The development of multiple linear regression model to estimate the peak shrinkage induced pressure is presented in Chapter 4. The scatter plots,

development of preliminary model, residual analysis, exploration of interacting terms, and model selection procedures are explained in detail.

Chapter 5 presents the studies conducted on biopolymer treated Grapevine and Joe Pool soils. It presents the selection of the optimum dosage of the biopolymer for the dam soils. It also presents the results of the different tests conducted on the soils treated with biopolymer, lime and lime plus fiber. A comparison is made among the different treatment methods by indicating the pros and cons of each treatment method.

Chapter 6 covers the 3D slope stability analysis of the Grapevine and Joe Pool dam slopes using the finite difference program FLAC3D. It also includes the unsaturated slope stability analysis as well as the studies on the effect of desiccation cracking in the stability of the dam slopes.

Chapter 7 presents the summary of the research study, conclusions based on the research, and recommendations for future research.

Chapter 2

Literature Review

2.1 Desiccation Cracking

Desiccation cracking of clayey soils has been a challenge for researchers for a long time. The pioneer research work in desiccation cracking dates back to early sixties (Corte and Higashi, 1960). Soil tends to shrink when it loses moisture. In particular, clayey soils rich in smectite clay minerals are prone to shrinkage, subsequent volume change, and cracking. The desiccation cracks have random orientations and patterns. It is difficult to predict the areal extent as well as depth of desiccation cracks due to complex nature of desiccation cracking phenomenon. Desiccation cracking adversely affects the mechanical, hydrological, physico-chemical and thermal properties of soil masses (Kodikara and Costa, 2013). It eventually reduces the overall stability and bearing capacity of soil masses. As a result the stability and integrity of the structures associated with these soils may be at risk.

Cracking in the soil masses resulting from physico-chemical processes are generally classified in three categories: desiccation cracks, syneresis cracks, and cracks due to freeze-thaw actions (Omidi et al., 1996). Desiccation cracks are formed during the dry period as a result of moisture loss due to evaporation and subsequent shrinkage (Omidi et al., 1996; Kodikara et al., 2000). On the other hand, syneresis cracks occur in sedimentary deposits due to variations in the inter-

particle forces resulting from substitution of interstitial water with a highly aqueous solution. Such cracks are described as discontinuous, sinuous and spindle in shape (Brown and Anderson, 1983; Omidi et al., 1996). The cyclic freeze-thaw in soil causes shrinkage and swelling cycles in the soil that also add in the cracking of the soil.

2.1.1 Mechanism of Desiccation Cracking

Desiccation cracking of a shrinking soil depends on environment and soil composition related factors such as temperature, humidity, wind, particle size distribution, and soil mineralogy (Kodikara and Costa, 2013). The mechanism of desiccation cracking of shrinking soil explained in many research studies (George, 1969; Towner, 1987; Morris et al., 1992; Fang, 1994; Omidi et al., 1996; Albrecht and Benson, 2001; Puppala et al., 2006; Costa et al., 2008; Puppala et al., 2011; Puppala et al., 2012; Kodikara and Costa, 2013) based on the unsaturated soil mechanics theory have been reported in following steps: 1) During the drying process, soil loses moisture and the matric suction of the soil increases. 2) An increase in matric suction increases the effective stress and a decrease in water content increases the tensile strength of the drying soil. 3) The increase in effective stress causes volumetric shrinkage of the soil. Clay soils, in particular, can shrink up to 50% of their original volume (Puppala et al., 2011). 4) When the soil undergoes shrinkage cracking related volume change, tensile stresses will be developed within the soil mass either due to the restrained

boundary condition or due to moisture gradient along the soil profile or combination of both. The tensile stress depends on the boundary conditions and shrinkage potential of the soil. On the other hand, the tensile strength depends on the matric suction and particle adhesion. Both the tensile strength and tensile stress evolve gradually with decrease in moisture content. 5) As the drying process continues, the tensile stress developed within the soil mass can exceed the tensile strength of the soil at some point causing the cracking of the soil.

Although, there has been some development in locating the point of maximum tensile stress (generally at the middle of the sample in a linear shrinkage bar test), the presence of the imperfections such as air bubbles and larger particles may lead to cracking at a different location where the tensile stress is lower. The tensile strength of the soil matrix considerably decreases due to the presence of the imperfections. This imparts difficulty in predicting the location of cracks.

2.1.2 Developments in Desiccation Cracking Studies

Westergaard (1926) identified shrinkage and air temperature as the major factors contributing in the desiccation cracking in soil-cement mixtures. George (1969) suggested that the influence of temperature on desiccation cracking is lesser than that of the soil moisture content. He also indicated that tensile stresses develop due to shrinkage of the soil. The stresses are even higher if the shrinkage is restrained due to external and/or internal boundary conditions. The shrinkage

stresses are higher on the surface due to higher shrinkage strains and decreases with the depth of the soil layer. He also highlighted that the stresses are relieved either in the forms of cracks or plastic flow. He described desiccation cracking as the tensile failure in the soil. Thus, his study suggests that tensile stresses during shrinkage exceed the tensile strength of the soil at that particular moisture content which subsequently develops desiccation crack. Costa et al. (2008) also suggested a similar mechanism of the desiccation cracking. According to the authors, the desiccation cracks are formed during drying of soil due to evaporation of water from the surface. As the soil loses moisture, it starts shrinking by generating tensile stresses. As the tensile stress exceeds the soil strength in tension the cracks are formed. Desiccation cracking is a very complex phenomenon owing to various interactions that happens between different factors such as boundary conditions, temperature, humidity, materials. Therefore simulating the desiccation cracking phenomenon is a complex task (Costa et al., 2008).

Towner (1987) conducted desiccation cracking studies on remolded clay specimens of same length by varying initial moisture levels. According to the author, if the soil is restrained against shrinkage in one direction, the soil shrinks anisotropically. Both the tensile stress and tensile strength are related to water content and increase with increase in matric suction. The tensile stress in the restrained direction exceeds the tensile strength at some point of time during drying and eventually develops a crack.

Morris et al. (1992) highlighted that micro cracks are subjected to tensile stress at the crack tips due to increased matric suction. These micro cracks grow and develop macro cracks. The soil matric suction depends on the pore size that is directly related to the particle size. Loss in soil moisture content due to evaporation causes increase in the matric suction. As a result effective stress acting on the soil increases, which causes the soil to shrink. Furthermore, the author also suggested that desiccation cracks due to increased soil suction are more easily formed in fine grained soils as opposed to the coarse grained soils. It is explained by the fact that the inter-particle pore spaces are smaller in fine grained soil. The smaller capillary space contributes to larger matric suction. He also indicated that more favorable conditions for desiccation cracking exist at the ground surface due to higher matric suction and absence of overburden stress. The extent of the crack depth is limited by the increased overburden stress and length of the crack is controlled by position of intersecting crack (Cyrus, 2008).

Albrecht and Benson (2001) conducted shrinkage studies in eight different natural clayey soils used for landfill liners and covers. The authors allowed the soil to undergo wetting and drying cycles. The authors concluded that volumetric shrinkage strains depend on soil properties and degree of compaction. An increase in plasticity index increased the shrinkage strain. Similar behavior was observed with increase in clay content. The volumetric shrinkage strain also increased with an increase in absolute difference between compaction and optimum moisture

contents. On the other hand, an increase in compaction effort was accompanied with decrease in the volumetric shrinkage strain. The specimens having larger shrinkage strains generally experienced more number of cracks. On the contrary, Peng et al. (2012) studied the effect of compaction on the shrinkage behavior of soils. By analyzing their own results and other data from the literature, the authors concluded that the soil shrinkage behavior is independent of soil compaction. The authors also claim that the soil shrinkage behavior of highly compacted soil can be estimated using that of slightly compacted soil.

Tensile stresses are developed in the drying surface layer as the water is lost from the surface during drying. Tensile stresses keep on increasing as the drying process continues. The stresses are finally relieved in the form of desiccation cracks (Fang, 1994). Desiccation cracks have more or less distinct geometric shapes that depend on the clay mineralogy, drying process, and the pore fluids (Fang, 1994).

According to Kodikara and Costa (2013), a major factor in formation of desiccation cracks is restrained shrinkage within the soil. Restraints can be both internal and external. Restrained shrinkage causes the tensile stresses in the drying soil mass. Desiccation cracks are formed when the tensile stresses becomes higher than the tensile strength. Costa et al. (2013) identified two factors that control desiccation cracking. The first is tensile stress and strain energy evolution when the soil is subjected to restrained shrinkage. The second factor is location of flaws

in the material that dictate the location of cracks regardless of the location of maximum tensile stress.

Peng and Horn (2005) classified four phases in a volumetric shrinkage curve: (a) structural shrinkage (b) proportional shrinkage (basic shrinkage), (c) residual shrinkage and (d) zero shrinkage. Structural shrinkage phase involves greater water loss and small volume change. This phenomenon is mainly due to structural pores representing biopores and inter aggregate pores (Braudeau et al., 2004). No-volume change at zero shrinkage indicates non-swelling micropores. The proportional and residual shrinkage phases are related mainly to swelling micropores related to expansive clay. Thus, non-swelling textural pores and the structural pores do not play a big role in soil volume change (Braudeau at al., 2004).

Hu et al. (2013) conducted experimental studies on two different soils and three different fluids to investigate the effects of surface tension, saturation vapor pressure, latent heat, and kinematic viscosity of fluids and compressibility of the solid particles. The authors observed different limiting void ratio and void ratio variation for different pore fluid. The study showed that the saturation vapor pressure, viscosity of the pore fluid and latent head of the fluid do not have significant effects on the shrinkage behavior of the soils. But, the limiting void ratio and the void ratio variation correlated well with the surface tension of the pore fluid. The authors indicated that the evaporative and fluid flow

characteristics of the pore fluid do not affect shrinkage of drying soils. Rate of drying showed strong correlation with the saturation vapor pressure and consequently the rate of volume change also correlates with saturation vapor pressure.

2.1.3 Extent of Desiccation Cracking

The matric suction increases substantially due to desaturation of micro pores in the fine grained soils and the effective stress increases. This causes the shrinkage of the soil during drying. According to Nahlawi and Kodikara (2006), the extent of desiccation cracks can be as high as 33 ft.

According to Lecocq and Vandewalle (2003) cracks that appear first are wider than succeeding cracks. Ritchie and Adams (1974) presented cases of desiccation cracking up to 30 mm wide and 2 m deep. Dronamraju (2008) conducted research on desiccation cracking of Grapevine and Joe Pool dam sites. The surfaces of both of the dam slopes were covered with vegetation. Even the presence of vegetative cover could not prevent the soil from cracking. He conducted digital image analysis to assess the crack extent and reported cracks as wide as 75 mm and as deep as 0.45 m. Lau (1987) used elastic and plastic equilibrium analysis in an attempt to predict the depth of desiccation cracking as shown in Figure 2-1.The mode of failure due to desiccation cracking of the soil was assumed to follow elastic equilibrium. However, the author could not verify the validity of the elastic and plastic equilibrium analyses due to lack of complete

data on the soil parameters, the actual depth of cracks, and matric suction profile in the field.

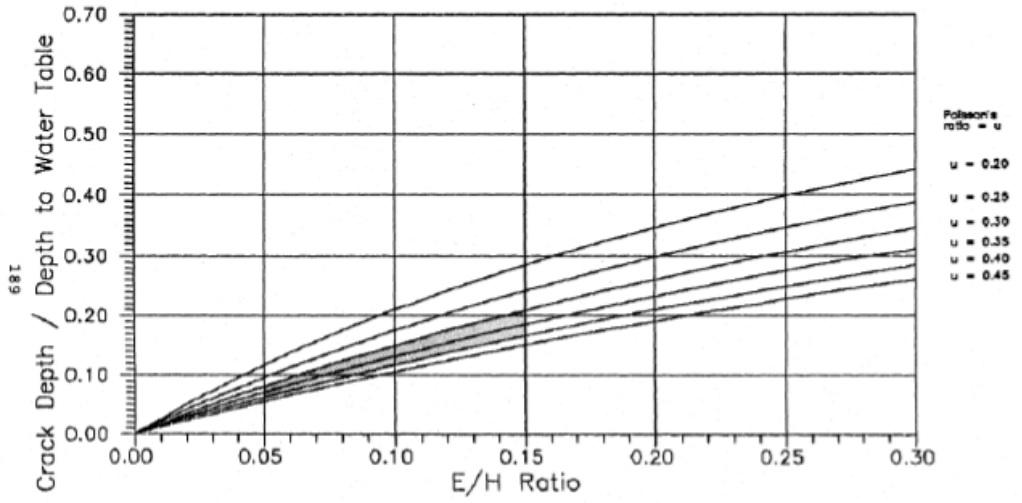

Figure 2-1 The predicted depth of cracks in Indian Head till using elastic equilibrium analysis (Lau, 1987)

2.1.4 Effects of Desiccation Cracking on the Tensile Strength

A number of studies conducted in the past indicated that an increase in initial water content increases the tensile strain at failure (Lau, 1987). Lau (1987) conducted desiccation cracking study and mentioned that soils are generally weak in tension. It is a general practice to neglect the tensile strength of the soil in the design of earth structures. Although there has been limited amount of research in the tensile properties of soil, it is reasonably assumed that the soil cracking takes place due to the evolution of tensile stress during drying. Fang and Chen (1972) demonstrated that increase in plasticity index increases the tensile strength but

decreases the unconfined compressive strength to tensile strength ratio as shown in Figure 2-2 and Figure 2-3.

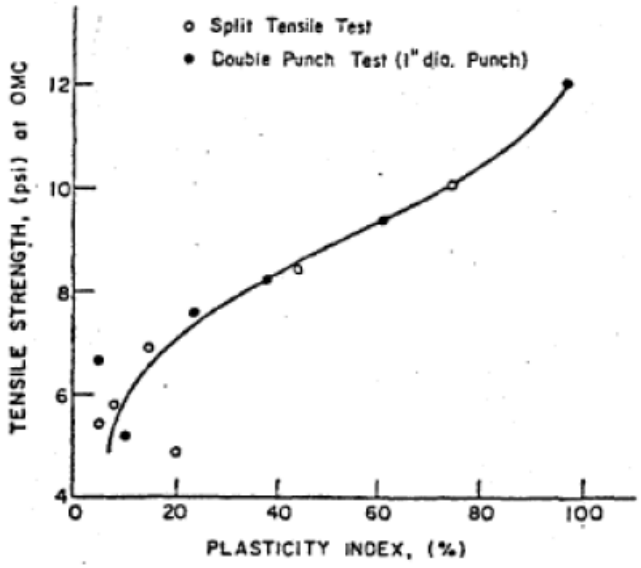

Figure 2-2 Plasticity index-tensile strength relationship (Fang and Chen, 1972)

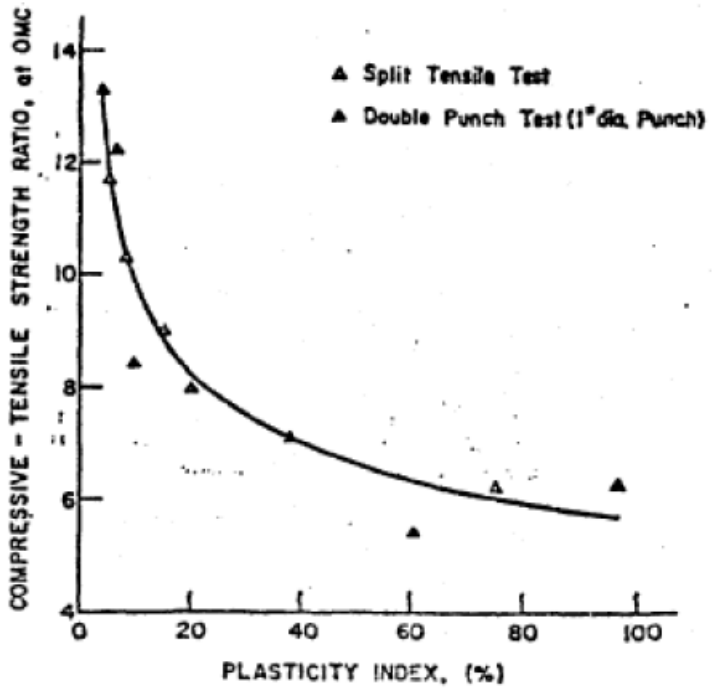

Figure 2-3. Plasticity index-compressive/tensile strength ratio relationship (Fang and Chen, 1972)

2.1.5 Effects of Desiccation Cracking on the Permeability

Vipulanandan and Leung (1991) introduced cracks and preferential flow paths in soil specimens by inserting syringe of various lengths into the compacted samples. The resulting hydraulic permeability was five times higher compared to the soil without the cracks. Omidi et al. (1996) conducted experiments on the influence of the desiccation cracks on the permeability of compacted soils. Fixed wall permeameters were used to measure the permeability. The author reported increase in permeability due to desiccation cracking as shown in Figure 2-4.

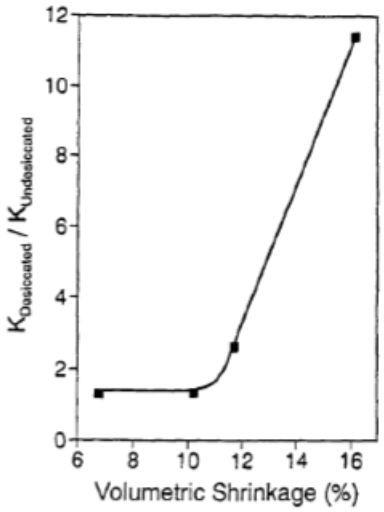

Figure 2-4 Variation in permeability with volumetric shrinkage strain (Omidi et al., 1996)

It is also apparent from Figure 2-4 that the desiccated over undesiccated permeability ratio increases by 1.3 to 11.5 times depending upon the shrinkage strain. Higher shrinkage strain is generally accompanied with more cracks thus increases the undesiccated permeability dramatically. On their study, Omidi et al. (1996) found that the effect of desiccation was small up to shrinkage strain of 11% and the effect is more prominent at shrinkage strain higher than 11%.

Dronamraju (2008) conducted laboratory experiments on different soils and concluded that soils with higher shrinkage potential strain are more likely form desiccation cracking.

2.1.6 Effects of Desiccation Cracking on Soil Suction

According to Lau (1987) the range of matric suction at the initiation of most of the desiccation cracks was 0 to 85 kPa. At higher soil suction, soil shrinks further and the crack widens. Further initiation of crack also depends on the geometry of cracking and size of intact soil segment. The authors also concluded that the desiccation cracks are generally anticipated to form at low soil suction (below 10 kPa) in most of the soils. Since the silty soils have higher compressibility compared to the clays, silts require higher matric suction at cracking. Thus, the expected matric suction at cracking for silts are mostly higher than that for clays. Some of the test results are shown in Table 2-1.

Table 2-1 A summary of cracking test results (Lau, 1987)

Cracking test no.	Time elapsed (hours)	Average matric suction (kPa)	w (%)	Average vert. strain (%)
T01	43.0	3.6	32.3	6.3
T02	35.4	3.6	32.6	6.3
T03	4.0	1.8	28.8	1.0
T04	22.5	4.5	33.0	6.9
T05	56.5	5.9	71.6	4.7
T06	81.5	11.9	27.6	9.3

2.1.7 Effects of Desiccation Cracking on the Slope Stability

Tension cracks formed at the crest of a slope generally reduce the factor of safety of the slope. Abramson et al. (2002) emphasized the role of water present in the tension cracks during rainfall. The water in the tension cracks apply

hydrostatic pressure and increase the driving force for slope failure. The author calculated the depth of the tension crack using the fundamental equation based on Rankine's earth pressure theory as:

$$z_c = \frac{2 \times c}{\gamma} \times tan^2\left(45 + \frac{\emptyset}{2}\right) \quad \text{2-1}$$

where, z_c - depth of tension crack

c – cohesion

$\emptyset$ - friction angle

γ - unit weight of soil

According to Abramson et al. (2002) the depth of the tension crack calculated based on the effective cohesion and friction angle is considerably less than calculated using undrained shear strength, because, effective cohesion is much smaller than undrained shear strength. The author recommended effective stress parameters to calculate the tension cracks in embankments and undisturbed natural slopes because undrained conditions due to sudden removal of lateral support may not have occurred. Chowdhury et al. (2010) indicated that equation proposed by Abramson et. al. (2002) is only relevant in the case of homogeneous soil because of the assumption of active Rankine state. It does not account for the geometrical effect, factor of safety, and pore water pressure within the slope.

Spencer (1973) also proposed a new equation to find the depth of desiccation cracks based on mobilized effective stress parameters and the pore pressure ratio r_u as:

$$z_c = \frac{2 \times c'_m}{\gamma(1 - r_u)} \times tan^2\left(45 + \frac{\emptyset'_m}{2}\right) \quad 2\text{-}2$$

where,

$$c'_m = \frac{c'}{FOS} \quad 2\text{-}3$$

$$\tan(\emptyset'_m) = \frac{\tan(\emptyset')}{FOS} \quad 2\text{-}4$$

$$r_c = \frac{u}{\gamma \times z} \quad 2\text{-}5$$

FOS = factor of safety

Equations 2-1 and 2-2 are identical when there is no pore pressure except that Equation 2-1 considers the total stress parameters and Equation 2-2 is expressed in terms of mobilized effective stress parameters. In Equation 2-2, the safety factor is unknown. Therefore an iterative analysis should be carried out to determine the correct values of the depth of the cracks and the factor of safety (Le, 2013).

McCarthy (2002) highlighted the effects of tension crack in the stability of a slope. According to the author, the cracks formed during the dry season get filled with water during rain. The water accumulated on such cracks exerts

hydrostatic pressure providing additional driving force for the slope movement. This action further increases the width of the shrinkage cracks and worsens the slope condition. The author illustrated this idea as shown in Figure 2-5.

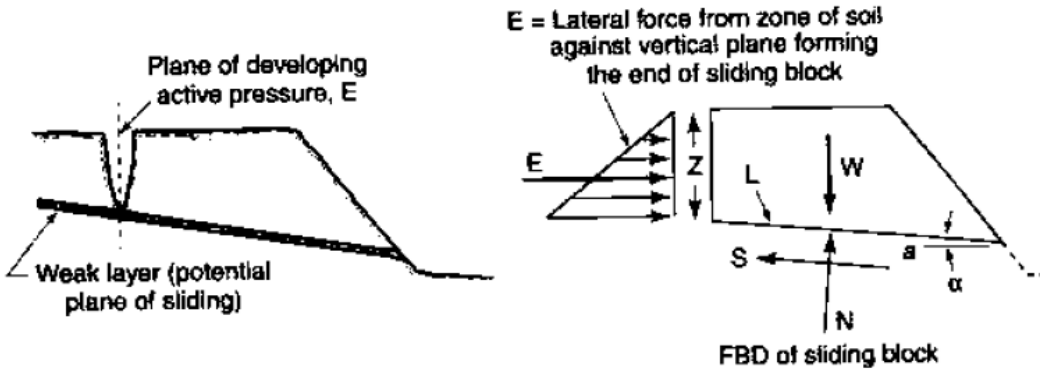

(a)

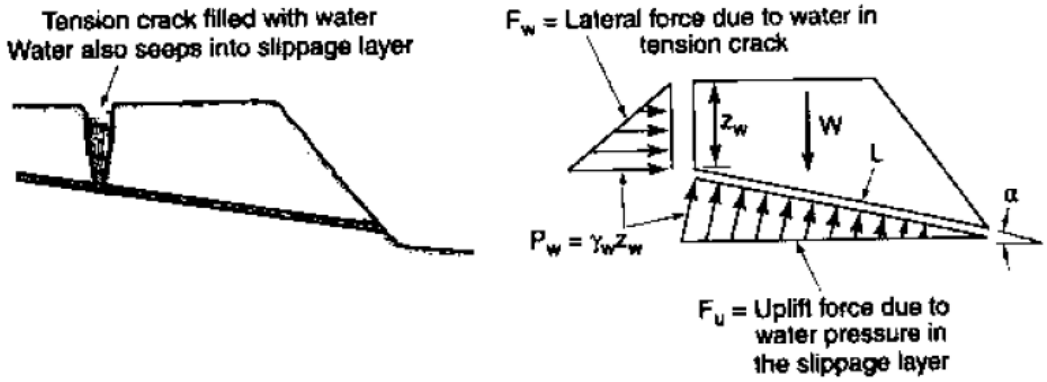

(b)

Figure 2-5 Block failure of a slope (a) influence of weak plane at top of sliding block, (b) influence of the hydrostatic pressure in the tension crack and slippage layer (McCarthy, 2002)

Based on the conditions presented in the Figure 2-5, McCarthy (2002) presented two expressions to calculate the factor of safety of a slope. For the case shown in Figure 2-5(a) he derived an expression as shown in Equation 2-6. And for the case in Figure 2-5(b) the expression is as shown in Equation 2-7.

$$FS = \frac{c \times L + (\mathrm{W} \times \cos(\alpha) + E \times \sin(\alpha)) \times \tan(\emptyset)}{W \times \sin(\alpha) + E \times \cos(\alpha)} \qquad 2\text{-}6$$

$$FS = \frac{c \times L + (\mathrm{W} \times \cos(\alpha) - F_u + F_w \times \sin(\alpha)) \times \tan(\emptyset)}{W \times \sin(\alpha) + F_w \times \cos(\alpha)} \qquad 2\text{-}7$$

where, α = the slope angle, and other notations are as shown in Figure 2-5.

2.1.8 Consideration of Tension Cracks in Stability Analysis

Some researchers have highlighted that the tension cracks do not considerably affect the factor of safety of an embankment (e.g. Spencer 1968, 1973). This statement can only be reasonable for the case of shallow tension cracks predicted by using Equations 2-1 and 2-2. Therefore the significance of the tension cracks on the stability of slopes is often discounted. However, deep tension cracks occurring in cut slopes can significantly affect the factor of safety of the slopes as in the case of slips in Bradwell (Skempton and La Rochelle, 1965). Sometimes progressive shear failure of slopes can be triggered by the tension cracks present in the slopes. Therefore, it is reasonable to carefully consider the tension cracks present in the slopes.

The shear resistance of the slip surface near desiccation cracks is often disregarded during the slope stability analysis (EM 1110-2-1902, dated 31st October, 2003). Figure 2-6 shows an example of the zone that is often discounted in the factor of safety calculations due to presence of the tension crack. If the soil in the slope has a very high cohesion intercept, tensile stresses are developed on the sides of the slices during stability analysis. The tensile stresses can also be present in the bases of the slices. This condition generally occurs near the upper part of the slip surface. These tensile stresses should be avoided unless the soil has considerable tensile strength that does not decrease with time (EM 1110-2-1902, dated 31st October, 2003). One way to avoid the tensile stresses is to create a vertical crack of a reasonable depth as depicted in Figure 2-6 (EM 1110-2-1902, dated 31st October, 2003). The part of the slip surface above the crack is then discounted in the factor of safety calculations.

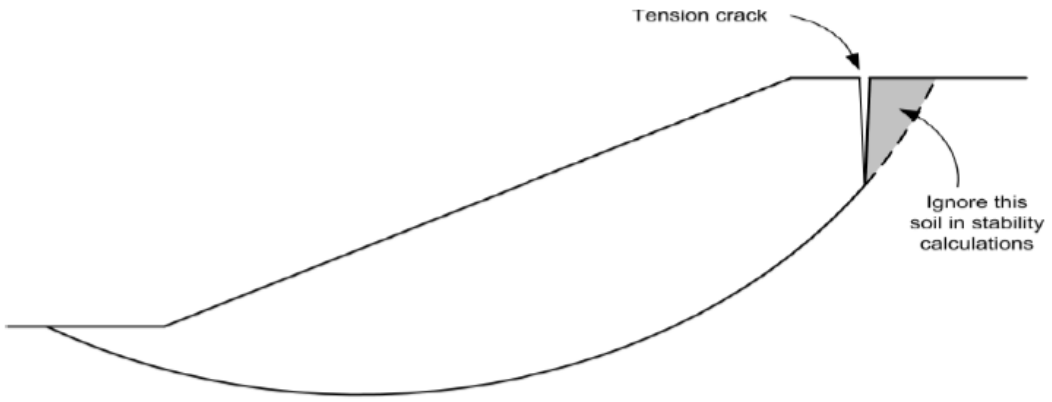

Figure 2-6 Schematic of the tension crack present in the crest (EM 1110-2-1902, dated 31st October, 2003)

2.2 Soil Treatment Methods to Mitigate Desiccation Cracking

Expansive soils are characterized as having higher volumetric swell/shrink behavior and lower to average strength properties (Puppala et al., 2006). Different treatment methods have been devised to address the desiccation cracking problems of these soils. One of the methods is chemical stabilization. Chemical stabilization primarily involves treatment of the expansive soils using lime and cement. Chemical stabilization improves soil strength and stiffness and also enhances durability. More importantly, it also limits the volumetric swelling/shrinkage of the soils (Hoyos et al., 2004). Different studies conducted in the University of Texas at Arlington (UTA) revealed that lime, fibers, and compost can be effective soil treatments for controlling desiccation cracking problems (McCleskey, 2005; Dronamraju, 2008). McCleskey (2005) explored the benefits of stabilizing two expansive soils from Grapevine and Joe Pool dam sites with lime, compost, and fibers and reported that the treatment methods were effective in controlling desiccation cracking.

2.2.1 Lime Treatment

Lime treatment is generally used for soil modification and soil stabilization. Mixing lime for stabilization of problematic soil has been used in construction for over 5000 years (Khattab et al., 2007). Compacted mixture of clay and lime were extensively used in the construction of pyramids of Shersi in

Tibet (Greaves, 1996; Little, 1995). Thus, it becomes evident that lime treatment has been historically implemented for soil improvement.

Study by Walker (1995) demonstrated that the soils with plasticity index higher than 20 are not appropriate for cement treatment because of excessive drying shrinkage, lower compressive strength and inadequate durability Guney et al. (2007) reported that the effect of lime treatment to control swelling decreased gradually with increase in the wetting-drying cycles. They also highlighted the limitation of lime stabilization technique at the places with higher wetting-drying cycles.

2.2.2 Polypropylene Fiber Treatment

Maher and Ho (1994) performed various experiments to determine the mechanical properties of kaolinite-fiber composite. The study indicated that randomly oriented fibers increased the compressive strength, ductility, tensile strength, and flexural toughness of the kaolinite clay. Nataraj and McMains (1997) also conducted compaction, direct shear, unconfined compression, and California bearing ratio tests on clay and sand reinforced with randomly distributed fibrillated fibers. The authors showed that fibers significantly increased the peak compressive strength, peak shear strength and CBR values of the clay and sand specimen. Miller and Rifai (2004) investigated the impact of fibers on the shrinkage cracking of compacted clay soils. The authors determined

that the optimum fiber content necessary to reduce desiccation cracks and increase maximum dry density was between 0.4 to 0.5%.

2.2.3 Compost Treatment

According to Puppala et al. (2004) the water holding properties and presence of fibers in compost can control the desiccation cracking of the compost stabilized subgrades. Compost can absorb moisture from the air and keep an adequate dampness in the soil to control the shrinkage related cracking of soils (Puppala et al., 2004). Intharasombat (2005) indicated that the appropriate proportion of compost resulted in reduced desiccation cracking of pavement shoulders. It was also noted that the bio-solids compost and cotton burr compost proved to be more advantageous in terms of enhancing the properties of the expansive soils among the various types of composts used. However, the compost treated soils have a drawback of high swell strains as a result of the hydrophilic characteristics of the compost (Puppala et al., 2004). The potential of the compost to control the soil erosion was explored by Xiao et al. (2006). It was found that vegetated compost and filtered compost were effective in controlling the erosion of slopes.

2.2.4 Use of Biopolymers as Soil Modifiers

Biopolymer is also called exopolymers or extracellular polymeric substances (EPS) (Sutherland, 2001). Biopolymers are often produced by microorganisms for their protection and/or to make the environment more

hospitable for their living (Maier et al. 2000). A biopolymer is an organic polymer that is produced naturally from living things. The biopolymers are mostly high molecular weight polysaccharides. These polysaccharides contain chemically active groups with electrical charges which make them actively interact with clay minerals (Sutherland 2001). Therefore, biopolymers are likely to affect soil behavior and engineering properties in different ways. In particular, the biopolymers should enhance the shear strength of soil to reduce erosion and surficial failure of slopes (Nugent, 2011). Dade et al. (1990) demonstrated that a biofilm produced by Alteromonas atlantica in sand can significantly increase its critical shear velocity required to start erosion.

The natural benefits of biopolymer is surface adhesion, self-adhesion of cells into biofilm, formation of protective barriers, water retention around roots of vegetation, and nutrient accumulation (Larson et al., 2012). Larson et al. (2012) studied the effectiveness of the biopolymer to increase slope stability, and reduce transport of solids in runoff water, reduce transport of heavy metals from small arm firing ranges, and reduce generation of dust. The authors selected four soil types for biopolymer treatment: silty sand, sandy silt, silt, and silty clay. Biopolymer extracted from Rhizobium tropici was used in this study. The study revealed that the biopolymer soil treatment effectively maintained the slope stability. Furthermore, the biopolymer treated soil produced lesser amount of dust compared to that of control soil at all relative humidity. Figure 2-7 shows the

experimental set up to study the erosion of the slope with and without the biopolymer treatment. The authors simulated one year rainfall event within 12 weeks, each week providing one month equivalent of weathering. Figure 2-8 shows the mass of soil retained in the simulated berms at the end of the experiments. The control soils seemed to lose significant amount of soil from the simulated berms. Whereas, the sections treated with biopolymers looked to retain higher amount of soil for similar rainfall events. Biopolymer dosage of 0.5% performed well as shown in the Figure 2-8.

Figure 2-7 Experimental set up to study the erosion of the slope with and without the biopolymer treatment (Larson et al., 2012)

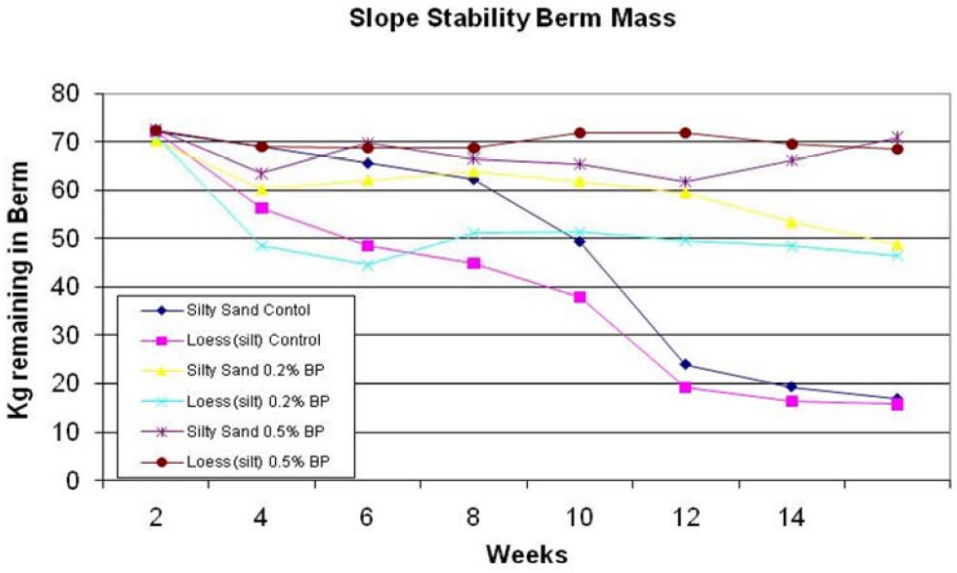

Figure 2-8 Soil mass lost at different biopolymer loading rate (Larson et al. 2012)

Larson et al. (2013) conducted field experiments on the biopolymer treated berm at Iowa army Ammunition Plant (IAAAP). The authors used different application methods for biopolymer treatment and planted fescue seeds on the treated and control slopes. Change in slope angle and surface roughness over time were compared for treated and untreated areas of the berm using LIDAR imaging technology as shown in Figure 2-9. The authors also compared the establishment of grass in the treated and control areas. Single surface application of the biopolymer and grass seeding using a hydroseeder was the most effective and simplest application method. All treated soils had higher amount of grass and root growth than the control area. Figure 2-10 shows the comparison between the control (left) and biopolymer treated section (right) after six months

of weathering. The average biomass of fescue grass in the biopolymer treated section increased significantly compared to the untreated area. Also the control section experienced excessive rutting compared to the biopolymer treated section.

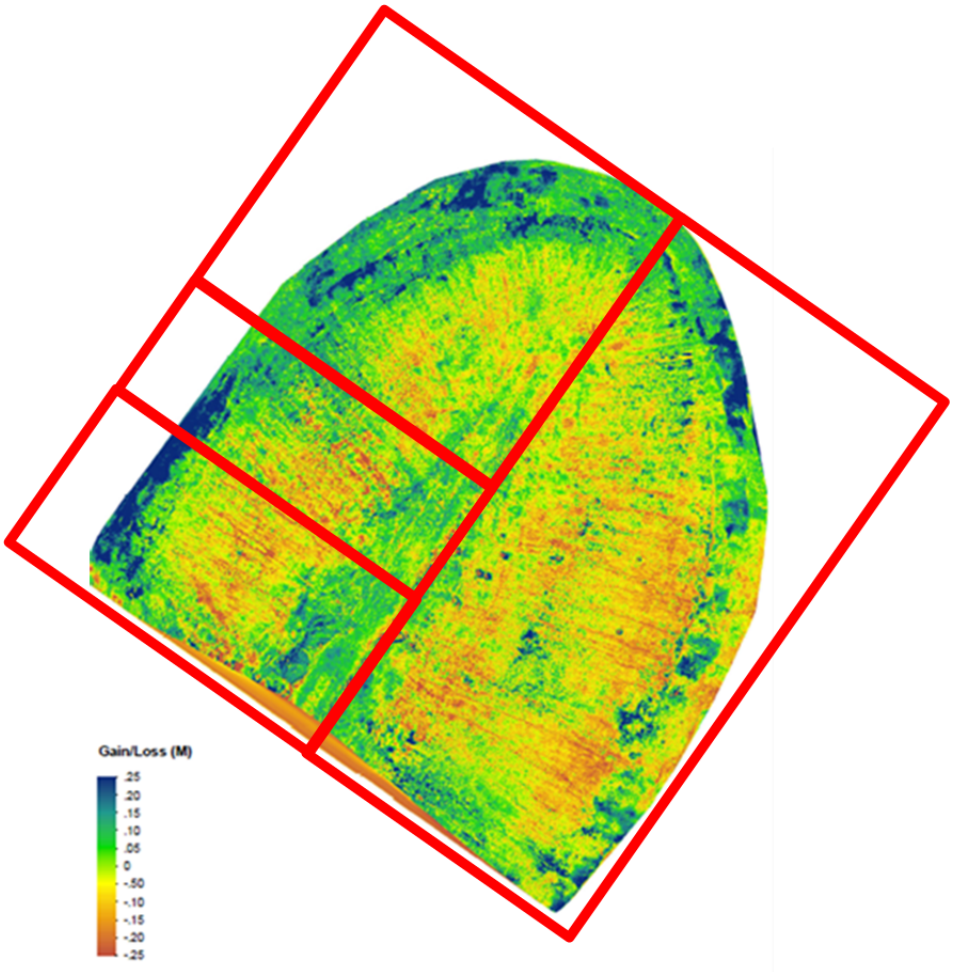

Figure 2-9 LIDAR image of the top view of berm showing changes in soil elevation (net gain and loss) by color differences (Larson et al., 2013)

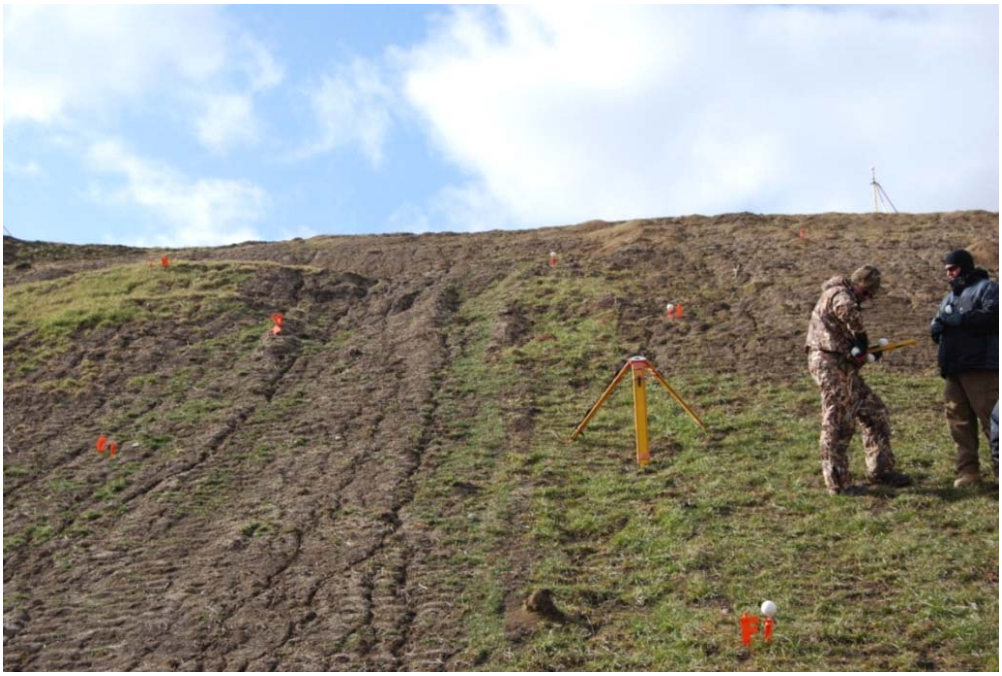

Figure 2-10 Comparison of surface rutting and vegetative growth after 6 months of weathering between control and biopolymer treated section (Larson et al., 2013)

Ivanov and Chu (2008) mentioned that the biopolymers produced by the microbes can be used for bioclogging and biocementation. Bioclogging is the production of pore-filling materials to decrease the hydraulic conductivity of soil. Biocementation is the production of binding materials through microbial processes to increase the soil shear strength. According to Ivanov and Chu (2008), facultative anaerobic bacteria and microaerophilic bacteria are the most suitable microorganisms for bioclogging or biocementation.

DeJong et al. (2013) assessed the progress, opportunities, and challenges in the field of biogeotechnology. According to the authors, the surface microbial processes can be applicable for mineral precipitation, gas generation, biofilm formation, and biopolymer generation. In addition, biogeotechnology can be applicable in achieving the cementation of sands to enhance bearing capacity and liquefaction resistance, carbon sequestration, soil erosion control, groundwater flow control, and remediation of soil and groundwater impacted by metals and radio-nuclides. DeJong et al. (2013) also mentioned that there are different challenges in biomediated ground improvement including successful implementation of laboratory processes in the field, in situ monitoring of reactions, product and properties, management of the by-products, and maintaining the longevity of the process.

Mitchell and Santamarina (2005) stated that biogeotechnology can modify the hydraulic conductivity, diffusion, and shear strength of the coarse grained soils. They also mentioned that extensive research is needed to clearly understand the effect of biomediated reactions on soil behavior. DeJong et al. (2008) indicated that compatibility between soil matrix and microbial size is the main aspect controlling the range of soils that can be improved by a given microbe through in-situ injection. Pre mixing of microbes with soils can improve the effectiveness of the treatment wherever applicable. The authors also stated that calcite precipitation reduces the pore space and imparts densification of the soil.

When the soil is subjected to shear or tension loading, it results in the breakage of the precipitated calcite and not the calcite and silica bond. It indicates that the calcite forms a stronger bond with the soil particles.

Chen et al. (2013) conducted a feasibility study on using xanthan gum and guar gum biopolymers to stabilize mine tailings. These biopolymers are naturally occurring biopolymers. Xanthan gum is an anionic bacterial extracellular polysaccharide and guar gum is a neutrally charged plant polysaccharide. The authors evaluated the liquid limit and the undrained shear strength of the sun dried mine tailing mixed with the biopolymer solutions at different dosages. The biopolymer increased both liquid limit and undrained shear strength and higher dosages yielding higher values. The authors attributed the increase in the liquid limit and the undrained shear strength to the high viscosity of the biopolymer solution present in the pores and the bonding between the biopolymer and mine tailing particles. The authors found guar gum to be more effective than xanthan gum due to higher viscosity of the guar gum solution than the xanthan gum solution at same concentration. Similar result was presented in a different study conducted by Nugent et al. (2009). Guar gum provided better particle bonding and lower degree of aggregation than the xanthan gum. Figure 2-11 shows the increase in undrained shear strength of the mine tailings at different dosages of biopolymer. It also shows the viscosity of the biopolymer solutions at 30% water content.

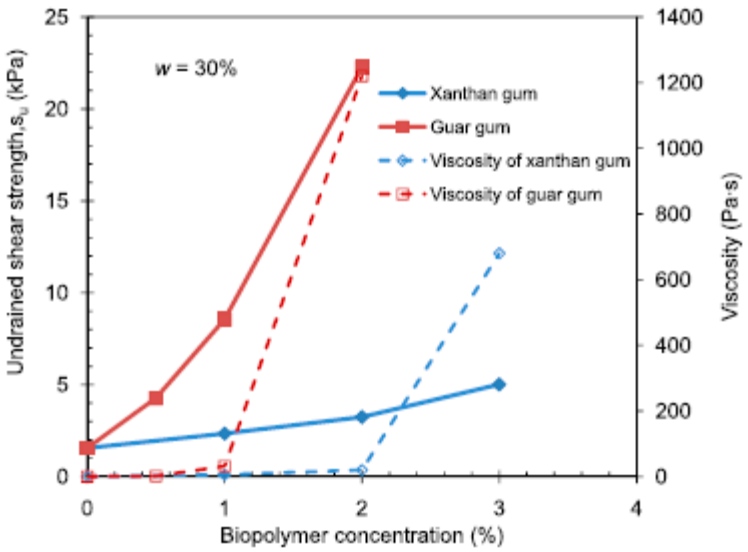

Figure 2-11 Biopolymer concentration versus undrained shear strength of mine tailing and viscosity of biopolymer solutions at water content of 30% (Chen et al., 2013)

Nugent et al. (2009) also studied the effect of the xanthan gum and guar gum biopolymers on the liquid limit of a kaolinite clay using varied biopolymer concentrations and background cations (Ca_2, Na, or K) in the pore fluid. The authors indicated that the liquid limit of the clay was increased due to biopolymers. The authors attributed the increase in the liquid limit to the increase in the viscosity of the pore liquid due to biopolymer. It was also found that the background cations present in the pore fluid alter the liquid limit of the soil. The key observations made in the study were: the liquid limit is likely to be decreased due to biopolymer-induced aggregation of clay particles; biopolymer solution viscosity is significantly increased by the polymer cross-linking consequently

increasing the liquid limit; the increase in liquid limit is also imparted in part by the formation of a clay-polymer interconnected network via cation bridging and hydrogen bonds; the electric double layer thickness is decreased and hence the liquid limit; and preferred adsorption of monovalent cations over biopolymer molecules decreases the liquid limit. The variations in the liquid limit is the net result of the all these interactions happening in the nanoscale (Nugent et al., 2009).

Nugent et al. (2011) studied the effect of xanthan gum and guar gum biopolymers on the erosional resistance of kaolinite. The authors used a cohesive strength meter to determine the critical value of shear stress (τ_{oCr}) of high water content muds. These high water content muds were considered representative of new hydraulically placed fill. The soil modified by guar gum showed nine times increase in the τ_{oCr}. Xanthan gum also increased the critical value of shear stress but provided much less improvement than guar gum in cations free mixtures because of electrostatic repulsion. However, cations in the pore fluid balance the repulsive effect and allow xanthan gum to establish a hydrogen bonding network between xanthan gum strands and kaolinite (Nugent et al. 2011). Cations responsible for forming biopolymer cross-linking often increase aggregation, and this tend to partly reduce the erosional resistance.

D'Cunha et al. (2009) studied the effect of biopolymer gel in reducing the permeability of the soil for the modification of preferential flow paths. The study

was focused in removing the residual Dense Non-aqueous Phase Liquids (DNAPL) from low permeability zone after the bulk phase has been removed. In the removal process of DNAPL from aquifer, the drive fluid sweeps through the path of high permeability leaving the residual contaminants in the zone of smaller permeability. The authors used biopolymer gel as sealant to block the preferential flow path so as to remove the DNAPL from low permeability zones. Based on the laboratory study, it was found that the biopolymer gel was effective in sealing the preferential glow paths and the residual DNAPL was reduced in volume by 90% of the total volume of residual DNAPL.

Khatami and O'Kelly (2013) tested biopolymer treated sand to study the improvement in strength of cohesionless soils. Agar and six modified starches were used as biopolymers over a range of concentrations, 1-4% agar and 0.5-1% starch. Fine sand with a particle size ranging from 0.06 to 0.4 mm was used in the study. Biopolymer treated cylindrical specimen were prepared to conduct unconfined compression strength test and unconsolidated undrained triaxial compression tests. Figure 2-12 shows the failure mode of a biopolymer treated cylindrical sand specimen during unconfined compression strength test. And, Figure 2-13 shows the unconfined compression strength of the sand when mixed with different dosages of the biopolymer. The authors indicated that the biopolymers can effectively improve the strength characteristics of sand. The increase in the strength of the sand was found to be directly dependent on the

concentration of the biopolymer. This study demonstrated that the biopolymer treatment can be used as an effective tool to modify soil behavior in terms of level of stiffness or ductility (Khatami and O'Kelly 2013).

Figure 2-12 Failure mode of a biopolymer treated sand specimen (Khatami and O'Kelly 2013)

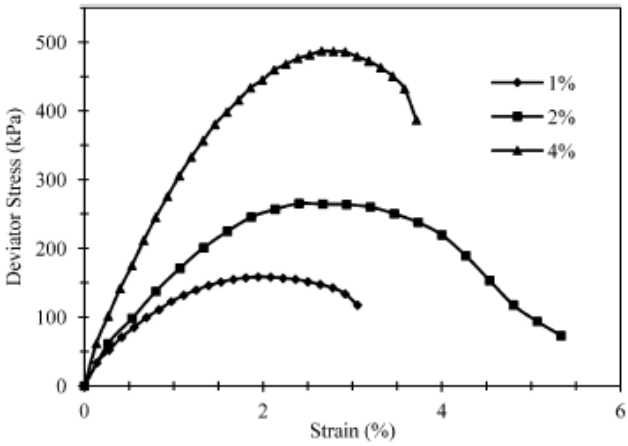

Figure 2-13 Unconfined compression test of sand treated with different dosages of biopolymer (Khatami and O'Kelly 2013)

Cole et al. (2012) studied the small-scale mechanical properties of biopolymers to improve the understanding of precisely how biopolymers strengthen soil. The authors presented the efforts in developing suitable methods to form biopolymer bonds in the granular materials. The results of the mechanical properties experiments on these bonds were also presented. An exopolysaccharide (EPS) biopolymer produced by Rhizobium tropici was used in the experiment. It was found that the stiffness of the bonds ranged from 1 GPa to 3.8 GPa after curing of 1 hour to extended curing times. The tensile strength of the bonds ranged from 16 to 62 MPa for bonds with neck area range of 0.01 to 0.06 mm^2. The cohesive failure strains during tensile loading ranged from 1.3 to 4.2%. Figure 2-14 shows the microscopic image of the bond between grains and the shrinkage of the biopolymer bond at different times after placement.

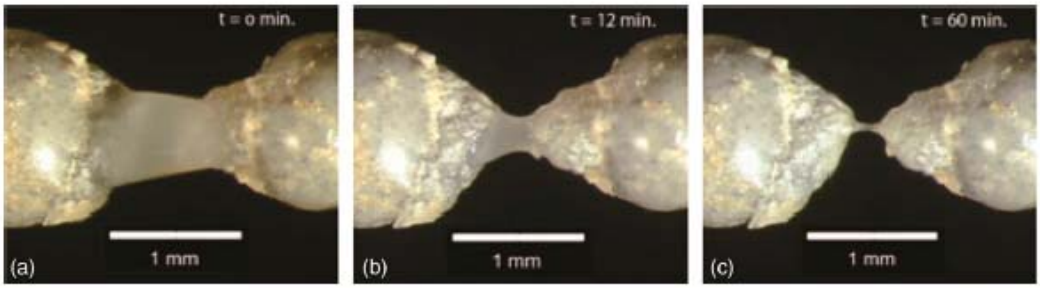

Figure 2-14 The biopolymer bond between two grains and the extent of shrinkage in the bond material (a) immediately after placement, (b) after 12 minutes and (c) after 60 min (Cole et al., 2012)

Chang and Cho (2012) used β-1,3/1,6-glucan biopolymer to stabilize a Korean residual soil called hwangtoh. Commercially available liquid gel of β-1,3/1,6-glucan biopolymer was mixed with the residual soil at different dosages and then cured at different temperatures. The compressive strength of the biopolymer treated residual soil was determined at different curing times. Results showed a significant increase in the compressive strength of residual soil that was attributed mainly to the particle surface adsorption and tensile strength of β-1,3/1,6-glucan biopolymer. Figure 2-15 shows the unconfined compressive strength test result of β-1,3/1,6-glucan treated Korean residual soil cured at 20^{o}C for different time period.

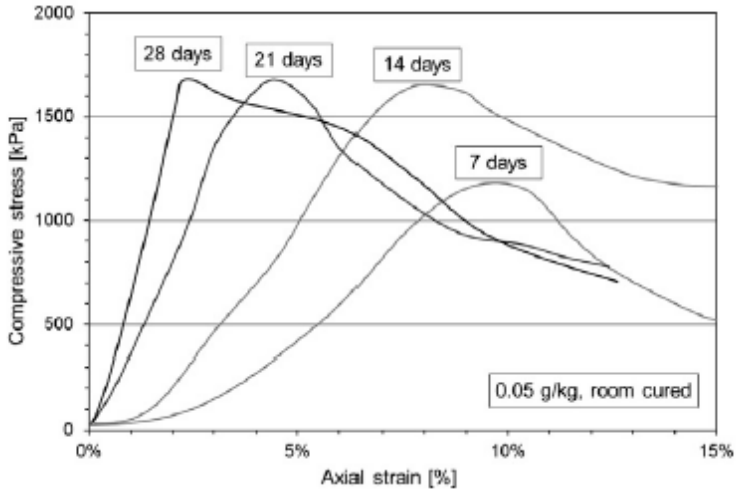

Figure 2-15 Unconfined compressive test results of β-1,3/1,6-glucan treated Korean residual soil with time (Chang and Cho, 2012)

Lai et al. (2014) studied the crosslinking reaction caused by blending different biopolymers and/or adding a crosslinking agent. The authors found that the crosslinked material showed a polymeric volume change and a viscosity increase because of chemical functional groups to form intra- and interpenetrating polymer networks (IPNs). The IPNs serve as a basic building block for a three-dimensional crosslinked biopolymer structure. This crosslinked biopolymer structure can be utilized in various applications such as an environmental barrier or containment to encapsulate and treat hazardous materials against toxic flow in a subsurface system (Lai et al., 2014).

Maghchiche et al. (2010) used biopolymers for water retaining and soil stabilization in arid and semiarid regions. The authors analyzed the effect of cellulose on arid and semiarid soil in North Africa. The biopolymer was characterized by viscosity, infrared spectroscopy, X-ray diffractometry, thermal analysis and scanning electron micrographs. It was found that the 0.5 g/L cellulose combined with 10 mg/L polyacrylamide could increase 60% water retention at arid soils compared with other polymers. This effect can be helpful in controlling the desiccation cracking of the expansive soils.

Orts et al. (2007) reported that application of low concentration of anionic, high purity polyacrylamide (PAM) reduces sediment in runoff water by more than 90% when added to irrigation water at rate of 1 to 2 kg ha^{-1} per irrigation.

2.3 Determining the Internal Stresses in a Drying Soil

Various environmental factors such as temperature, cyclic wetting and drying, relative humidity that are instrumental in imparting highly non-linear shrinkage behavior in the drying soil making the study of cracking more complex (Kodikara and Costa, 2013). Experimental modeling of desiccation cracking of soils was first conducted on rectangular boxes (Corte and Higashi, 1960; Miller et al., 1998; Yesiller et al., 2000; Laxmikantha et al., 2006). Nahlawi and Kodikara (2006) introduced experimental tests using long molds. The experiments were controlled to produce parallel cracks perpendicular to the axis of the mold. Kindle (1917), Groisman and Kaplan (1994), Toramaru and Matsumoto (2004), Costa (2009), and Puppala et al (2011) conducted experiments on circular specimens. Later Costa (2009) introduced image analysis to capture the shrinkage strain development of the drying clay samples. Konard and Ayad (1997) investigated cracking and patterns in field cell in soft clay.

Various interactions taking place among soil particles and pore fluids are the sources of the evolution of internal stresses in a drying soil mass (Abou Najm et al., 2009). Internal stresses in soils can occur due to natural as well as human induced activities. Suction, soil structure, physicochemical forces can control the internal stresses. However, assessing these internal stresses and linking these to soil behavior is still a challenge. Abou Najm et al. (2009) related the internal stresses to the water content using the restrained ring test. In current state of the

art, researchers use empirical correlation between matric suction and moisture content as well as shrinkage/swelling curves or effective stress theory in case of saturated soils (Terzaghi, 1936) and unsaturated soils (Bishop, 1959). Internal loading such as moisture gradient, and external loading such as load from foundation also contribute to stresses in the soil. Experimental studies have revealed that internal stresses develop when soil lose moisture and shrinks causing the change in the pore water pressure, shear strength (Escario and Saez, 1986, Fredlund et al., 1987), and compressive strength (Aitchison, 1957) . Soil internal stresses have been generally understood through the perspective of effective stress theory accounting for suction (Abou Najm et al., 2009).

Abou Najm et al. (2009) and Costa (2009) introduced restrained ring test to determine the tensile strength of soils at which shrinkage cracks initiate. Recently, Puppala et al. (2011) devised a new test to determine the shrinkage induced pressure in a drying soil. This test gave insight into the role of shrinkage induced pressure as a part of desiccation cracking from drying environment.

Abou Njam et al. (2009) used a restrained ring to measure the internal stresses in the unsaturated soil during drying. The authors calibrated a restraining ring by measuring the hoop strain occurring due to known radial stress. The calibrated ring was then used to monitor the hoop strain induced on the ring from the drying soil at different moisture contents until a crack appears in the soil sample. The radial and hoop stresses developed on the soil sample were back

calculated using hoop strain measured during the test. The schematic diagram of the restrained ring test is presented in Figure 2-16.

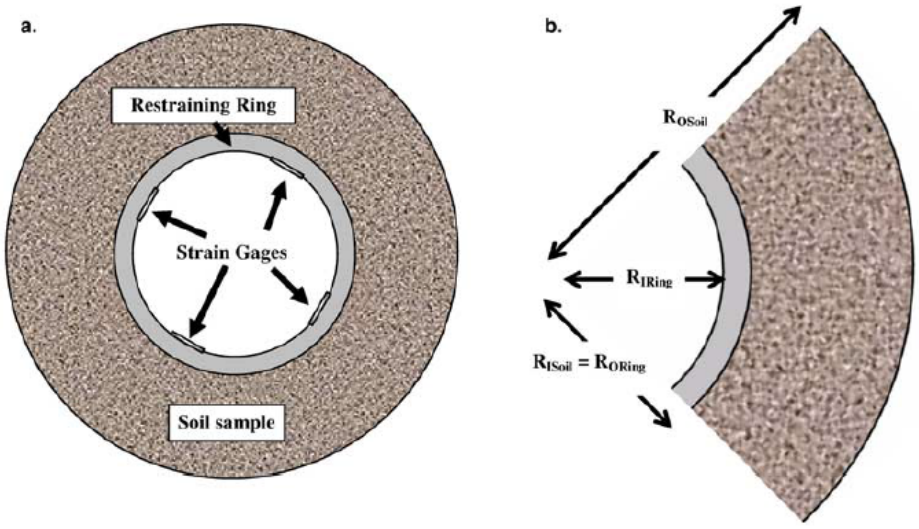

Figure 2-16(a,b) Schematic diagram of the restrained ring experiment (Abou Njam et al., 2009)

The internal stresses in the tangential direction (σ_θ) and radial direction (σ_r) can be calculated as shown below:

$$P_{Internal,Isoil(t)=}-\varepsilon(t)_{Ring}E_{Ring}\frac{\left(R^2{}_{ORing}-R^2{}_{IRing}\right)}{2R^2{}_{ORing}} \quad 2\text{-}8$$

$$\sigma_{\theta=}P_{Internal,Isoil}\frac{\left(R^2{}_{ORing}\right)}{R^2{}_{OSoil}-R^2{}_{ORing}}\left(1+\frac{R^2{}_{OSoil}}{r^2}\right) \quad 2\text{-}9$$

$$\sigma_{r=}P_{Internal,Isoil}\frac{\left(R^2{}_{ORing}\right)}{R^2{}_{OSoil}-R^2{}_{ORing}}\left(1-\frac{R^2{}_{ORing}}{r^2}\right) \quad 2\text{-}10$$

Where, $P_{Internal,Isoil(t)}$ is the internal compressive stress acting on the restraining ring, $\varepsilon(t)_{Ring}$ is the time dependent strain measured at the inner surface of the restraining ring, R_{IRing} is the inside radius and R_{ORing} outside radius of the restraining ring, and E_{Ring} is the modulus of elasticity of restraining ring. The radial compressive stress and the hoop stress both are the maximum at the ring soil interface and decrease gradually towards the outer radius of the sample. The radial stress becomes zero at the sample outer boundary whereas the hoop stress will be the minimum, but not necessarily zero.

Kodikara and Choi (2006) presented a simplified analytical model for desiccation cracking of clay layers in laboratory tests as shown in Figure 2-17. The authors presented an analytical solution for maximum tensile stress developed at the mid-section of the soil layer as shown below:

$$\sigma_{x,max} = E\alpha\Delta w\left[1 - \frac{1}{cosh(\beta L/2)}\right] \qquad 2\text{-}11$$

where, E is Young's modulus of clay, α is rate of change in linear shrinkage strain with change in moisture content, Δw is change in moisture content, β is a parameter depends on interface shear stiffness, Young's modulus, and cross section area of soil layer, and L is the length of the soil layer.

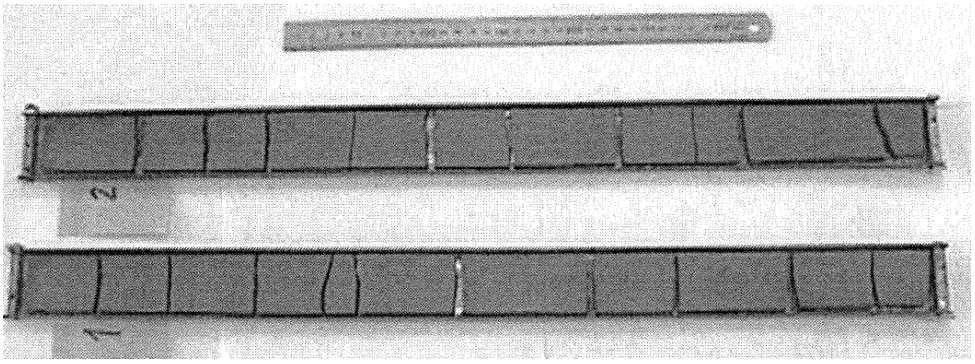

Figure 2-17 Cracking pattern of compacted clay in long molds (Kodikara and Choi, 2006)

2.3.1 Inter-particle Forces During Drying

According to Raj (2008) particle size can give an indirect measure of the inter-particle forces. Depending upon the nature of the interaction between particles, the inter-particle forces can be broadly classified as gravitational forces (or mass derived forces), and surface bonding forces (or surface-derived forces). According to Terzaghi et al. (1996), if the soil particles are smaller than about 0.002 mm, the influence of mass derived forces become less significant compared to the surfaced-derived forces. According to Ranjan and Rao (2005), the nature of the ions present, their size and concentration, and other environmental conditions are the major factors that detect the interaction between clay particles. The net force between the particles is the algebraic sum of the attractive and repulsive forces. The inter-particle force decreases with increase in distance from the surface (Ranjan and Rao, 2005).

2.4 Expansive Soils

Expansive soils are the soils that expand when in contact with moisture, and shrink upon drying. These soils are very problematic to structures and often avoided in constructions. These kinds of soils are predominantly present in semi-arid (Jones and Holtz, 1973). The mineralogical composition and pore size distribution of soils mainly detect the swell-shrink behavior of expansive soils (Pedarla, 2013). Past stress history conditions as well as prevailing stress conditions in part influence the expansive behavior of soils. These soils often have damaging effects on pavements and other civil structures. And, according to Nelson and Miller (1992) soil characteristics, environmental factors, and state of stresses are the major parameters dictating the swell-shrink behavior of a subgrade soil. Although these soils are considered unsuitable for urban infrastructure construction, rapid population growth and urbanization has made it difficult to avoid these areas (Williams, 2003). Consequently, damages in infrastructures due to expansive soils have increased dramatically. According to Jones and Holtz (1973), the annual damage costs were estimated about $2 to $9 billion in the United States alone. The authors also mentioned that the these damages cost more than damages due to earthquakes, floods, hurricanes and tornadoes. Figure 2-18 shows the areas where expansive soils are found in abundance in the United States.

The areas highlighted in Figure 6 experience subsoil related problems that are mainly attributed to volumetric shrinkage and swelling occurring long dry periods and subsequent periods of heavy rain in short duration (Chen, 1988; Nelson and Miller, 1992). The repeated swell-shrink actions of expansive soils impart serious distress to infrastructures like pavements and light buildings. Some of the associated problems are discussed below.

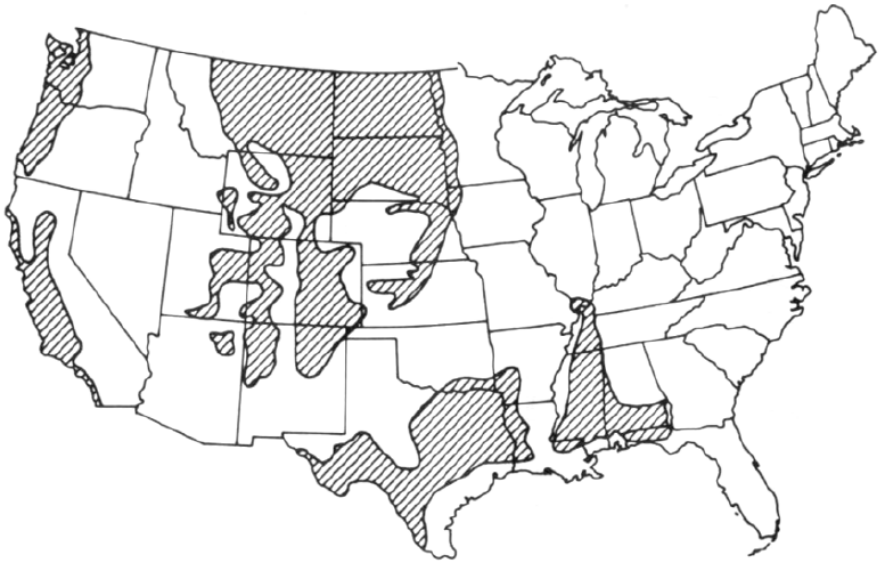

Figure 2-18 Areas encompassing expansive soils in the United States (Chen, 1988)

2.4.1 Expansive Soil Problems

2.4.1.1 Slope failures

Expansive soils are one of the prime causes for many slope failures. McCleskey et al. (2008) presented the surficial slope failures of Grapevine dam in North Texas. The nearby borrow material used in the construction of the dam

invariably contained the expansive soils present in that region. The slope of the dam experienced desiccation induced cracking during long dry spells. Water infiltrated into the slope during rainfall through the opening created by desiccation cracks. Infiltration of rain water increased the pore water pressure in the slope and reduced the soil strength. That ultimately triggered the surficial slope failures (McCleskey et al., 2008). Water entering through the desiccation induced cracks during rainfall often gets stored in these cracks. Thus the water exerts hydrostatic pressure and initiates a failure starting from the crack position. Examples of surficial slope failures occurring in the Joe Pool dam and Grapevine Dam in the state of Texas are shown in Figure 2-20 (a) and (b) respectively. These figures clearly show the damaging effects and extent of destruction in these dam slopes.

Figure 2-19 Surficial slope failures triggered due to desiccation cracks in Joe Pool dam (McCleskey et al., 2008)

Figure 2-20. Surficial slope failures triggered due to desiccation cracks in Grapevine dam (McCleskey et al., 2008)

2.4.1.2 Building foundation failures

Al Rawas et al. (2005) investigated the building foundation failures due to expansive soils in the Arabian Gulf. The mineralogical compositions of rocks and expansive soils present in northern Oman were studied. The authors employed x-ray diffraction technique in their study and identified that the smectite clay mineral present in the expansive soil in the region was the reason for the foundation failures. The authors found only small amount of Kaolinite, Illite, and Palygorskite in the expansive soils under the investigation. The authors indicated the presence of smectite clay mineral as the primary reason for the swelling. A secondary mechanism of swelling was observed due to presence of gypsum.

2.4.1.3 Pavement failures

Distortion and cracking of the pavement is a common problem caused by expansive soils. Desiccation cracking of the underlying subgrade soil during dry period imparts poor support to the pavement layers and induce the failure of the pavement. In addition, swelling of the expansive subgrade soil at the locations of poor drainage conditions result in heaving of the pavement layers. Differential swelling of the pavement layers induce shear forces and moments on pavement. If the pavement is not designed to address such kind of loadings, failure of the pavement is inevitable.

The extent of cracking and damages of the pavement layers can be extensive and sometimes be higher than the original construction costs. Puppala et al. (2012) investigated the performance of pavements traversing expansive soils. Lime stabilization technique was found to be effective to alleviate the distress on the pavements. Figure 2-21 shows an example of pavement distress due to shrink-swell action.

Figure 2-21 Shrink-swell induced pavement distress (Puppala et al., 2012)

2.5 Clay Mineralogy

Mineralogical composition is a most important property of fine grained soils. According to Terzaghi et al. (1996), the force of gravity acting on clay particles are very small compared to the electrical forces acting at the surface of the particle. A material with predominant surface charge is considered to be in the colloidal state. The colloidal particles present in the soils are mainly the clay particles (Terzaghi et al., 1996). The clay minerals are generally formed from weathering of rock. However, the clay minerals have a different crystal structures than the parent minerals (Terzaghi et al., 1996). The various kind of minerals found in clay are Kaolinite, Halloysite, Allophane, Illite, Chlorite, Montmorillonite, and Attapulgite (Terzaghi et. al. 1996). However, the most

common minerals found in clays are Kaolinite, Illite and Montmorillonite. The swelling and shrinkage behavior of clay soils are primarily governed by the mineralogical composition (Terzaghi et. al. 1996). . The clay minerals are crystalline hydrous aluminosilicates forming a lattice structure formed by atoms placed in layers. And each of the clay minerals has a different arrangement and chemical composition (Terzaghi et al., 1996).

Clay minerals consist of silica tetrahedron and alumina octahedron units. They form tetrahedral and octahedral layers respectively, different combination of which makes a unit sheet of the various types of clay (Terzaghi et al., 1996). Therefore clay minerals are part of a family called phyllosilicates or layered silicates. Many sheets of films like this pile together to make a single particle of clay (Terzaghi et al., 1996). The layering arrangement of these silica and alumina sheets detect clay mineral group. The surface of the clay particles ordinarily carry negative charge, however, negative or positive charge can occur on the broken edge of the particle (Terzaghi et al., 1996). Figure 2-22 shows different type of clay minerals structures.

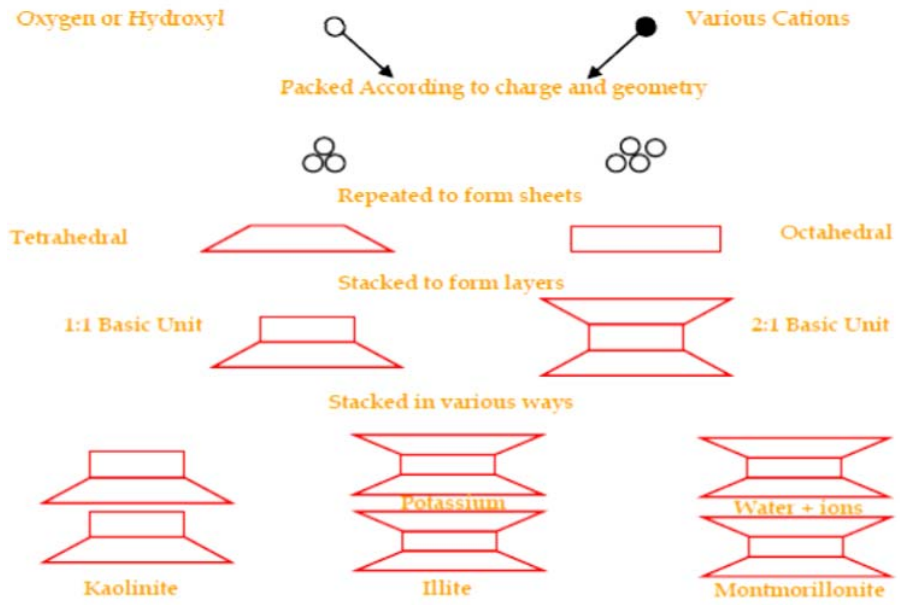

Figure 2-22 Schematic of different structures of dominant clay minerals (Chittoori, 2008)

Generally, different types of minerals present in a clayey soil are indirectly identified by conducting the tests like specific surface area (SSA), cation exchange capacity (CEC), and total potassium (TP). Cations present on the clay particles can be replaced by other cations. For example, potassium can be replaced by calcium or hydrogen. Thus, these cations are exchangeable cations. CEC is the quantity of the exchangeable cations required to balance the negative surface charge. CEC is measured in miliequivalents per 100 g of dry soil. A higher value of CEC suggests presence of highly active minerals like Montmorillonite. Similarly SSA and TP also add in identifying and quantifying

different minerals in clay soils. For example, Chittoori and Puppala (2011) identified different clay minerals percentages based on the measurement of CEC, TP and SSA. Details of the measurement techniques of these properties are elaborated in the next chapter.

2.5.1 Illite

Illite is a most common type of clay mineral present in stiff clays (Terzaghi et al., 1996). It is also referred as weathered mica or fine grained mica. In macroscopic form, the crystal structure of mica is comparable to muscovite mica in because its primary unit is a layer consists of two silica tetragonal sheets. However, the stacking of the sheets in the microscopic level is not as regular compared to that in well-crystallized mica. Figure 2-23 presents the structure of the mineral Illite as well as its scanning electron micrograph (SEM). In general, Illite particles are 10 to 30 nm in thickness, have breadth/thickness ration of 15 to 30, and have SSA of 80 to 100 m^2/g.

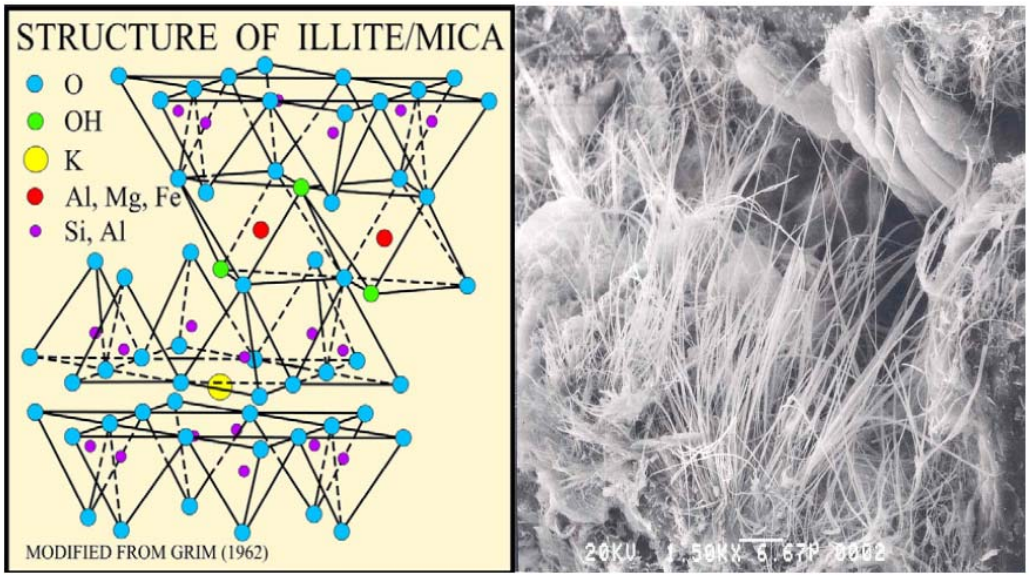

Figure 2-23 Structure and SEM of mineral Illite (Source: http://en.wikipedia.org/wiki/File:Illstruc.JPG)

High concentrations of Aluminum and Potassium in an alkaline environment facilitate the formation of Illite (Thompson and Ukrainczyk, 2002). In micas, the locations of contact points are less which results in the weaker cohesive forces among the crystallites (Thompson and Ukrainczyk, 2002).

2.5.2 Kaolinite

Kaolinite is one of the most commonly present clay minerals in sedimentary and residual soils. A unit sheet of Kaolinite consists of alternate silicon tetrahedral layer and aluminum octahedral layer with shared oxygen in-between (Terzaghi e al., 1996). A unit sheet of kaolinite is 0.7 nm thick. The aluminum oxide/hydroxide sheets are called gibbsite sheets. The bond between gibbsite sheets and the layers is generally weaker which results in cleavage and

softness of the mineral (Mitchell and Soga, 2005). The structure of Kaolinite and the Serpentine Group are alike and these groups are often considered as one Kaolinite-serpentine group. Kaolinite has the same chemical structure as that of minerals Nacrite, Dickite, and Halloysite. All four minerals form by alterations of aluminum rich silicate minerals such as feldspars. A typical particle of kaolinite consists of a pile of sheets forming a stiff hexagonal plate with flat-faced edges (Terzaghi et al., 1996). A kaolinite particle is approximately 100 nm thick and has a breadth/thickness ratio of about 5 to 10. The specific surface area of Kaolinite is about 5 to 10 m^2/g (Terzaghi et al., 1996). Figure 2-24 shows the structure and SEM of kaolinite mineral.

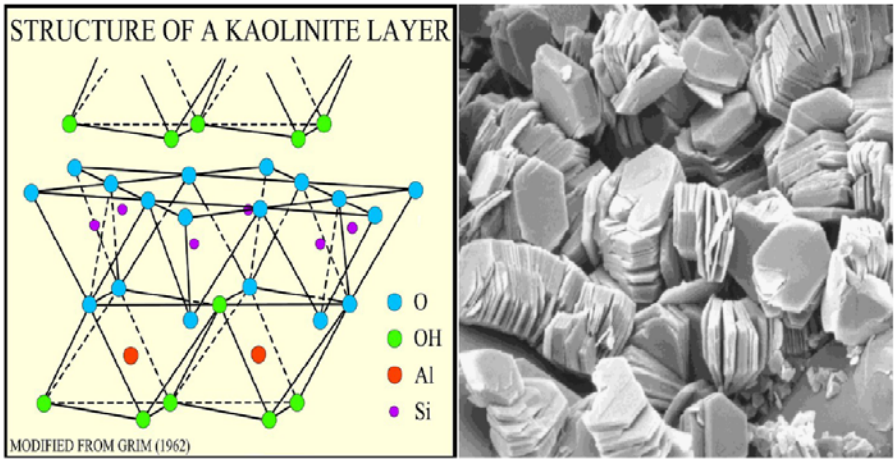

Figure 2-24 Structure and SEM pictures of Kaolinite (Source: http://www.uni-kiel.de/anorg/lagaly/group/jose/Kaolinite.gif)

2.5.3 Montmorillonite

Montmorillonite is the most common member of smectite clay minerals group. Smectite mineral group also incorporates other minerals like Nontronite, Beidellite, Hectorit, Saponite, and Sauconite (Terzaghi et al., 1996). Montmorillonite is the main mineral in some clays and shales and in some residual soils formed from volcanic ash (Terzaghi et al., 1996). Smectite minerals have high water absorption capacity that reduces the soil strength. A unit sheet of Montmorillonite is similar to that of the micas (Terzaghi et al., 1996). Figure 2-25 shows the structure of mineral Montmorillonite.

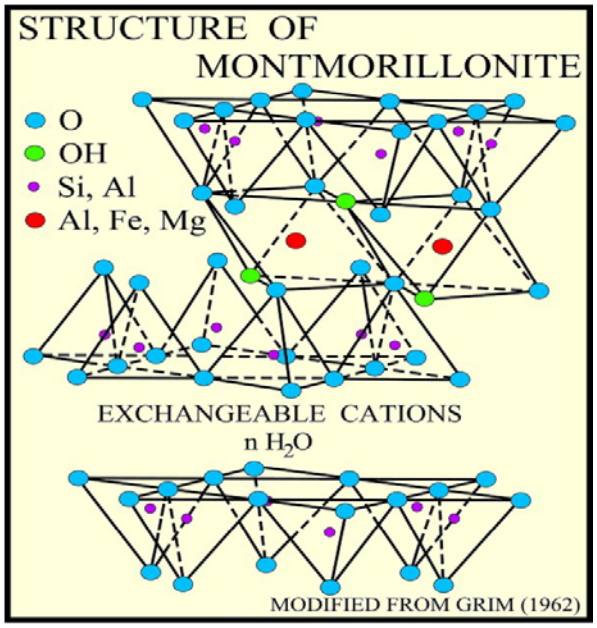

Figure 2-25 Structure of mineral montmorillonite (Source: http://pubs.usgs.gov/of/2001/of01-041/htmldocs/clays/smc.html)

The octahedral aluminum of Montmorillonite is partially replaced by magnesium atoms. Each of this isomorphous substitution creates a unit negative charge at the location of the replaced atom, which is often neutralized by exchangeable cations like Ca^{+2} and Na^{+} situate at the surface of the sheets (Terzaghi et al., 1996). The negative charge of smectite minerals and their expansive behavior makes them highly reactive in presence of moisture (Terzaghi et al., 1996). The specific surface area of Montmorillonite typically ranges from 600 to 800 m^2/g (Terzaghi et al., 1996). Borchardt reported the cation exchange capacity of smectite minerals to be between 47 to 162 meq/g. Figure 2-26 shows the SEM of Montmorillonite. The swelling of the clays is mainly attributed to the water absorption capacity of highly reactive mineral like montmorillonite (Mitchell and Soga, 2005).

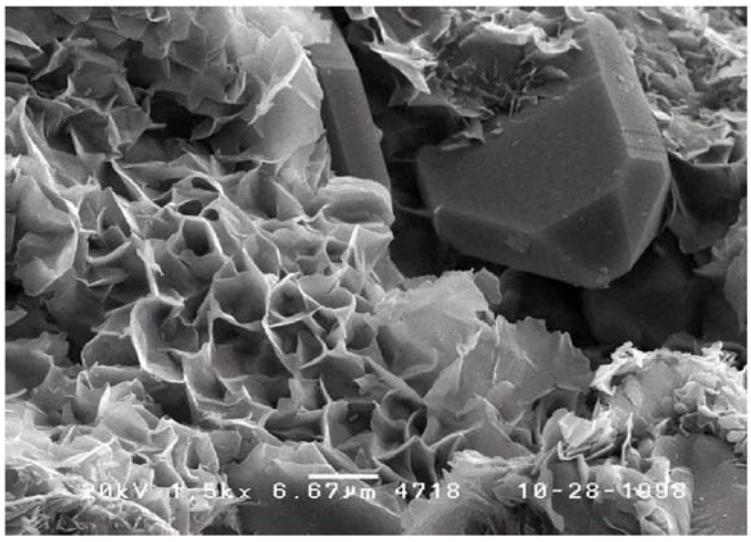

Figure 2-26 SEM of mineral montmorillonite (Pedarla, 2013)

2.6 Soil Water Characteristics Curve (SWCC)

Soil water characteristics curve (SWCC) provides a conceptual understanding between the amount of water and its energy state in soils. The SWCC has emerged as an interpretive model that uses elementary capillary model to explain the distribution of water in the voids (Fredlund et al., 2012) SWCC is generally determined by maintaining a known value of suction on the soil sample and then measuring the water content at equilibrium condition. A common method of laboratory determination of SWCC is to use axis translation technique (Fredlund et al., 2012). In axis translation technique the pore water and pore air pressure in the soil sample is maintained by using a high air entry (HAE) ceramic disk. The ceramic disk allows only water to permeate through it when the air pressure is below its air entry value. Thus, a difference between higher air pressure and lower water pressure can be maintained in the soil below the air entry value of the HAE disk. The difference is the matric suction (Fredlund et al., 2012).

Soil suction can be divided into two components; osmotic suction and matric suction. Osmotic suction represents the suction in the soil due to the presence of dissolved salts. And, matric suction is the difference between the air pressure and water pressure (u_a-u_w) in the pore fluid (Fredlund et al., 2012). Figure 2-27 shows an example of a typical SWCC curve. In the curve the point where the curve abruptly drops indicates the air pressure at which air enters into

the soil pores and is termed as air entry value (Ψ_a) (Fredlund and Houston, 2009). The water content corresponding to the lower point of inflection of the curve is called the residual water content (θ_r). Other important parameters of the SWCC are saturated water content and slope of the curve between the air entry and residual condition (Fredlund and Houston, 2009). Three zones of desaturation can be seen in the curve.

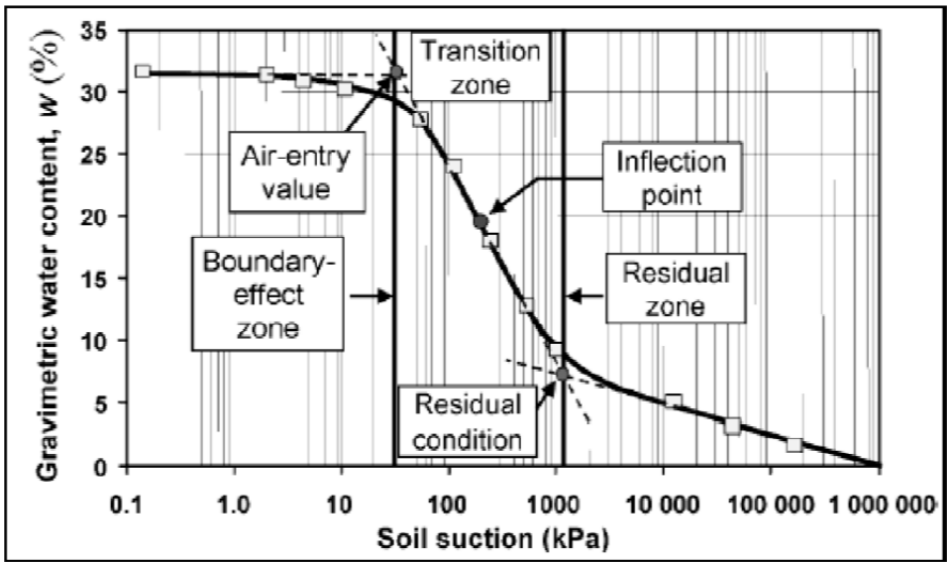

Figure 2-27 A typical SWCC curve (Fredlund and Houston, 2009)

The parameters air entry value and residual water content, and the type of the soil govern the shape of a SWCC curve. Coarser soil particles contain larger voids and release the pore moisture rather easily at a lower value of matric suction (Fredlund and Rahardjo, 1993). On the other hand the small pores in fine grained soil can hold the moisture even at very high suction levels. Therefore it is evident that the shape and characteristics of the SWCC depends on the pore size

distribution of the soil (Fredlund and Rahardjo, 1993). Therefore, the SWCC of a soil is different for wetting and drying as shown in Figure 2-28. The hysteresis effect implies that there is no unique SWCC (Fredlund et al., 2012). Pressure plate apparatus, Tempe cell, psychrometer method, potentiometer, and filter paper techniques are some of the common methods in determination of SWCC. The methods employed in the current study are explained in Chapter 3.

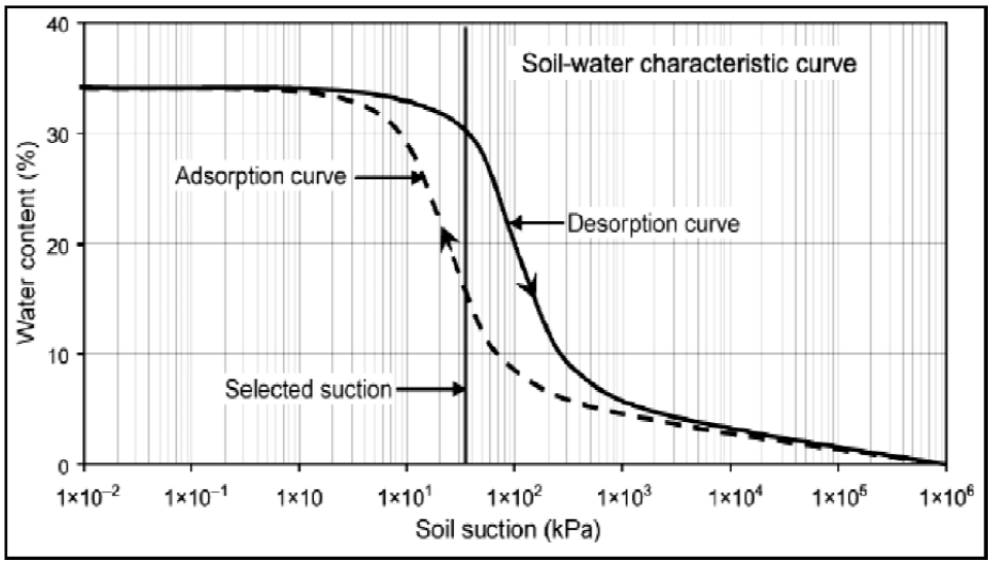

Figure 2-28 SWCC for wetting and drying processes (Fredlund and Houston, 2009)

2.7 Limit Equilibrium Method for Slope Stability Analysis

According to Duncan and Wright (2005) the basic requirement for stability of slopes is that the shear strength of the soil must be greater than the shear stress required for the equilibrium. Therefore the crucial cause of instability in the soil is that the shear strength of the soil is less than the shear stress acting

on the soil mass (Duncan and Wright, 2005). The condition of failure, when the soil shear strength is less than shear stress, can be reached in two ways: through decrease in the shear strength of the soil; through increase in the shear stress required for equilibrium (Duncan and Wright, 2005). There can be different factors behind the reduction in the shear strength of the soil. Some of the key factors that cause reduction in soil shear strength include increase in pore water pressure, development of cracks in the soil mass, increase in the void ratio of the soil mass by swelling, development of slickensides, creep under sustained load, strain softening, and weathering (Duncan and Wright, 2005).

On the other hand, the influential factors that cause increase in the soil shear stress include increased surcharge at the top of the slope, water pressure in the cracks at the top of the slope, increase in the soil weight due to increased water content, excavation at the bottom of the slope, and earthquake shaking (Duncan and Wright, 2005). Increased pore water pressure is one of the primary reasons for the failure of the slopes in most of the cases (Duncan and Wright, 2005). Desiccation cracking of the soil further helps the water to seep into the slope during rain. The cracks provide preferential flow paths for the water and additional pore water pressure develops due to seepage along the slope (Dronamraju, 2008; Le, 2013). Increase in ground water table can be another vital factor in slope failure. Increased water table can reduce the effective stresses within the slope. If the soil does not have sufficient permeability to quickly drain

the increased pore water pressure the shear strength is reduced because of the increased pore water pressure.

Limit equilibrium method is popularly used in analyzing the stability of slopes. This is a simple and versatile method which is based on the concept that the geometry of the potential failure surface is known beforehand and the slope can be divided into several finite vertical slices (Oh and Lu, 2014).

According to Duncan and Wright (2005) the limit equilibrium is a condition on which the mobilized shear strength of the soil mass is just in equilibrium with the shear stress acting on the soil mass. Therefore, the equilibrium shear stress is equal to the available shear strength divided by some factor called factor of safety. The factor of safety is defined as the ratio between available shear strength and the equilibrium shear stress Duncan and Wright (2005). In terms of total stress, the equilibrium shear stress is expressed as shown in Equation 2-12.

$$\tau = c_d + \sigma \tan \phi_d \qquad 2\text{-}12$$

where, c_d and ϕ_d are the mobilized cohesion and friction angle respectively.

In terms of effective stress, the equilibrium shear stress is expressed as shown in Equation 2-13.

$$\tau = c'_d + (\sigma - \mathrm{u}) \tan \phi'_d \qquad 2\text{-}13$$

where, c'_d and ϕ'_d are the mobilized cohesion and friction angle respectively in terms of shear strength and u is the pore water pressure.

2.7.1 Two-dimensional Slope Stability Analysis Methods

There are many limit equilibrium techniques for slope stability analysis depending on the equations of equilibrium that are included and the assumptions made about the inter-slice forces (Bishop, 1955; Morgenstern and Price, 1965; Spencer, 1967; Duncan, 1996). Some of the limit equilibrium methods are namely infinite slope method, logarithmic spiral method, Swedish circle method, ordinary method of slices, Bishop method, and Spencer's method (Duncan and Wright, 2005). Among the aforementioned methods, some of the methods consider equilibrium for the entire soil mass to have the movement. Only single free body diagram is used to determine the equilibrium condition in this method (Duncan and Wright, 2005). The Swedish circle and infinite slope methods fall in this category. In other procedures the soil mass is divided into a finite number of slices. Equilibrium condition is sought on each slide for slope stability analysis. In general these procedures are called procedures of slices (Duncan and Wright, 2005). The ordinary method of slices, simplified Bishop method, Spencer's method are the examples of the method of slices (Duncan and Wright, 2005).

In the limit equilibrium procedures, there are three equilibrium that are to be satisfied : 1) vertical force equilibrium, 2) horizontal force equilibrium, and 3) moment equilibrium (Duncan and Wright, 2005). All the limit equilibrium

procedures satisfy at least one of the three equilibrium conditions. A number of slip surfaces must be assumed to find the slip surface that has the minimum factor of safety. This surface is called critical surface and the factor of safety associated with the critical slope is called critical factor of safety (Duncan and Wright, 2005).

2.7.2 Three-dimensional Slope Stability Analysis Methods

Simplification of real three-dimensional (3D) problems as 2D problems often produces satisfactory results. However, in some cases, for example in the case of slopes with curvature, the 3D slope analysis may be an appropriate method. In conducting the case studies of failed slopes, back analysis can be conducted using both 2D and 3D methods. By comparison, the 2D back analysis produces lower factor of safety than the 3D analysis (Chowdhury, 2010).

By definition, 3D analysis methods consider 3D shape of the failure surface. These methods, like 2D methods, are based on assumptions to obtain the statistically determinate definition of the problem (Albataineh, 2006). The techniques to do that involve either decreasing the number of the unknowns associated with the problem or increasing the equations of equilibrium or both such that two number are equal (Albataineh, 2006).

Albataineh (2006) indicated following cases where three dimensional analysis becomes important: (1) when slope geometry is rather complex which poses difficulty in selecting a single 2D section to analyze. (2) when the geometry

of the slope and the slip surface vary significantly in lateral direction, (3) when the slope materials are nonhomogeneous or anisotropic, (4) when the slope has concentrated loads, (5) when the slope has a complex shear strength and/or pore water pressure which requires combining the effects of slope geometry and shear strength to determine movement direction producing minimum factor of safety, (6) when it is required to back calculate the shear strength of a failed slope.

Three-dimensional slope stability analysis methods based on limit equilibrium technique have been developed since 1960s. Duncan (1992) noted that a number of studies has presented higher FOS for 3D analysis than the corresponding 2D analysis. However, some opposite outcomes were also reported (Chowdhury, 2010). Some of the 3D slope stability analysis methods are discussed below:

Anagnosti (1969) modified Morgenstern-Price (1967) 2D method to develop a 3D method for determination of the factor of safety of the potential sliding mass of different shapes. The fundamental assumption in this method is the distribution of interslice shear forces that fulfills all equilibrium requirements. The results from this method when compared with corresponding 2D slices showed that this method increased the actual FOS by over 50%. Sensitivity analysis revealed that the calculated FOS was not very sensitive to the interslice shear assumption (Albataineh, 2006).

Hovland (1977) presented a general approach for 3D slope stability analyses. The method is based on the assumptions associated with the 2D ordinary method of slices, but instead of using slices, columns were considered in the calculation. All inter-column forces acting on the vertical sides of the columns are ignored. The normal and shear stresses acting on the base of each column are calculated based on the components of the weight of the column in respective directions. In addition, the motion of the sliding mass is assumed to be in only one direction and the equilibrium of the system is calculated for this direction.

Hovland (1977) found that 3D factors of safety are usually higher than 2D factors of safety after a analyzing a number of corresponding 2D and 3D cases. He further indicated that the landslides in cohesive soils may follow a wide shear surface geometry consequently resembling 2D case. However, failures in granular soil may follow a 3D wedge type surface. In general, the ratio factor of safety is sensitive to the shear strength parameters as well as the geometry of the 3D failure surface.

Chen (1981), and Chen and Chameau (1983) conducted a comprehensive study on the three-dimensional effects of slope stability covering a wide range of soil parameters. They presented techniques for the stability analysis of block surfaces as well as rotational surfaces. This method was derived as an extension of spencer's method (1967) and produced lower FOS than Hovland's method.

The stability of translational slides is analyzed using BLOCK3 software. The block analysis is divided into three parts as shown in Figure 2-29. Figure 2-29(a) shows the free body diagram for calculation of the total force acting on the central block from the active block. This force is a function of the FOS. Figure 2-29(b) shows the free body diagram for calculation of the force acting on the central block from the passive block. This force is also a function of FOS. Figure 2-29(c) shows the free body diagram for the calculation of the base side and end forces on the central block. A symmetry condition is assumed for the analysis. Other major assumptions include: (a) there are no shear forces in the boundaries between active and central blocks, and passive and central blocks, (b) the inclinations of the bottom surfaces for active and passives zones respectively were $(45+\varphi/2)$ and $(45-\varphi/2)$ with horizontal, and (c) water table is far below the ground surface.

Chen's study of translational slides brought following conclusions: (a) 3D FOS are generally larger than 2D FOS and this effect is more prominent in cohesive soils, (b) 3D FOS is smaller than 2D FOS in case of wedge type failure, (c) 3D effects becomes prominent with lower strength of weak soil stratum, and (d) reducing inclination of the ends of the central block cause a higher factor of safety due to higher end areas.

In case of rotational movement, the 3D failure surface was assumed to have homogenous soil and composed of central cylinder attached by two semi-

ellipsoids at the two ends. A computer program, LEMIX, was developed to analyze the slope using limit equilibrium approach. (Albataineh, 2006). The sliding mass is considered to be symmetrical and divided into several vertical columns; a free body diagram of a column is shown in Figure 2-30. The movement is only in x-y plane therefore the shear stresses along y-z plane are assumed to be zero. The intercolumn shear forces are considered parallel to the base of the column. The intercolumn normal stress is assumed to be varying linearly with depth. The orientation of the intercolumn forces is considered to be same throughout the whole failure mass.

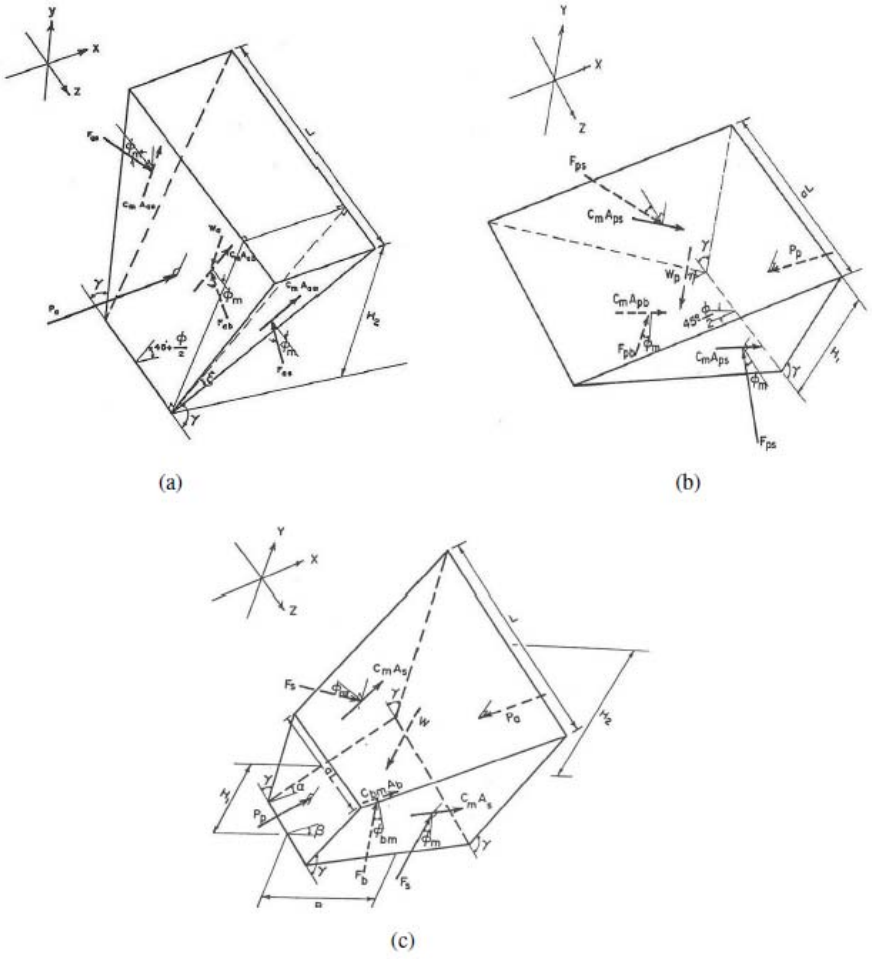

Figure 2-29 Free body diagram of: (a) active case, (b) passive case, and (c) central block (Chen, 1981)

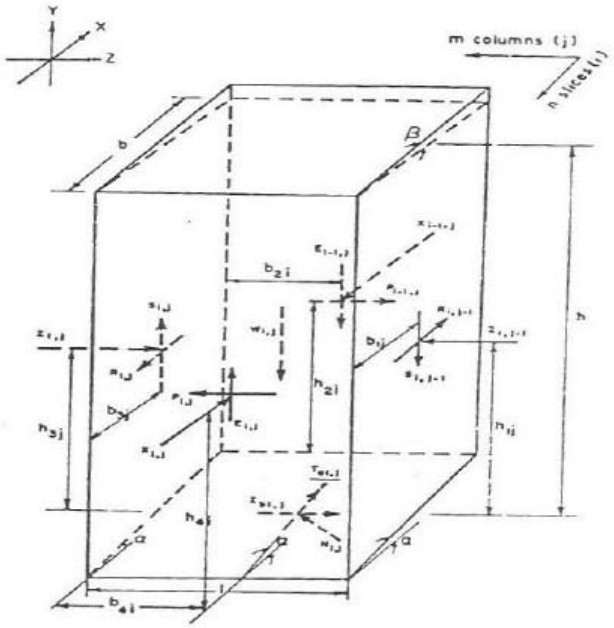

Figure 2-30 Free body diagram of a soil column on the sliding mass (Chen, 1981)

Based on the analysis of rotational slides, Chen (1981) concluded that the 3D effects are more significant for soils with high cohesion and low friction angle. Based on the size of the moving soil, 3D effects are more significant at smaller lengths of sliding mass. In case of soils with low cohesion and high friction angle, the 3D FOS may be slightly smaller than that for corresponding 2D case. Pore-water pressure can also cause the 3D effects to be greater.

2.8 Effect of Rainfall in Surficial Slope failures

Desiccation cracks provide opening to the water into the slope during rainfall. Water easily infiltrates through the cracks thus increasing the pore water pressure and consequently reducing the shear strength. The combined effect of these factors triggers the slope failure (Rahardjo et al., 1995; Cho and Lee., 2002).

As the slope saturates at greater depth, the permeability increases in the direction of slope and seepage occurs parallel to the slope (Day, 1996). Different factors that contribute to the failure of any slope during rainfall include intensity, rainfall characteristics, soil characteristics, and topography (Church and Miles, 1987). The situation worsens as the weight of the soil increases.

The resisting factor is the soil shear strength. The turf and vegetation also provides resistance against failure. Plant root network enhances shear strength of soil. Reduction of soil moisture due to transpiration helps in gaining strength (Waldron, 1977; Day 1993). The reinforcing effects of natural and synthetic fiber proved to increase shear strength (Gray and Ohashi, 1983; Day 1996).

Lim et al (1996) monitored suction at different depths on a slope consisting of soil having plasticity index of almost 30% during rainfall. The test included soils from 1.0 to 1.7 m depth. The slope was originally covered with vegetation. The total width of the slope was divided into 3 test sections called bare ground surface, grass surface, and canvas over grass surface sections. The reported changes in matric suction were higher in the bare surface compared to grass and canvas covered surface. There was only little variation of matric suction in the canvas covered section.

McCleskey et al. (2008) reported many surficial slope failure occurred in Grapevine Dam in the state of Texas, USA. The authors analyzed the rainfall data

and compared it with the slope failure incidents. It was revealed that almost all of the slope failure incidents happened after rainfall events.

2.8.1 Slope Stability Analysis of Unsaturated Slopes

An unsaturated slope invariably poses higher stability than when it is wet. Therefore, the stability of a slope is affected by evaporation, evapo-transpiration and rainfall infiltration at the interface of soil and atmosphere (Rahardjo et al., 2007). Fredlund (1978) defined the shear strength of unsaturated soils as:

$$\tau = c' + (\sigma - u_a)tan\emptyset' + (u_a - u_w)tan\emptyset^b \qquad 2\text{-}14$$

where, τ = shear strength of soil

c' = effective cohesion

σ = total normal stress

u_a = pore air pressure in the soil

u_w = pore water pressure in soil

$\emptyset'$ = angle of internal friction

$\emptyset^b$ = angle of internal friction with respect to changes in suction

Ching et al. (1999) analyzed safety of two cut slopes in Hong Kong. One of the slopes was 35 m high with a slope angle of 60^o. The slope consisted of residual soils and weathered granite. The bed rock was located 20 to 30 m below the slope surface. Water table was located near the bed rock. The authors monitored the soil suction in the field using tensiometers. The average value of angle $\emptyset^b$ was assumed to be 15^o. It was reported that the factor of safety increased

considerably with increase in suction at beginning and remained almost constant at higher suction level. The factor of safety of the Fung Fai Terrace site and Thorpe Manor site were 0.86 and 1.05 before taking into account the suction. With the suction considered the factor of safety for the sites increased to 1.01 and 1.25 respectively.

2.9 Summary

This chapter presented the literature review on desiccation cracking, its effect in slope stability, modeling of desiccation cracking. Different factors responsible for the shrinkage and desiccation cracking were studied in detail. This chapter also comprises of a review of the previous research in the areas of amendment of soils, influence of soil suction on slope stability, conventional slope stability methodologies, and unsaturated slope stability. Major findings from this literature review can be summarized below:

1. The mechanism of desiccation cracking has been explained based on the unsaturated soil mechanics theory. Soil loses moisture during drying resulting in increased matric suction of the soil. The increase in matric suction increases the effective stress and the increase in effective stress causes volumetric shrinkage of the soil. Both the tensile strength and tensile stress evolve gradually with decrease in moisture content. As the drying process continues, the

tensile stress developed within the soil mass can exceed the tensile strength of the soil at some point causing the cracking of the soil.

2. Expansive soils have been stabilized using wide verity of admixtures including lime, cement, compost, fibers, and biopolymers. Lime treatment has been the oldest, economical and most effective treatment method for expansive soils. Compost and fibers have also proved to be advantageous. Biopolymer stabilization has been emerging as a new method. The application of biopolymer to mitigate soil cracking and surficial slope failures has not been well explored.
3. Internal stresses developed within the drying soil plays central role in the desiccation cracking. Restrained ring test and linear shrinkage tests in long molds can be used in determining the internal stresses. Yet, the existing experimental procedure and analytical solutions for internal stress evolution are too specific and/or complex for routine laboratory tests.
4. The swelling and shrinkage behavior of clay soils are primarily governed by the mineralogical composition. Different minerals of a clayey soil can be quantified using cation exchange capacity (CEC), total potassium (TP), and specific surface area (SSA) tests. Montmorillonite has highest specific surface area ranging from 600

to 800 m^2/g. It absorbs more moisture and increases shrinkage and swelling potential of soils.

5. Two dimensional slope stability analyses often give lower FOS than 3D slope stability analysis. Soil suction plays a key role in the surficial slope stability of soil. The FOS of a slope can decrease significantly when the dry slope becomes wet during a wet season.

Chapter 3

Laboratory Experimental Programs

3.1 Introduction

The main objective of this dissertation research was to characterize the shrinkage behavior of clay soils. The shrinkage behaviors of five high plasticity clays (CH) and equal number of low plasticity clays (CL) were studied in the present characterization studies. The shrinkage characterization is based mainly on various tests including shrinkage induced pressure (SIP) test, linear shrinkage bar test, indirect tensile strength (IDT) test, soil water characteristics curve (SWCC) studies. Also, digital image correlation technique was used to study the soil behaviors during drying, shrinkage and cracking. In addition, basic laboratory tests were also conducted to determine the basic soils properties, engineering properties, and chemical and mineralogical composition of the soils.

The second objective of this study was to develop soil treatment methods to control the desiccation cracking induced surficial failures. Biopolymer treatment method was selected and studied as a new treatment method. This treatment and its performance was compared with the previously developed lime treatment and lime plus fiber treatment methods. The treatment methods were analyzed to study changes in the shrinkage behavior of the soil and their influence in reducing the desiccation cracking problem. The test methods used in the shrinkage characterization of the untreated soils were repeated to compare the

changes brought in by the introduction of soil additives. The soil treatment methods and their results are presented in Chapter 5.

3.2 Soil Selection

Pedarla (2013) collected eight different clays from different geological formations in his study as shown in Figure 3-1. The expansive soil were sampled from Anthem, Burleson, Colorado, Grayson, Keller, Oklahoma, San Antonio, and San Diego. The same soils were also considered in this study. Furthermore, the Grapevine soil and Joe Pool soils from North Texas, previously studied by McCleskey (2005), Dronamraju (2008), and Le (2013) for mitigating surficial slope failures in the dam slopes, were also included in this study. Overall ten different soils were used in this study. However, only Grapevine and Joe Pools soils were considered for developing treatment methods to control desiccation cracking.

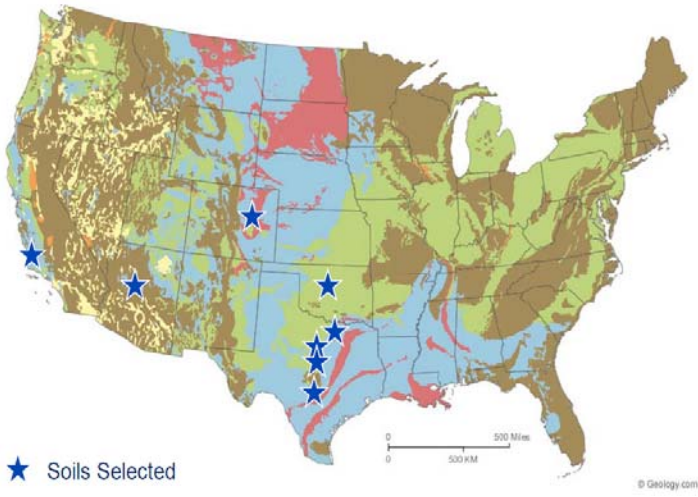

Figure 3-1 Soils selected from different geological formations (Pedarla, 2013)

3.3 Basic Laboratory Tests

Lab experiments were conducted to determine the basic soil properties of the soils. The basic soil tests included sieve analysis, hydrometer analysis, Atterberg limits tests, and specific gravity tests. The procedures followed in conducting these tests are described below. The test results were compared with the results presented by the previous researchers at UTA.

3.3.1 Sieve Analysis

The particle size distributions of the soils were determined based on ASTM standard procedure for sieve analysis of fine and coarse aggregates (ASTM C136-01). A representative sample of each soil was brought in the lab and air dried for almost seven days. The foreign materials were removed from the soils after breaking the big chunks using a rubber hammer. The soil was further broken using gentle impact of rubber tipped pestle. Then the soil was kept in oven for drying. Oven dried soil was then sieved through a stack of sieves using a sieve shaker as shown in Figure 3-2. Wet sieve analysis was performed on the fine soils retained in the No. 200 sieve. Hydrometer analysis was conducted on the soil passing No. 200 sieve to determine the particle size distribution of the fines.

Figure 3-2 The sieves stacked and placed in mechanical sieve shaker

3.3.2 Hydrometer Test

Hydrometer analysis was conducted using ASTM 152 H type hydrometers. The test was conducted following the procedures outlined in ASTM D 422.

3.3.3 Atterberg Limits Test

The Atterberg limit tests were carried out in accordance with ASTM D4318-05 to determine the liquid and plastic limits of the soils. These limits can

give the approximate indication of the shrinkage and swelling potential of the soils. The water content at the boundary between liquid state and plastic state of the soil is termed as liquid limit (LL). And, the water content at the boundary between plastic and semi-solid state is called plastic limit (PL) (Lambe and Whitman, 2000). A flow curve was developed for each soil to determine their liquid limit. The water content corresponding to the 25 number of blows, i.e. liquid limit, was then determined on the respective flow curves of the soils. Plastic limit test was also conducted. Finally, the plasticity indices of the soils were obtained by subtracting plastic limits from the liquid limits of the soils. Plasticity index characterize the plasticity characteristics of the soil.

3.3.4 Specific Gravity Test

Specific gravity (G_s) is an important parameter in determining weight volume relationships of soils. It is defined as the ratio between of the masses of equal volume of soil solids and water. The specific gravities of the soils were determined in accordance with Standard Test Methods for Specific Gravity of Soil Solids by Water Pycnometer Method (ASTM D854-14).

3.3.5 Basic Laboratory Test Results

The soils were tested for basic soil classification, specific gravity (G_s) and Atterberg limits and the results are presented in Table 3-1. The Atterberg limits of the soils are also shown in Figure 3-3. Grayson soil and Keller soil respectively exhibited the highest and the lowest plasticity index among the soils.

The soils passing through No.200 were used for Hydrometer analysis. The summary of the gradation analysis is given in Table 3-2. The sand, silt, and clay fraction of the soils are also presented in Figure 3-4. Grayson soil has the highest clay fraction and Grapevine soil has the lowest clay fraction.

Table 3-1 Atterberg limits, specific gravity, and USCS classification of the soils

Soil	Liquid limit (%)	Plasticity index (%)	Specific gravity	USCS classification
Anthem	48	27	2.72	CL
Burleson	55	37	2.72	CH
Colorado	63	42	2.7	CH
Grapevine	30	13	2.69	CL
Grayson	75	49	2.73	CH
Joe Pool	58	34	2.71	CH
Keller	25	11	2.7	CL
Oklahoma	41	21	2.8	CL
San Antonio	67	43	2.79	CH
San Diego	42	28	2.72	CL

Table 3-2. Summary of the gradation analysis

Soil	% Gravel	% Sand	% Silt	% Clay
Anthem	0	14	54	32
Burleson	0	10	38	52
Colorado	0	15	39	46
Grapevine	0	42	40	18
Grayson	0	8	37	55
Joe Pool	0	30	50	20
Keller	0	20	46	34
Oklahoma	0	22	48	30
San Antonio	0	14	34	52
San Diego	0	38	39	23

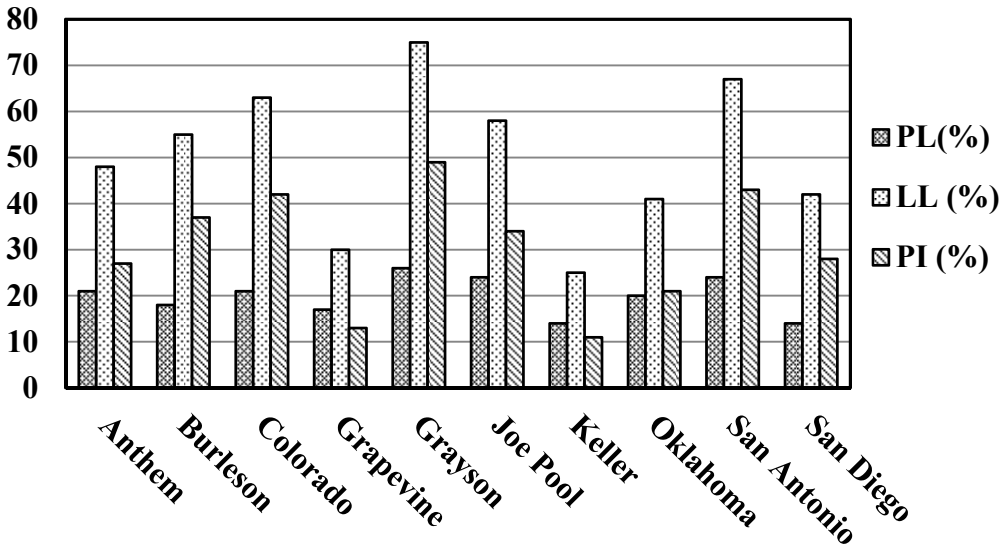

Figure 3-3 Atterberg limits of the soils

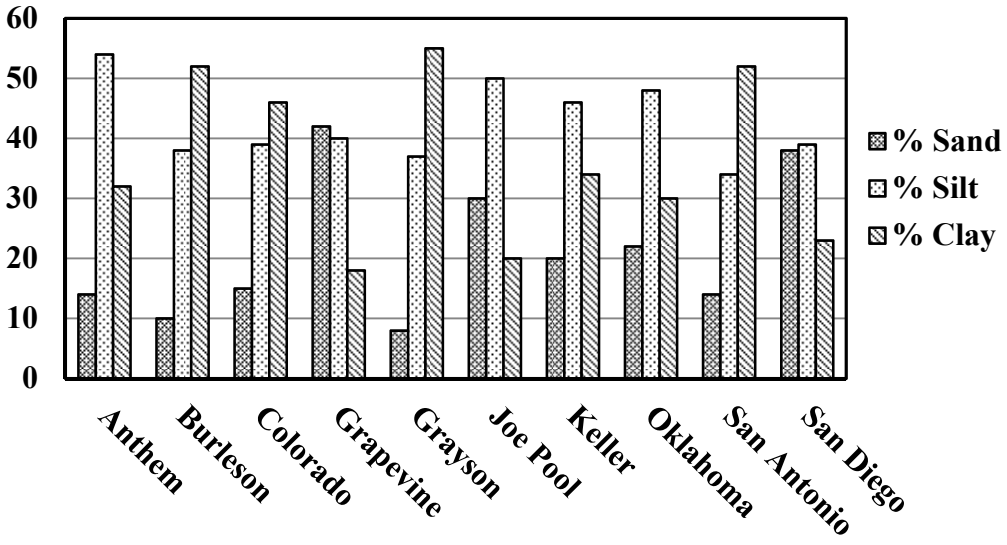

Figure 3-4 Sand, silt, and clay fraction of the soils

3.4 Standard Proctor Test

Standard proctor tests were conducted in accordance with Standard Test Methods for Laboratory Compaction Characteristics of Soil Using Standard Effort (ASTM D698). The moisture content versus dry density curves were obtained from the tests. The moisture content corresponding to the maximum dry density is called optimum moisture content. The optimum moisture contents and maximum dry densities of the soils were determined. Table 3-3 shows the maximum dry density (MDD) and optimum moisture content (OMC) of the soils. The maximum dry densities and optimum moisture contents of the soils are also presented graphically in Figure 3-5Figure 3-6 respectively.

Table 3-3 Maximum dry density and optimum moisture contents of the soils

Soil	MDD (kg/m^3)	OMC (%)	95% MDD (kg/m^3)
Anthem	1720	18	1634
Burleson	1633	19	1551
Colorado	1649	19	1567
Grapevine	1733	18	1646
Grayson	1457	24	1384
Joe Pool	1494	12	1419
Keller	1890	14	1796
Oklahoma	1593	24	1513
San Antonio	1608	22	1528
San Diego	1736	17	1649

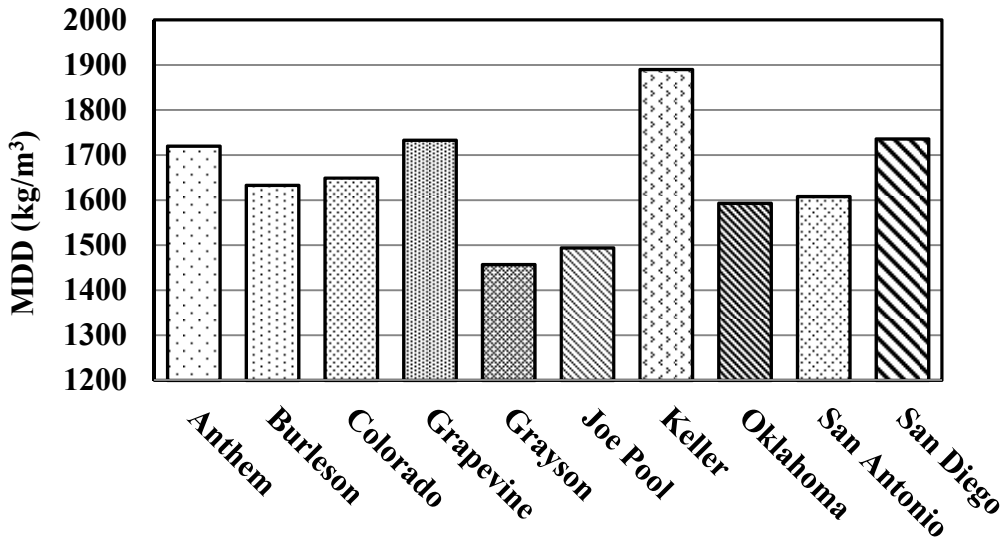

Figure 3-5 Maximum dry densities of the soils obtained from standard proctor compaction test

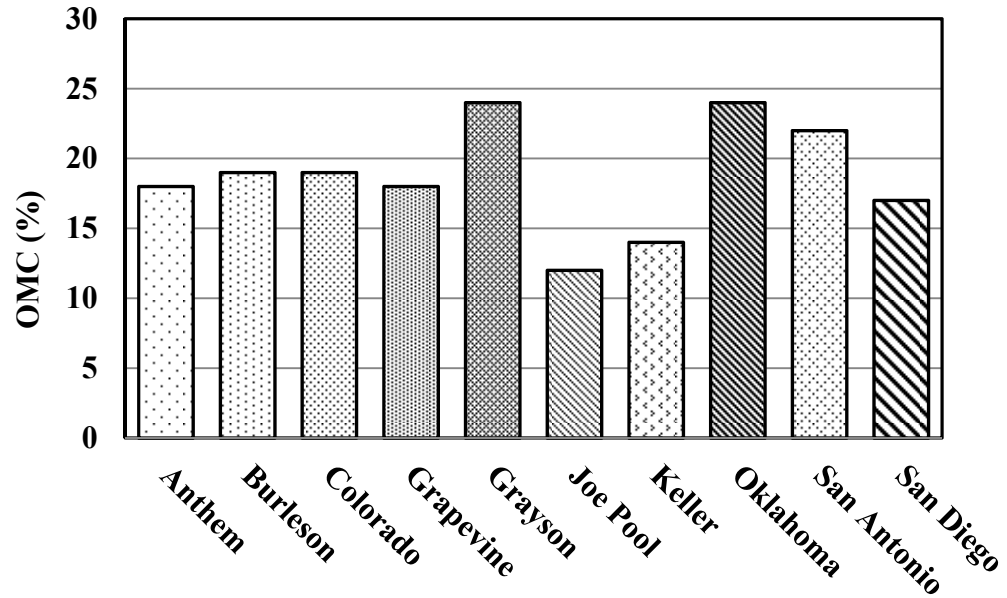

Figure 3-6 Optimum moisture contents of the soils obtained from standard proctor compaction test

3.5 Direct Shear Test

Direct shear tests were conducted on the untreated and treated soils from Grapevine and Joe Pool dam sites. Soil selection for treatment studies was based on the frequent occurrence of the surficial slope failures in these dam sites in the past. Direct shear test was used to measure the drained peak shear strength and fully softened shear strength parameters of the soils. The tests were performed at the normal stresses ranging from 50 to 200 kPa (1044 to 4176 psf). A very slow shearing rate of 0.005 mm/min (0.0002 in/min) was used in the tests. Automated direct shear equipment capable of maintaining constant normal stress and shearing rate was used in the experiments. The readings from the force and displacement sensors were also recorded automatically in the computer. Figure 3-7 shows the picture of the direct shear machine. The results from the direct shear test are presented in chapter 5.

Figure 3-7 Direct shear test apparatus used in this study

3.6 Torsional Ring Shear Test

Torsional ring shear test was used to measure the residual and fully softened shear strength of the untreated as well as treated soils form Grapevine and Joe Pool dam sites. ASTM D7608 was followed for performing ring shear tests for determining drained fully softened shear strengths of soils. Similarly ASTM D6467 was followed for performing the ring shear tests for residual

strengths. The tests were conducted at the normal stresses ranging from 50 to 200 kPa.

The Bromhead torsional ring shear device holds the soil between two porous inserts. The water can drain out of the specimen from the top and bottom surfaces of the specimen. The device produces torque on the specimen by forcing a shear plane in the sample. The device is capable of producing a constant rate of shear displacement on the specimen. The shearing rate can be adjusted using different combinations of gear wheels. The range of available displacement rate of the device varies from 44.52 to 0.018 mm/min.

The soil specimen is placed in the annular shape container having thickness of 5 mm and inner and outer diameters of 70 and 100 mm respectively. Figure 3-8 shows the soil specimen placed in the annular ring of the device. Since the specimen is confined radially in the annular container, friction develops between the soil and inner and outer wall of the annular container. This friction causes a shear plane to occur near the top surface because the wall friction is minimum near the top surface of the specimen.

Soil specimen was prepared at a consistency of liquid limit. The soil paste was then kept in the annular space of the lower platen. Any air bubbles entrapped in the specimen was expelled by tapping the specimen. Then, the upper platen was gently placed on top of it. The specimen is then consolidated before shearing. The final consolidation pressure required for each shearing is reached by applying

the pressure in increments so that the load increment ratio of one is maintained. Then the soil specimens were sheared at a very slow rate of 0.02 mm/min. Two ring gauges record the force resistance developed by the specimen during shearing. The ring gages readings were converted into corresponding shear stresses. Figure 3-9 shows a picture of the ring shear device and the test setup for the experiment. The results from the ring shear test are presented in chapter 5.

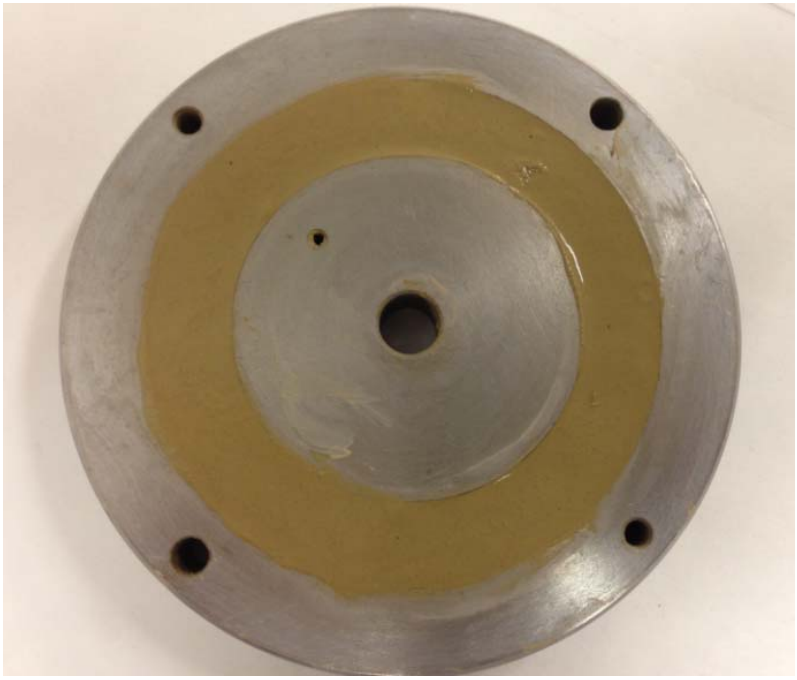

Figure 3-8 Soil specimen placed in the annular mold of the ring shear device

Figure 3-9 Bromhead ring shear device and test setup

3.7 Determination of Cation Exchange Capacity (CEC)

Cation exchange capacity is the ability of the soil to exchange free cations that are available in the exchange locations (Pedarla 2013). The most common method in current practice for determining CEC is the method proposed by Chapman (1965). Same method was employed in the current study. CEC provides a basis to determine the presence of the minerals in the soil. A high value of CEC indicate the presence of mineral Montmorillonite and the soil will have a high shrink/swell potential. On the other hand, a low CEC value hints at the presence of non-expansive clay minerals like Kaolinite or Illite. The test method for determining CEC involves addition of saturating solution and then

replacement of the adsorbed cations using an extracting solution. Different steps followed during the experiment are presented in Figure 3-10. Ammonium acetate (NH_4OAc) at pH 7 was used as saturating solution. The soil specimen was first treated with 30% hydrogen peroxide (H_2O_2) solution. The solution was stirred for half an hour and set aside for 16 hours. Ammonium acetate solution was added to the prepared solution to ensure that all exchange locations are occupied by the NH_4^+ ions.

The solution was filtered through a Buchner funnel. During the filtering process, the soil was washed with 4 different 25 ml additions of ammonium acetate. The washing process was to expel all the cations from the soil solution that had been replaced by ammonium ions. Any excess ammonium acetate in the soil was then removed by 8 different 10 ml additions of 2-propanol. This process also aids in the removal of excess ammonium. The CEC of the soil specimen can be obtained by replacing the ammonium ions. This was achieved by washing the specimen with 8 different additions of 1M potassium chloride (KCl) solution. Although K^+ and NH_4^+ have the same electronegativity, K^+ has higher molecular weight and thus substitutes the NH_4^+ ions in the process.

The concentration of NH_4^+ ions in the KCl extract gives the CEC of the soil. More details on this experiment can be found in Chittori (2008). The steps to determine CEC of the soils are as shown in Figure 3-10 below.

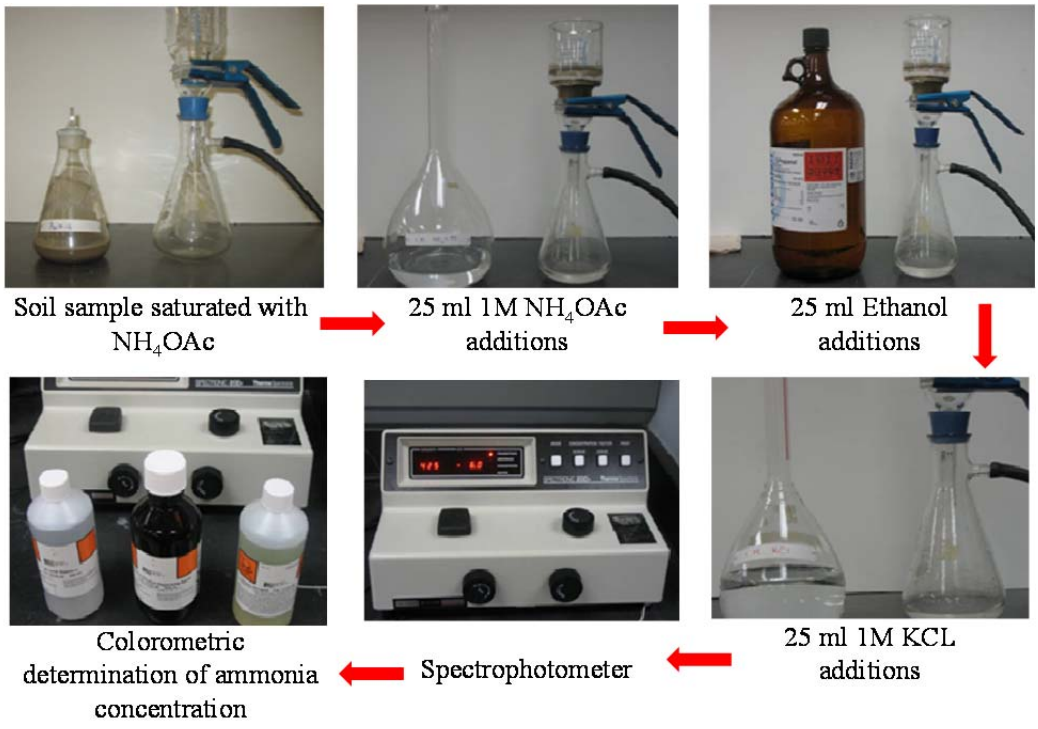

Figure 3-10 Procedural steps followed in the CEC determination of soils

3.8 Total Potassium (TP) Test

According to Mitchell and Soga (2005), Illite is a clay mineral constituting potassium ions. The presence potassium Feldspars can lead to potassium ions from Kaolinite; however these are not common and hence potassium presence is only linked to Illite. The amount of Illite clay mineral in a given soil can be determined by measuring the amount of potassium ions in the soil. The current research followed the procedure outlined in Knudsen et al. (1984) to determine the quantity of total potassium available in the soils. This method is based on double acid digestion technique presented by Jackson (1958). Two acids

(Perchloric acid and Hydrofluoric acid) are usedto break the mineral structure of the soil and remove the potassium ions from the mineral structure. The concentration of the potassium ions in the extracted solution can be obtained using spectrophotometer or any other suitable device.

The TP test procedures are presented in Figure 3-11. First of all, 0.1 g of soil was taken in a Teflon digestion vessel. The original test method recommends the use of platinum vessels as the hydrofluoric acid dissolves silica and glass is mainly made of silica. However, the usage of expensive platinum vessel was not feasible due to cost constraints. Hence, other possible alternatives were considered and Teflon vessel was found to have resistance to the acids that are used in TP test. The other reason Teflon vessel was selected was its high temperature tolerance (200^{o}C). Hence, 0.1 g soil specimen was taken in the Teflon vessel. Then, 5 ml of hydrofluoric acid and 0.5 ml of perchloric acid were added on it. Hydrofluoric acid dissolves the silicate mineral structure and frees the interlayer cations. Perchloric acid, on the other hand, oxidize the organic matters in the soil specimen. The vessel was then kept on a hot plate heated to 200^{o}C. Then the soil specimen was cooled and another addition of the acids is made and reheated on the hot plate. This process was repeated to make sure all the interlayer cations are freed. Finally, 6N HCl was added and the amount of potassium in this solution was obtained by using a spectrophotometer. The procedural details on the TP tests followed in the current study can be found in Chittoori (2008).

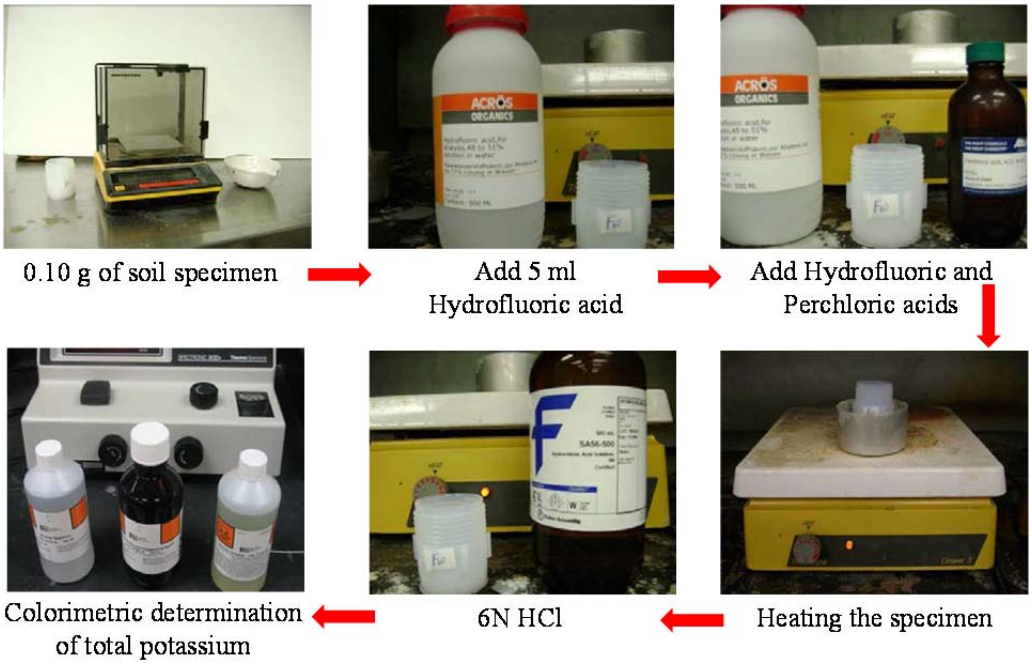

Figure 3-11 Total potassium test procedure

3.9 Specific Surface Area (SSA)

Specific surface area is the total surface area of particles contained in a unit mass of soil. So, SSA is directly related to the particle size of the soil. Fine grained particles have higher specific surface area than the coarse grained soil. Soils with higher SSA have higher potential to shrink/swell. The most common method of determining SSA is the adsorption of ethylene glycol monoethyl ether or EGME in short (Carter et al., 1986). This method involves saturating prepared soil specimens, equilibrating them by applying vacuum over a calcium chloride – EGME ($CaCl_2$-EGME) solvate, and weighing to find the point when the equilibrium is reached. SSA is then determined from the mass of retained EGME

compared to that retained by pure montmorillonite clay assumed to have a SSA of 810 m^2/g (Carter et al., 1986).

The SSA test method was fully evaluated for the geotechnical application by Cerato and Lutenegger (2002) and indicated that the method is applicable to a wide range of mineralogy and can measure SSA ranging from 15 to 800 m^2/g. The procedure for determination of SSA using EGME method has also been detailed in Chittoori (2008). Details of the procedural steps of this method are shown in Figure 3-12.

Chittoori (2008) presented an artificial neural network model to obtain percentage minerals present in clay based on CEC, TP, and SSA. The same method was employed in the current study to find the percentages of the minerals on the clay soils used in this study. Based on the methodology for quantification of minerals proposed by Chittoori and Puppala (2011), minerals were quantified in the present test soils and these results are presented in Table 3-4 and Table 3-5, respectively.

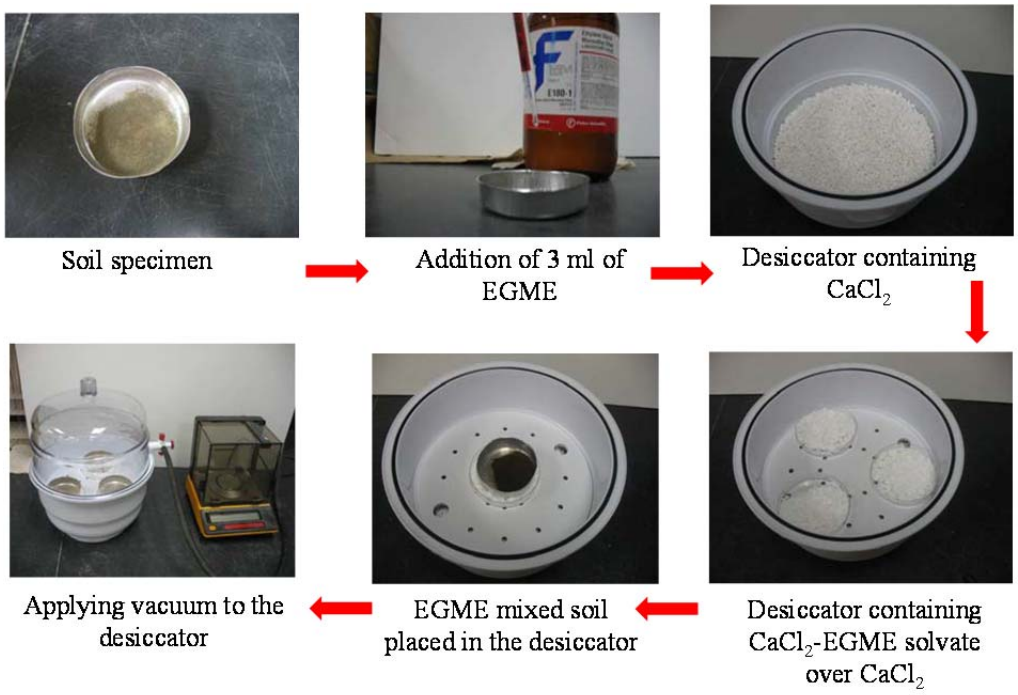

Figure 3-12 Different steps to be followed for SSA test

Table 3-4 Results of mineralogical tests performed on the soils

Soil	CEC (meq/100g)	TP	SSA (m2/g)
Anthem	71.7	1.46	118.5
Burleson	100.1	1.17	132.4
Colorado	91.6	2.10	185.0
Grapevine	64.1	-	81.3
Grayson	116.1	1.43	223.0
Joe Pool	113.1	1.65	107.2
Keller	60.0	1.10	115.0
Oklahoma	63.3	4.20	76.3
San Antonio	97.4	1.85	192.4
San Diego	87.2	1.51	92.6

Table 3-5. Mineralogical compositions of the soils

Soil	% Montmorillonite	% Illite	% Kaolinite
Anthem	25.2	24.4	50.4
Burleson	33.7	19.6	46.7
Colorado	35.7	35.0	29.3
Grapevine	20.3	-	-
Grayson	43.3	24.0	32.7
Joe Pool	35.1	27.6	37.3
Keller	21.9	18.4	59.7
Oklahoma	19.7	70.0	10.3
San Antonio	37.8	30.9	31.3
San Diego	26.9	25.3	47.8

3.10 Digital Image Correlation Technique for Shrinkage Study

3.10.1 Background

Digital image correlation (DIC) is an easy-to-implement yet a powerful optical method for measuring deformations (Pan et al., 2009). Therefore DIC has been popularly employed in the surface deformation measurements in the field of experimental mechanics. This technique allows the highly accurate measurements of full-field displacements and strains (Pan et al., 2006). The measurements are obtained by processing the digital images of the specimens before and after the deformation. The basic principle of DIC technique is to compare the same physical points in the reference and deformed images (Pan et al., 2009). A region of interest (ROI) is defined in the reference image before correlation analysis. Only the regularly spaced pixels within the ROI are considered for analysis rather than taking all the points.

A DIC set-up includes a source of uniform white light and a high resolution computer controlled camera to record the images of deformation of the surface under investigation. The out of plane deformations can be measured using a 3D DIC technique. In 3D DIC requires two different cameras to take simultaneous pictures from two different directions. However, the calibration of the cameras must be performed before the experiment. The accuracy of the calibration dictates the performance of the 3D DIC.

3.10.2 Experimental Procedure

Due to limited resources, these expensive experiments were conducted only on four different soils including two control and treated soils each; Grapevine soil, Joe Pool soil, and 8% lime mixed Grapevine and Joe Pool soils. Two experimental setups were used. In the first setup only one specimen was tested. And three specimens were tested in second setup. The DIC software utilized for both cases was GOM Optical Measuring Technique's ARAMIS software.

3.10.2.1 Experimental setup for one specimen

Figure 3-13 shows the experimental setup for the 3D DIC test for one specimen. Two 50 mm cameras were mounted on the camera stand as shown in Figure 3-14. The spacing between cameras was fixed at 472 mm and the camera angle was 25 degrees. The calibration object used was a GOM specific 175 x 140 mm panel as shown in Figure 3-15. The specimen was kept at a distance of 1150

mm from center of the camera slider bar. The resulting camera calibration produced a measurement volume of 175 x 150 mm. The calibration deviation was 0.017 pixels.

First, drying of soil was attempted using the lamps as shown in Figure 3-13. But the light from the lamps was not suitable for proper illumination of the specimen. Therefore, the specimen illumination was achieved using the LED lights for a consistent distribution of lighting and also to minimize specimen heating and therefore the noise. The LED light is shown in Figure 3-16. Since the soil was allowed to dry in the room temperature and humidity conditions, the drying rate was relatively slower than the SIP tests. Therefore, the frame rate of 12 frames per hour was set. The test lasted for 94 hours. And a total of 1128 frames were taken.

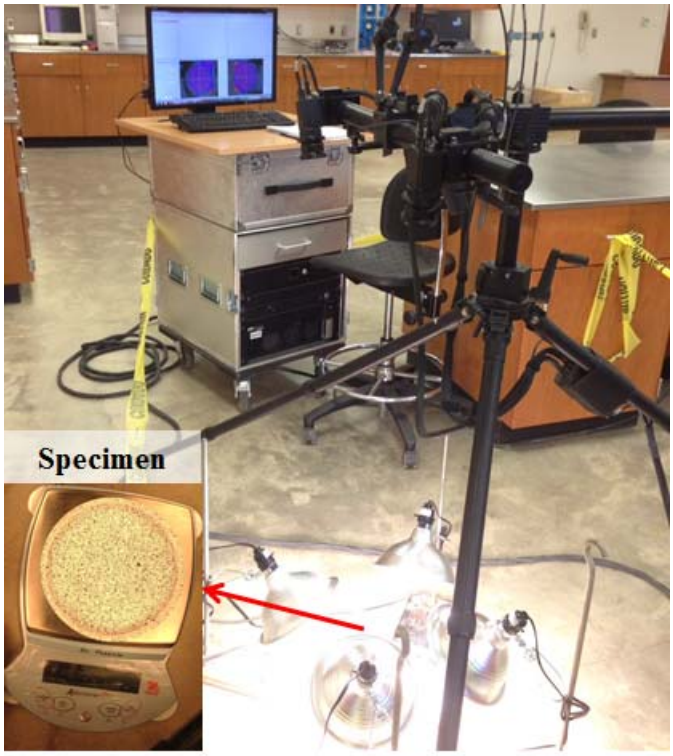

Figure 3-13 3D DIC experimental setup for one specimen

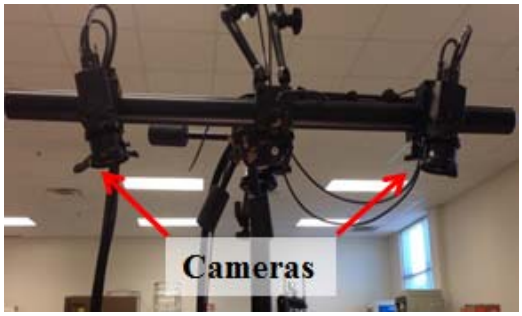

Figure 3-14 50 mm cameras used in the experiment

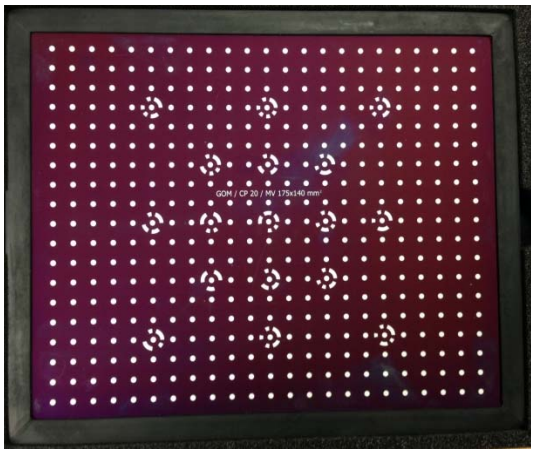

Figure 3-15 Calibration panel (175 x 140 mm)

Figure 3-16 LED light used in the experiment

3.10.2.2 Experimental setup for three specimens

Figure 3-17 shows the experimental setup for the 3D DIC test for three specimens. In this case, two 17 mm cameras were mounted on the camera stand with 680 mm spacing in between. The camera angle was 25 degrees. The

calibration was achieved using GOM specific 1000 x 800 mm calibration cross as shown in Figure 3-18. The specimens were kept at a distance of 1620 mm from center of the camera slider bar. The resulting camera calibration produced a measurement volume of 750 x 630 mm. The calibration deviation was 0.024 pixels. LED light used in the previous case was also used in this case. Frame rate of 6 frames per hour was used in this case. The test lasted for 91 hours. And a total of 546 images were taken.

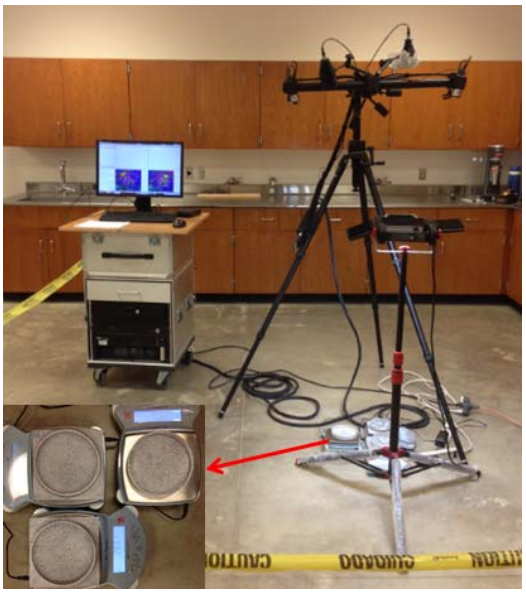

Figure 3-17 3D DIC experimental setup for 3 specimens

Figure 3-18 Calibration object (1000 x 800 mm)

3.10.2.3 Specimen preparation

The soils were prepared approximately to the liquid consistency and allowed to homogenize for 24 hours before the test. Then, the soils were transferred into the mold. The mold was 120 mm in diameter and 20 mm deep. However the thickness of the soil was approximately 10 mm. The surface under the study must have a stochastic speckled pattern to accurately measure the deformations. Therefore the speckle pattern was prepared by spraying thin coat of flat white paint base and randomly spraying flat black paint on top of it. The specimen prepared with the speckles is shown in the inset of Figure 3-13 and

Figure 3-17. The specimens were then kept in a weighing balance to continuously monitor the moisture loss during the test.

Noise test was conducted before each experiment was started. Once the noise level was obtained below the admissible limit the test was started and the system continuously took the pictures at predefined time intervals. Both tests were run for 4 days. The test was stopped when no new cracks appeared for a long time and also the moisture loss rate was slowed down. Figure 3-19 through Figure 3-22 show the cracking of the Grapevine soil, Joe Pool soil, 8% lime treated Grapevine soils and 8% lime treated Joe Pool soil respectively, at the end of the test.

Once the test was over, post processing was conducted to analyze the test results. The first task in post processing is selecting an area of interest in the initial picture. This is called masking in ARAMIS. A circular area covering the specimen was selected for the analysis. Then a starting point was selected in the masked area. The starting point is very important in the sense that ARAMIS must be able to clearly identify the point in every picture that will be used in the deformation measurement. The vertical deformation, shrinkage strain, crack length and width were the key information collected from the DIC. Figure 3-23 presents an example of the strain contours obtained after the post processing of the images. The blue areas represented the compression field, and the red areas indicate the tension field. The cracks were occurred in the tension field. The

tension field represents the location of maximum tensile stress due to shrinkage movement within the soil.

Figure 3-19 Cracking of the Grapevine soil at the end of the test

Figure 3-20 Cracking of the Joe Pool soil at the end of the test

Figure 3-21 Cracking of 8% lime treated Grapevine soil at the end of the test

Figure 3-22 Cracking of the 8% lime treated Joe pool soil at the end of the test

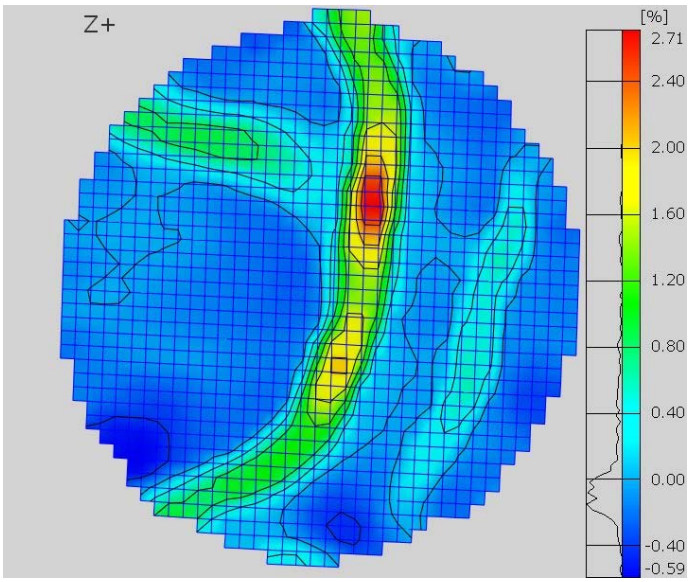

Figure 3-23 Strain contours of a specimen during drying and cracking

3.10.3 Analysis and Discussion

The initial soil specimen thickness was measured at different locations using precision calipers. An average initial specimen thickness was determined based on the measurements. Similarly, the average final specimen thickness was also determined by measuring the thickness of each segment at the end of the test. The water content of the specimens was continuously monitored using the balance.

An example of the crack length measurement using the ARAMIS software is presented in Figure 3-24. First, line segments were drawn along the crack length. Then, the length of each segments were determined as shown in Figure

3-24. Later, the total crack length was determined by adding the lengths of the individual segments. The procedure was repeated on the both sides of the crack. The average crack length was determined by averaging the lengths on the both sides of the crack. The lengths of other cracks were also determined using similar procedure.

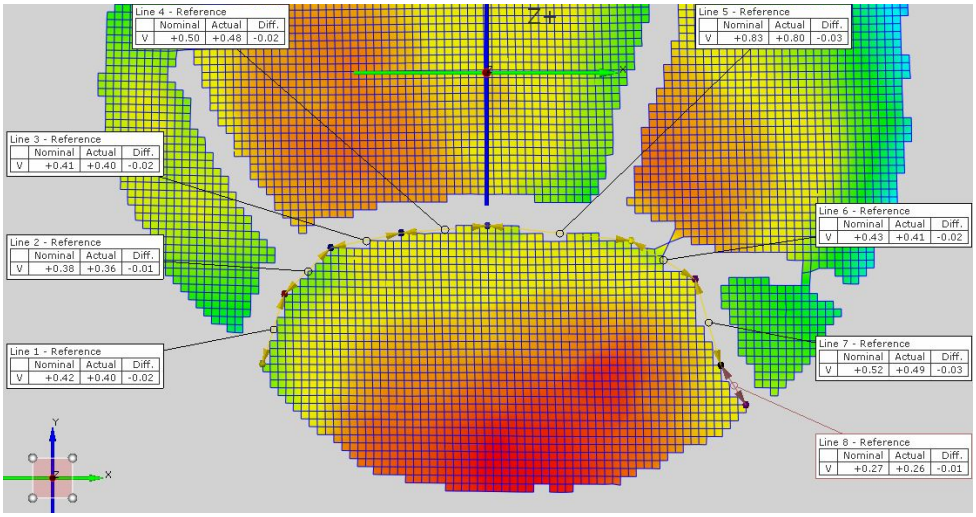

Figure 3-24 Crack length determination using ARAMIS software

Similarly, an example for determining the crack width is presented in Figure 3-25. First, two points were selected on both sides of the crack to make the line joining them was perpendicular to the crack at that location. Then, the distance between these points were determined at the beginning and end of the test. The difference between final and the initial distances gives the opening of the crack at the location. The terms nominal, actual, and diff. as shown in Figure 3-25 represent the original distance, final distance, and crack width respectively. The

values in the figure were in inch units. They were later converted into millimeters. The similar procedures were repeated for each crack. The crack widths were measured at multiple locations to determine average width of each crack.

The crack widths shown in Figure 3-25 are the ones at the end of the test. Only the final crack width does not reveal when the crack was formed and how did the width increase with drying. With the program used in the analysis, it was possible to find the initiation of the cracks and the increase in the width with time. An example of such analysis is presented in Figure 3-26. As it can be observed from the plot, the distance between two points across the crack of a soil specimen decreased slightly due to shrinkage before the crack appeared. After the crack is formed the crack width rapidly increases for first few hours and then the gap increases at a slower rate afterwards.

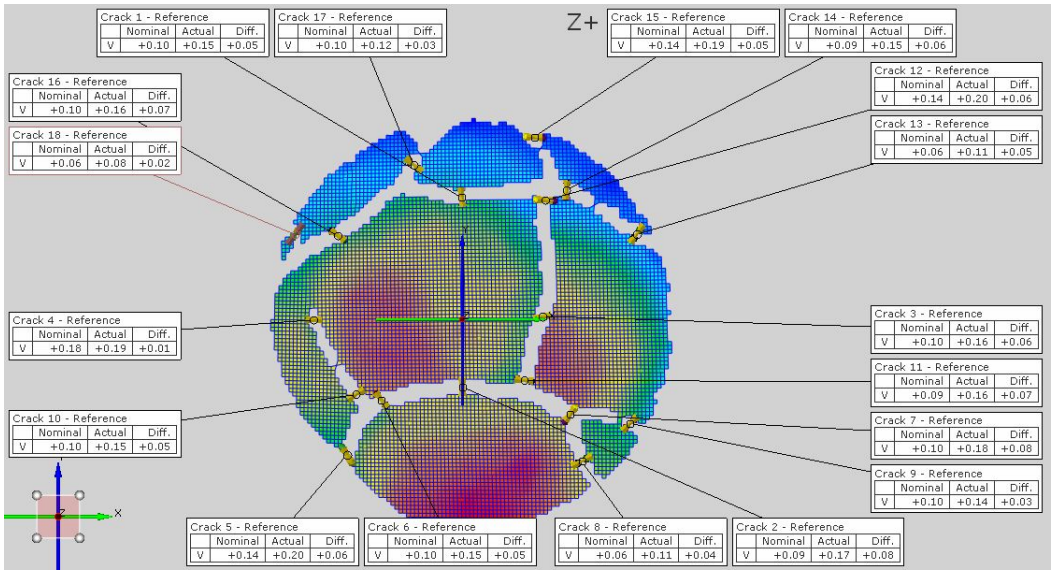

Figure 3-25 Crack width measurement using ARAMIS software

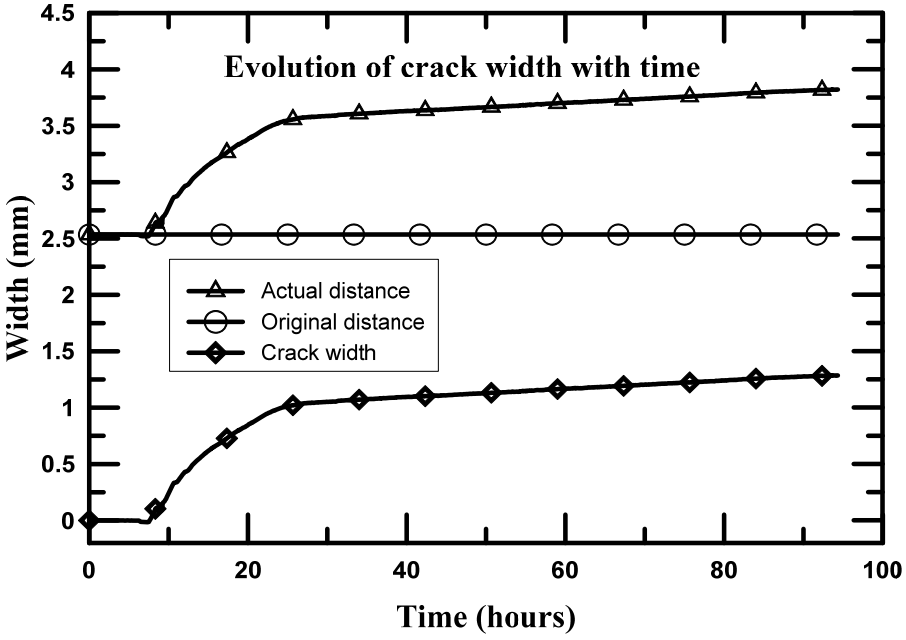

Figure 3-26 Change in distance between two points across the crack

All the cracks shown in Figure 3-25 were further analyzed to find the time of crack development for individual cracks. Figure 3-27 shows the evolution of crack widths with time for different cracks at different locations. Figure 3-28 gives an even closer view of the crack evolution. It becomes evident from the figures that the distance between the points decreases first due to shrinkage. Then the crack appears due to tensile stress occurring in the soil mass due to shrinkage. Once the crack is developed the crack width increases rapidly for few hours and then it increases at a slower rate. Crack 17 was the first and crack 4 was the last to occur in the soil specimen discussed in this example. Crack 4 was the last to appear in the specimen. Crack 4 shows the maximum shrinkage before forming

the crack. But the crack width remains fairly smaller compared to all other cracks. Cracks 2 and 7 appear almost at the same time and also show the similar maximum width although the evolution history is little different. Thus, with the help of DIC system it becomes possible to precisely track the crack evolution in a dying soil mass.

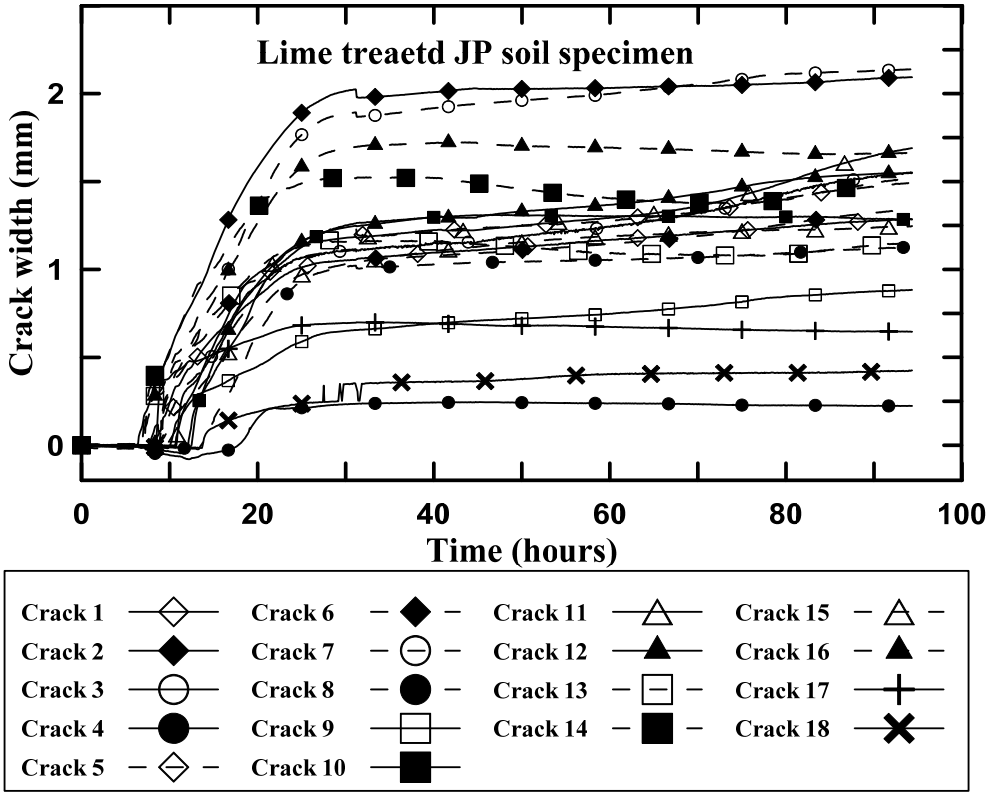

Figure 3-27 Evolution of crack width with time

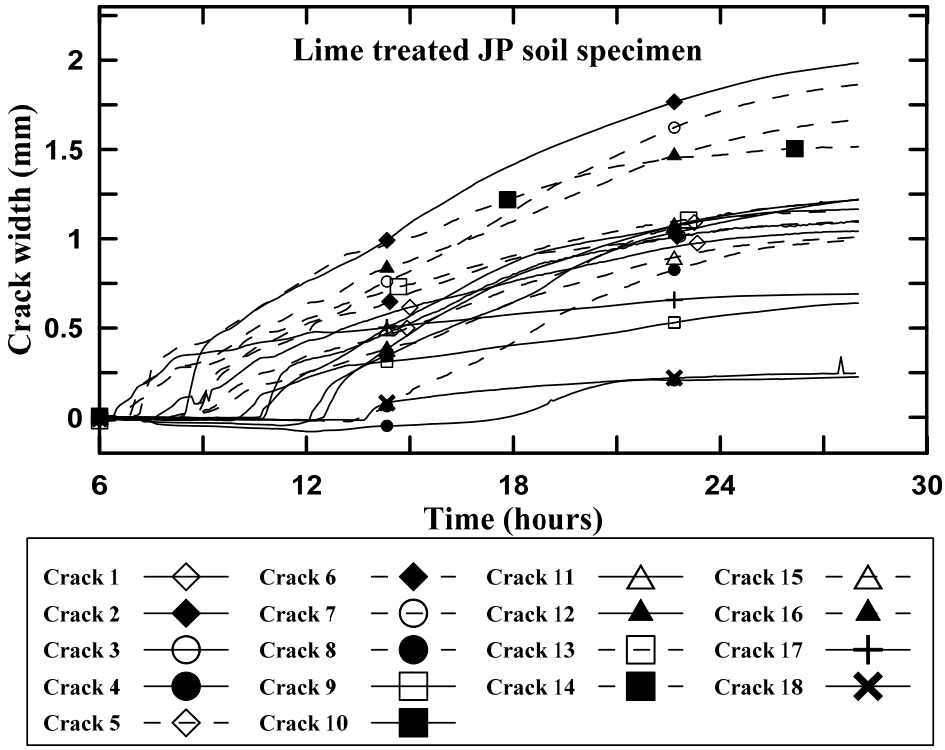

Figure 3-28 A closer view of the initiation and evolution of different cracks

Thus, all crack related information was obtained from the DIC technique for all four soil specimens. The summary of the test conditions and test results are presented in Table 3-6. The total area of the crack was obtained by first calculating the area of individual cracks and then summing them up together. Total length of crack was also calculated by adding the individual crack length. The amount of cracking was quantitatively represented by Crack Intensity Factor (CIF), similar to the one used by Atique and Sanchez (2011). CIF is the ratio between the total area of crack divided by the total area of soil.

Table 3-6 Summary of the shrinkage test results obtained from DIC

Parameters	Soils			
	GV control	JP control	GV lime treated	JP lime treated
Initial thickness (mm)	9.9	10.1	10.3	9.8
Final thickness (mm)	9.1	9.1	9.9	9.1
Test duration (hours)	91	91	91	94
Initial moisture content (%)	38.6	49.5	35.6	48.5
Cracking tensile strain (%)	0.36	2.31	2.71	0.86
Cracking moisture content (%)	34.5	40.7	31.9	44.9
No of cracks	16	17	1	6
No of crack segment	22	25	2	8
Total length of cracks (mm)	719.6	606.4	113	430.9
Average width of cracks (mm)	1.4	2.1	0.5	1.1
Total area of cracks (mm^2)	1162.5	1493.8	56.5	571.2
CIF (%)	10.3	13.2	0.5	5.1

The locations of first cracks in the specimens are presented in Figure 3-29 through Figure 3-32. Cracking of the specimens initiated nearly at the middle of the specimens. These observations were consistent with the analytical model proposed by Kodikara and Choi (2006) which highlighted that the maximum tensile stresses occur at the mid-section of the soil layer. Theoretically, the maximum tensile stress occurs at the middle of the specimen, but the presence of flaws can create a crack in other locations were the tensile stress may not be maximum (Costa et al. 2008). It is often possible for the initial cracking to occur at the edge where the soil has poor bonding with the wall of the container. However, the initial cracks were well within the soil specimens for all the

experiments conducted in this research. Simultaneous occurrence of multiple cracks is also possible as observed in the case of 8% lime treated Joe Pool soil specimen where two cracks are formed nearly at the same time. The subdivisions of the specimens take place in the similar way by developing cracks in the middle of the successive fragments. As shown in Figure 3-19 through Figure 3-22, cracks intersect each other almost orthogonally. This is consistent with the crack patterns presented by Costa et al. (2008) and Sanchez et al. (2013).

The crack width, crack area of the high plasticity Joe Pool soil was higher than that of the low plasticity Grapevine soil. As shown in Table 3-6, the average crack width and crack area of the Joe Pool soil were 2.1 mm and 1493.8 mm2 respectively. Similarly, those of the Grapevine soil were 1.4 and 1162.5 mm2 respectively. The effect of lime treatments were evident from the comparison of the cracking characteristics of untreated and lime treated soil specimens. The crack widths, crack number, crack lengths and total crack area were tremendously decreased for the lime treated soils specimens. The average crack widths for lime treated Grapevine and Joe Pool soils are 0.5 and 1.1 mm respectively compared to 1.4 and 2.1 mm of the untreated ones. The crack areas also reduced significantly from 1162.5 and 1493.8 mm2 to 56.5 and 571.2 mm2 respectively for Grapevine and Joe Pool soil specimens. As a result, the crack intensity factor (CIF) reduced from 10.3% to 0.5% in case of Grapevine soil, and from 13.2% to 5.1% in case of Joe Pool soil.

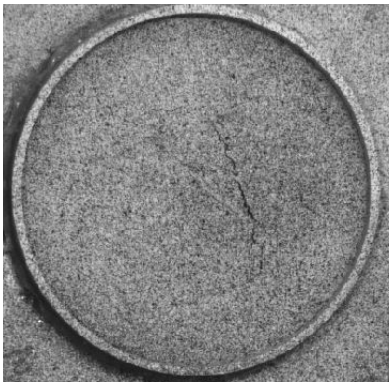

Figure 3-29 Initiation of first crack in Grapevine soil specimen

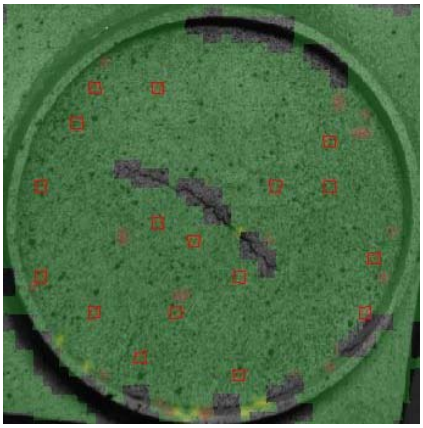

Figure 3-30 Initiation of first crack in Joe Pool soil specimen

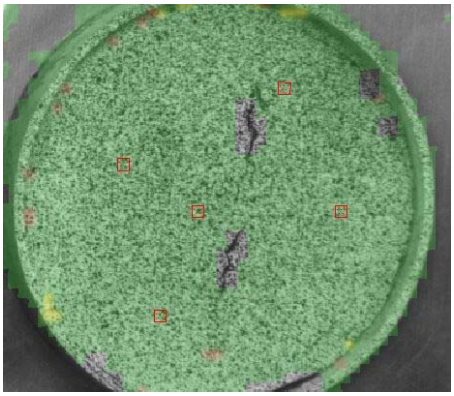

Figure 3-31 Initiation of first crack in 8% lime treated Grapevine soil specimen

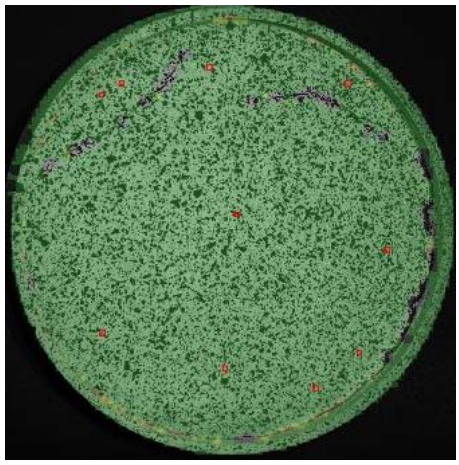

Figure 3-32 Initiation of crack in 8% lime treated Joe Pool Soil Specimen

The following discussion is presented based on the analysis of the lime treated Joe Pool soil specimen. Lime treated Joe Pool soil specimen was selected for this discussion because of the uncomplicatedness of the crack network compared to that of untreated Grapevine and Joe pool soils. Vertical displacement profile along two sections, vertical and horizontal displacement of crack edges, and lifting off of the crack edges of the lime treated Joe Pool soil specimen are discussed in the subsequent sections.

The vertical displacement profile of a predefined section at different time intervals can also be analyzed using the DIC technique. Two sections passing through the middle of the lime treated Joe Pool soil specimen in X and Y directions were selected as shown in Figure 3-33 and Figure 3-34 respectively. The sections along X and Y directions are referred to as sections 0 and 11, respectively in the current discussion. Both sections pass through two cracks.

These cracks are referred as left and right cracks in case of section 0 and top and bottom cracks in case of section 11 depending upon their location on Figure 3-33 and Figure 3-34 respectively. The vertical displacements along the sections at different times were analyzed and presented as shown in Figure 3-35 and Figure 3-36.

Before formation of a crack, the pair of points on the both sides of the crack move relative to each other. However, the points can move independently once the crack is developed. The freedom of their movements after crack is formed is evident from the Figure 3-35 and Figure 3-36. In case of right crack and left crack the vertical displacement of points in opposite directions after cracking is more obvious. One side of the crack is going down and the other side of the crack is lifting off. The lifting off of soil due to shrinkage is called the curling up of the soil (Kodikara et al., 2004). The lifting off of the soil can happen at the edges or in the middle. As it can be seen from Figure 3-35, two edges of the central segment settle more than the middle part of the segment. This is due to the curling up happening in the middle of the segment. However in the case of Section 11, one edge of the segments was settling down while the other one was lifting off. Thus, different curling behavior of the crack segments was observed in two mutually perpendicular directions.

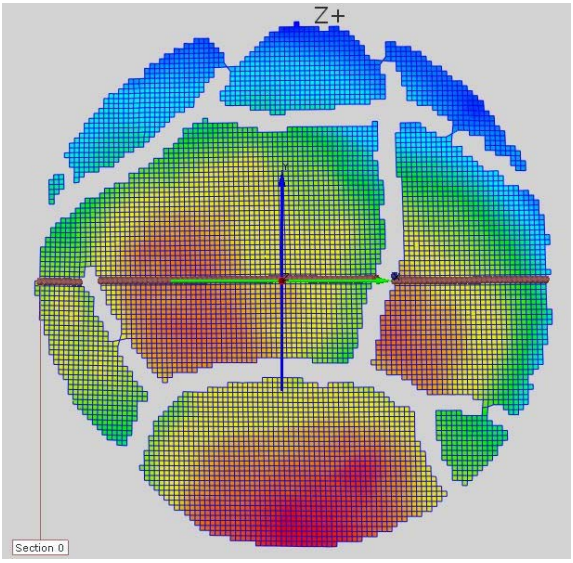

Figure 3-33 A section along X direction passing through middle of the lime treated Joe Pool soil specimen (Section 0)

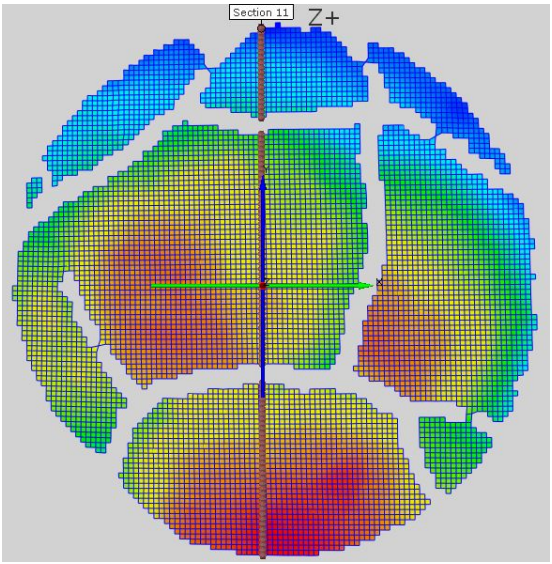

Figure 3-34 A section in Y direction passing through middle of the lime treated Joe Pool soil specimen (Section 11)

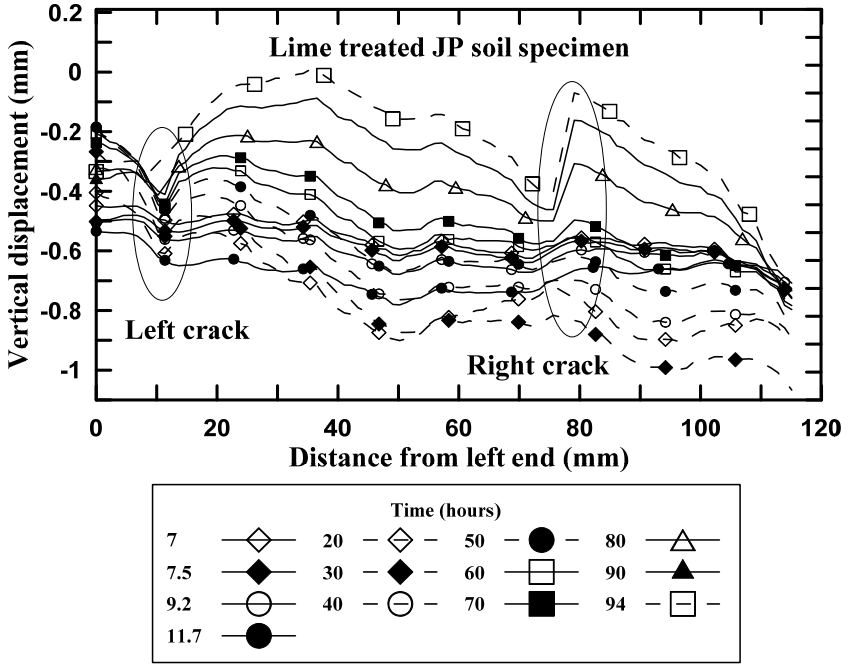

Figure 3-35 Vertical displacement profile of the specimen along section 0

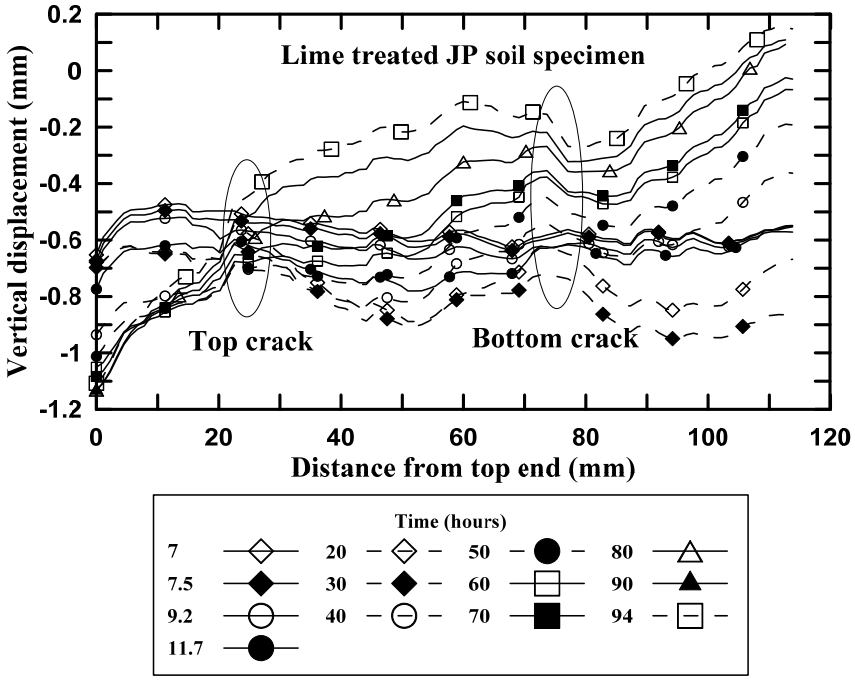

Figure 3-36 Vertical displacement profile of the specimen along section 11

The locations and nomenclatures of different points used in the analysis of lime treated Joe Pool soil specimens are as shown in Figure 3-37. The vertical and horizontal displacements of the two sides of the both cracks along section 0 were also computed and are presented in Figure 3-38 and Figure 3-39 respectively. Stage points 22 and 23 correspond to the right crack and stage points 24 and 25 correspond to the left crack along the section 0. Points 22 and 25 were on the left side and points 23 and 24 were on the right side of the respective cracks.

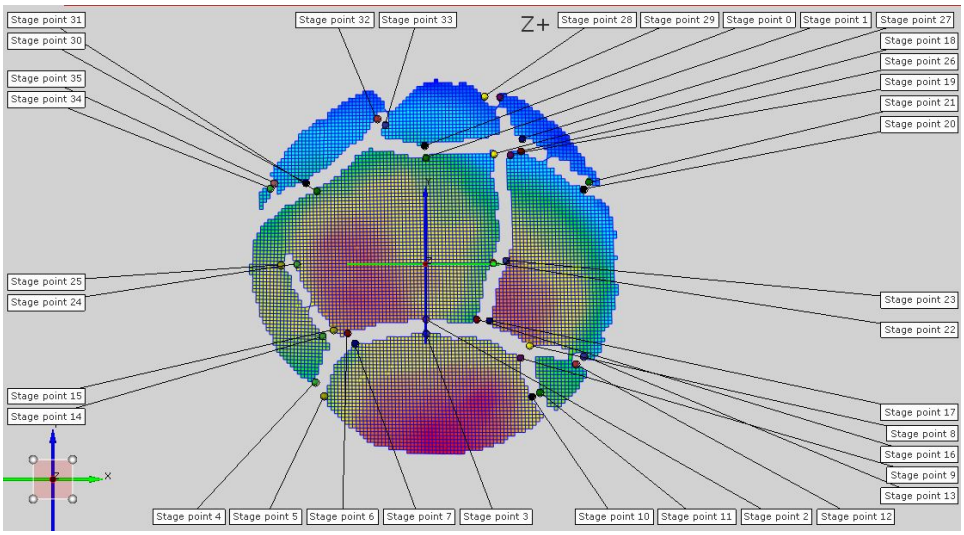

Figure 3-37 Locations and nomenclatures of different points used in the analysis of lime treated Joe Pool soil

It can be observed from the Figure 3-38 that the pair of points 22-23 and 24-25 show similar settlement behavior throughout the test. First the points show settlement and then the edges start lift off gradually. Points 24 and 25 start curling up before points 23 and 23. Point 23 shows significantly higher curling up

compared to point 22, which was also observed in Figure 3-35. Figure 3-38 also suggests that the edges of the respective cracks were moving upward after the formation of the cracks.

Since the substantial amount of crack movement of these points in horizontal plane takes place in the X direction, the displacement of the points in the X direction was also computed. All the points moved in the positive X-direction (i.e., towards the right) except point 22. Points 24 and 22 both belonged to a same crack segment and were located at the opposite sides. The segment was a biggest segment in the specimen and the shrinkage movement of these points was higher compared to the points 23 and 25. Points 23 and 25 belonged to different crack segments. Point 25 showed higher movement than point 23 because it belonged to a bigger crack segment compared to that of point 23.

The vertical and horizontal displacements of the two sides of the both cracks along section 11 were also computed and are presented in Figure 3-40 and Figure 3-41 respectively. Stage points 0 and 1 correspond to the top crack and stage points 2 and 3 correspond to the bottom crack along the section 11.

It can be observed from the Figure 3-40 that the pair of points 0-1 and 2-3 show similar settlement behavior throughout the test. First the points show settlement and then the edges start lift off gradually. Points 2 and 3 show relatively higher curling up compared to points 0 and 1, which was also observed in Figure 3-36.

Since the substantial amount of crack movement of these points in horizontal plane takes place in the Y direction, the displacement of the points in the Y direction was also computed. Points 0 and 2 moved towards positive Y direction and point 1 and 3 towards negative Y direction. Points 1 and 2 both belonged to a same crack segment and were located at the opposite sides. The segment was a biggest segment in the specimen and the shrinkage movement of these points was higher compared to the points 0 and 3.

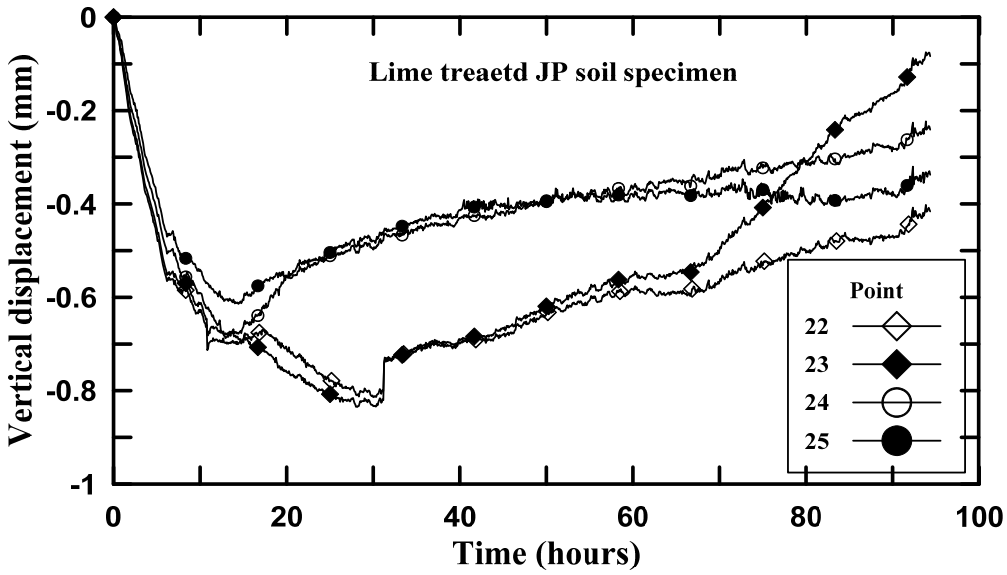

Figure 3-38 Vertical displacement of edges of left and right cracks at different time

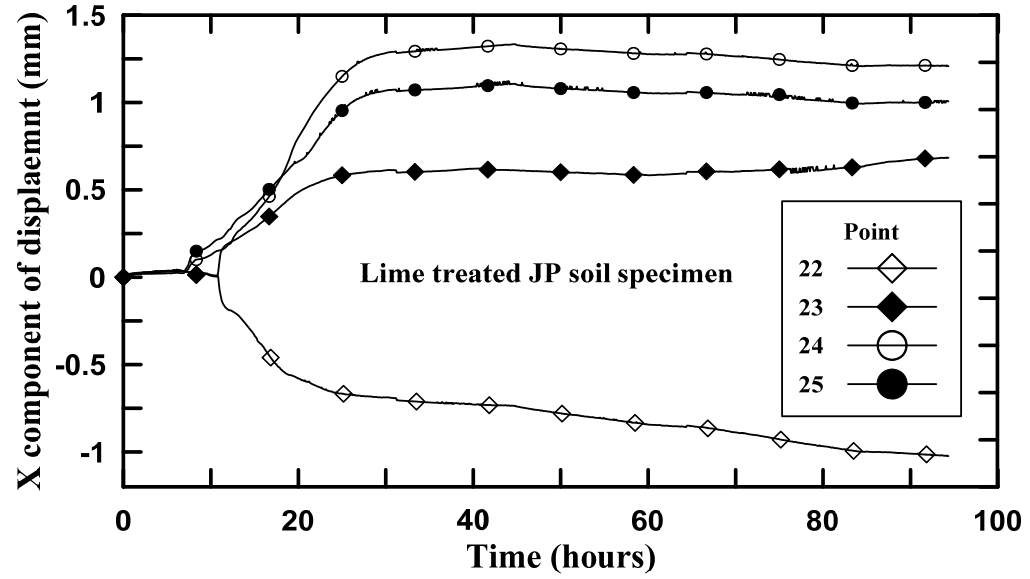

Figure 3-39 Horizontal displacement of edges of left and right cracks at different time

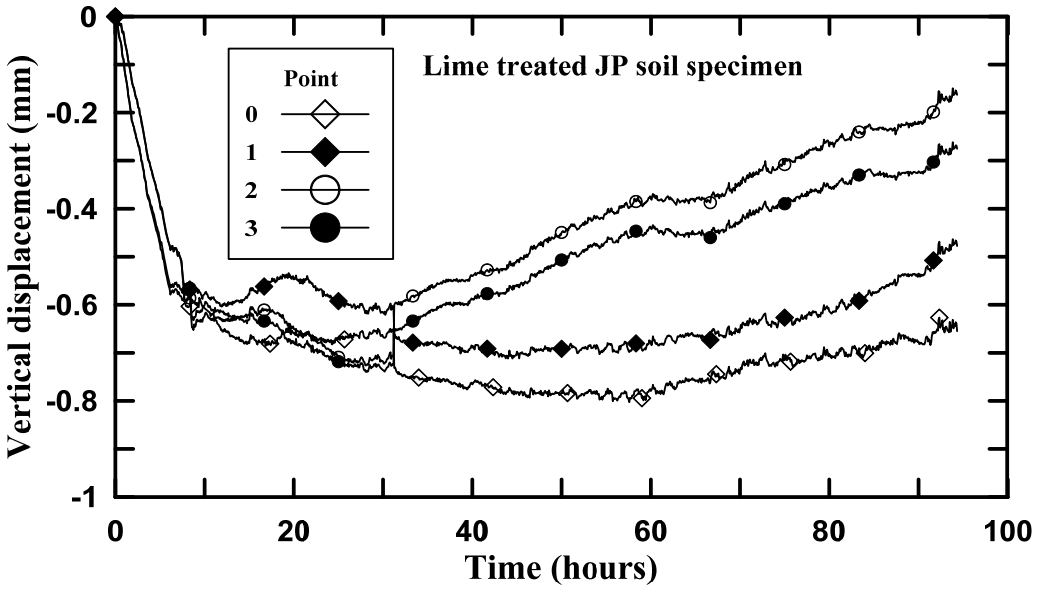

Figure 3-40 Vertical displacement of edges of top and bottom cracks at different time

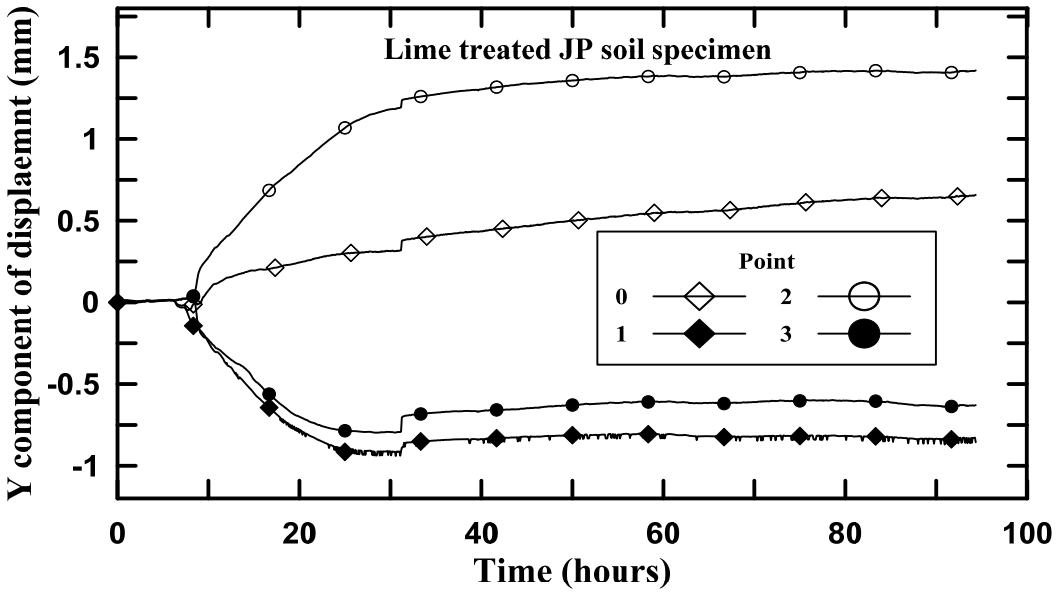

Figure 3-41 Horizontal displacement of edges of top and bottom cracks at different time

From above discussion, it was clear that the curling up of the soil cells or soil fragments happens during the shrinkage tests. The edge or the part of soil specimen that is lifting off will not be in contact with the mold. It results in difficulties in tracking the change in the thickness of the specimen once the curling up or lifting off the edge begins. The curling up of the specimen is mostly inevitable in case of clayey soil specimens. Thus the digital image analysis procedures being proposed by researchers in measuring the volume change of the clayey specimens during drying must address this phenomenon. Otherwise, the volume measurement based only on the elevation of top surface of the soil specimen will be mistaken.

3.11 Soil Suction Studies

Soil water characteristics curve (SWCC) is a representation of the fundamental behavior of soil matric suction with moisture content property. Different methods has been practiced to determine the SWCC. Present research utilized filter paper method, pressure cell method, and WP4C dewpoint potentiometer to determine the SWCCs of the soils. The methods are presented in the following sections.

3.11.1 Filter Paper Method

The filter paper method was used in accordance with the Standard Test Method for Measurement of Soil Suction (ASTM D5298). Filter paper method can be used to determine the matric suction of undisturbed as well as remolded soil specimens. This method is founded on the assumption that the moisture content of the filter paper comes into equilibrium when kept with the soil in a closed environment for a period of time. The equilibrium stage is generally achieved through vapor moisture exchange or liquid exchange.

If the filter paper is placed in direct contact with the soil specimen, the equilibrium is achieved due to liquid exchange. The recorded moisture of the filter paper gives the matric suction of the soil specimen. However, if the filter paper is suspended above the soil specimen in a closed container without contact, the moisture transfer occurs through vapor exchange. The resulting moisture content of the filter paper yields the total suction of the soil.

The water content of the filter paper can be related to the suction value as given in the filter paper calibration curve designed by researchers. The calibration curve was used to obtain the suction of the soils. In this research, filter paper method is used to measure the matric suction over higher ranges.

The filter papers used in this research are in compliance with ASTM E832. Figure 3-42 shows the Whatman No. 42 filter papers used in this research. Similarly, Figure 3-43 shows the calibration curve for Whatman No. 42 filter paper.

Figure 3-42 Filter paper technique for measuring matric suction

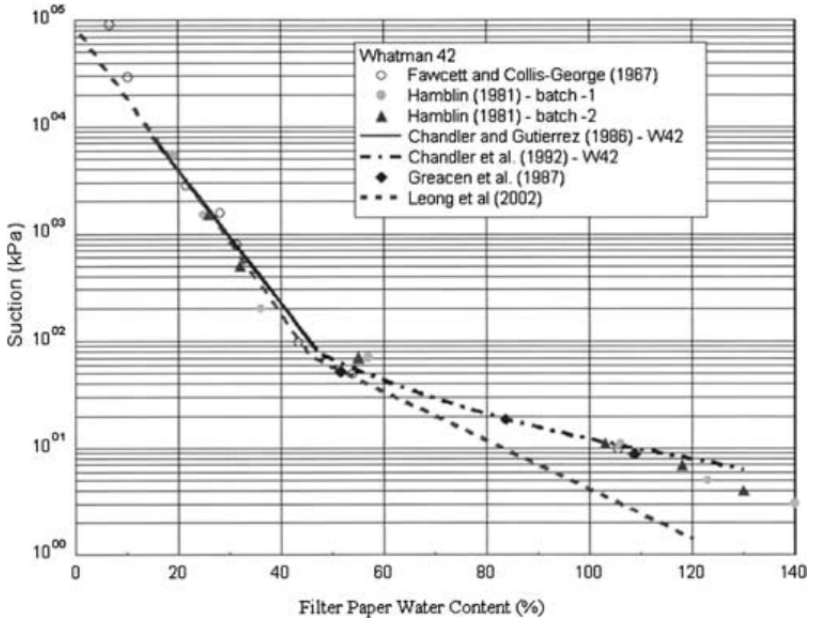

Figure 3-43 Calibration curve for Whatman No. 42 filter paper

3.11.2 Pressure Cell Apparatus

The pressure cell apparatus utilizes the axis translation method for determining the matric suction of the soil. The axis translation is achieved with the help of a high air entry (HAE) value disk. This disk allows water to flow and prevents air passing through its micro-pores when saturated. Thus the disk acts as an interface between the soil, air and water. The pressure cell apparatus used in the current study is presented in Figure 3-44.

When the air pressure is increased inside the cell, the water is expelled out from the soil pores. The expelled water is collected in the burette columns. Air pressure of known value is maintained for a period of time until the pore water stops flowing out. The flow of water into the burettes is continuously monitored

during the test. Cease in increase in the water height in the burette column is indicator of the equilibrium condition. Then, a known pressure of even higher magnitude is applied. And, the process is repeated for each increment in the air pressure. The air pressure can only be increased within some range defined by the air entry value of the HAE disk. In the current research the air entry value of the HAE disk was 500 kPa. Filter paper method was used to determine the matric suction of the soils above this value.

Figure 3-44 Pressure cell apparatus used in the current study

3.11.3 WP4C Dewpoint Potentiometer

The WP4C measures suction based on chilled mirror Dewpoint technique, a technique of determining the relative humidity of the air above a sample in a closed chamber. The relative humidity measured is related directly to the water potential of the soil at equilibrium.

WP4C potentiometer was used to determine the SWCC of the slurry soils only. The potentiometer was initially calibrated using potassium chloride solution at 25^{o}C before the experiment. Slurry soil specimens were prepared at the consistency of liquid limit. The specimens were allowed to dry in the air and also using the heating lamp as required to reach the different levels of water content and suction. The soil sample was kept in the WP4C potentiometer to determine the soil suction. The suction of the soil specimens were recorded as displayed by the machine and the soil was immediately taken out to determine the water content. Figure 3-45 shows the potentiometer and the precision balance used in this study.

Figure 3-45 WP4C Potentiometer and precision balance used in the measurement of soil suction

The SWCC curves of the soils determined using the WP4C potentiometer are presented from Figure 3-46 to Figure 3-55. The SWCC curves are plotted between the gravimetric water content and total soil suction. The WP4C potentiometer is generally effective in determining relatively higher suction values. Consequently, the points in the SWCC curves are more scattered in the low suction range. Relatively well-defined trend is observed in the higher suction range. These suction values can be related to the shrinkage induced pressures of the soils by using the moisture content of soil measured during the SIP test. The measurement of SIP and its relation with soil suction is described in section 3.13.

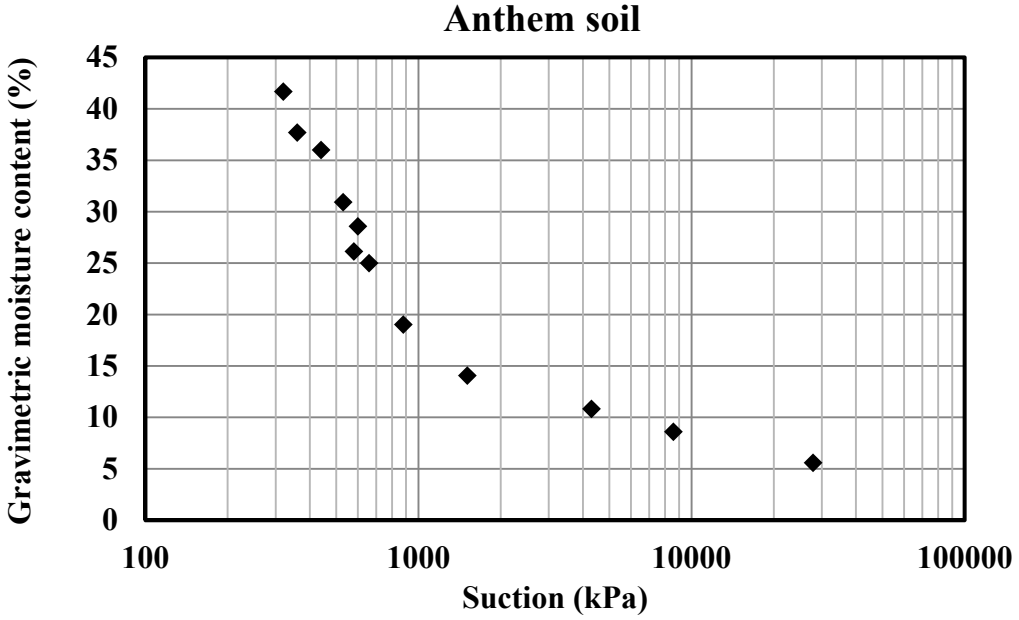

Figure 3-46 SWCC curve for the Anthem slurry soil

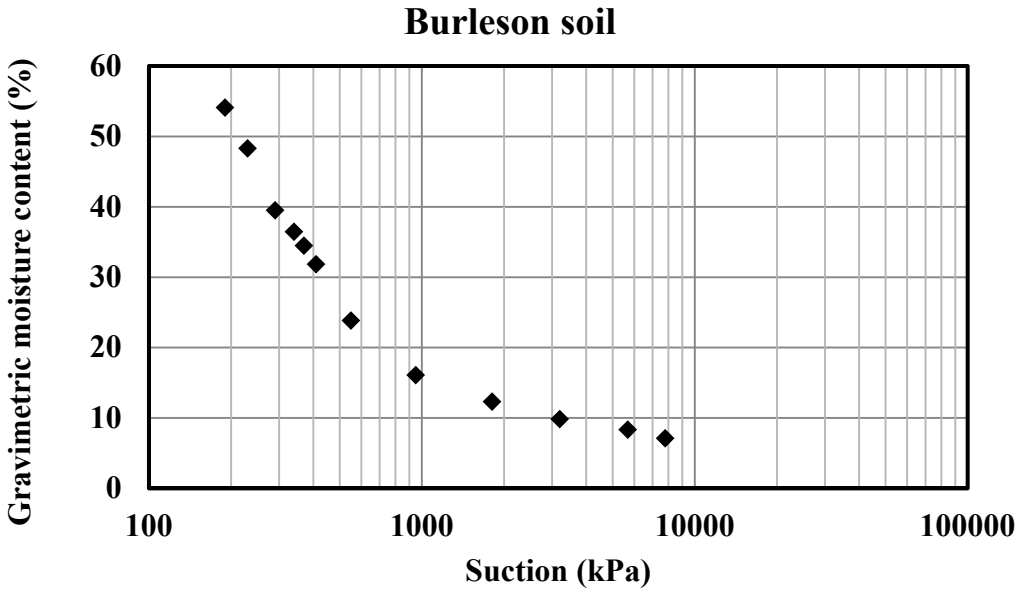

Figure 3-47 SWCC curve for Burleson slurry soil

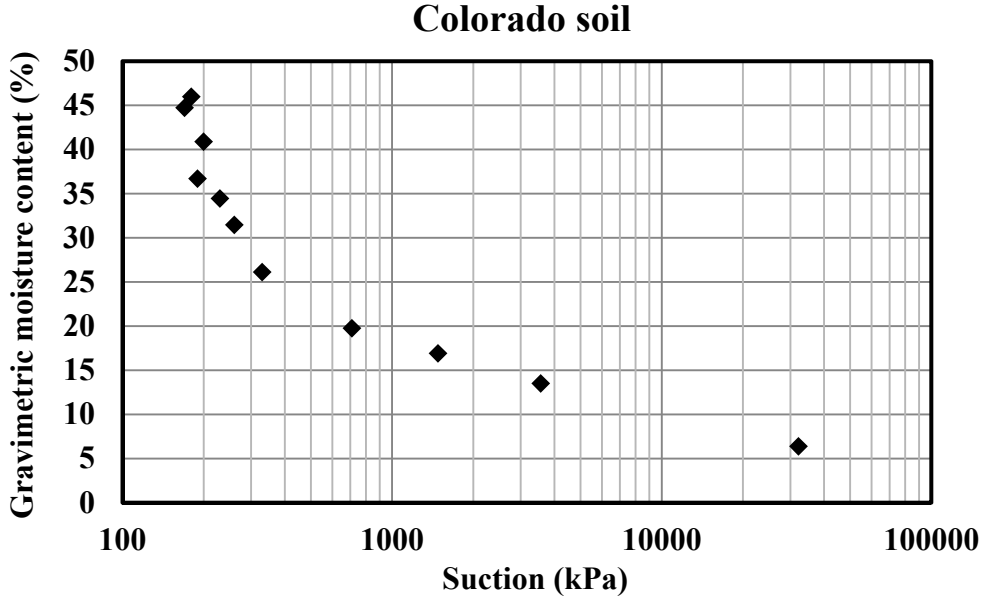

Figure 3-48 SWCC curve for Colorado slurry soil

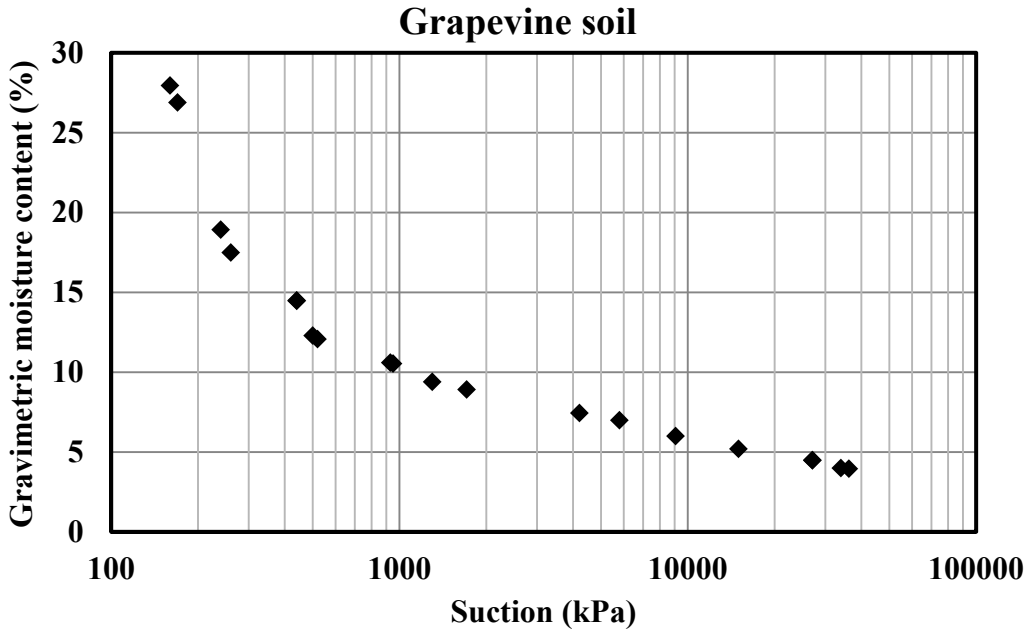

Figure 3-49 SWCC curve for Grapevine slurry soil

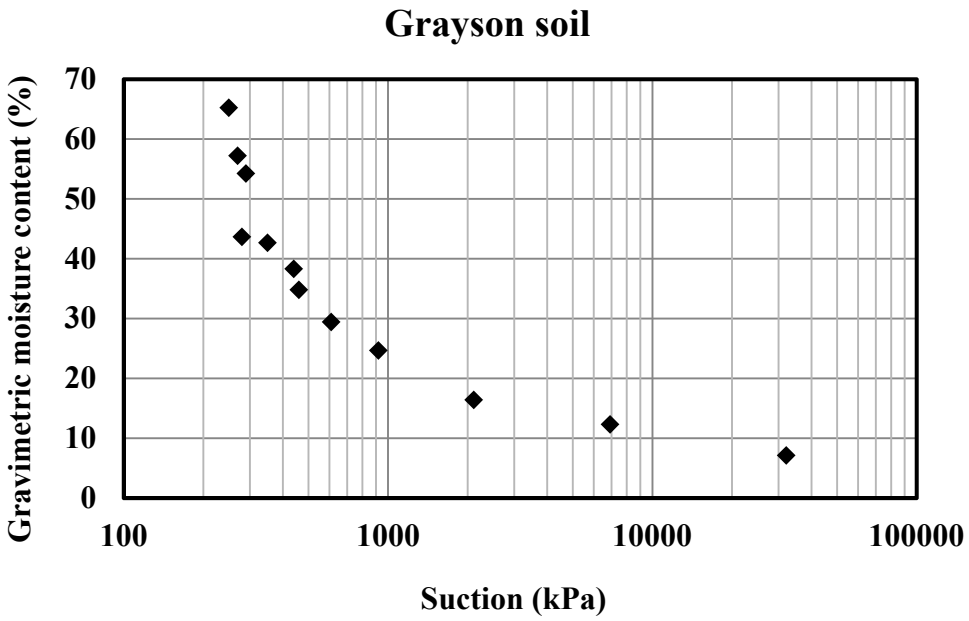

Figure 3-50 SWCC curve for Grayson soil slurry

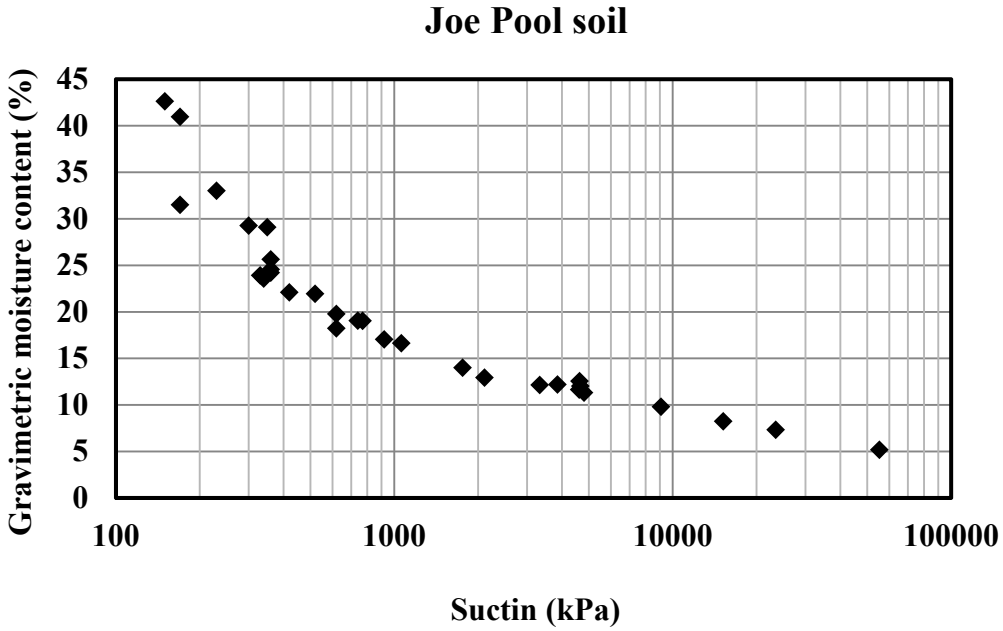

Figure 3-51 SWCC curve for Joe Pool slurry soil

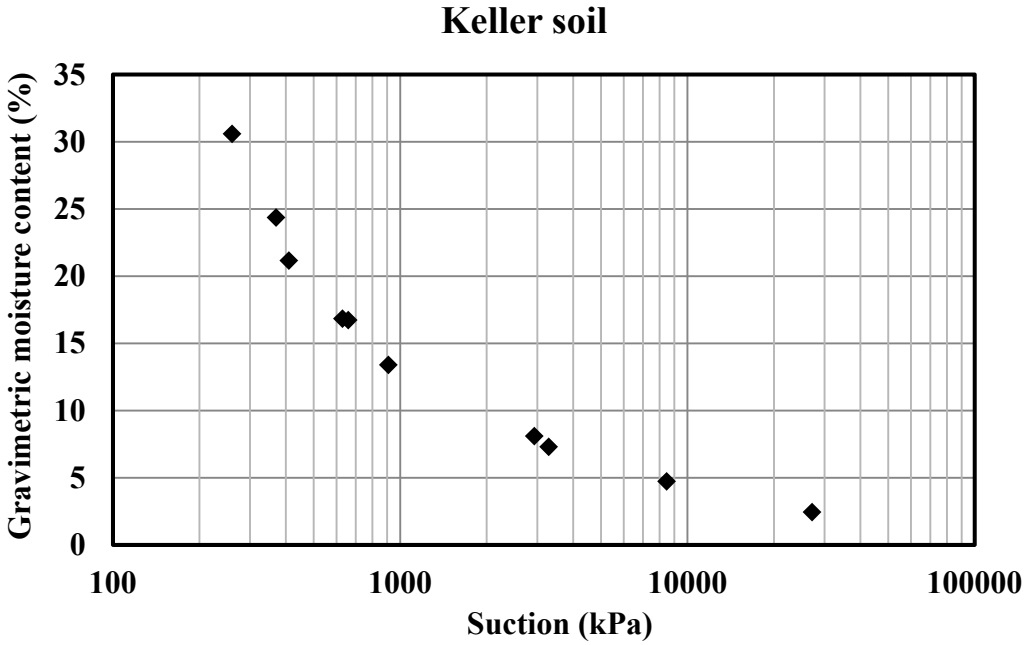

Figure 3-52 SWCC curve for Keller slurry soil

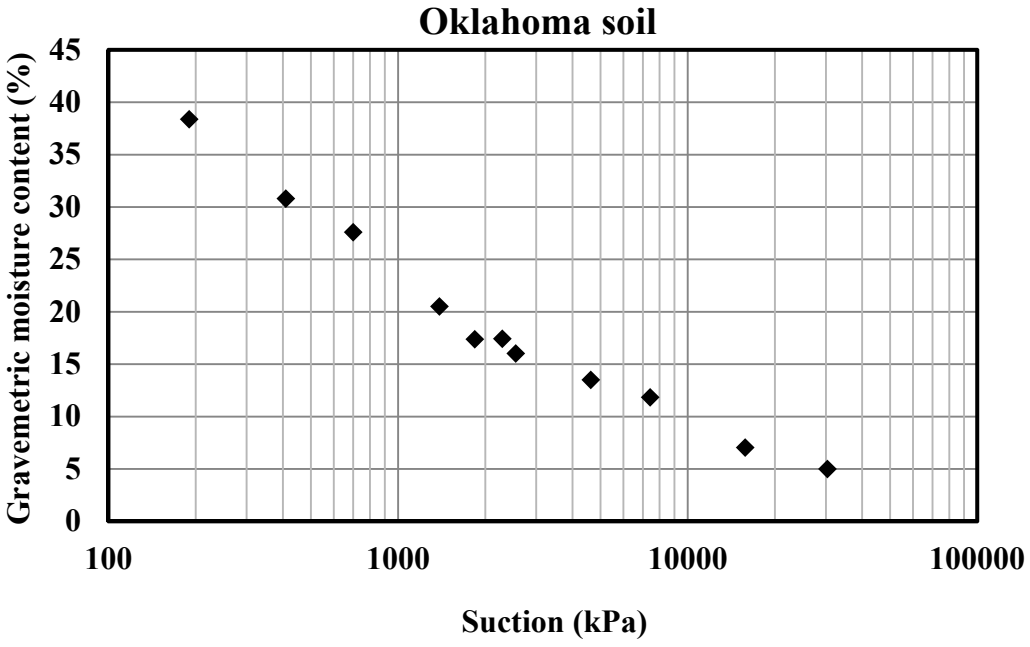

Figure 3-53 SWCC curve for Oklahoma slurry soil

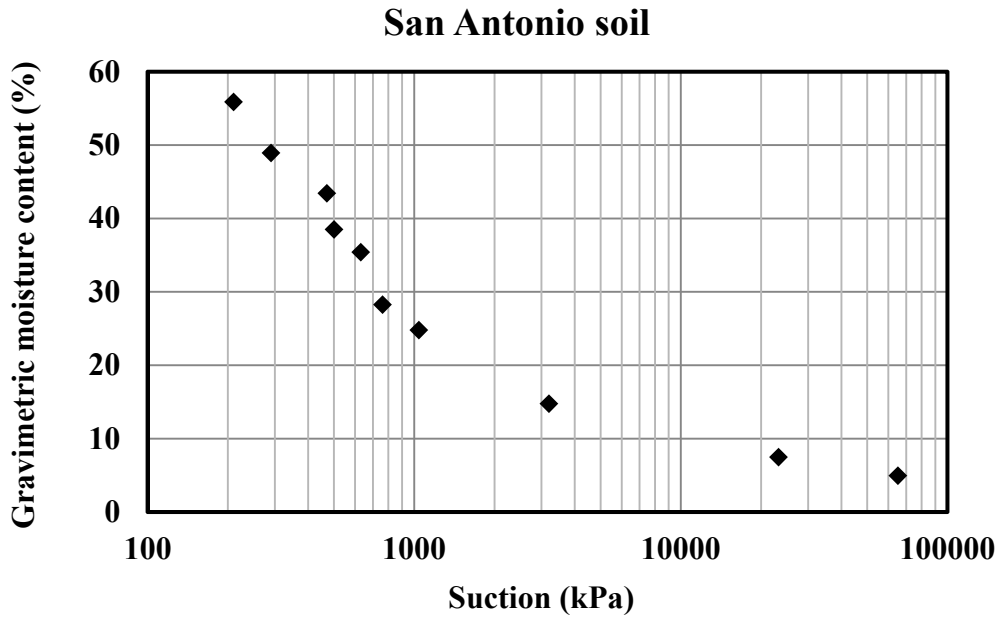

Figure 3-54 SWCC curve for San Antonio slurry soil

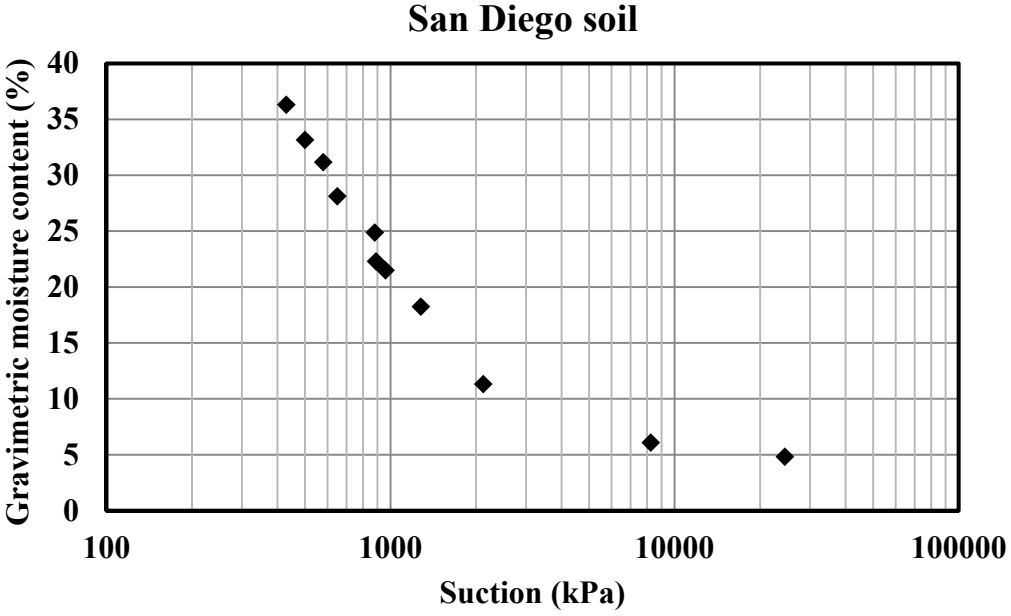

Figure 3-55 SWCC curve for San Diego slurry soil

3.12 Indirect Tensile Strength Test (IDT)

Indirect tensile strength test was used to measure the tensile strength of the untreated and treated soils used in this study. The tensile strength of materials is generally obtained by performing a direct uniaxial tensile test. In the direct test the specimen is pulled apart to find its strength. However, it is inconvenient to perform direct tensile test on soils. Therefore, the indirect tensile strength or splitting tensile strength test is considered and performed in the current study. The results from the IDT tests are compared with the shrinkage induced pressure of the soils. The indirect tensile strength represents the force required to break the physical bond between particles. And shrinkage induced pressure gives the force of attraction or bonding between the particles when subjected to drying.

The IDT test was conducted in accordance with ASTM D3967, Standard Test Method for Indirect Tensile Strength of Intact Rock Core Specimen. Even though the specimens used in the current research are clays, the characteristics of tensile force acting on the specimen are still the same as the rock specimen. The specimens used in the experiment were circular disk like specimens. Two kind of specimen were prepared in the study; slurry soil and compacted soil specimens. In case of slurry soil, the soil was first mixed with water to bring them to a liquid consistency (LL+10%). Then the soil was molded using small cylindrical shaped moisture cans as shown in Figure 3-56. The soil specimens were allowed to air dry in the room temperature and humidity conditions.

The tests were mostly conducted on dried specimens with some residual moisture contents. However, few attempts were also made to measure the tensile strength at relatively higher moisture contents to study the evolution of tensile strength with the loss of moisture content. The dimensions (diameter and thickness) of the specimens vary depending upon the shrinkage potential of the soils. The diameters and thicknesses of the specimens were measured before the test. Moisture contents of the specimens were also determined to relate the strength and moisture content. The specimens used in these tests should be free from cracks and have a thickness to diameter ratio of 0.2 to 0.75 as per ASTM D3967. Prior to the testing, the sides of the specimens were prepared to have a smooth surface. Rough surfaces were trimmed to avoid stress concentration. The air dried slurry soil specimens made ready for the experiment are shown in Figure 3-57. Figure 3-58 shows the IDT test setup used in the current study. The tests were conducted to measure the load that induced a cracking along the vertical diameter of the specimens as shown in Figure 3-58.

Figure 3-56 Slurry soil specimens molded for IDT

Figure 3-57 Slurry soil specimens dried in air and made ready for testing

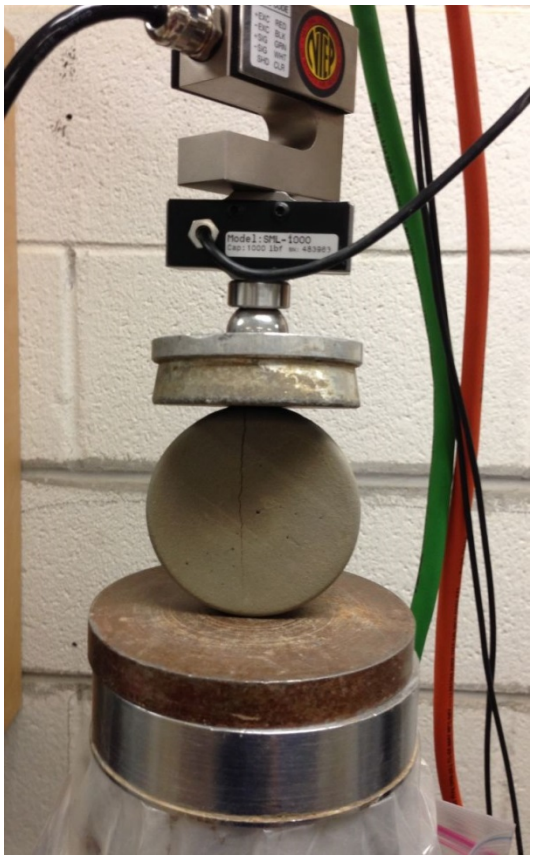

Figure 3-58. Indirect tensile strength test (IDT) on dry soil specimen

According to ASTM D3967, the indirect tensile strength of the specimen can be calculated as per the following Equation:

$$\sigma_t = \frac{2P}{\pi LD} \quad 3\text{-}1$$

where, σ_t = indirect tensile strength,

P = maximum load measured at failure of the specimen,

L = thickness of the specimen

D = diameter of the specimen

The summary of the IDT test results of the slurry soil specimens are presented in the Table 3-7. It can be observed from the Table 3-7 that the Grayson soil has the highest and San Diego soil has the lowest indirect tensile strengths. Soils are generally very weak in tension and the tensile strength is generally ignored in the calculations. But, the IDT conducted on the slurry soils yielded significantly high tensile strength. It should be noted that the specimens were made from very fine clayey soils passing sieve No.40. The slurry soil was allowed to dry slowly inside the room environment for a long period of time. Also, the specimens were small in size. All these factors contributed to the very high tensile strengths of the soils.

On the other hand, the soil in the field contains wide ranges of particle sizes. Organic matter is also present in soils in natural conditions. The locations of bigger size particles and organic matters can create a weaker soil. We have already observed the linear shrinkage strains as high as 18% in the soils in the current study. The areal shrinkage strain is twice the linear shrinkage strain. When the soil shrinks in the field, the areas weakened by the bigger size particles crack first. That causes the lower tensile strength of the soil mass. But, the tensile strength of small fragment within the soil mass can still be higher. The tensile strength measured in this test represents the strength of the fragments that are representative of major portion of the soils specimen.

Table 3-7 Summary of the IDT test results for slurry soil specimens

Soil	Moisture content range (%)	No. of specimens	Mean IDT (kPa)	Standard deviation (kPa)
Anthem	5.5 - 6.4	5	647.3	50.3
Burleson	5.8 - 7.2	6	743.4	71.3
Colorado	5.1 - 7.4	7	957.0	85.8
Grapevine	3.9 - 5.0	10	381.8	32.3
Grayson	8.0 - 9.0	7	1218.8	99.5
Joe Pool	4.4 - 5.8	10	877.6	107.14
Keller	3.3 - 3.7	3	526.1	77.3
Oklahoma	4.1 - 5.9	6	486.0	74.7
San Antonio	7.1 - 9.2	6	1024.9	167.4
San Diego	3.3 - 4.8	5	482.9	69.7

Additional IDT tests were conducted on the soils in order to study the tensile strengths of compacted specimens. The specimens were compacted at 95% of maximum dry density and optimum moisture content conditions. Compacted specimens were prepared using static compression method. The specimens were covered in air tight plastics wrap and kept in the moisture room for seven days before testing. The tests were conducted similar to that of slurry specimens. The summary of the IDT test results of the compacted soil specimens is presented in Table 3-8. It can be observed from the Table 3-8 that the tensile strengths of the soils vary from 15.0 to 28.4 kPa. Compacted specimens yielded more uniform results than the slurry soils as evident from the smaller standard deviations.

Figure 3-59 shows the average tensile strengths of slurry soils plotted against that of compacted specimens. Although the plot does not show a strong

correlation between these two parameters, a general upward trend of the scattered points is observed. This implies that, the soil showing higher tensile strength at compacted state has a tendency to have a higher tensile strength.

Table 3-8 Summary of IDT test results for compacted soil specimens

Soil	Moisture content range (%)	No. of specimens	Mean IDT (kPa)	Standard deviation (kPa)
Anthem	18.3 - 19.2	3	20.1	1.18
Burleson	20.3 - 21.0	3	20.7	0.34
Colorado	19.1 - 20.5	3	26.8	0.84
Grapevine	18.9 - 20.0	6	19	1.12
Grayson	23.8 - 25.5	3	24.8	0.5
Joe Pool	11.6 - 13.7	6	21.2	1.12
Keller	14.7 - 15.3	3	20	0.95
Oklahoma	23.7 - 24.6	3	18.1	0.55
San Antonio	23.3 - 24.0	3	28.4	1.21
San Diego	20.2 - 21.2	3	15	2.48

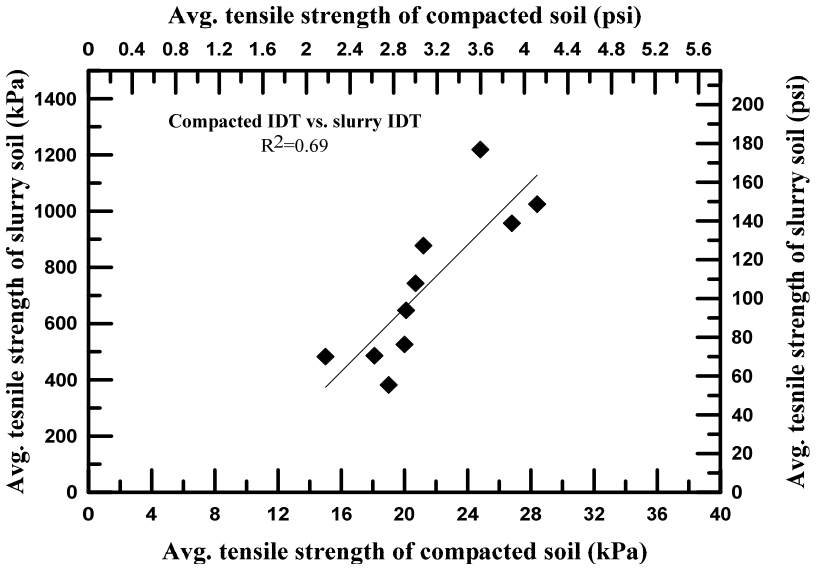

Figure 3-59 Compacted vs. slurry soil's tensile strength

3.13 Shrinkage Induced Pressure Test

3.13.1 Introduction

Shrinkage induced pressure test was first devised by Puljan (2010) as a master's thesis research in the University of Texas at Arlington (UTA). The shrinkage induced pressure (SIP) test gives direct measurement of the internal shrinkage stress of a drying slurry soil specimen. Shrinkage Induced Pressure (SIP) test is a novel test method that measures the shrinkage force of soil specimen during the drying process. This test assumes the shrinkage force to be isotropic. As a result, it is easier to measure a shrinkage force directly by placing a force sensor in the liquid soil medium and by inducing the soil to compress the sensor when it undergoes drying.

3.13.2 The Force Sensor

The development of this new method was made possible by innovation of a sensor known as Force Sensor (FS) (Tekscan 2015). Force Sensor is fundamentally a flexible printed circuit contained within very thin polymer substrates. Owing to its paper-thin construction, flexibility, and force measurement ability, the force sensor can measure the internal stresses developed within the soil matrix during drying. It is the key component of the experiment that allowed direct measurement of the shrinkage pressure. The sensor is strong enough to stand up to most environments (Tekscan 2015). The active sensing

area is a 9.5 mm (0.375 in.) diameter circle at the end of the sensor. Figure 3-60 shows the picture of some force sensors used in the SIP tests.

Figure 3-60 The force sensors used in the SIP tests

The sensor is made of two layers of substrate. This substrate is made of polyester film. On each layer, a conductive material is applied, followed by a layer of pressure-sensitive ink (Tekscan, 2015). Then the two layers were bonded together using an adhesive to form the sensor. The silver circle on top of the pressure-sensitive ink is the active sensing area of the sensor. Silver extends from the sensing area to the connectors at the other end of the sensor, forming the conductive leads. The sensor comes with a solderable male square pin.

The FS can be easily integrated into a circuit to measure the change in its resistance. The force-to-voltage circuit adopted in the current study is shown in Figure 3-61. The sensor acts as a variable sensor in an electronic circuit. It has a very high resistance. The resistance of the sensor decreases with an increased pressure applied on the active area. Change in resistance causes variation in the

output voltage of the circuit. Depending upon the setup, an alternation could then be performed to increase or decrease the sensitivity of the sensor. The sensor is flexible enough to allow for non-intrusive measurements in materials. They can be attached to many surfaces and can also be combined with plastic or metal films for greater stiffness and added protection from abrasion. Some important features and specifications of the sensors are given in

Table 3-9.

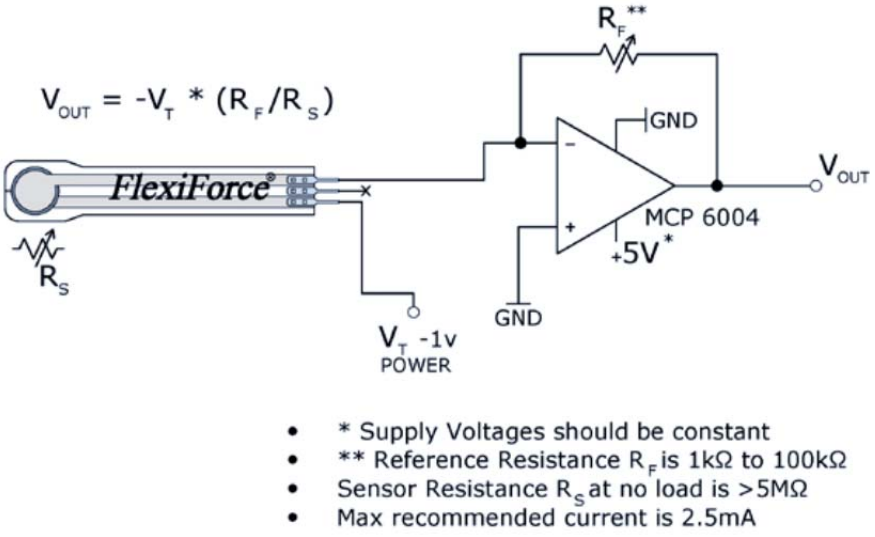

Figure 3-61 The force-to-voltage circuit employed in this study

Calibration of the sensors is required at the beginning of each experiment to convert the measured output voltage to the pressure units. Each of the sensors used in this study were calibrated before using them in the experiment. Calibration of the sensors is performed by loading the active area with a series of

known pressures and recording the corresponding voltage outputs from the circuit. The corresponding calibration equations were determined for individual sensors using correlation between pressure and output voltage. Figure 3-62 shows the experimental setup for the calibration of the sensors.

Table 3-9 A 201 model force sensor's specifications and features

Thickness	0.208 mm (0.008 in.)
Length	203 mm (8 in.)
	452 mm (6 in.)
	102 mm (4 in.)
	51 mm (2 in.)
Width	14 mm (0.55 in.)
Sensing area	9.53 mm (0.375 in.)
Connector	3-pin male square pin
Force ranges	0-4.4 N (1 lb.), 0-110 N (25 lb.) and 0-440 N (100 lb.)
Operating temperatures	-9 to 60^{o}C (15^{o}F to 140^{o}F)
Linearity error	+/-3%
Repeatability	+/-2.5% of full scale (conditioned sensor, 80% force applied)
Hysteresis	<4.5% of full scale (conditioned sensor, 80% force applied)
Drift	<5% per logarithmic time scale (constant load of 90% sensor rating)
Response time	<5 microsecond
Temperature sensitivity	Output variance up to 0.36% per ^{o}C.

The following procedures were used in the calibration of the sensors:

1. The sensors were connected to the data logger and the initial voltage data was measured.

2. The sensors were warmed up by placing the estimated maximum test load onto the active area for approximately 3 seconds. This process is called conditioning and was repeated 4-5 times.
3. Each sensor was calibrated by placing different known loads on the active area. The known load was applied to an area bigger than the sensing area to make sure that the active area is fully covered. The pressure was calculated using the known loading area and load. Thus, pressure was used in the calibration instead of the load.
4. The drift error expected during the testing was also determined. Drift is the change in the sensor output when a constant force is applied over a period of time. The resistance of the sensor constantly decreases under a sustained constant load. So, it is important to consider the drift effect in the calibration of the sensor.

Calibration curve was finally obtained by correlating the voltage outputs with the corresponding applied pressures.

3.13.3 SIP Test Procedure

The soil collected from the field was first dried and then pulverized. The representative soil passing through #40 sieves was mixed with deionized water to bring it to a liquid consistency. The soil was kept in a humidity chamber for 24 hours for homogenization. Then, the soil slurry was transferred into 7.6 cm

diameter moisture cans. The moisture cans were prepared for the SIP tests by opening 20 mm wide slits on the wall of the cans. These slits allowed the placement of the sensors inside the soil matrix in a horizontal orientation as shown in Figure 3-63. The inside surface of the moisture cans was lightly coated with lubricating oil to facilitate free shrinkage of the soil by reducing the adhesion with can base. Light tapping was applied to remove any entrapped air within the soil slurry. It also helps in achieving better contact between the force sensor and the soil slurry. Finally, the force sensors were inserted through the slit as shown in the Figure 3-64.

Figure 3-62 Experimental setup for the sensor calibration

Drying the slurry at high temperature immediately after molding did not yield satisfactory results. The first reason can be the lack of proper contact between the soil and the sensor. Secondly, the high moisture content gradient occurring in the soil caused the soil to crack at the surface while the soil underneath was still fully saturated to develop any shrinkage pressure. Therefore,

the specimens were first subjected to air drying in the room temperature for 16 hours to ensure proper contact of soil with sensor.

Figure 3-63 Horizontal orientation of the sensor inside the moisture can

Figure 3-64 Sensors inserted into the soil matrix through the opening on the side wall of the moisture can

The air dried specimens remain mostly saturated before accelerating the drying process by using a heating source. Two different heating methods were attempted in the current study. In the first method the specimens were oven dried as shown in Figure 3-65. The soil specimens were weighted at frequent intervals so that the moisture content with time could be established. Later it was observed that, the process of weighing the specimen by moving it in and out from the oven

caused some disturbance on the system which was indicated by the noises appeared in the output from the sensors. It often caused a sharp drop in the output voltage. Later, a new method of heating was devised to avoid the disturbance occurring during the weighing process.

In this method, accelerated drying was achieved by using heating lamps. The heating lamps were located in such a way that a temperature of approximately 40^{o}C is maintained throughout the experiment and the temperature was also monitored continuously. Figure 3-66 shows the complete experimental setup for the SIP test using the second method of heating. The specimens were put above the weighing scales to monitor the change in moisture content. So, it eliminated the disturbance caused by moving the specimens during weighing. Unlike in the oven drying, the specimens were easily visible to take pictures from the top during drying. Thus, this method proved to be more advantageous due to the possibility of digital image analysis of the shrinkage and cracking of the soils. Eventually, the second method was selected in this study.

During the drying, the voltage outputs from the sensors were automatically recorded at every 32 seconds using the data acquisition system. The data logging system and the computer used in recording the output are shown in Figure 3-65. The voltage outputs from the sensors were recorded continuously until a crack appears or constant voltage reading was reached or soil was

completely dry. The change in diameter and the thickness of the specimen were also monitored at regular time intervals using a precision caliper.

Figure 3-65 SIP test setup for the oven drying method

Figure 3-66 SIP test setup by using the heating lamps

SIP tests were conducted on three replicate specimens for each soil. The change in moisture content and the volumetric strain of the specimens were also recorded at regular time intervals. The moisture content of the soil is related to the soil suction as given in the SWCC curves presented in section 3.11. Also, the SIP of the soil at a particular moisture contents can be obtained by relating the continuous SIP data from the data logger and manually recorded moisture content information. Thus, a relationship between the soil suction and the SIP value can be established. SIP test results for the soils are presented in the following sections.

3.13.4 SIP Test Results

3.13.4.1 Anthem soil

The variations in radial, vertical, and volumetric shrinkage strains of the soil as well as the moisture content variation with time are shown in Figure 3-67. Similarly the SIPs exhibited by the soil at different suction levels are presented in Figure 3-68. Since the soil remains fairly saturated at the beginning of the experiment, no SIP was recorded at the early stages. SIP started building up when the suction was nearly 150 kPa in test 1 and 300 kPa in tests 2 and 3. The SIP increases with increase in the soil suction thereafter. The peak SIPs in the tests 1, 2 and 3 are 141.3, 159.3, and 156.5 kPa, respectively. The final radial, vertical, and volumetric strains are 13.5, 20.4 and 47.5%, respectively. Similarly, the moisture content of the soil was 3.7% at the end of the test.

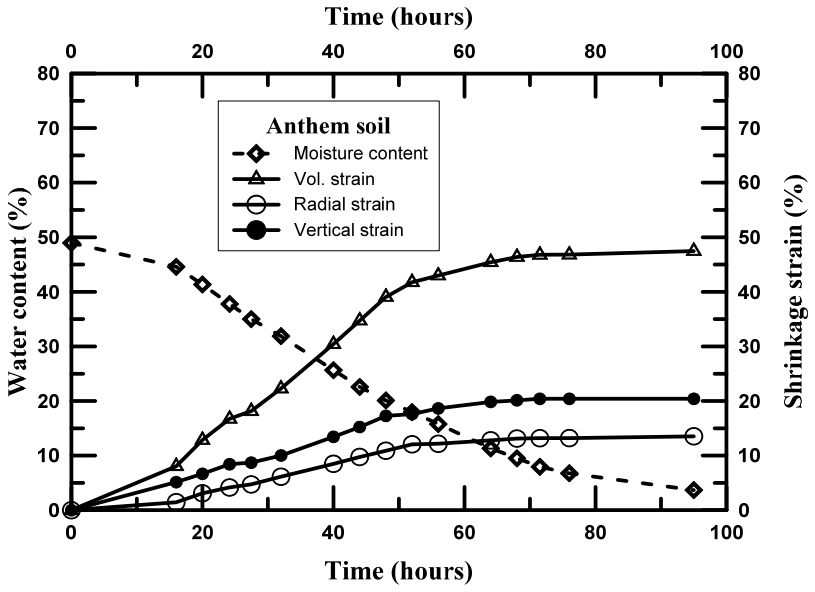

Figure 3-67 Time vs. moisture content and shrinkage strains plot of Anthem soil

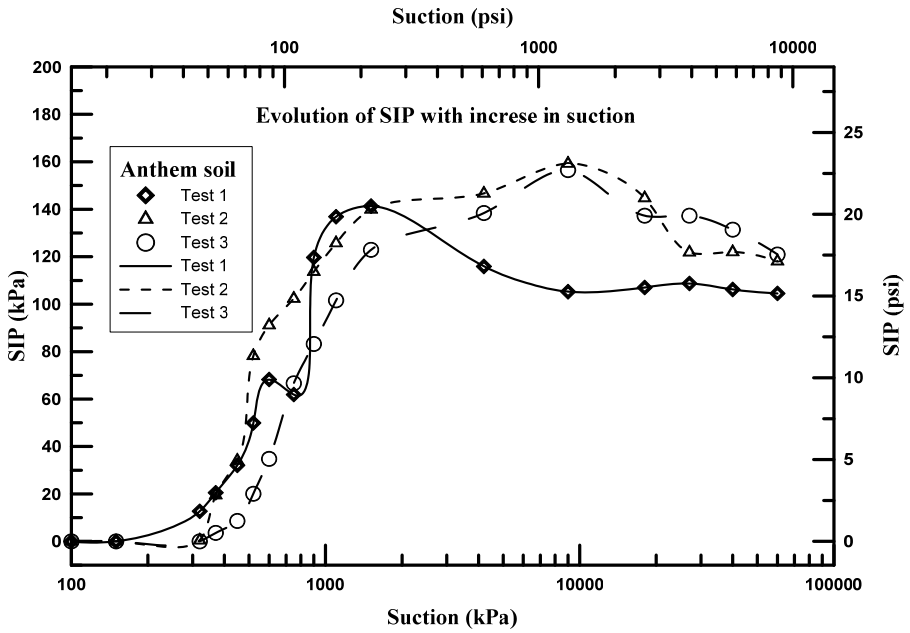

Figure 3-68 SIP vs. suction curve for Anthem soil

3.13.4.2 Burleson soil

The variations in radial, vertical, and volumetric shrinkage strains of the soil as well as the moisture content variation with time are shown in Figure 3-69. Similarly, the SIPs exhibited by the soil at different suction levels are presented in Figure 3-70. SIP started building up when the suction was nearly 300 kPa in tests 1 and 2, and 100 kPa in case of test 3. The peak SIPs in the tests 1, 2 and 3 are 160.6, 170.3, and 188.9 kPa, respectively. And, the final radial, vertical, and volumetric strains are 19.8, 23.9 and 63.5%, respectively. Similarly, the moisture content of the soil was 5.7% at the end of the test.

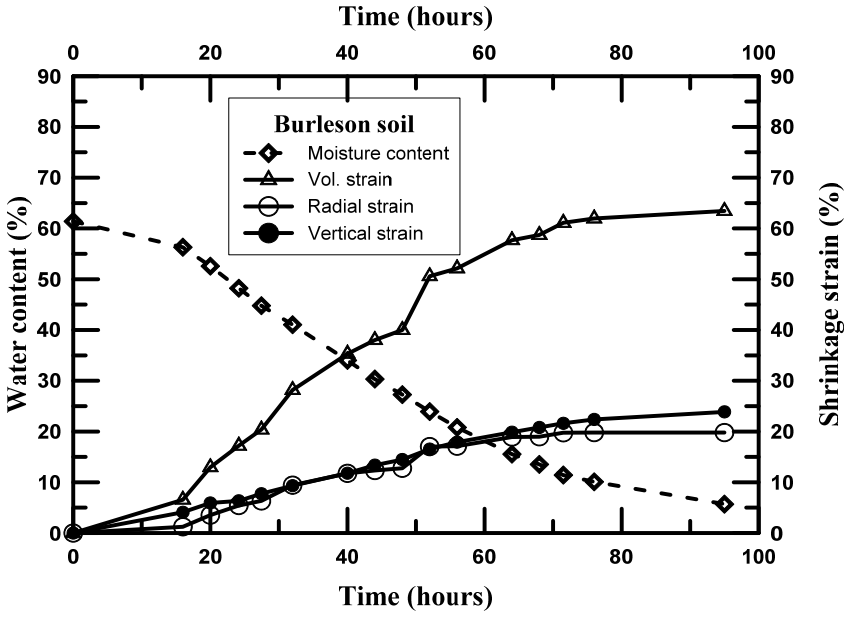

Figure 3-69 Time vs. moisture content and shrinkage strains plot of Burleson soil

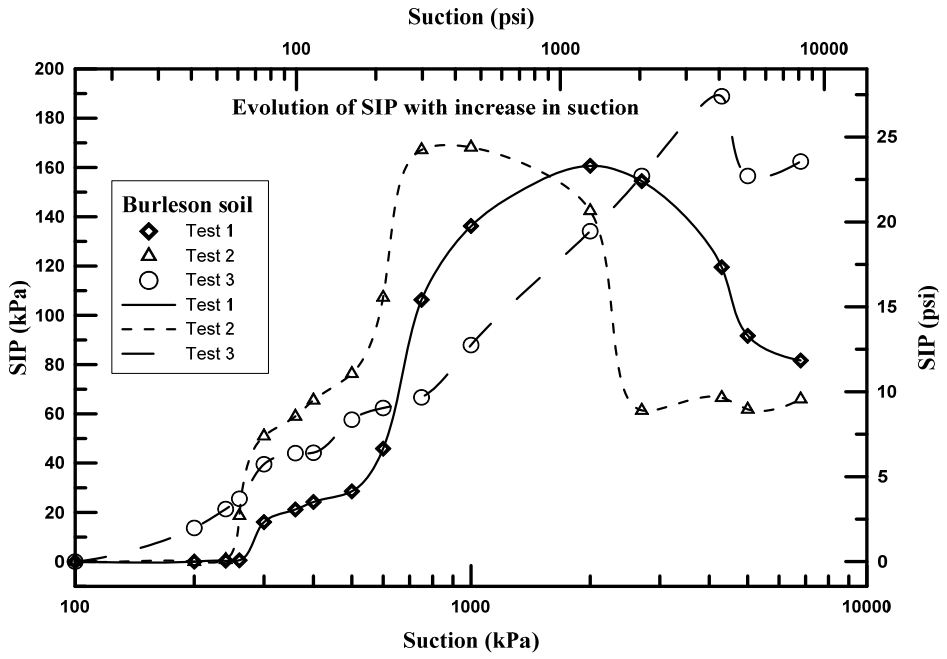

Figure 3-70 SIP vs. suction curve for Burleson soil

3.13.4.3 Colorado soil

The variations in radial, vertical, and volumetric shrinkage strains of the soil as well as the moisture content variation with time are shown in Figure 3-71. Similarly, the SIPs exhibited by the soil at different suction levels are presented in Figure 3-72. SIP started building up when the suction was nearly 10 kPa in tests 1 and 3, and 100 kPa in case of test 2. The peak SIPs in the tests 1, 2 and 3 are 185.5, 144.1, and 166.8 kPa, respectively. And, the final radial, vertical, and volumetric strains are 19.8, 22.2 and 61.8%, respectively. Similarly, the moisture content of the soil was 5.1% at the end of the test.

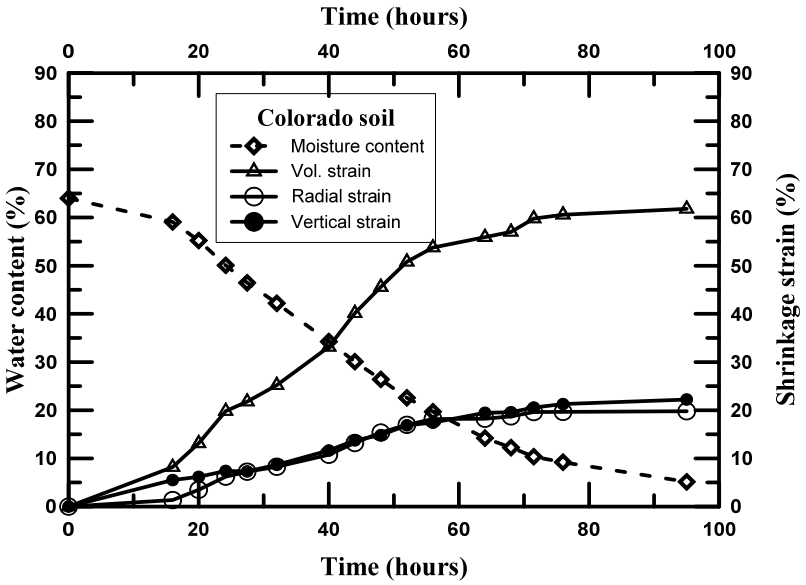

Figure 3-71 Time vs. moisture content and shrinkage strains plot of Colorado soil

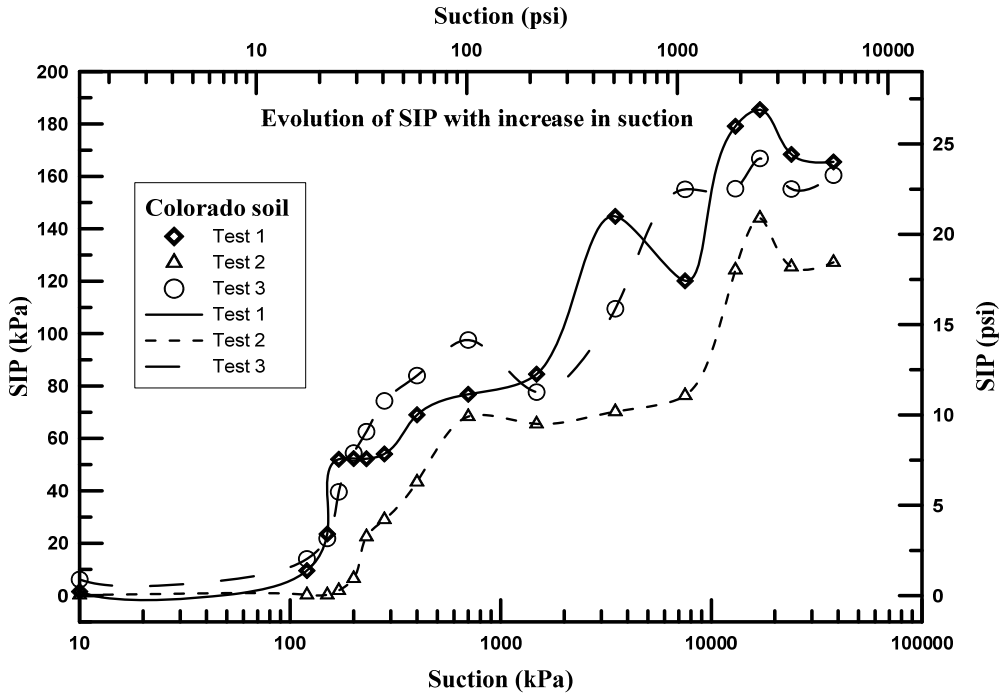

Figure 3-72 SIP vs. suction curve for Colorado soil

3.13.4.4 Grapevine Dam soil

The variations in radial, vertical, and volumetric shrinkage strains of the soil as well as the moisture content variation with time are shown in Figure 3-73. Similarly, the SIPs exhibited by the soil at different suction levels are presented in Figure 3-74. SIP started building up when the suction was nearly 100 kPa in test 2, and 200 kPa in case of tests 1 and 3. The peak SIPs in the tests 1, 2 and 3 are 77.9, 55.8, and 63.4 kPa, respectively. And, the final radial, vertical, and volumetric strains are 11.9, 14.7 and 38.5%, respectively. Similarly, the moisture content of the soil was 2.9% at the end of the test.

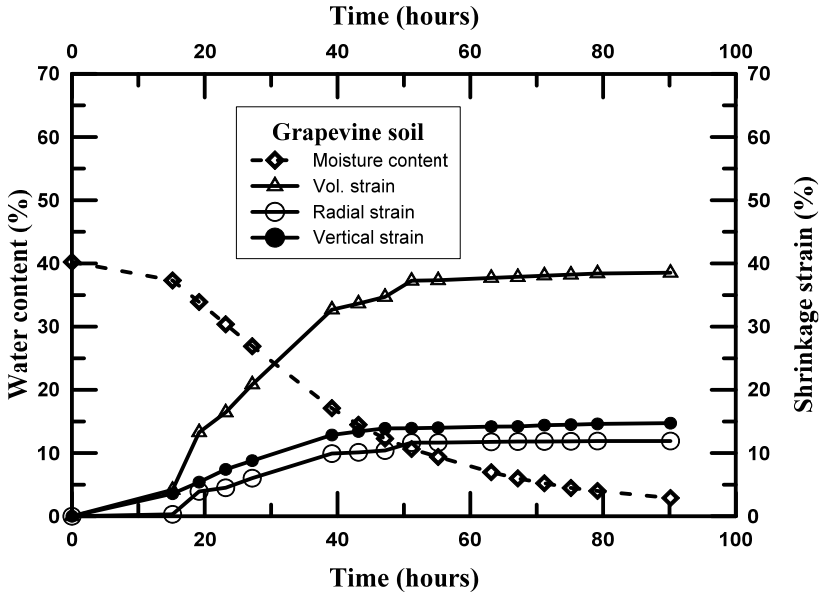

Figure 3-73 Time vs. moisture content and shrinkage strains plot of Grapevine Dam soil

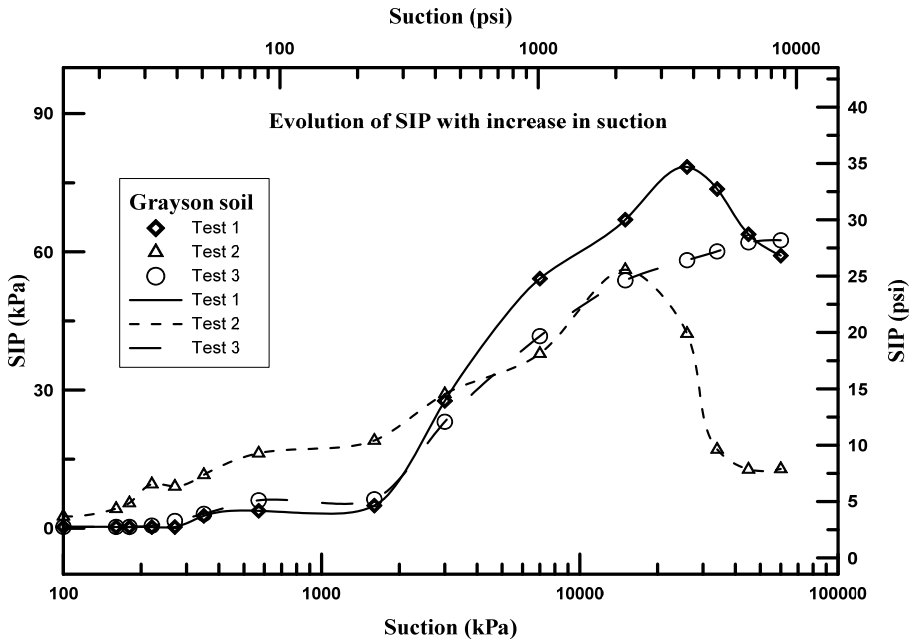

Figure 3-74 SIP vs. suction curve for Grapevine Dam soil

3.13.4.5 Grayson soil

The variations in radial, vertical, and volumetric shrinkage strains of the soil as well as the moisture content variation with time are shown in Figure 3-75. Similarly, the SIPs exhibited by the soil at different suction levels are presented in Figure 3-76. SIP started building up when the suction was nearly 250 kPa in all three tests. The peak SIPs in the tests 1, 2 and 3 are 253.0, 247.5, and 228.9 kPa, respectively. And, the final radial, vertical, and volumetric strains are 20.2, 23.4 and 63.8%, respectively. Similarly, the moisture content of the soil was 7.2% at the end of the test.

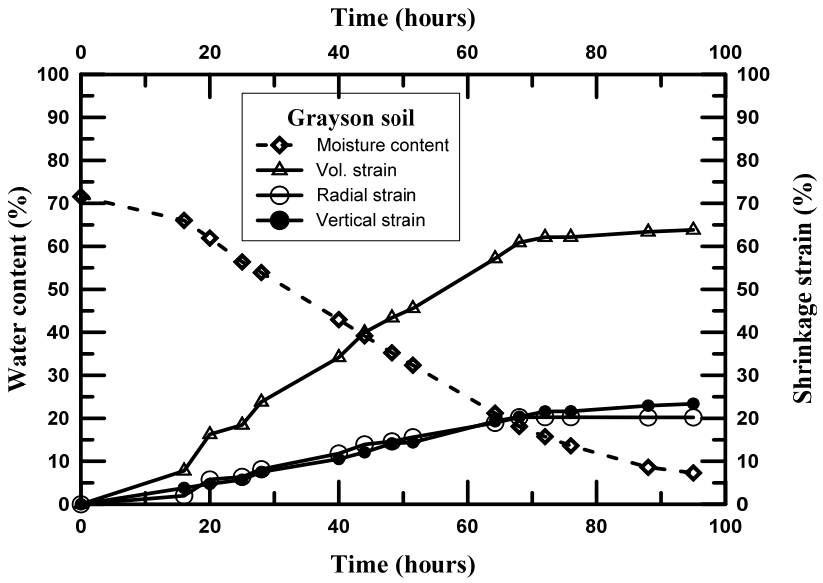

Figure 3-75 Time vs. moisture content and shrinkage strains plot of Grayson soil

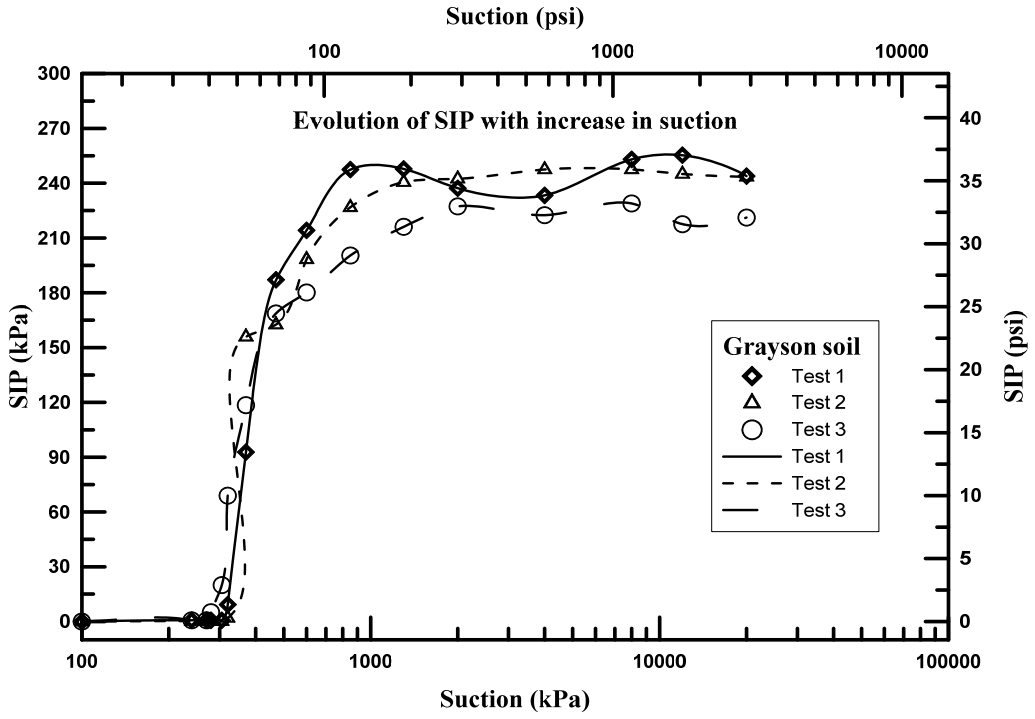

Figure 3-76 SIP vs. suction curve for Grayson soil

3.13.4.6 Joe Pool Dam soil

The variations in radial, vertical, and volumetric shrinkage strains of the soil as well as the moisture content variation with time are shown in Figure 3-77. Similarly, the SIPs exhibited by the soil at different suction levels are presented in Figure 3-78. SIP started building up when the suction was nearly 100 kPa in tests 1 and 2, and 200 kPa in case of test 3. The peak SIPs in the tests 1, 2 and 3 are 151.0, 169.6, and 163.4 kPa, respectively. And, the final radial, vertical, and volumetric strains are 18.3, 19.4 and 56.0%, respectively. Similarly, the moisture content of the soil was 5.2% at the end of the test.

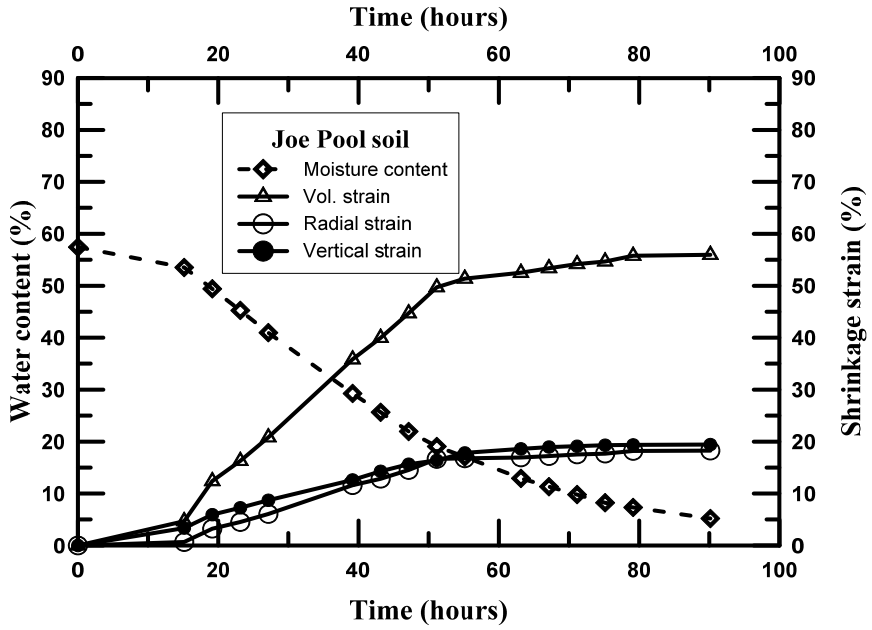

Figure 3-77 Time vs. moisture content and shrinkage strains plot of Joe Pool Dam soil

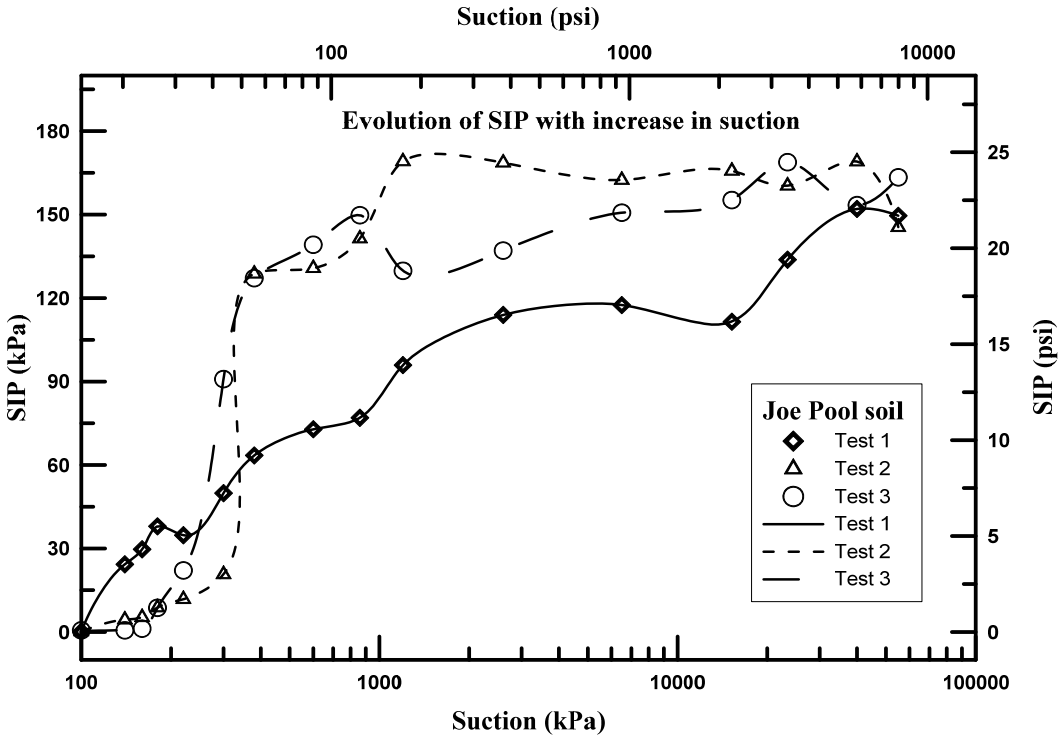

Figure 3-78 SIP vs. suction curve for Joe Pool Dam soil

3.13.4.7 Keller soil

The variations in radial, vertical, and volumetric shrinkage strains of the soil as well as the moisture content variation with time are shown in Figure 3-79. Similarly, the SIPs exhibited by the soil at different suction levels are presented in Figure 3-80. SIP started building up when the suction was nearly 300 kPa in test 1, and 200 kPa in case of tests 2 and 3. The peak SIPs in the tests 1, 2 and 3 are 137.9, 124.8, and 129.6 kPa, respectively. And, the final radial, vertical, and volumetric strains are 12.0, 17.6 and 41.6%, respectively. Similarly, the moisture content of the soil was 1.3% at the end of the test.

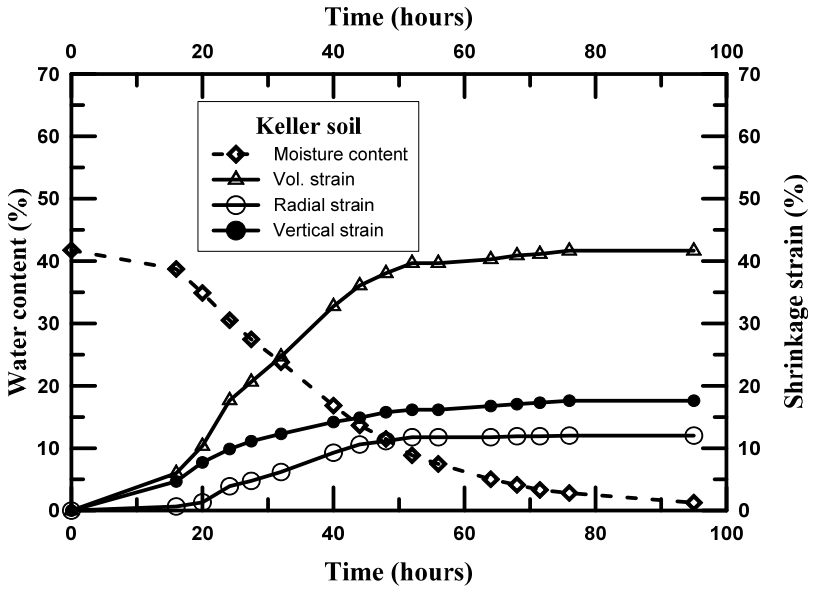

Figure 3-79 Time vs. moisture content and shrinkage strains plot of Keller soil

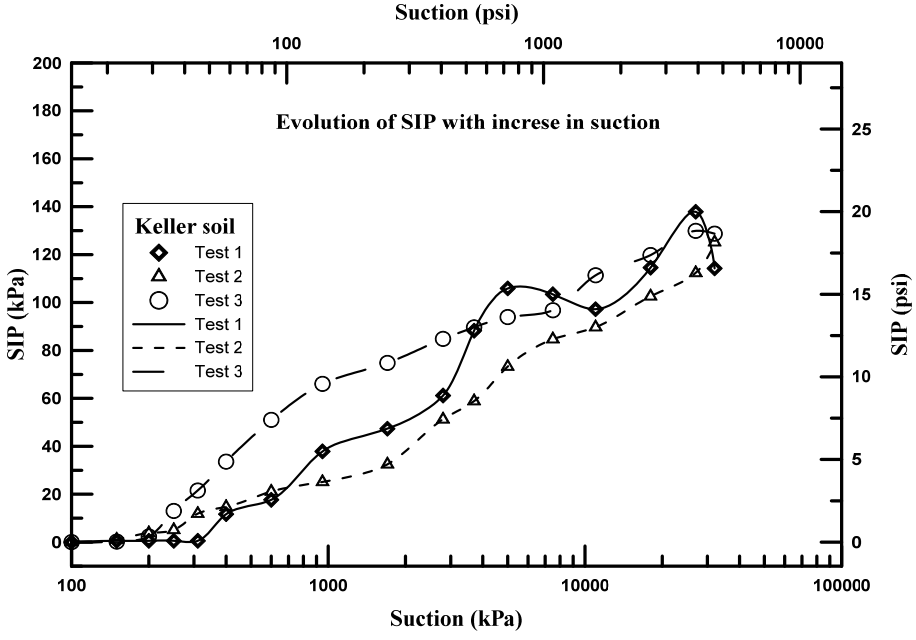

Figure 3-80 SIP vs. suction curve for Keller soil

3.13.4.8 Oklahoma soil

The variations in radial, vertical, and volumetric shrinkage strains of the soil as well as the moisture content variation with time are shown in Figure 3-81. Similarly, the SIPs exhibited by the soil at different suction levels are presented in Figure 3-82. SIP started building up when the suction was nearly 150 kPa in test 2, and 200 kPa in case of tests 1 and 3. The peak SIPs in the tests 1, 2 and 3 are 84.1, 111.0, and 93.8 kPa, respectively. And, the final radial, vertical, and volumetric strains are 13.1, 18.8 and 45.0%, respectively. Similarly, the moisture content of the soil was 5.9% at the end of the test.

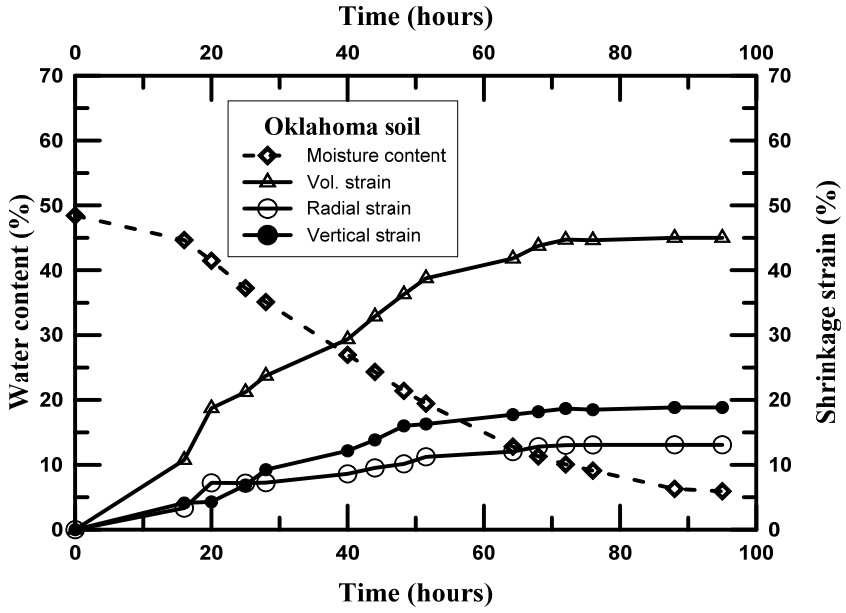

Figure 3-81 Time vs. moisture content and shrinkage strains plot of Oklahoma soil

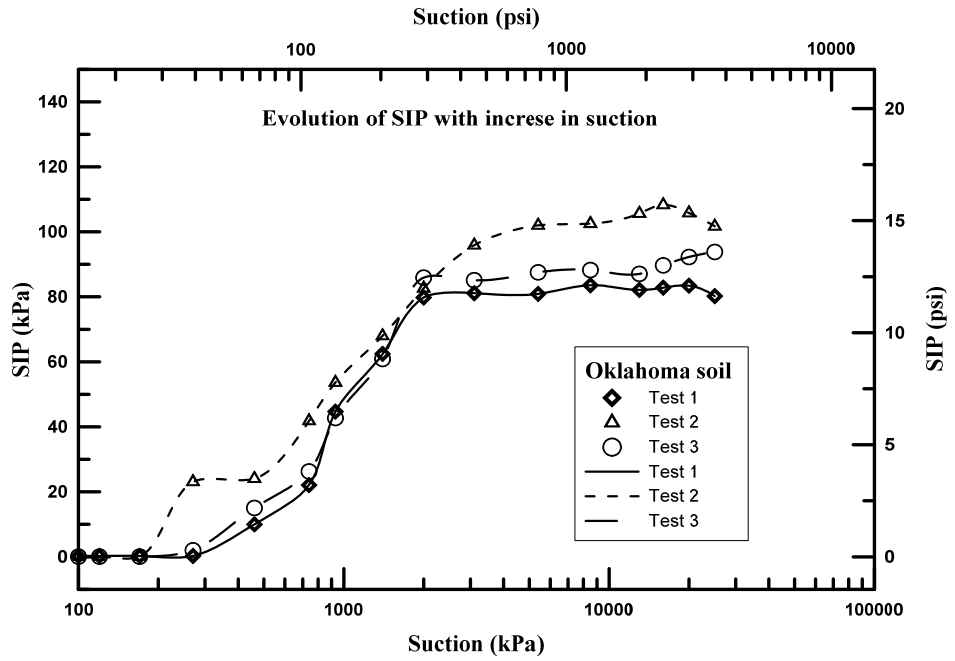

Figure 3-82 SIP vs. suction curve for Oklahoma soil

3.13.4.9 San Antonio soil

The variations in radial, vertical, and volumetric shrinkage strains of the soil as well as the moisture content variation with time are shown in Figure 3-83. Similarly, the SIPs exhibited by the soil at different suction levels are presented in Figure 3-84. SIP started building up when the suction was nearly 300 kPa in test 2, and 100 kPa in case of tests 1 and 3. The peak SIPs in the tests 1, 2 and 3 are 229.6, 244.8, and 215.1 kPa, respectively. And, the final radial, vertical, and volumetric strains are 20.0, 24.0, and 64.0%, respectively. Similarly, the moisture content of the soil was 7.1% at the end of the test.

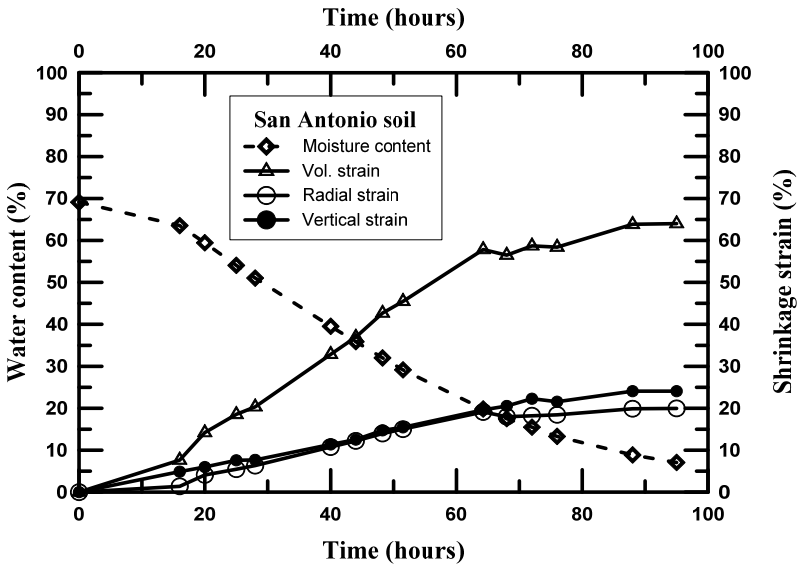

Figure 3-83 Time vs. moisture content and shrinkage strains plot of San Antonio soil

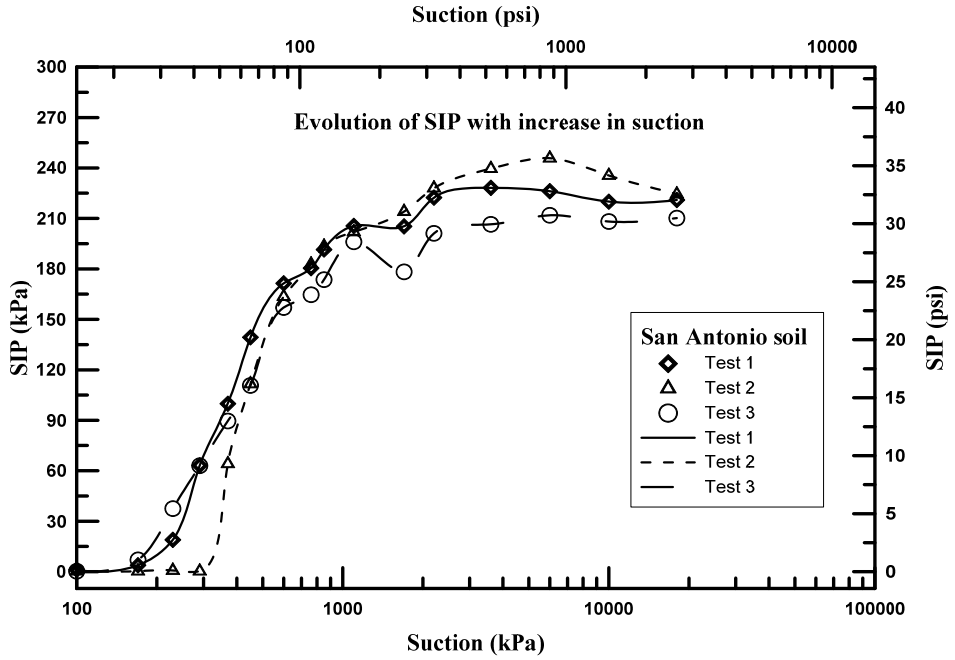

Figure 3-84 SIP vs. suction curve for San Antonio soil

3.13.4.10 San Diego soil

The variations in radial, vertical, and volumetric shrinkage strains of the soil as well as the moisture content variation with time are shown in Figure 3-85. Similarly, the SIPs exhibited by the soil at different suction levels are presented in Figure 3-86. SIP started building up when the suction was nearly 300 kPa in all three tests. The peak SIPs in the tests 1, 2 and 3 are 105.5, 101.4, and 83.4 kPa, respectively. And, the final radial, vertical, and volumetric strains are 9.3, 15.8, and 34.4%, respectively. Similarly, the moisture content of the soil was 5.1% at the end of the test.

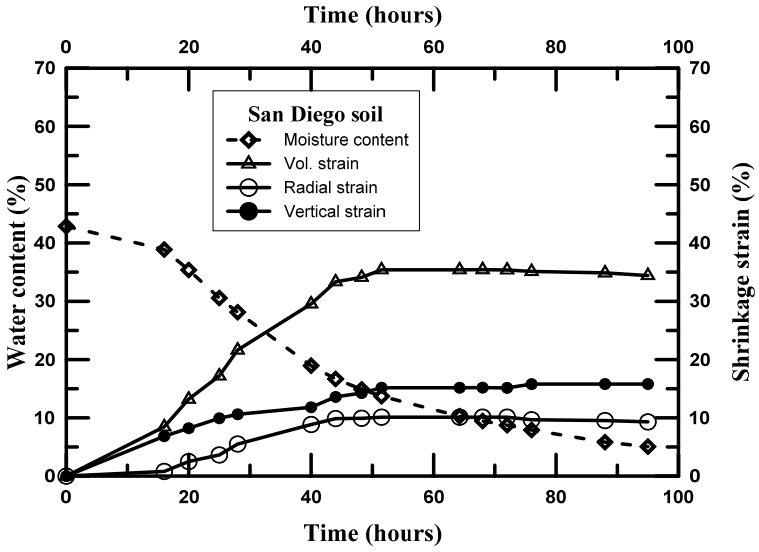

Figure 3-85 Time vs. moisture content and shrinkage strains plot of San Diego soil

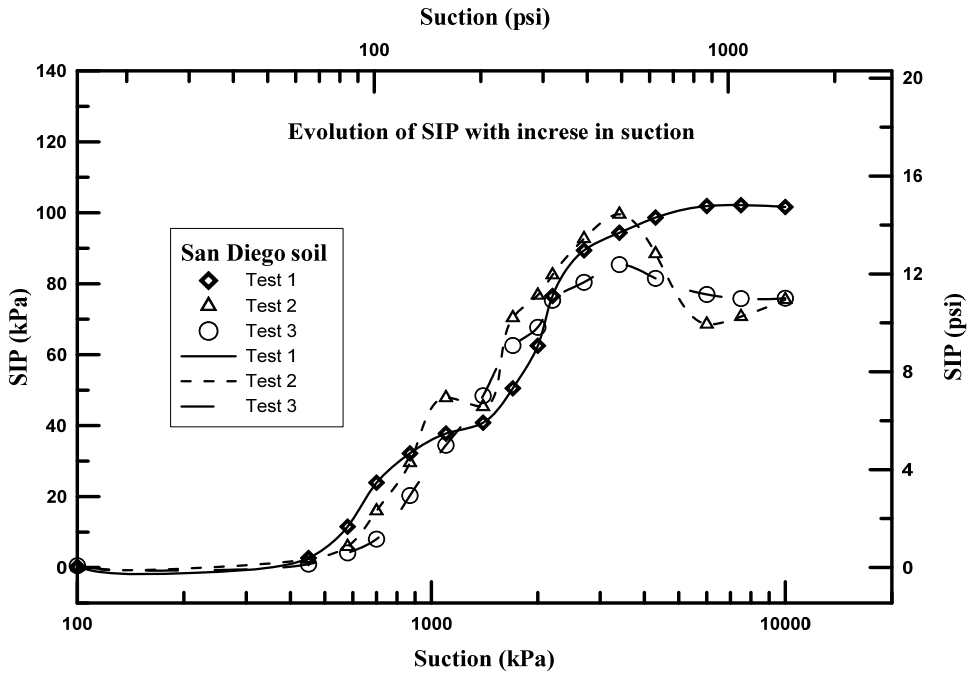

Figure 3-86 SIP vs. suction curve for San Diego soil

3.13.5 Analysis of SIP Test Results

In general, early stage of the drying was characterized by high water content where the soil also did not experience a significant shrinkage strain. During the 16 hours of air drying in the beginning, the change in water content for all soil remained within 5.5%. However, the volumetric shrinkage strains varied from 4.1% for Grapevine soil to 10.7% for Oklahoma soil. The shrinkage taking place in the early stages of the drying is called structural shrinkage. The suction and the SIP remained small during the structural shrinkage phase.

Soils started losing moisture and shrink at a faster rate after accelerating the drying using external heat source. This started second phase of drying called

the proportional shrinkage phase. In this stage, the water content decreased significantly and the shrinkage strain also increased proportionately. The decrease in the moisture content significantly increases the soil suction. As the suction increases, the SIP also increases rapidly in the proportional shrinkage phase until the SIP reaches a peak value. The proportional shrinkage phase is related mainly to swelling of micropores of the expansive clays (Braudeau et al., 2004). The Shrinkage induced pressure increased significantly and reached the peak.

The final stage of drying is called residual shrinkage where there were very small changes in the volumetric shrinkage strains even if the moisture content was decreasing. In this stage the SIP remained almost constant or decreases if any cracks were developed in the specimen.

The vertical shrinkage strains were higher than the radial shrinkage strains. Individual soils show a different behavior in the evolution of SIP with suction. Anthem, Grayson, Oklahoma, and San Antonio soils develop significant amount of SIP within the suction levels of 2000 kPa. Then, the SIP evolves more gradually showing a plateau at higher suction. In case of Colorado and Keller soils, SIP keeps on increasing until a very high suction is attained. The SIP of the Colorado soil increases continuously until the suction range of 10 to 20 MPa. The SIP of the Keller soil also increases until the very high suction range of 30 to 35 MPa. Some soil specimens develop a crack after reaching the peak SIP value then the SIP shows a drastic decrease. On other cases, the SIP remains almost at

constant level after the peak was reached. In the latter case, the specimens do not show any cracks. The suction versus SIP curves reveal that for the soils attaining high SIPs at lower suction ranges, the SIP level remains almost constant with an exception for the Anthem soil. It was observed that the SIP of the soil drops suddenly after developing a crack at a peak SIP value.

Table 3-10 gives a summary of the peak SIPs of the soils. The mean of peak SIP of the soils are also presented graphically in Figure 3-87. Grayson and Grapevine soils experienced the highest and lowest SIPs respectively. The variability of the peak SIPs of each soil was also calculated. The standard deviations range from 6.6 to 14.8 kPa except for the Colorado soil. Colorado soil exhibited the maximum standard deviation of 20.7. With the exception of the Colorado soil, the overall repeatability of the peak SIPs seems satisfactory.

Table 3-10 Summary of the Peak SIPs of the soils

Soil	Peak SIP (kPa)				
	Test 1	Test 2	Test 3	Mean	Standard deviation
Anthem	141.3	159.3	156.5	152.4	9.7
Burleson	160.6	170.3	188.9	173.3	14.4
Colorado	185.5	144.1	166.8	165.5	20.7
Grapevine	77.9	55.8	63.4	65.7	11.2
Grayson	253.0	247.5	228.9	243.2	12.6
Joe Pool	151.0	169.6	163.4	161.3	9.5
Keller	137.9	124.8	129.6	130.8	6.6
Oklahoma	84.1	111.0	93.8	96.3	13.6
San Antonio	229.6	244.8	215.1	229.8	14.8
San Diego	105.5	101.4	83.4	96.8	11.7

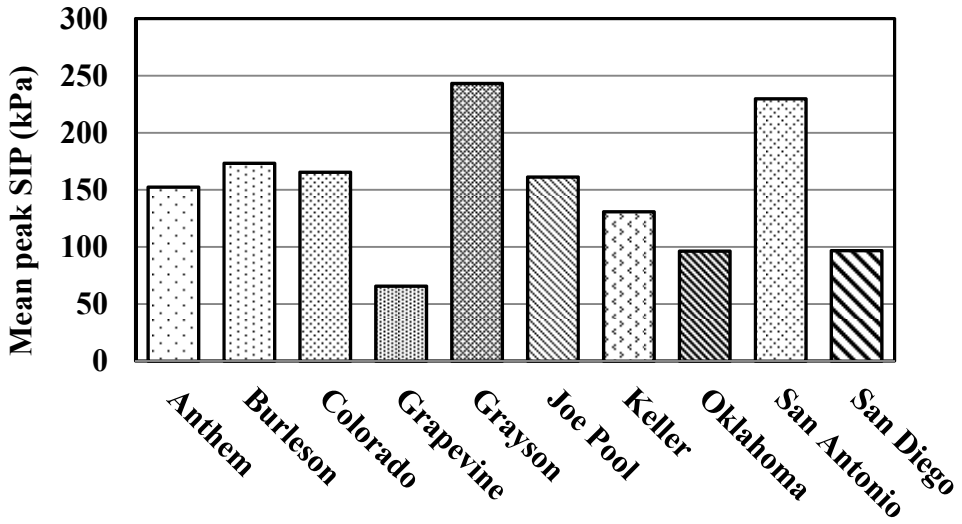

Figure 3-87 Mean peak SIP of the soils

The summary of the shrinkage strains of the soils are presented in Table 3-11. The vertical shrinkage strains are higher than the radial shrinkage strains. Grayson and Grapevine soils exhibited the maximum and minimum shrinkage strains.

Table 3-11 Summary of the shrinkage strains of the soils

Soil	Final shrinkage strain (%)		
	Radial	Vertical	Volumetric
Anthem	13.5	20.4	47.5
Burleson	19.8	23.9	63.5
Colorado	19.8	22.2	61.8
Grapevine	11.9	14.7	38.5
Grayson	20.2	23.4	63.8
Joe Pool	18.3	19.4	56
Keller	12	17.6	41.6
Oklahoma	13.1	18.8	45
San Antonio	20	24	64
San Diego	9.3	15.8	34.4

The peak average SIPs of the soils were plotted against the corresponding volumetric shrinkage strains as shown in Figure 3-88. The plot shows an overall upward trend; with an increase in shrinkage strain is associated with an increase in shrinkage pressure. The linear regression between the parameters yielded a coefficient of determination of 0.77. It demonstrates that the shrinkage induced pressure can be used as an estimator for the volumetric shrinkage potential of the soils.

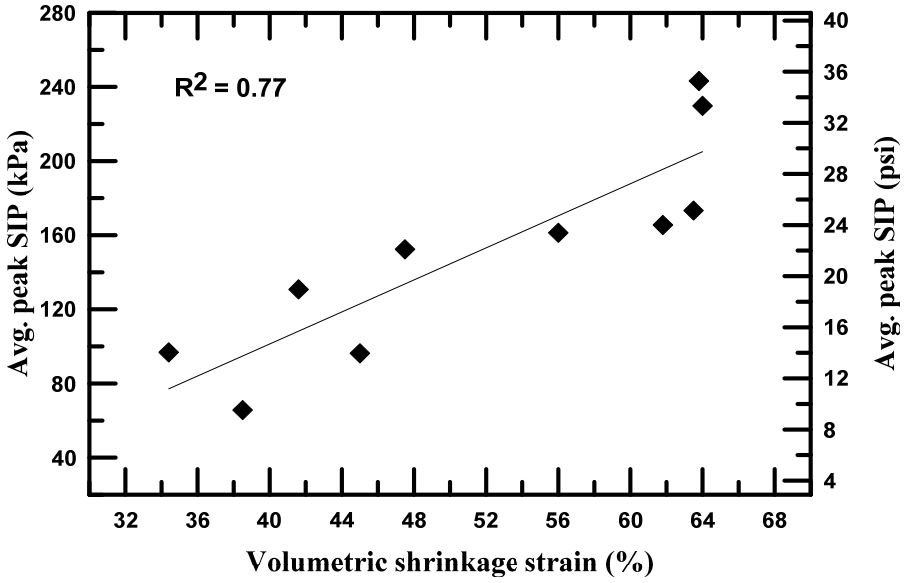

Figure 3-88 Volumetric shrinkage strain vs. average peak SIP of soils

Table 3-12 provides the comparison between the SIP and IDT of slurry soil specimens. The comparison of results show that the percentage of the ratios between SIP and IDT values varies from 17.2 to 24.9%, which means the actual SIP value is very smaller than the indirect tensile strength of the slurry soil

specimens. There could be two reasons for relatively higher values of IDT test results. First, the IDT test results generally yield higher strength than the axial tensile test. Second reason is because of the specimen size effect. The specimens used in IDT were about 70 mm in diameter. A small size of specimen generally shows greater strength. It does not represent the tensile strength of a big mass but only the strength of an intact unit.

Table 3-12 Comparison between SIP and IDT of the slurry specimens

Soil	Mean IDT (kPa)	Mean SIP (kPa)	SIP/IDT (%)
Anthem	647.3	152.4	23.5
Burleson	743.4	173.3	23.3
Colorado	957.0	165.5	17.3
Grapevine	381.8	65.7	17.2
Grayson	1218.8	243.2	20.0
Joe Pool	877.6	161.3	18.4
Keller	526.1	130.8	24.9
Oklahoma	486.0	96.3	19.8
San Antonio	1024.9	229.8	22.4
San Diego	482.9	96.8	20.0

Similarly Table 3-13 presents the comparison between the SIP and the IDT of the compacted specimens. It is observed that the tensile strengths of the compacted specimens are in the range of 11.9 to 18.8% of their corresponding SIPs except for the Grapevine soil. For grapevine soil the IDT to SIP ratio is 28.9% which is distinctly higher than that for the rest of the soils. But, overall

comparison suggests that the IDT of the compacted specimens are very smaller than the corresponding SIP of the soils.

Table 3-13 Comparison between SIP and IDT of compacted specimens

Soil	Mean IDT (kPa)	Mean SIP (kPa)	IDT/SIP (%)
Anthem	20.1	152.4	13.2
Burleson	20.7	173.3	11.9
Colorado	26.8	165.5	16.2
Grapevine	19.0	65.7	28.9
Grayson	24.8	243.2	10.2
Joe Pool	21.2	161.3	13.1
Keller	20.0	130.8	15.3
Oklahoma	18.1	96.3	18.8
San Antonio	28.4	229.8	12.4
San Diego	15.0	96.8	15.5

3.14 Linear Shrinkage Bar Test

Linear shrinkage bar test characterizes the shrinkage potential of the soils. The tests used in this research were conducted in accordance with the procedure established by the Texas Department of Transportation (TEX-107-E standard method). The slurry soil specimens prepared and placed in the molds are shown in Figure 3-89.

Soil specimens were prepared at moisture contents of little higher than liquid limit. The consistency of the soil was achieved as described in TEX-107-E. The slurry specimens were then kept in the linear shrinkage test molds. The size of the mold is 19 x 19 x 127 mm (0.75 x 0.75 x 5 in.). The soil specimens were

kept in room temperature for first twelve hours after molding. Then they were oven dried at 100^{o}C. The length, width, and height of the dry specimens were measured using precision Vernier calipers. Finally, the linear shrinkage strains were calculated based on the measured dimensions after drying. Figure 3-90 shows the pictures of the soil specimens after drying in the oven. The test was conducted on three replicate test specimens for each soil. Then average linear shrinkage strain was calculated from the three tests and is presented in Figure 3-91. Similarly, the moisture contents of the soil slurries at the time of molding are presented in Figure 3-92. Figure 3-93 presents the linear shrinkage strain versus Montmorillonite content of the soils. A general trend of the plot shows that the shrinkage strain is higher for higher Montmorillonite content of soil.

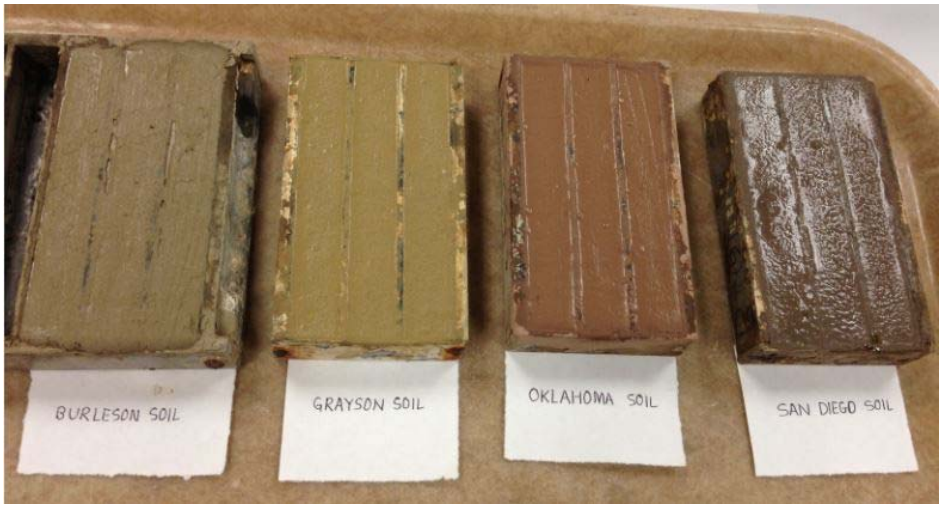

Figure 3-89 Soil specimens kept in the mold for linear shrinkage bar test

Figure 3-90 Soil specimens after drying in the oven

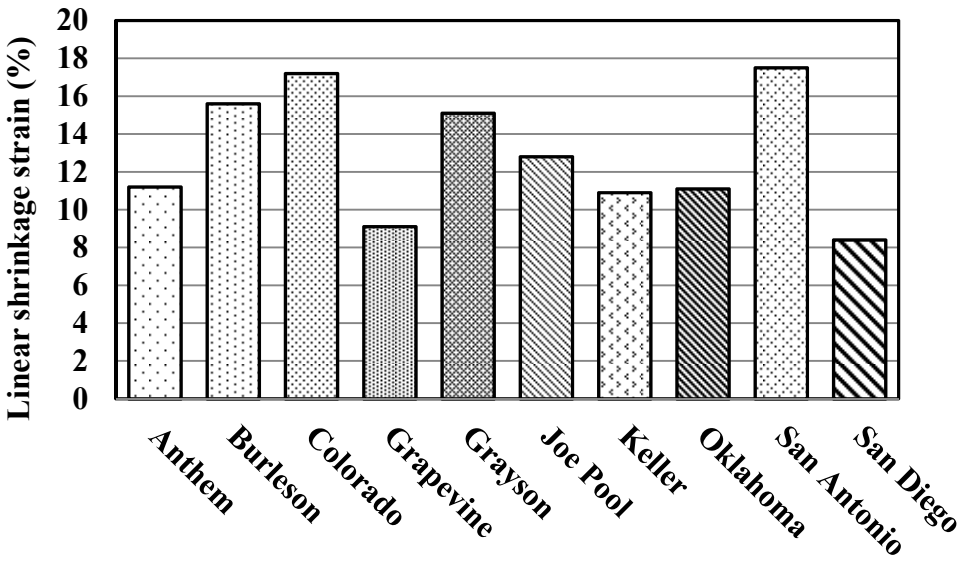

Figure 3-91 Linear shrinkage bar test result

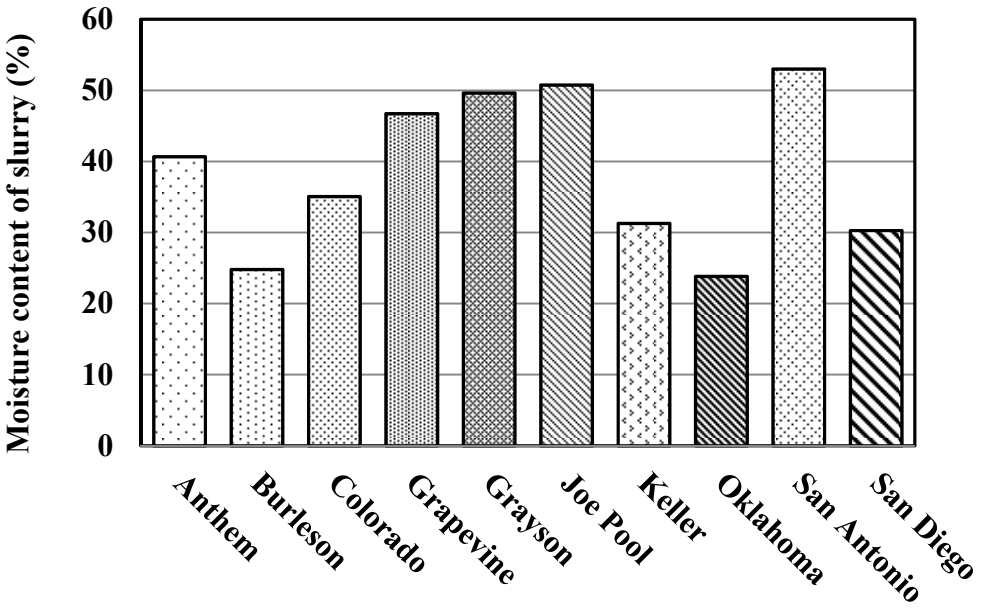

Figure 3-92 Moisture contents of the soil slurries at the time of molding

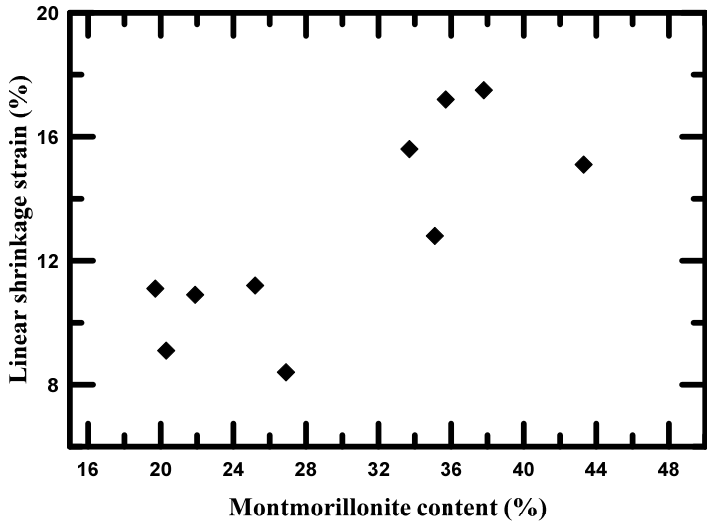

Figure 3-93 Linear shrinkage strain vs. Montmorillonite content of the soils

3.15 Summary

This chapter presented the complete description of various experiments conducted in the current study. More focus was given on the shrinkage characterization tests including linear shrinkage test, indirect tensile strength test, shrinkage induced pressure test, SWCC determination, and digital image correlation technique. Some of the findings from the experiments are also presented. The rest of the experimental results is presented in following chapters depending upon the organization of this dissertation.

One important aspect of tensile strength characterization should be specified here. Tensile stress can generate due to inherent desiccation or shrinking or due to external loading induced flexure conditions. This research focuses more on shrinkage or desiccation induced cracking and this should be the main focus of this research as this often induces major damage to infrastructure.

Chapter 4

Statistical Regression Modeling of SIP Results

4.1 Introduction and Background

As discussed in Chapter 3, the peak SIP value is an indicator of the shrinkage potential of soils. It also provides a measure of the maximum shrinkage stress within the soil during drying. However, the factor governing the magnitude of peak internal stress of a given soil has not been assessed yet. In addition, there is lack of statistical model to predict the peak shrinkage induced pressure of soils. Therefore, development of a statistical model to relate the peak SIP with the basic soil properties is presented in this chapter. Statistical analysis software (SAS) was used to conduct the regression analyses. Multiple linear regression (MLR) analyses were used to incorporate necessary soil variables. In addition, the model assumptions were thoroughly investigated to verify the model accuracy. The analyses were based on the soil properties and SIP results obtained in Chapter 3. Overall 10 soils were used in the analyses. Each soil provided 3 SIP results making data sets of 30.

4.2 Preliminary Investigation on Multicollinearity

Clay contents and clay minerals are the most important factors causing swell/shrink behavior in soils. In addition, there are other soil properties such as liquid limit, plasticity index, particle size distribution, specific surface area, cation exchange capacity etc., which can be used as predictor variables in the statistical

model for projecting the SIP. The soil parameters assessed in this preliminary investigation are content of mineral Montmorillonite, liquid limit, plasticity index, clay fraction, cation exchange capacity, and specific surface area. These factors are reported in literatures to have significant effect on the shrinkage behavior and shrinkage induced pressure of a soil.

According to Kutner et al. (2005), the independent variables of a multiple regression model should have minimal mutual correlation. However, the variables are frequently correlated in real-world situations. Mutually correlated predictor variables of MLR models cause a condition called multicollinearity. Multicollinearity is a serious problem of MLR model and must always be avoided in a good model. Multicollinearity can reduce the coefficient of regression or increase the variance rendering the predictability of a model erroneous (Stevens, 1995).

Therefore, the aforementioned soil properties were plotted against each other to assess the interrelationship between the soil variables as shown in Figure 4-1 through Figure 4-5. These scatter plots are particularly important to diagnose in the preliminary stage of the MLR model development to avoid possible multicollinearity among the predictor variables. It can be observed from the figures that the soil plasticity parameters liquid limit and plasticity index were highly correlated with the Montmorillonite content of the soil. The corresponding R^2 values were 0.88 and 0.9 for liquid limit and plasticity index respectively.

Similarly, the cation exchange capacity and the specific surface area were also highly correlated with the Montmorillonite having the R^2 values of 0.87 and 0.75 respectively. These observations indicated that the shrinkage behavior of a soil explained by soil parameters liquid limit, plasticity index, cation exchange capacity, and specific surface area can be well represented by the parameter Montmorillonite content alone. Inclusion of these parameters in a MLR model along with the Montmorillonite content will cause multicollinearity. Therefore, these parameters are not taken into consideration for further analyses of MLR model.

The plot between clay content and Montmorillonite content show a relatively small R^2 value of 0.48. This indicates that the parameters are not highly correlated. At this stage, we can include clay content along with montmorillonite content to predict the SIP of the soils. We can later assess the severity of the multicollinearity between these two parameters during rigorous model development stage. The correlation between clay content and other parameters were not assessed because they were already discounted in the analysis for being highly correlated with Montmorillonite content.

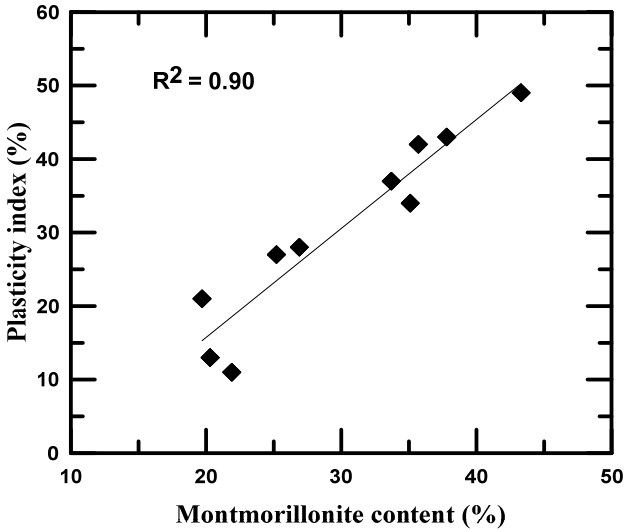

Figure 4-1 Montmorillonite content vs. plasticity index plot

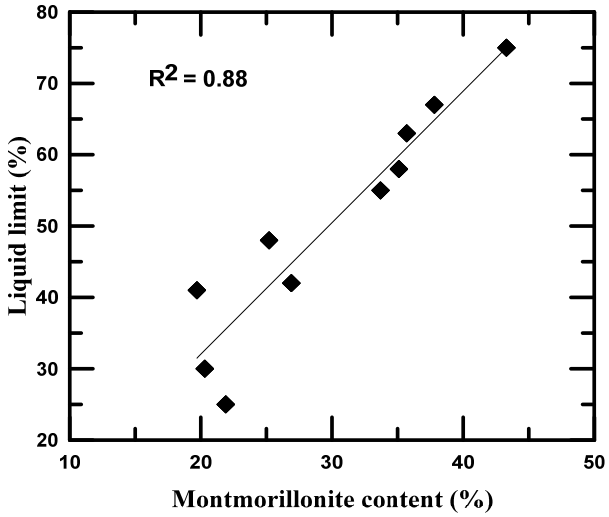

Figure 4-2 Montmorillonite content vs. liquid limit plot

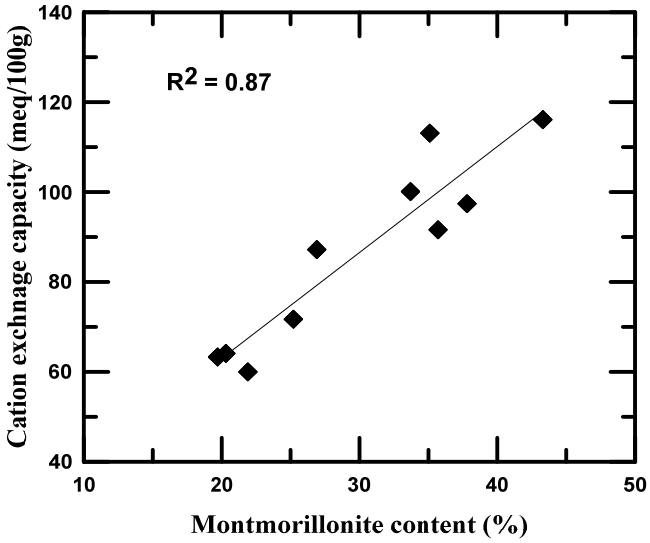

Figure 4-3 Montmorillonite content vs. cation exchange capacity plot

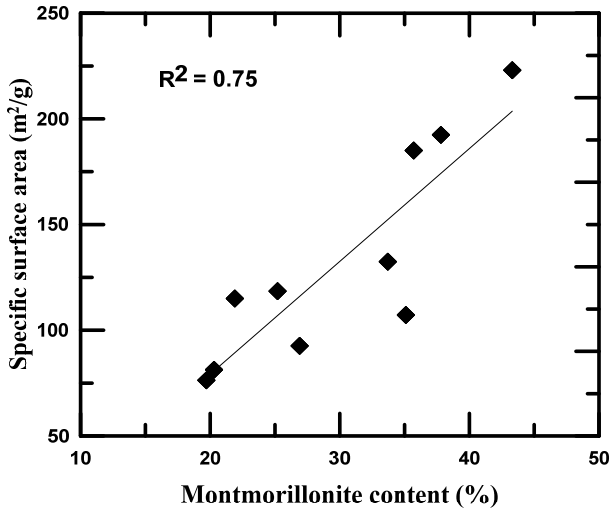

Figure 4-4 Montmorillonite content vs. specific surface area plot

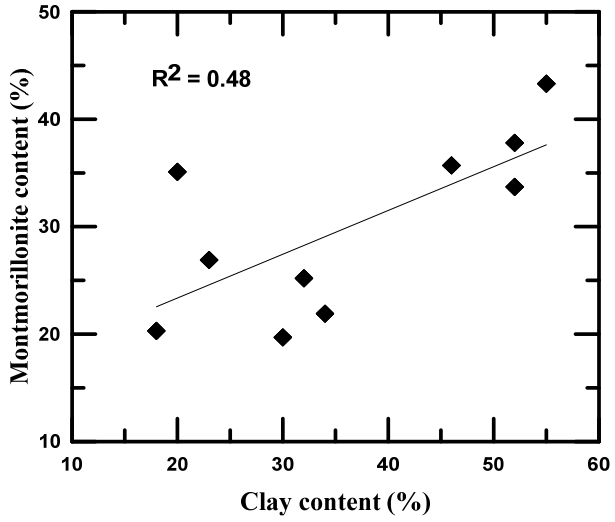

Figure 4-5 Clay content vs. Montmorillonite content plot

4.3 Scatter Plots and Correlations among Variables

The scatter plots between the predictor variable and dependent variable are shown in Figure 4-6 and Figure 4-7. The scatter plot between SIP and Montmorillonite showed an overall upward trend meaning positive correlation between these two variables. Moreover, the observed relationship also exhibited a linear trend with a coefficient of determination of 0.77. Similarly, the scatter plot between SIP and clay percentage also showed a linear upward trend with coefficient of determination of 0.66. In addition, as shown in Figure 4-5, the plot between clay content and Montmorillonite content provided relatively random scatters. A correlation matrix was generated to see the inter-relationship among the three variables as shown in Table 4-1. It becomes evident from the table that the predictor variables clay fraction and montmorillonite percentage exhibited a

strong linear correlation with the dependent variable SIP. Also, the correlation coefficient between two predictor variables fell slightly below the flagging threshold of 0.7. This coefficient can possibly be a source of serious multicollinearity problem. Further analyses will be conducted in subsequent sections to evaluate its effects on the MLR model.

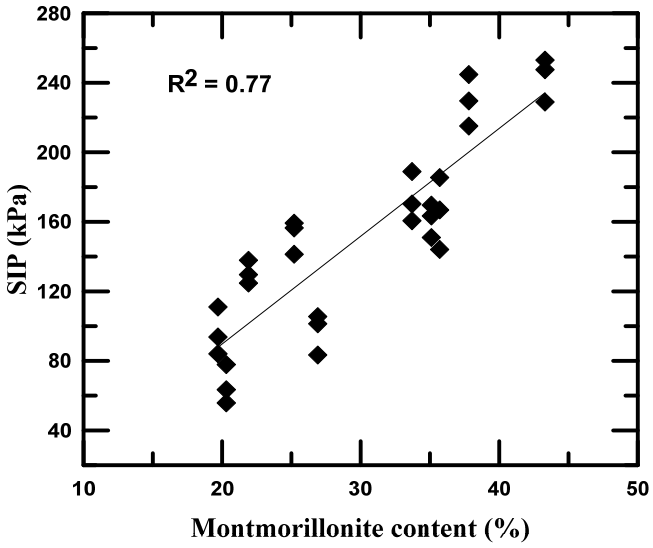

Figure 4-6 Scatter plot of SIP against Montmorillonite content

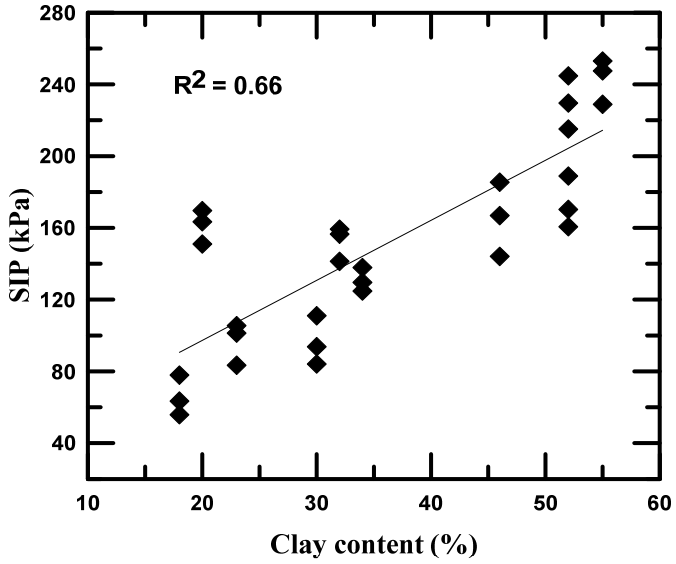

Figure 4-7 Scatter plot of SIP against clay content

Table 4-1 Correlation matrix of the variables used in the MLR model

	SIP	Clay content	Montmorillonite
SIP	1.00	0.81	0.88
Clay content	0.81	1.00	0.70
Montmorillonite	0.88	0.70	1.00

4.4 Verification of Preliminary Model

To begin with, a MLR model relating SIP with the clay and Montmorillonite contents can be expressed as shown in the following equation:

$$Y_i = \beta_0 + \beta_1 X_{i1} + \beta_2 X_{i2} + \varepsilon_i \quad 4\text{-}1$$

where, i = no of observations (1,2……30), Xi1 = clay content (%), Xi2 = Montmorillonite content (%),Yi = shrinkage induced pressure (SIP) (kPa), β_0, β_1 and β_2 are unknown model parameters and ε_i is error term.

The model parameters β1 and β2 can represent the change in the mean response E[Y] when an independent variable is increased by a unit by keeping rest of the independent variable in the model unchanged. The parameters β_0, β_1, and β_2 were estimated based on method of least squares.

All the statistical analyses in this chapter were run using SAS software. A preliminary regression analyses was carried out to study the mutual relationships of the variables. The SAS software generated output of the analysis of variance (ANOVA) is as shown in Table 4-2. A very high regression sum of square (SSR) in comparison to error sum of squares (SSE) was observed from the ANOVA. The analysis resulted coefficient of determination of 85% in the preliminary analysis. It indicated that the model seems to explain 85% of the variation in SIP based on the current data set.

Table 4-2 Summary of ANOVA of preliminary regression analysis

Source	DF	Sum of Squares	Mean Square	F value	$P_r > F$
Model	2	77219	38610	76.8	< 0.0001
Error	27	13574	502.73		
Corrected total	29	90793			

Root MSE	Dependent mean	Coefficient of Variation	R^2	Adjusted R^2
22.42	151.5	14.80	0.85	0.84

Table 4-2 *continued*

Variable	DF	Parameter estimate	Standard error	t value	Pr>|t|	Type I SS	Variance inflation
Intercept	1	-35.24	16.25	-2.17	0.039	688568	0.00
X1	1	1.59	0.43	3.72	0.0009	59767	1.94
X2	1	4.31	0.73	5.89	<0.0001	17452	1.94

The MLR model is based on few assumptions important assumptions. The model assumptions are:

1. The current MLR model for to be reasonable
2. The residuals to have constant variance
3. The residuals to be normally distributed
4. The residuals to be uncorrelated
5. No outliers
6. The predictors not to be highly correlated to each other.

Therefore, in addition to analysis of variance, it is also required to check the MLR model adequacy for the given data. The regression model should be assessed for constant error variance, multicollinearity among the predictor variables, normality of error terms, and outliers (Kutner et al., 2005).

The compliance of the model with the stated assumptions is generally assessed based on graphical plots. The model assumptions can further be examined by using appropriate statistical tests to verify the conclusions based on graphical plots.

4.4.1 Check for Adequacy of MLR Model Form

The applicability of the MLR model for a given data set can be assessed by plotting the residuals against the predictor variables. The examples of residuals versus predictor variables plots are shown in Figure 4-8 through Figure 4-10. Figure 4-8 and Figure 4-9 show clear curvature with concavity upward and downward respectively. The curvature suggests that the MLR model form is not appropriate. Moreover, the curvature situations points out at incorporating second degree terms as well. On the contrary, Figure 4-10 shows well scattered distribution of residuals. The plot does not follow any specific trend implying an adequate condition for application of MLR model to the given data.

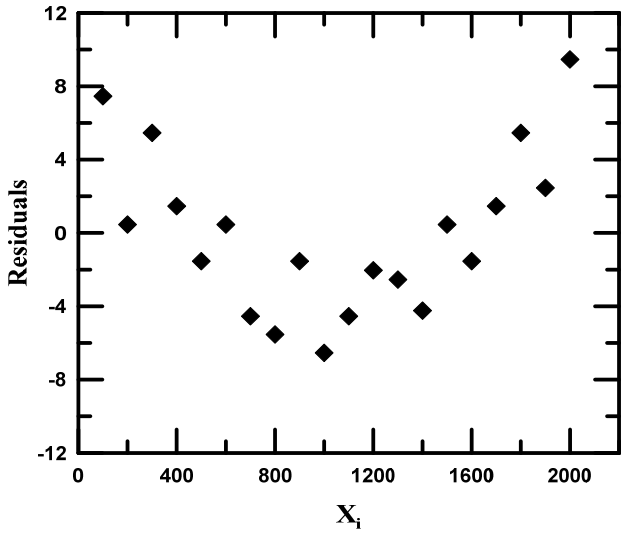

Figure 4-8 Example of residual plot with concavity upward curve

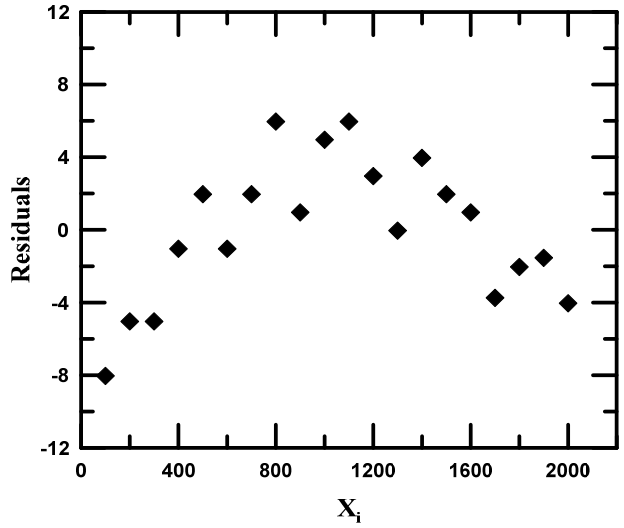

Figure 4-9 Example of residual plot with concavity downward curve

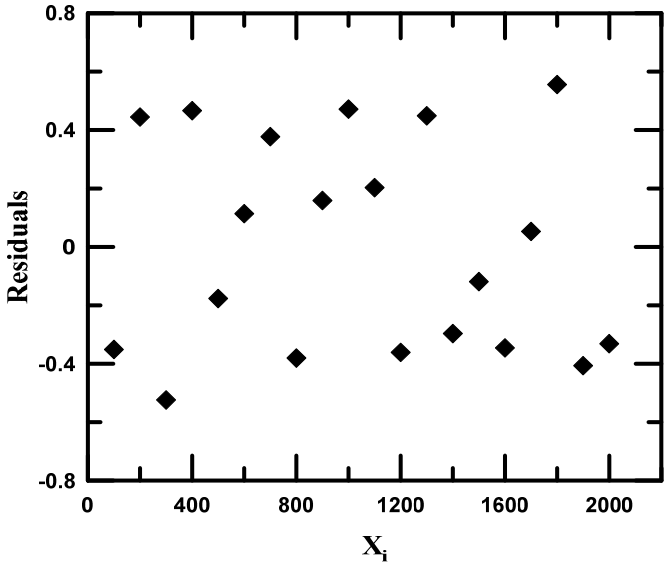

Figure 4-10 Example of residual plot with well scattered points

The model form is generally evaluated by plotting residuals against predictor variables. The residuals were plotted against the predictor variables as shown in Figure 4-11 and Figure 4-12. The plots did not suggest any obvious

curvature. Also, no linear upward or downward trends were observed. The residuals were well scattered along a horizontal band and centered within the horizontal axis, suggesting no need for transformation on the predictor variables at this point.

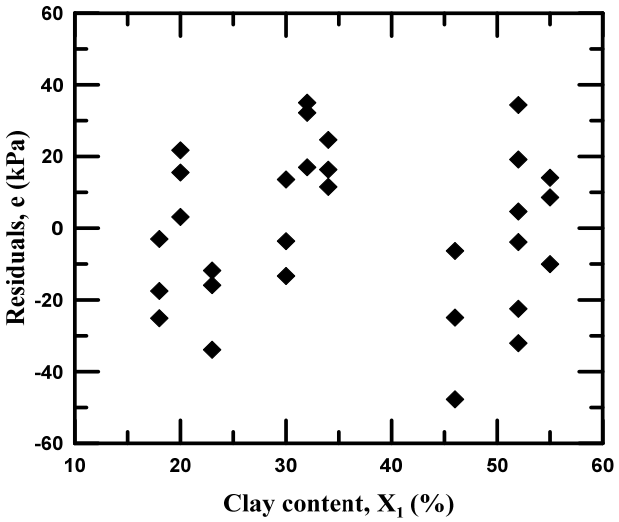

Figure 4-11 Clay content vs. residuals plot

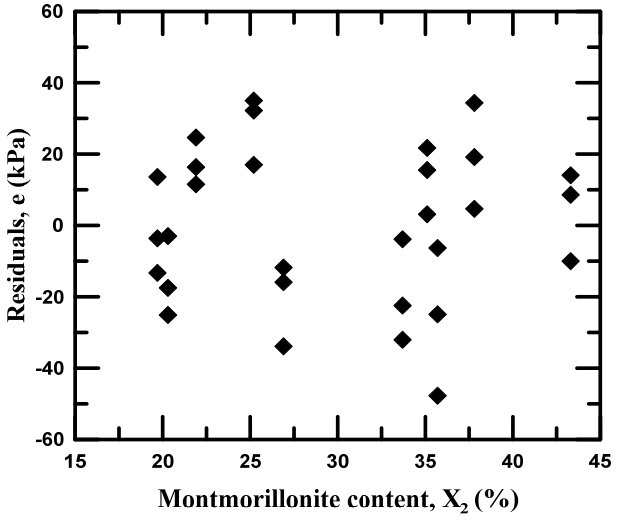

Figure 4-12 Montmorillonite content vs. residuals plot

4.4.2 Check for Constant Variance of Residuals

The assumptions of constant variance of the residuals of the MLR model can be assessed by plotting the residuals against the predicted values. If the data is well scattered without indicating any distinct trend, that would suggest constant error variance. On the other hand, a funnel shaped trend of the plot would indicate non-constant variance.

The residuals were plotted against the predicted values as shown in Figure 4-13. The plot showed that the residuals were well scattered. Any obvious funnel shape was not present in the plot. Therefore, there was not a need for transformation on the response variable at that point. Modified Levene test was also conducted to check the non-constant variances. In this test the data were divided into two groups, small predictor group and large predictor group, based on the median of the predicted values (Y_{hat}). Both groups consisted of 15 observations each as shown in the Table 4-3. The output from the test performed using SAS program is shown in Table 4-3. The first part of the Levene test was to check if the variances of the both groups of data are equal. The following test statistics was followed:

Hypothesis:

H_0: $\sigma_{d1} = \sigma_{d2}$ (variances are equal) versus

H1: $\sigma_{d1} \neq \sigma_{d2}$ (variances are not equal)

Decision rule: reject H_0 if $p < \alpha$ (0.1)

From SAS output, $p = 0.43$

As $p > \alpha$, means failed to reject H_0. Therefore, at 0.1 level of significance, it was concluded that the variances of the both groups were equal. It indicated that equal variance t-test should be used to check the non-constant variance. The following test statistic was followed for testing non-constant variance:

Hypothesis:

H_0: means of d_{i1} and d_{i2} populations are equal versus

H_1: means are not equal

Decision rule: reject H_0 if $p < \alpha$ (0.1)

From SAS output, $p = 0.93$

As $p > \alpha$, means failed to reject H_0. Therefore, at 0.1 level of significance, it can be concluded that the means d_{i1} and d_{i2} populations were equal, hence, constant variance of residuals assumption was valid. This test agreed with the observation made in Figure 4-13. Both the test and the plot concluded that error variance was constant.

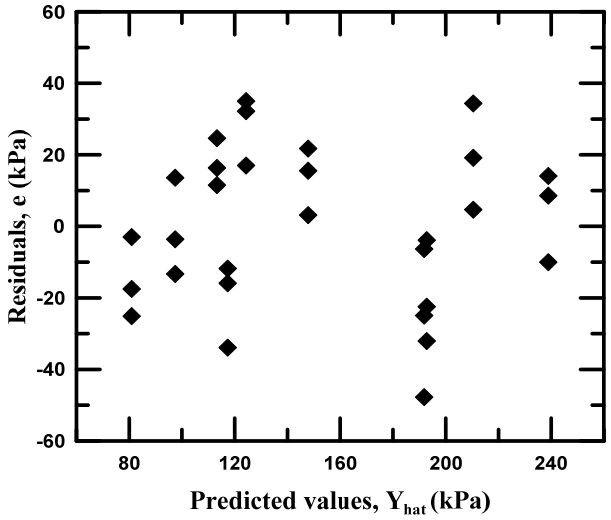

Figure 4-13 Predicted values (Y_{hat}) vs. residuals plot

Table 4-3 Summary of Modified Levene test results

Group	N	Mean	Std Dev	Std Err	Minimum	Maximum
1	15	18.1	11.33	2.92	0	37.99
2	15	17.7	14.05	3.62	0	50.87
Diff (1-2)		0.39	12.77	4.66		

Group	Method	Mean	95% CL Mean		Std Dev	95% CL Std Dev	
1		18.1	11.81	24.37	11.33	8.30	17.88
2		17.7	9.92	25.48	14.05	10.28	22.16
Diff (1-2)	Pooled	0.39	-9.15	9.94	12.76	10.13	17.26
Diff (1-2)	Satterthwaite	0.39	-9.17	9.95			

Method	Variances	DF	t Value	Pr > |t|
Pooled	Equal	28	0.08	0.9338
Satterthwaite	Unequal	26.8	0.08	0.9339

Method	Num DF	Den DF	F Value	Pr > F
Folded F	14	14	1.54	0.4316

4.4.3 Check for Normality of Residuals

The normality of the residuals in the MLR model can be assessed by using normal probability plot. If the plot follows a distinct linear trend then it suggests the normality of the residuals. The normal probability plot for the current analysis is shown in Figure 4-14. A fairly normal trend was observed in the normal probability plot. Although a relatively shorter tail was observed at the right side of the distribution, it does not seriously deviate from the normality. Normality can be further tested at level of significance of 0.1. The SAS output for the normality test is shown in Table 4-4. The following test statistics was followed for testing the normality of the error terms:

Hypothesis:

H_0: normality is satisfied versus

H_1: normality is violated

Decision rule: reject H_0 if $\rho < C(\alpha,n)$

For $\alpha = 0.1$ and $n = 30$, $C(0.1,30) = 0.971$

From SAS output, $\rho = 0.99 > C(0.1,30) = 0.971$. Hence, we fail to reject H_0. It was concluded the normality was satisfied at the level of significance of 0.1.

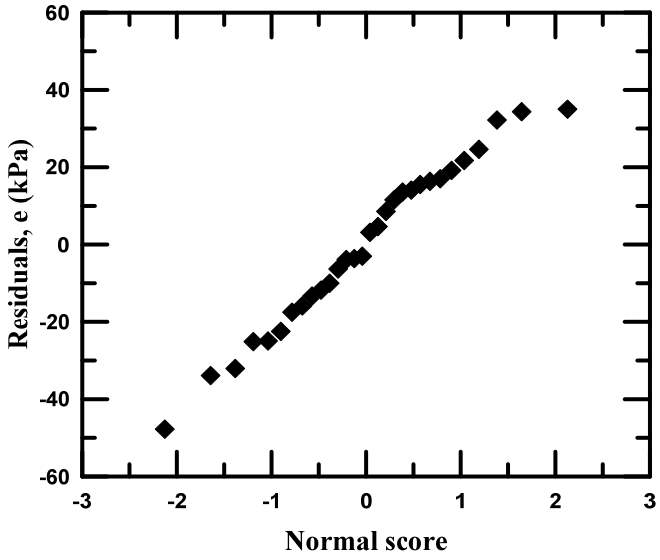

Figure 4-14 Normal probability plot of residual

Table 4-4 Summary of normality test result

	Residuals, e	Normal scores, enrm
Residuals, e	1	0.99
Normal scores, enrm	0.99	1

4.4.4 Check for Outlier and Their Influence

Some extreme observations that do not follow the general trend of the majority of the data are known as outliers. Outliers can create sizable inaccuracy in least square method by shifting the fitted line disproportionately towards the outlying observation (Kunter et al., 2005). Outliers can be identified by using the residual plots as well as statistical tests. Outliers in the response variable (Y-outlier) and predictor variables (X-outlier) can be diagnosed separately. If there is any outlier in the data, its influence on the model should be quantified. Y-outliers

can be removed from the model if it occurred due to typo error or if there was any error in the observation that was not saved in a correct way. In any different case they should be included in the model. The plots analyzed and examined for the model assumptions did not show any outlier. An X-outlier can also be identified by comparing leverage value or h_{ii} value with the cutoff value of 2p/n, p being the number of model parameters and n is number of observation. If h_{ii} is smaller than the cutoff value it is not an X-outlier. X-outlier is identified if h_{ii} is bigger than the cutoff value. The cutoff in the current model is (2x3)/30 = 0.2. Based on the output Table 4-5, observations 25, 26, and 27 were identified as x-outliers. They were flagged as likely influential points. Further diagnostics was conducted to check the influence of these outlying observations.

A Y-outlier is identified by calculating studentized deleted residuals or t_i and comparing these values with the cutoff also known as Bonferoni outlier test based on Bonferoni simultaneous intervals. The studentized deleted residual t_i is calculated as:

$$t_i = \frac{d_i}{\sqrt{MSE_i(1-h_{ii})}} = e_i\sqrt{\frac{n-p-1}{SSE(1-h_{ii})-e_i^2}} \qquad 4\text{-}2$$

These values were also calculated for each observations using SAS software and presented in Table 4-5 as tres. The Bonferoni outlier test checks if

$$|t_i| > t\left\{1 - \frac{a}{(2 \times n)}; n - p - 1\right\} = t\left\{1 - \frac{0.1}{(2 \times 30)}; 30 - 3 - 1\right\} \quad 4\text{-}3$$
$$= t\{0.998,26\} = (between\ 3.0669 - 3.435)$$

The observation is considered as Y-outlier if the absolute value of tres is greater than the cutoff value. The absolute maximum value of t_i from the table was 2.19, which was smaller than the cutoff value of 3.435. Therefore, no Y-outlier was identified by the test.

There were three X-outliers (observations 25, 26, and 27) in the regression model detected based on Leverage values calculated with the SAS software. The influence of the individual outliers on the model can be examined based on three metrics: (a) influence on single fitted value (DFFITS), (b) influence on all model coefficients (Cook's distance), and (c) influence on the individual regression coefficients (DFBETAS). And these parameters are calculated as follows:

$$DFFITS = t_i \sqrt{\left(\frac{h_{ii}}{1 - h_{ii}}\right)} \quad 4\text{-}4$$

$$Cook's\ distance, D_i = \frac{e_i^2}{pMSE}\left(\frac{h_{ii}}{(1 - h_{ii})^2}\right) \quad 4\text{-}5$$

$$DFBETAS_{k(i)} = \frac{b_{k-}b_{k(i)}}{\sqrt{c_{kk}\, MSE_i}} \quad 4\text{-}6$$

The influence of the outliers on the regression model was analyzed using DFITS, DFBETAS and Cook's distance and the SAS output for the analysis is presented in Table 4-6. The cutoff value for the Cook's distance is given by

F(0.5;p,n-p) = F(0.5;3,27)=0.81. The cutoff point for DFITS and DFBETAS for medium dataset is 1. The SAS result showed that all the DFITS, DFBETAS, and Cook's distance values were below the respective cutoff values. Therefore no observation was poised to have big influence on the regression model.

Table 4-5 SAS output summary of the outlier test results

Obs	SIP	Clay	Montmorillonite	y_{hat}	e	tres	cookdi	h_{ii}	dffitsi
1	141.3	32	25.2	124.30	17.00	0.78	0.010	0.047	0.170
2	159.3	32	25.2	124.30	35.00	1.60	0.042	0.047	0.364
3	156.5	32	25.2	124.30	32.20	1.47	0.035	0.047	0.332
4	160.7	52	33.7	192.77	-32.07	-1.50	0.072	0.088	-0.476
5	170.3	52	33.7	192.77	-22.47	-1.05	0.035	0.088	-0.326
6	188.9	52	33.7	192.77	-3.87	-0.18	0.001	0.088	-0.055
7	144.1	46	35.7	191.84	-47.74	-2.19	0.092	0.055	-0.569
8	166.9	46	35.7	191.84	-24.94	-1.14	0.025	0.055	-0.277
9	185.5	46	35.7	191.84	-6.34	-0.29	0.002	0.055	-0.069
10	228.9	55	43.3	238.92	-10.02	-0.48	0.012	0.134	-0.186
11	247.5	55	43.3	238.92	8.58	0.41	0.009	0.134	0.159
12	253	55	43.3	238.92	14.08	0.67	0.023	0.134	0.263
13	137.9	34	21.9	113.26	24.64	1.15	0.043	0.089	0.362
14	124.8	34	21.9	113.26	11.54	0.54	0.009	0.089	0.166
15	129.6	34	21.9	113.26	16.34	0.76	0.019	0.089	0.236
16	84.1	30	19.7	97.42	-13.32	-0.63	0.015	0.104	-0.212
17	93.8	30	19.7	97.42	-3.62	-0.17	0.001	0.104	-0.057
18	111	30	19.7	97.42	13.59	0.64	0.016	0.104	0.216
19	229.6	52	37.8	210.44	19.16	0.89	0.024	0.082	0.266
20	215.1	52	37.8	210.44	4.66	0.22	0.001	0.082	0.064

Table 4-5 *continued*

21	244.8	52	37.8	210.44	34.36	1.60	0.076	0.082	0.494
22	83.4	23	26.9	117.30	-33.90	-1.57	0.063	0.072	-0.449
23	101.4	23	26.9	117.30	-15.90	-0.74	0.014	0.072	-0.203
24	105.5	23	26.9	117.30	-11.80	-0.55	0.008	0.072	-0.150
25	163.4	20	35.1	147.86	15.54	0.79	0.062	0.229	0.427
26	169.6	20	35.1	147.86	21.74	1.10	0.121	0.229	0.605
27	151	20	35.1	147.86	3.14	0.16	0.003	0.229	0.085
28	55.8	18	20.3	80.90	-25.10	-1.18	0.052	0.101	-0.398
29	77.9	18	20.3	80.90	-3.00	-0.14	0.001	0.101	-0.046
30	63.4	18	20.3	80.90	-17.50	-0.82	0.025	0.101	-0.274

Table 4-6 SAS output for the analyses of influence of individual observation on the model

Obs	Residual	R Student	Hat Diag H	Cov Ratio	DFFITS	DFBETAS		
						Intercept	x1	x2
1	16.999	0.7706	0.0465	1.0976	0.1702	0.1211	0.0221	-0.0785
2	34.999	1.6487	0.0465	0.8716	0.3642	0.259	0.0473	-0.1679
3	32.199	1.5047	0.0465	0.9143	0.3324	0.2364	0.0431	-0.1533
4	-32.0689	-1.5347	0.0879	0.9465	-0.4764	0.0671	-0.348	0.1414
5	-22.4689	-1.0513	0.0879	1.0836	-0.3263	0.046	-0.2384	0.0969
6	-3.8689	-0.1774	0.0879	1.2233	-0.0551	0.0078	-0.0402	0.0163
7	-47.7367	-2.3694	0.0546	0.6589	-0.5693	0.2067	-0.1379	-0.1389
8	-24.9367	-1.1507	0.0546	1.0206	-0.2765	0.1004	-0.067	-0.0674
9	-6.3367	-0.2857	0.0546	1.1735	-0.0686	0.0249	-0.0166	-0.0167

Table 4-6 *continued*

10	-10.0156	-0.473	0.1339	1.2603	-0.186	0.1306	-0.0283	-0.0942
11	8.5844	0.405	0.1339	1.2689	0.1593	-0.1118	0.0242	0.0806
12	14.0844	0.668	0.1339	1.2287	0.2627	-0.1844	0.04	0.133
13	24.6366	1.1584	0.0889	1.0569	0.3617	0.275	0.1713	-0.2836
14	11.5366	0.5318	0.0889	1.1898	0.1661	0.1262	0.0786	-0.1302
15	16.3366	0.7573	0.0889	1.1512	0.2365	0.1798	0.112	-0.1854
16	-13.315	-0.6202	0.1042	1.1962	-0.2115	-0.1814	-0.0752	0.1653
17	-3.615	-0.1673	0.1042	1.2461	-0.057	-0.0489	-0.0203	0.0446
18	13.585	0.633	0.1042	1.1941	0.2159	0.1851	0.0768	-0.1687
19	19.1622	0.8886	0.0822	1.1155	0.266	-0.1237	0.1145	0.0424
20	4.6622	0.2132	0.0822	1.2139	0.0638	-0.0297	0.0275	0.0102
21	34.3622	1.65	0.0822	0.9051	0.4939	-0.2296	0.2125	0.0788
22	-33.9004	-1.6154	0.0717	0.9055	-0.449	-0.1976	0.3058	-0.1268
23	-15.9004	-0.7296	0.0717	1.1352	-0.2028	-0.0892	0.1381	-0.0573
24	-11.8004	-0.539	0.0717	1.1669	-0.1498	-0.0659	0.102	-0.0423
25	15.5373	0.7836	0.2292	1.3547	0.4274	-0.0576	-0.3802	0.3419
26	21.7373	1.109	0.2292	1.2648	0.6048	-0.0815	-0.538	0.4838
27	3.1373	0.1565	0.2292	1.4488	0.0853	-0.0115	-0.0759	0.0683
28	-25.0985	-1.1895	0.1008	1.0624	-0.3983	-0.3344	0.1604	0.0918
29	-2.9985	-0.1384	0.1008	1.2427	-0.0464	-0.0389	0.0187	0.0107
30	-17.4985	-0.818	0.1008	1.154	-0.2739	-0.23	0.1103	0.0632

4.4.5 Check for Multicollinearity

Initial observation of plots as well as Pearson's coefficients of the dataset indicated that the independent variables did not have high correlation. Similar results were suggested by the variance inflation factor (VIF). The VIF is a measure of how the variances of the estimated regression coefficients are inflated as compared to when the predictor variables are not linearly correlated. The VIFs also shows how serious is the correlation of each predictor with the rest of the predictors. The observed VIFs of the independent variables were close to 1. It suggested that the multicollinearity problem is not very serious in the model. The VIFs and the parameter estimates calculated from SAS are shown in Table 4-7.

Table 4-7 SAS output for calculation of VIFs of the predictor variables

Variable	DF	Parameter estimate	Standard error	t value	Pr>|t|	Type I SS	Variance inflation
Intercept	1	-35.24	16.25	-2.17	0.0391	688568	0.00
X1	1	1.59	0.43	3.72	0.0009	59767	1.94
X2	1	4.31	0.73	5.89	<0.0001	17452	1.94

Now, having the entire model assumptions verified, the preliminary model incorporating SIP (Y) with clay content(X_1) and Montmorillonite content (X_2) can be presented as:

$$Y = -35.238 + 1.592X_1 + 4.309X_2 \qquad 4\text{-}7$$

The SIP tests were conducted on clayey soils. Therefore, clay content cannot be zero. Furthermore, Montmorillonite is a clay mineral and cannot be

zero in clayey soils with high shrink-swell potential. Thus, the scope of the model did not include $X_1=X_2=0$, and the intercept '-35.238' did not have a meaning on its own. On the other hand, β_1 gives the increase in the mean response of Y by 1.592 kPa for per unit increase in clay content when the Montmorillonite content remains constant. Similarly, β_2 indicates the increase in the mean response of Y by 4.309 kPa for per unit increase in Montmorillonite content when the clay content remains constant.

ANOVA of the current model presented earlier in Table 4-2 can be finalized and discussed now. ANOVA indicated that the error sum of squares (SSE), regression sum of square (SSR), and total sum of square (SSTO) were 77219, 13574, and 90793 respectively. SSR is the explained variability for the response variable. SSE is the unexplained variability in the shrinkage induced pressure of the soil and forms a part of the total variability. SSTO is the total variability of the SIP variable.

The coefficient of determination, R^2, shows the variability in the SIP explained by the model with two predictor variables clay fraction and montmorillonite. R^2 is the ratio of SSR divided by SSTO and was equal to 0.85 for this analysis. Adjusted R^2 is another indicator of coefficient of determination. It was calculated as 1-{(SSE/(n-p))/(SSTO/(n-1))}. From the SAS output shown in Table 4-2, it was equal to 0.84. A greater difference between R^2 and adjusted R^2 indicates that at least one variable is not explaining much. In this model, these

values were close enough to conclude that both variables are required in the model

The significance of each predictor in the model can be analyzed by the p value obtained in the SAS output (Table 4-2). The p values indicated that the predictors in the model were significant at 0.1 level of significance.

F test can be conducted to determine if a regression relationship exists between the response variable and the predictor variables. The p value was less than 0.0001. Therefore, a regression relationship exists between response variable and all the predictor variables at 0.1 level of significance.

4.4.6 Exploration of Interactions

The interaction terms can be explored by using three different plots; i.e. residual vs. interaction terms, residual vs standardized interaction terms, and partial regression plots of the interaction terms. These plots are as shown in Figure 4-15 through Figure 4-18. These plots did not reveal any specific trend. Therefore, no interaction terms were considered in the model.

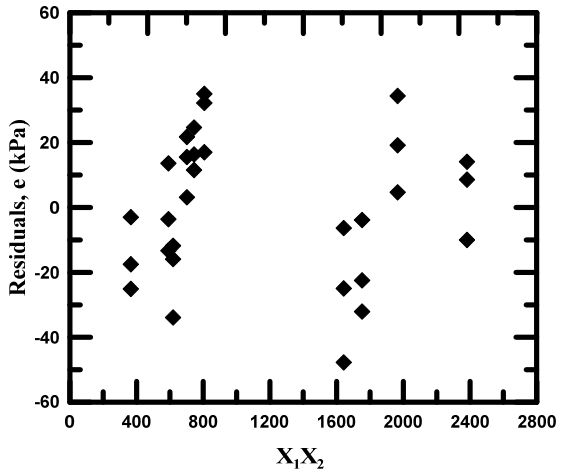

Figure 4-15 Residuals plotted against the interaction term

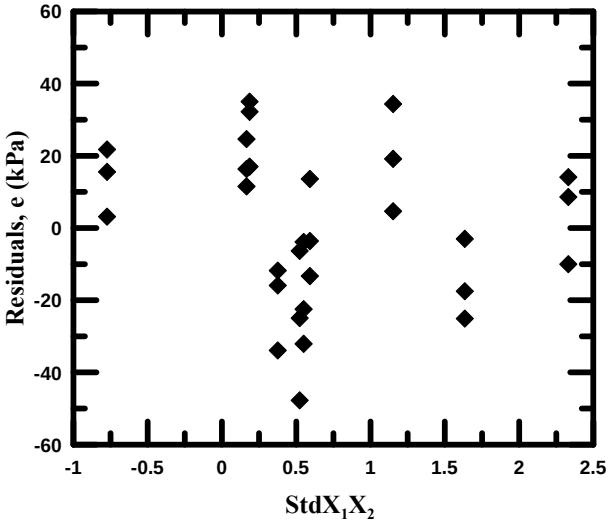

Figure 4-16 Residuals vs. standardized interaction term

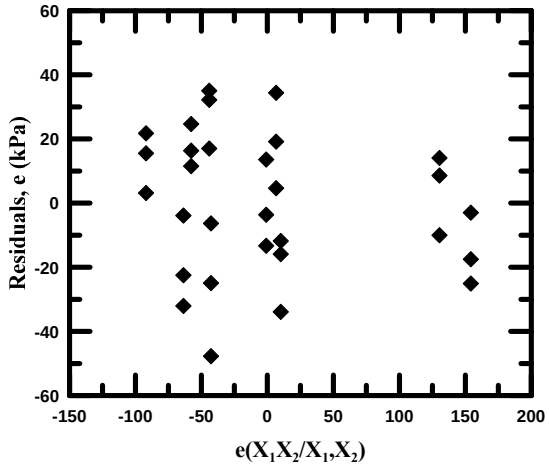

Figure 4-17 Partial regression plot of interaction terms

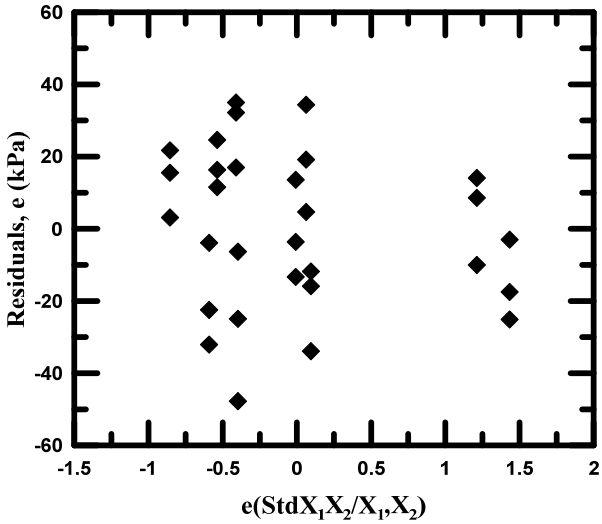

Figure 4-18 Partial regression plot of standardized interaction terms

4.5 Selection of Final Model

Different possible models and relative significances of predictor variables were analyzed using three different methods. Potential best models were searched

using best subset method, stepwise regression, and backward elimination methods.

4.5.1 Best Subset Method

Best subset method was used to analyze all possible regression subsets. Every possible subset was evaluated to determine the best regression model. A best model is identified by higher R^2 and adjusted R^2 values with a lower SSE and MSE values. In addition, Mallow's Cp was also considered as a criterion to determine the best model. A potential best model will have Mallow's Cp and number of parameters almost equal. However, this criterion alone may not work well. The maximum number of predictor variables that are required in the model can also be decided by monitoring adjusted R^2 value. If addition of a new predictor variable in an existing model reduces the adjusted R^2 value, then the newly added predictor is considered redundant. It hints that from that instant, models with equal or greater number of variables should not be involved at the model searching procedure. R^2, Mallow's Cp, and the Akaike's Information Criteria (AIC) can also aid in comparing between potentially best models. The summary of the best subset method of model search is presented in Table 4-8.

Table 4-8 Summary of model search using best subset method

Number in model	Adjusted R-square	R-square	Cp	AIC	SBC	Variables in Model
2	0.8394	0.8505	3	189.44	193.64	x1 x2
1	0.7658	0.7739	14.8	199.85	202.65	x2
1	0.6461	0.6583	35.7	212.24	215.04	x1

4.5.2 Backward Elimination Method

The model search with backward elimination begins with all the predictor variables in the model. Then, statistically insignificant variables are eliminated in the following steps. The analysis continues until all insignificant variables are removed from the model. Eventually, this process provides one best model at the end of the search process. In this current analysis, all the predictor variables were significant at 0.05 level of significance and no variables were eliminated in the process. The output from the model search process using backward elimination is as shown in the Table 4-9.

Table 4-9 Summary of model search using backward elimination

Variable	Parameter estimate	Standard error	Type II SS	F value	Pr > F
Intercept	-35.237	16.25	2363.95	4.7	0.0391
x1	1.59	0.43	6958.05	13.84	0.0009
x2	4.31	0.73	17452	34.71	<.0001

4.5.3 Stepwise Regression Method

Stepwise regression method uses backward elimination and forward selection algorithm to search potential good models. In the process of model search, the predictor variable with highest statistical significance is included first in the model and regression analysis is carried out. In the second step, another predictor variable is added in the previous model and the procedure is repeated. Statistical significance tests (i.e. F statistic) are utilized to select the parameters.

The output from the stepwise regression method form SAS software is presented in Table 4-10. The tests were conducted at 0.05 level of significances for both entry and exit cases.

Table 4-10 Summary of model search using stepwise regression

Step	Variable entered	Variable removed	No. variables in	Partial R-square	Model R-square	Cp	F value	Pr > F
1	x2	-	1	0.7739	0.7739	14.84	95.82	<.0001
2	x1	-	2	0.0766	0.8505	3	13.84	0.0009

All model search methods showed that both clay fraction as well as montmorillonite were necessary to explain the shrinkage induced pressure of the slurry clay soils. Therefore, the best model correlating clay fraction and montmorillonite can be presented as follows:

$$Y = -35.238 + 1.592X_1 + 4.309X_2$$

where, Y = shrinkage induced pressure (kPa), X_1 = clay fraction (%), and X_2 is montmorillonite (%).

The range of model: Y=[55.8, 253], X1=[18,55], X2[19.7,43]

4.6 Comparison of Predicted and Measured SIP

Six different clayey soils were collected again from different locations of Texas to compare the predicted and measured SIP. The soils and respective clay and Montmorillonite contents are listed in Table 4-11. However, the Montmorillonite content of Grapeland soil, and both clay and Montmorillonite

contents of Waco soil fell out of the range of the model. Therefore, only Cleburne, Denton, Mansfield, and Plano soils were used in the model validation.

Table 4-11 Properties of the soils used for model validation

Soils	Clay Content (%)	Montmorillonite content (%)
Cleburne	22.1	20.4
Denton	39.4	20.4
Grapeland	38.32	18.57
Mansfield	49.9	42.82
Plano	54.3	29.6
Waco	17.1	50.7

Two SIP tests were conducted Cleburne, Denton, Mansfield and Plano soils. Figure 4-19 shows the time versus SIP plot obtained from the tests. The peak SIPs were determined from the test and compared with the peak SIP predicated from the model. The comparison between the measured and predicted SIP is shown in Figure 4-20. The plot shows that the measured and predicted SIPs were in good agreement.

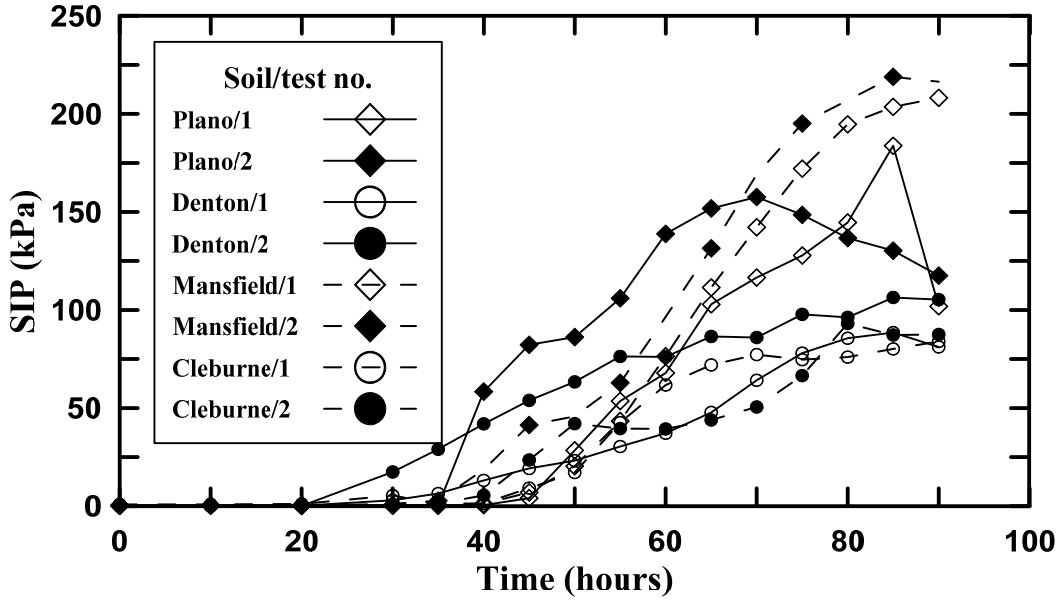

Figure 4-19 Time versus SIP for the soils used in model verification

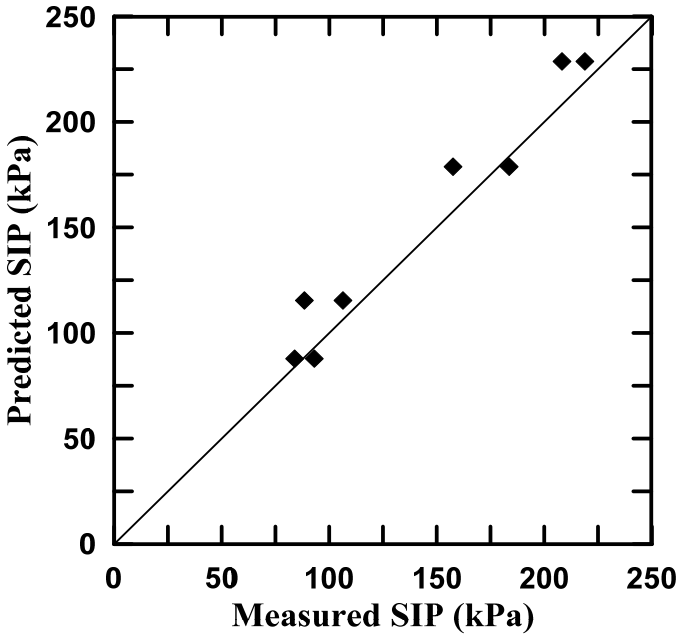

Figure 4-20 Comparison of predicted and measured SIP

4.7 Summary

Multiple linear regression model to predict the peak SIP of clayey soils was presented in this chapter. The model was checked for model adequacy, constant variance of residuals, normality of residuals, outliers and their influence, and multicollinearity among the predictor variables. The possibility of adding any interaction terms was also analyzed. However, the interaction terms deemed unnecessary in the model. The best model was determined using the three model search methods. Finally, the predictability of the model was assessed and verified by using the SIP results on new sets of soils.

Chapter 5

Strength, Swell and Shrinkage Characterization of Biopolymer Treated Soils

5.1 Introduction and Background

Soils present a wide variability in the North Texas area including high and low plasticity clays. Volumetric changes in soils are predominant due to the expansive clays present in the region (Le, 2013). The major rolled earthfill dams constructed in the area, including Grapevine and Joe Pool dams, utilized the on-site soils. The soils used in the dams included high plasticity clays. Repeated weathering (wetting-drying) cycles have produced desiccation cracking within high plasticity fill materials in these dam slopes (McCleskey, 2005). Moreover, the infiltration of rainwater into the desiccation cracks saturates the top soil surface and softens the soils thereby causing surficial slope failure (Dronamraju, 2008; Le, 2013).

Previous research studies conducted at the University of Texas at Arlington (UTA) investigated the advantages of utilizing lime-treated and lime plus fiber treated soils to mitigate surficial slope failures (McCleskey, 2005; Dronamraju, 2008; Le, 2013). The long term slope movement data collected from Grapevine and Joe Pool dams demonstrated that the aforementioned soil treatment methods considerably reduced the deformation of slope resulting from desiccation cracking compared to the untreated condition.

The improvements were reported based on the shear strength parameters measured in the laboratory as well as the field monitoring of the slope movements in the treated sections. The shrinkage characterization studies conducted on the treated soils were based on linear shrinkage bar and volumetric shrinkage tests. No attempts were made to investigate the evolution of internal stresses, tensile strength of the drying soils, and its effect in the desiccation cracking. Therefore, in the current study, ground improvement studies are being evaluated as a part of the proposed shrinkage characterization methods and tools. Tests performed included experiments on the control and treated soils using the SIP test, IDT test, SWCC, and digital image correlation studies. These tests provided highlights of the underlying mechanism associated with desiccation cracking and associated improvements imparted by the admixtures.

Conventional soil stabilizing materials, such as ordinary cement or lime, have several limitations, especially from the environmental perspective. The production of cement and other stabilization materials is known as a great contributor of CO_2 to the atmosphere. It may also cause several disturbances within the soil mass, such as high pH and other problems due to the chemical reactions during mixing (Bremmer, 2001). The use of recyclable materials as soil stabilizers have proved to be economical, effective, and environment friendly. This study introduces the use of Biopolymer as sustainable soil stabilization technique for shallow slope failures.

Biopolymer is a product mainly formed by microorganisms for their own protection and/or to make the environment more hospitable for their living (Maier et al., 2000). It is also called exopolymers or extracellular polymeric substances (EPS) (Sutherland, 2001). The main source of biopolymer is plants, but it can also be obtained from different types of tress and even produced by bacteria. The biopolymers are mostly high molecular weight polysaccharides. These polysaccharides contain chemically active groups with electrical charges which make them actively interact with clay minerals (Sutherland 2001). Therefore, biopolymers are likely to affect soil behavior and particularly enhance the shear strength to reduce erosion and shallow failure of slopes (Nugent 2011).

This chapter presents the laboratory test results conducted on biopolymer amended Grapevine and Joe Poll dam soils. A commercially available biopolymer called Guar Gum is used in the current study. The optimization of biopolymer dosage using direct shear tests and swell pressure tests is explained first. The improvement in the shear strength parameters of treated soils at different percentage of the biopolymer was considered and used to decide the optimum dosage.

In the meantime, an increase in the swell pressure due to the usage of biopolymer treatment was monitored and it was also considered as an additional factor in the stabilizer mix design. Different shrinkage characterization studies,

including linear shrinkage bar test, SIP test, indirect tensile strength tests, SWCC, and digital image correlation techniques are presented in subsequent sections.

5.2 Optimization of the Biopolymer Dosage

First of all, the optimum dosage of the biopolymer for the treatment of both Grapevine and Joe Pool soils were determined by considering shear strength and swell pressure properties as two key parameters. Shear strength is generally considered as the lone criteria in devising a soil stabilization technique. In the case of biopolymer stabilization of soils, however, it is important to assess the swell pressure of the stabilized soil because of the moisture affinity of the biopolymer. The experimental study consisted of mixing the soils with a commercially available biopolymer (Guar-Gum). Four different dosages selected for the mix design. The amounts of the biopolymer added on the soils for different dosages were 0.25%, 0.5%, 1%, and 1.5% of the weight of the dry soil. Strength and swell parameters of treated mixtures were obtained by performing direct shear test and swell pressure tests respectively. In this chapter, the terms GV, JP, BP, DS, and TRS denote Grapevine, Joe Pool, biopolymer, direct shear, and torsional ring shear, respectively.

5.2.1 Direct Shear Test

First of all, Grapevine and Joe Pool soils were mixed with biopolymer and compacted at the 95% of maximum dry density and optimum moisture content of the control soils. The direct shear specimens were prepared by static compression

of the soil-biopolymer-water mixture. The 25 mm thick and 63.5 mm diameter specimens were then covered in an air tight plastic wrap and kept in a humidity chamber. The specimens were allowed seven days of curing time before the test. The direct shear tests were performed at the normal stresses of 50, 100, and 200 kPa. A drained test was performed by allowing the soil to shear at very slow shear rate of 0.005 mm/min (0.0002 in/min). Figure 5-1 through Figure 5-5 show the direct shear test results for Grapevine Dam soils. Similarly, Figure 5-6 through Figure 5-10 show the direct shear test results for Joe Pool Dam soils.

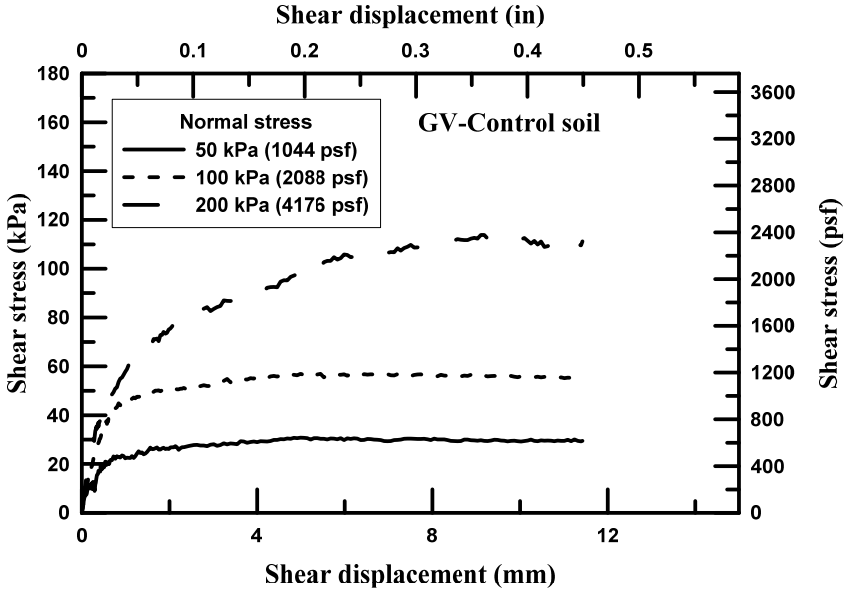

Figure 5-1 DS test results for Grapevine control soil

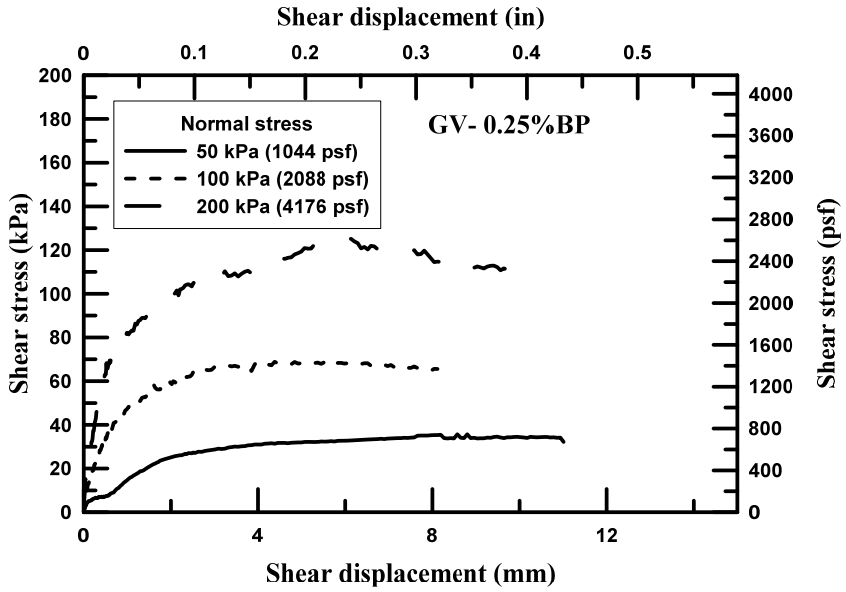

Figure 5-2 DS test results for Grapevine soil treated with 0.25% biopolymer

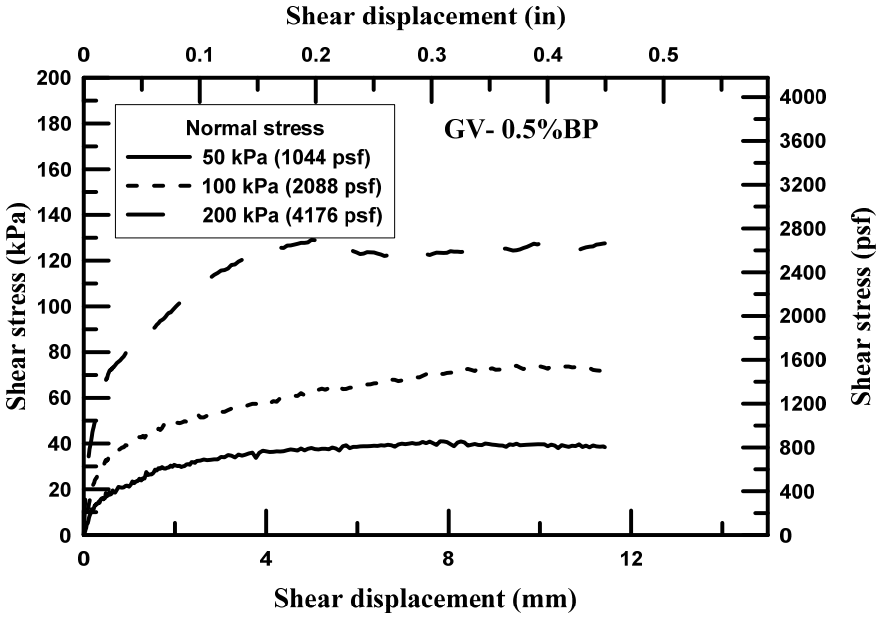

Figure 5-3 DS test results for Grapevine soil treated with 0.5% biopolymer

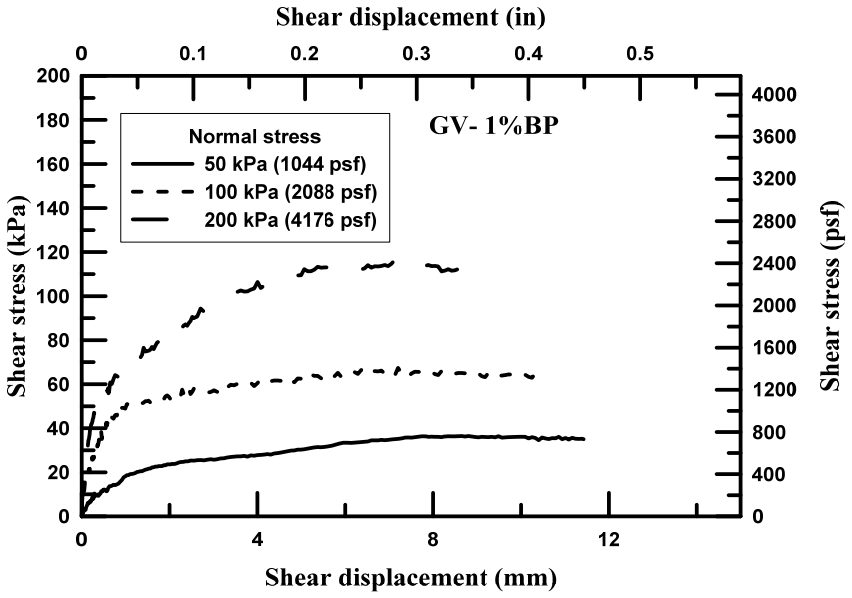

Figure 5-4 DS test results for Grapevine soil treated with 1% biopolymer

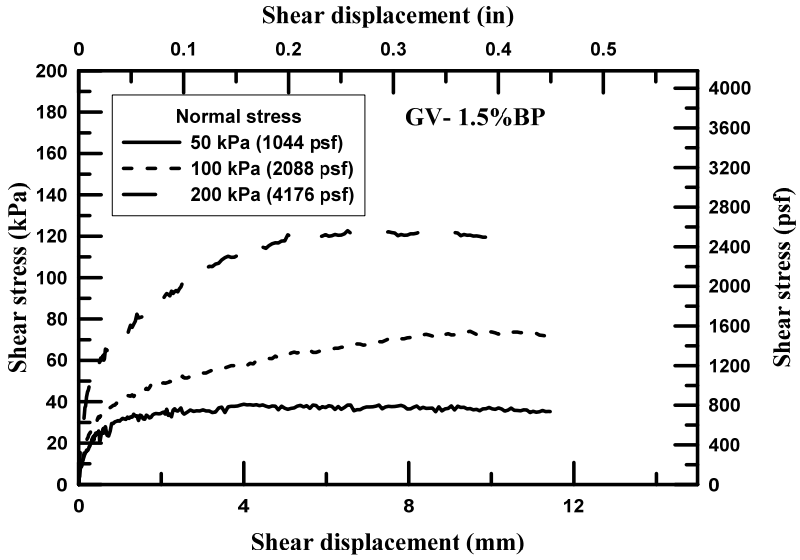

Figure 5-5 DS test results for Grapevine soil treated with 1.5% biopolymer

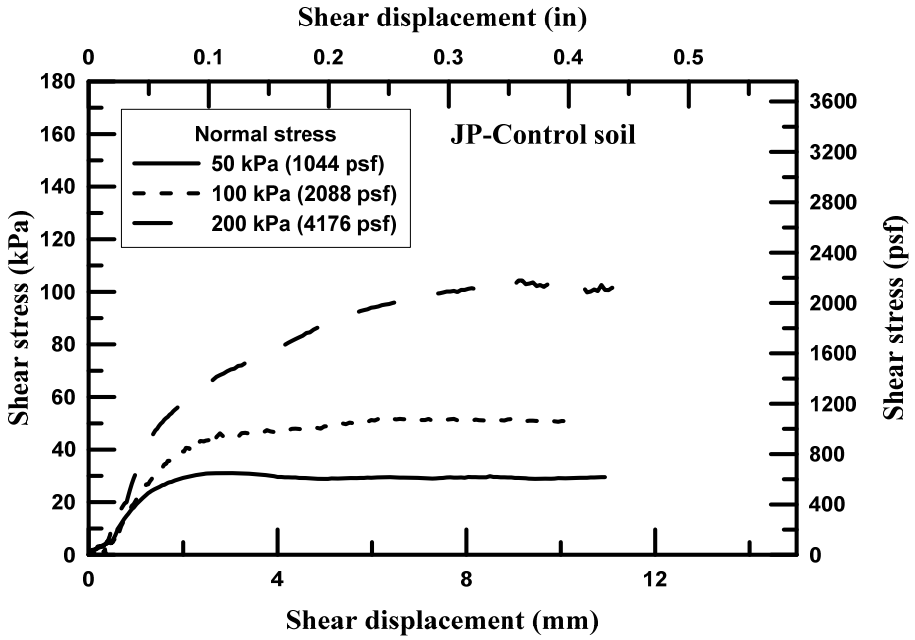

Figure 5-6 DS test results for Joe Pool control soil

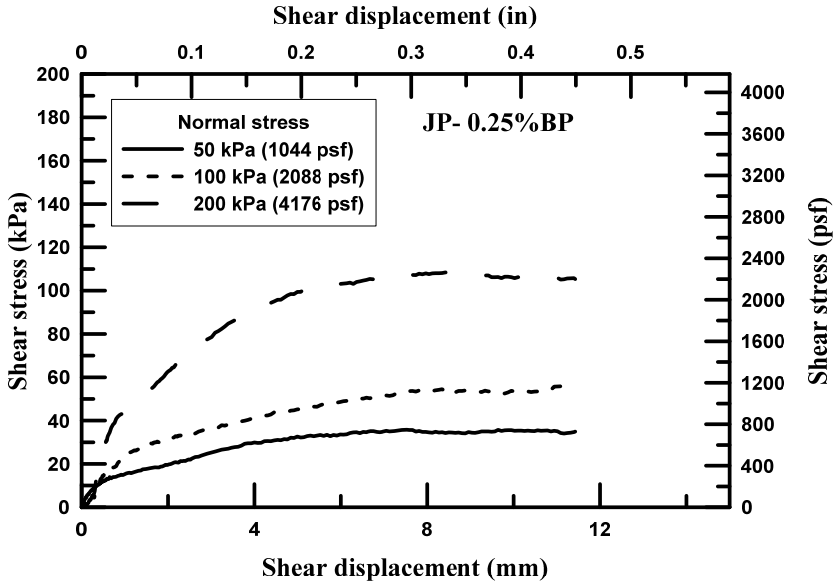

Figure 5-7 DS test results for Joe Pool soil treated with 0.25% biopolymer

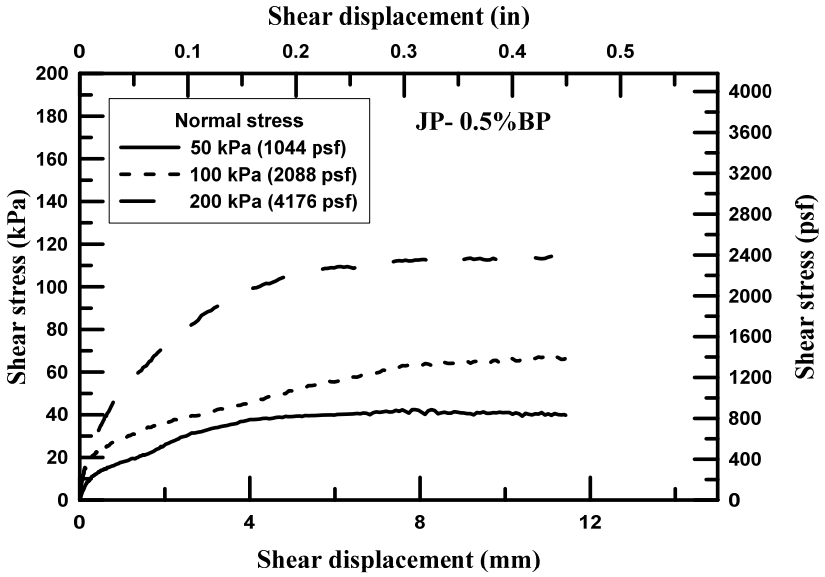

Figure 5-8 DS test results for Joe Pool soil treated with 0.5% biopolymer

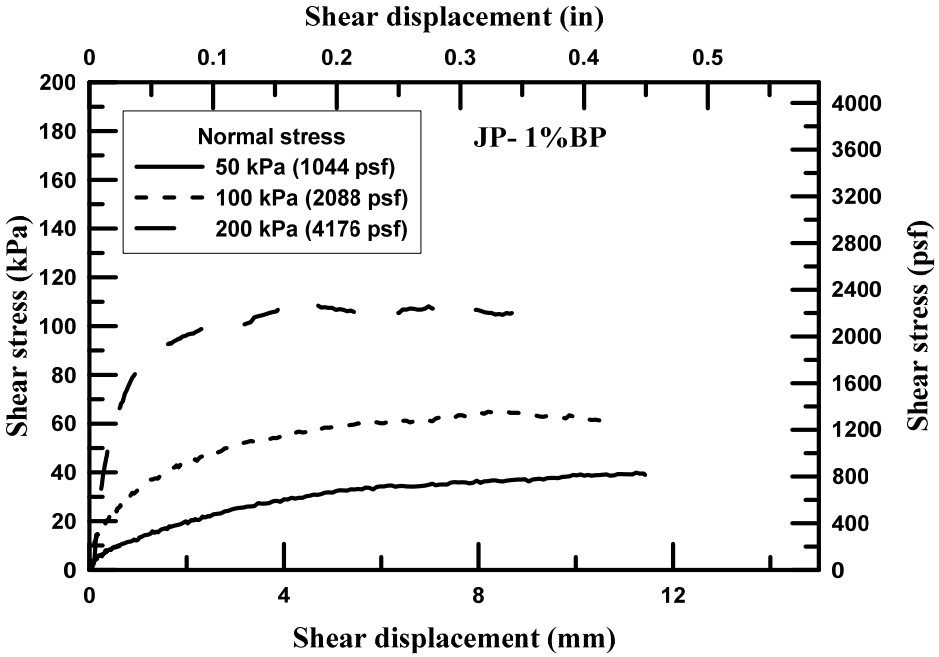

Figure 5-9 DS test results for Joe Pool soil treated with 1% biopolymer

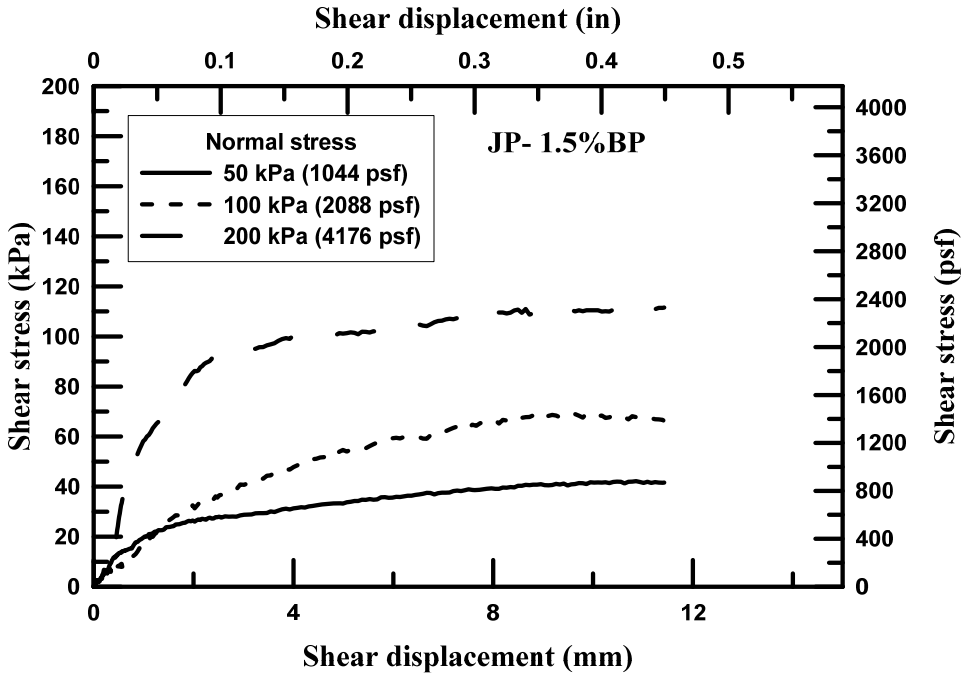

Figure 5-10 DS test results for Joe Pool soil treated with 1.5% biopolymer

Figure 5-11 shows the failure envelope of the control and biopolymer treated Grapevine soils. The control soil showed the minimum shear strength. The shear strengths of the treated soils increased with increase in biopolymer content up to the biopolymer dosage of 0.5%. The treated soil with biopolymer dosages of 1% and 1.5% showed lower shear strengths than 0.5% biopolymer treated soil. The shear strengths for both 1% and 1.5% biopolymer dosages were observed to be even lower than that of the 0.25% dosage of biopolymer. The slopes of the failure envelopes were observed to be almost the same. That means, the addition of biopolymer is principally affecting the effective cohesion of the Grapevine soil.

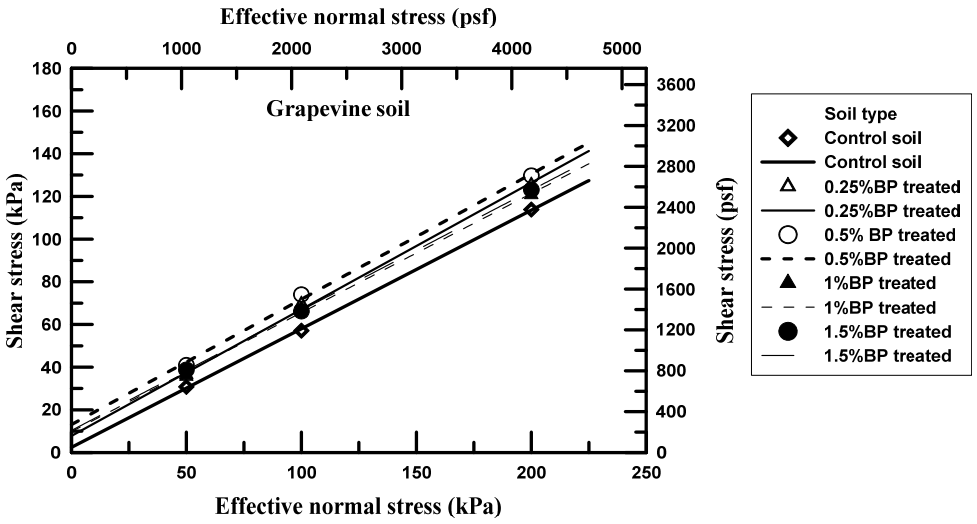

Figure 5-11 Failure envelopes of the Grapevine soils

Figure 5-12 shows the failure envelopes of the control and biopolymer treated Joe Pool soils at different dosages. The control soil showed the minimum shear strength. The shear strength of the treated soils increased with increase in biopolymer content up to the biopolymer dosage of 0.5%. The treated soil with biopolymer dosages of 1% showed shear strength lower than for the 0.5% dosage. The shear strength again increased for the 1.5% biopolymer dosage.

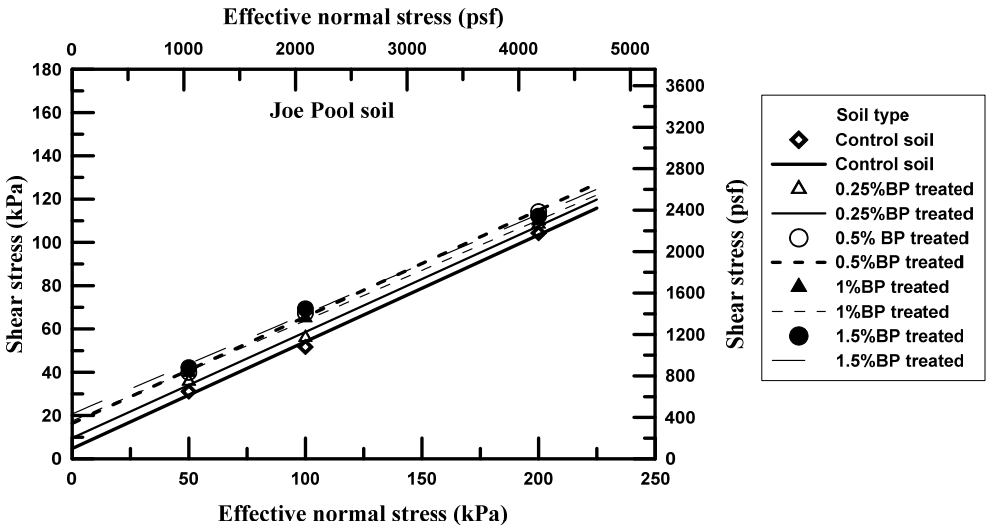

Figure 5-12 Failure envelopes of the Joe Pool soils

Figure 5-13 and Figure 5-14 respectively present the variation in the effective cohesions and friction angles with biopolymer dosages for both soils. The effective cohesion of the Grapevine soils increased abruptly up to a biopolymer dosage of 0.5% then it started decreasing gradually. The effective cohesion for 1% and 1.5% biopolymer contents were lower than that for 0.5% biopolymer. On the other hand, the friction angle remained almost at constant level over the range of the biopolymer contents. However, the friction angles for 0.25% and 0.5% dosages were slightly higher than that for the rest of the soils.

Similarly, the effective cohesion of the Joe Pool Soil showed a major increase up to 0.5% dosage and then it increased gradually at higher concentrations. The 1.5% dosage had the maximum effective cohesion. On the other hand, the friction angles of the biopolymer treated Joe Pool soils were

smaller than that of the control soil, even though the difference was fairly small. The friction angle showed a gradual downward trend with increase in the biopolymer dosage.

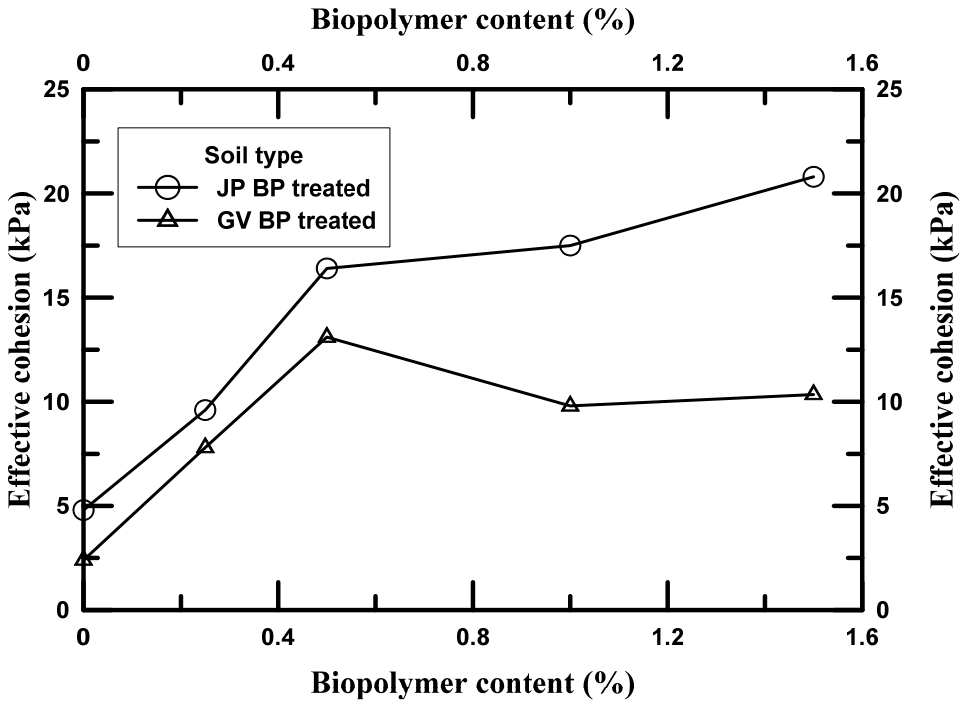

Figure 5-13 Variation in the effective cohesions of the Grapevine and Joe Pool soils at different dosages of biopolymers

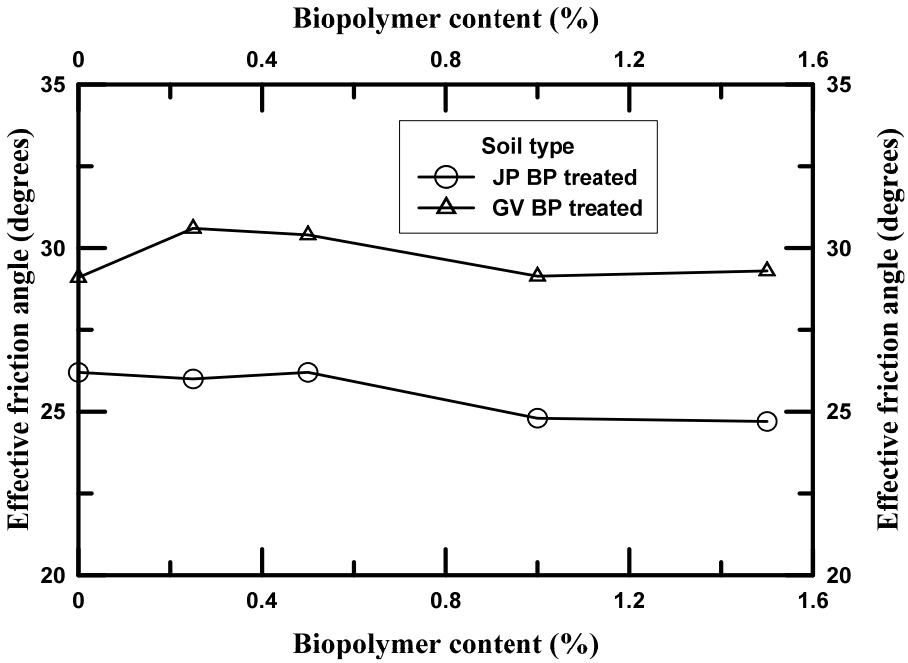

Figure 5-14 Variation in the effective friction angles of the Grapevine and Joe Pool soils at different dosages of biopolymers

5.2.2 Swell Pressure Test

Various past studies have explained about the moisture affinity and moisture holding capabilities of the biopolymers. When the guar gum was mixed with the water in UTA lab it showed excessive swelling forming a very thick paste like consistency as shown in Figure 5-15. Although the biopolymer mixed soils seemed to be advantageous in terms of shear strength, it might aggravate the swelling characteristics of the soils. Therefore swelling pressure tests were also conducted on the control and biopolymer treated specimens to assess their swelling characteristics.

Figure 5-15 Swelling of biopolymer upon adding water

The experiments were conducted in a computer controlled consolidation equipment available in UTA. The experimental setup and the equipment used in the test are shown in Figure 5-16. The equipment had a LVDT to monitor the vertical movements and a load cell to measure the pressure acting on the specimen. The sensors were connected to a computer through a data logger. The specimens were 25.4 mm in thickness and 63.5 mm in diameter. The specimens were confined in the consolidation rings to measure the one dimensional swell tests as shown in the inset of Figure 5-16. The setup was made ready and a very small seating load of 0.24 kPa (5 psf) was applied to make sure that a proper contact was made before beginning of the experiment. Water was added on the water bath to saturate the specimen and the swell pressure and time elapsed were taken immediately.

Figure 5-16 Experimental setup for the swell pressure tests

Unlike in the conventional load back swell pressure test, this equipment maintains the specimen thickness constant, thereby allowing the soil to exert swell pressure in the vertical direction. This option can be selected in the program while setting up the experiment as shown in Figure 5-17. The upward push applied by the soil was measured by the load cell and converted into pressure automatically. The swell pressure and elapsed time was displayed in the monitor as shown in Figure 5-18. As it can be seen from Figure 5-18 that the specimen did not experience vertical strain, meaning the thickness was constant during the test. The

advantage of this swell pressure test compared to the conventional swell pressure test is that the swell pressure can be measured continuously with respect to time instead of getting just one value. Thus, it makes possible to measure the effect of creep in the swell pressure of the soil. This benefit is not available in the conventional load back swell pressure test. Therefore this method was adopted in the current study.

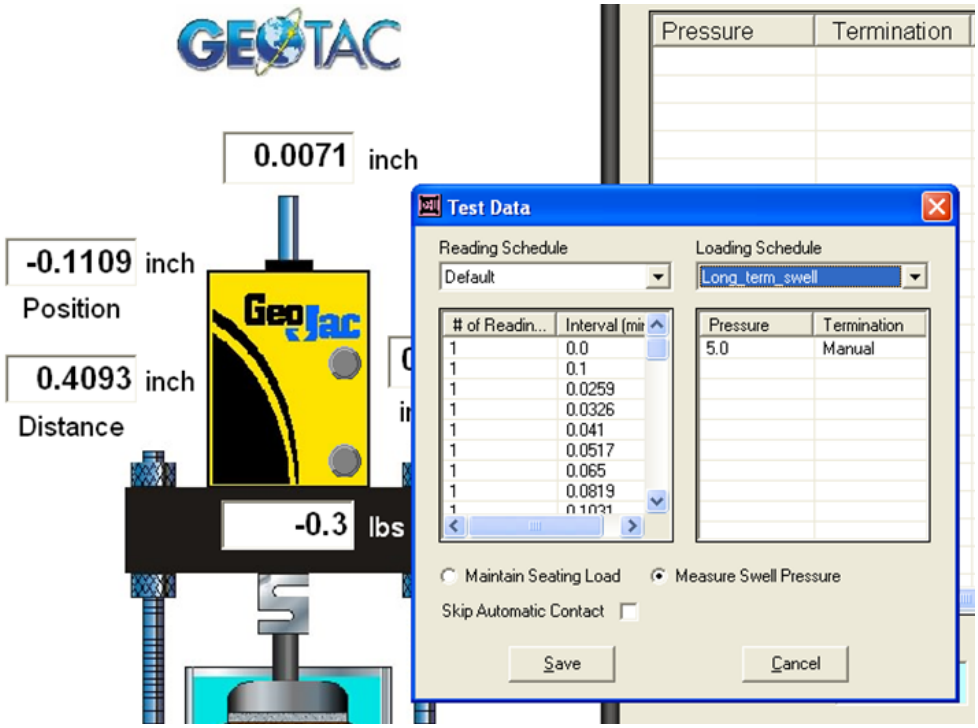

Figure 5-17 Screen shot showing the swell pressure measuring option

The swell pressure test results for the Grapevine soils are presented in Figure 5-19. Same for the Joe Pool soils are presented in Figure 5-20. The swell pressure started increasing immediately after the water was added. The swell pressure reached the peak value within 24 hours of adding water in each case. As

it can be seen from the figures, the swell pressures of the biopolymer treated soils were higher than the untreated soil. Furthermore, a higher concentration of biopolymer exhibited higher swell pressure. The peak swell pressures for 1 and 1.5% dosages were significantly higher than that for the 0.25 and 0.5% biopolymer concentrations. In all cases, the swell pressure decreased when the experiment was continued for long time. The reduction in the swell pressure was higher at higher dosages and lower at lower dosages. Thus it shows that the swell pressure does not sustain at constant level for a longer period under the loading conditions.

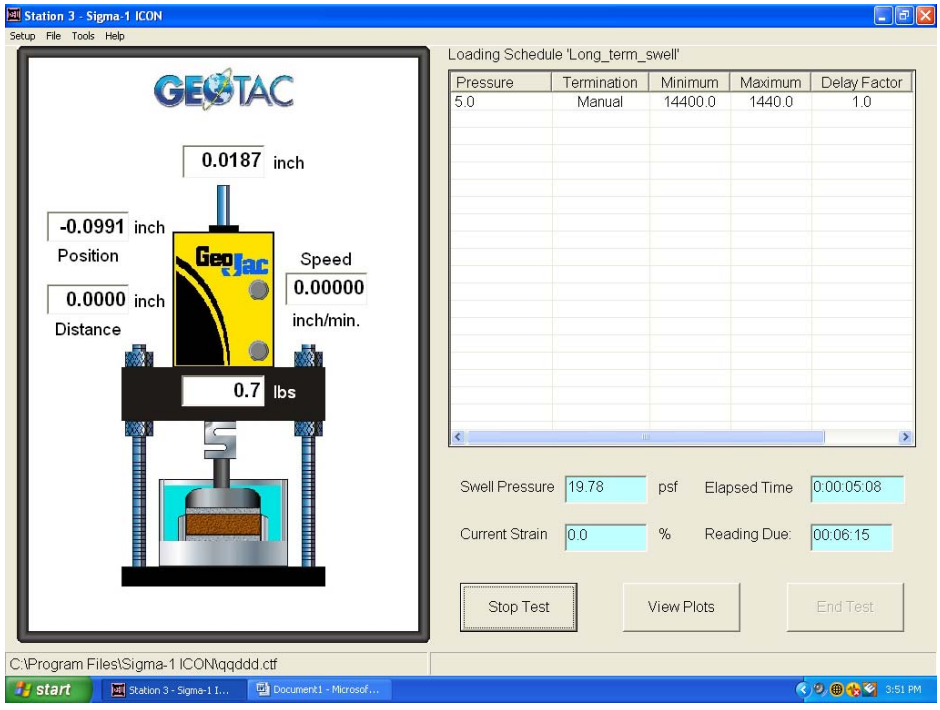

Figure 5-18 Screen shot showing the readings during the test

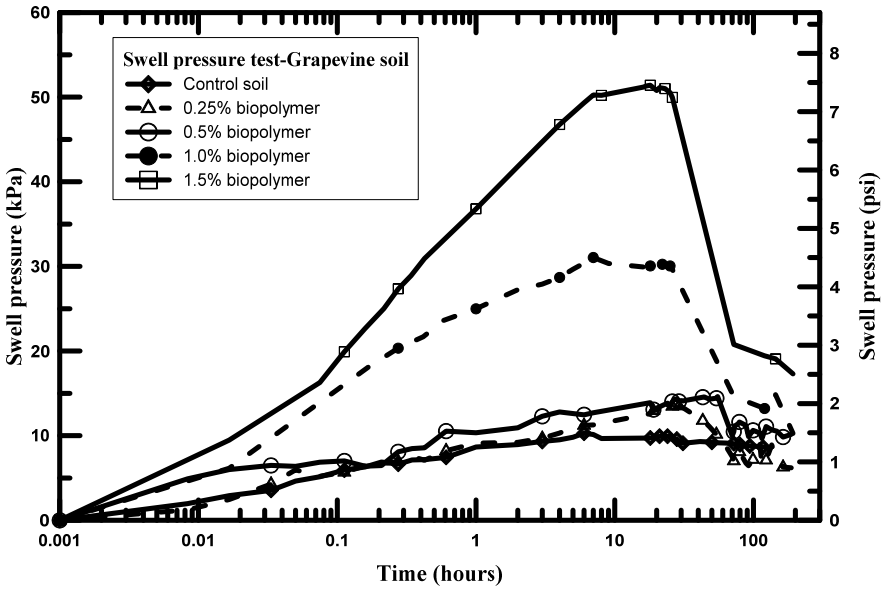

(a)

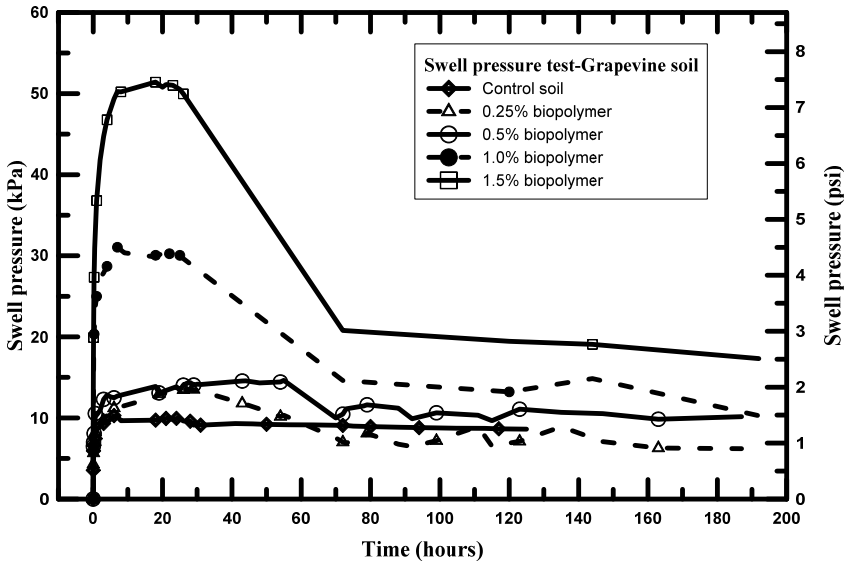

(b)

Figure 5-19 Swell pressure test results for Grapevine soils; (a) time in log scale, (b) time in decimal scale

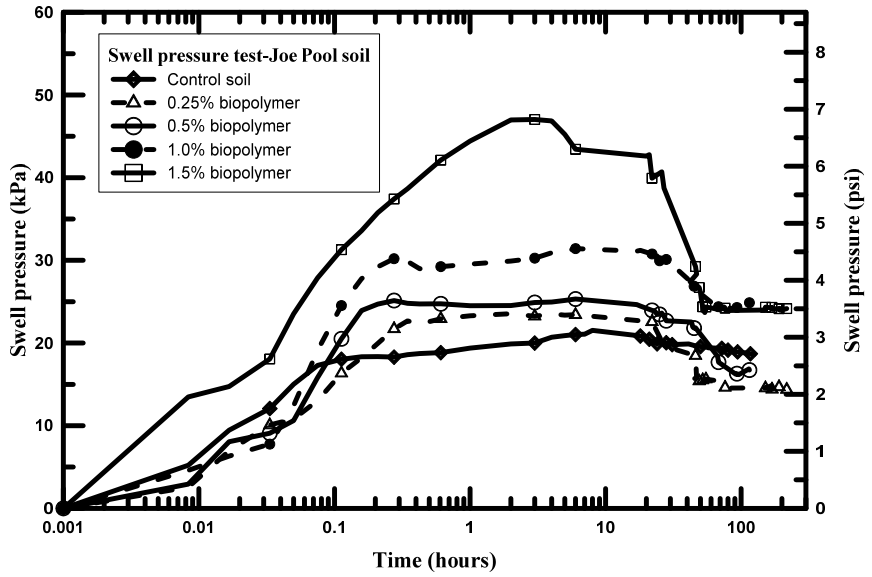

(a)

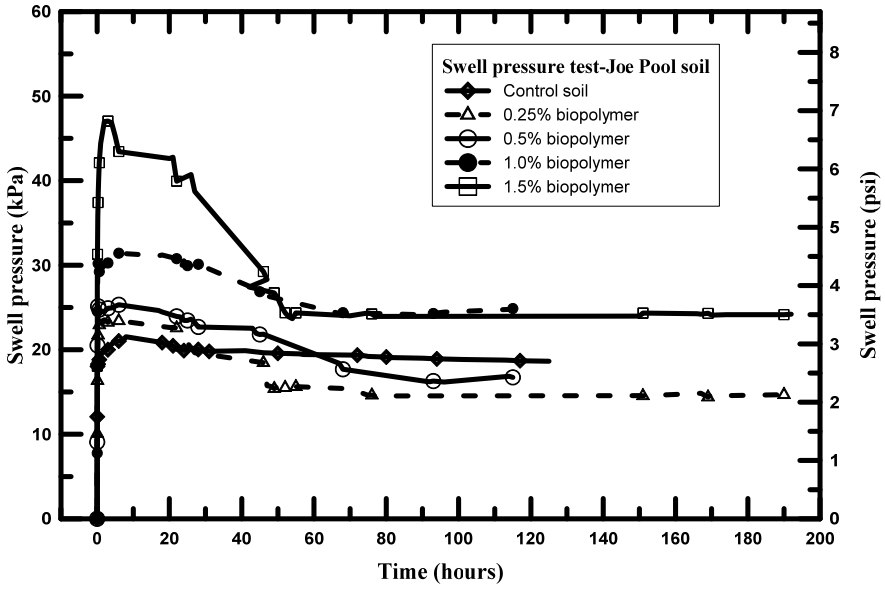

Figure 5-20 Swell pressure test results for Joe Pool soils; (a) time in log scale, (b) time in decimal scale

(b)

Considering both shear strength and swell pressure of the soils, 0.5% biopolymer was determined as the efficient dosage for both Grapevine and Joe Pool soils. The rest of the experiments conducted on biopolymer treated soils explained in this chapter are for 0.5% dosage for both of the soils.

5.3 Standard Proctor Test Results

The standard proctor tests were conducted on the 0.5% biopolymer treated soils. The compaction curves are as shown in Figure 5-21 and Figure 5-22. The optimum moisture content and maximum dry density for the biopolymer treated Grapevine soils were 19% and 1644 kg/m3 (102.6 pcf). Similarly the optimum moisture content and maximum dry density of the biopolymer treated Joe Pool soil were 24% and 1474 kg/m3 (92 pcf) respectively.

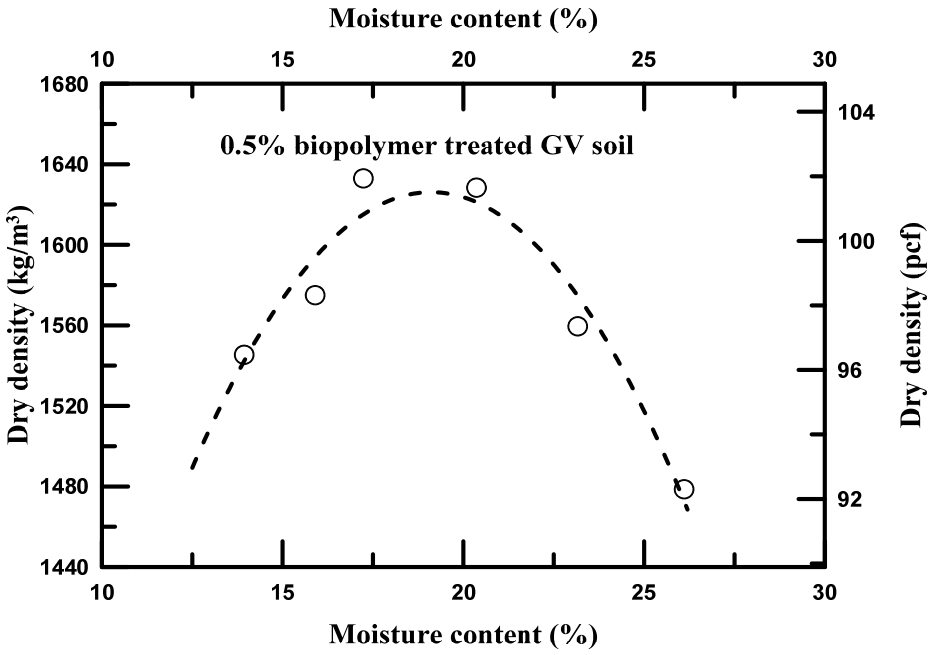

Figure 5-21 Compaction curve for biopolymer treated Grapevine soil

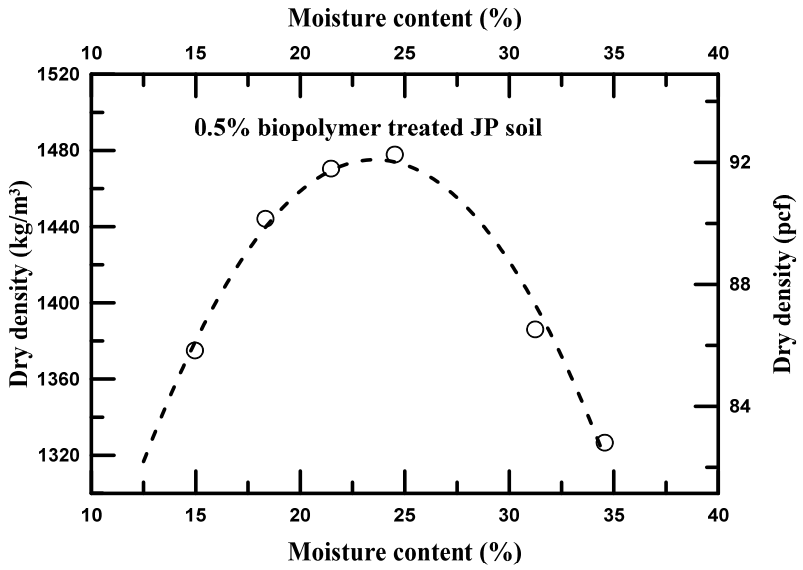

Figure 5-22 Compaction curve for biopolymer treated Joe Pool soil

5.4 Unconfined Compression Strength Test

The unconfined compression strength tests were conducted on the control and biopolymer treated specimens. The specimens were prepared by compacting the soil at 95% of maximum dry density and optimum moisture content condition. The specimen were prepared by static compression method. The specimens were allowed to cure for a period of 7 days before testing. The displacement controlled tests were conducted using a loading rate of 2.27 mm/min. The tests results are presented in Figure 5-23. The ultimate stress (q_u) of the control and biopolymer treated Grapevine soils were 84.4 and 112.4 kPa respectively. Similarly, the same for the Joe Pool soils were 125.4 and 159.6 kPa respectively. The resulting undrained cohesions (c_u) of the soils were 42.2, 56.2, 62.7, and 79.8 kPa

respectively for Grapevine control, biopolymer treated Grapevine, Joe Pool control and biopolymer treated Joe Pool soils respectively.

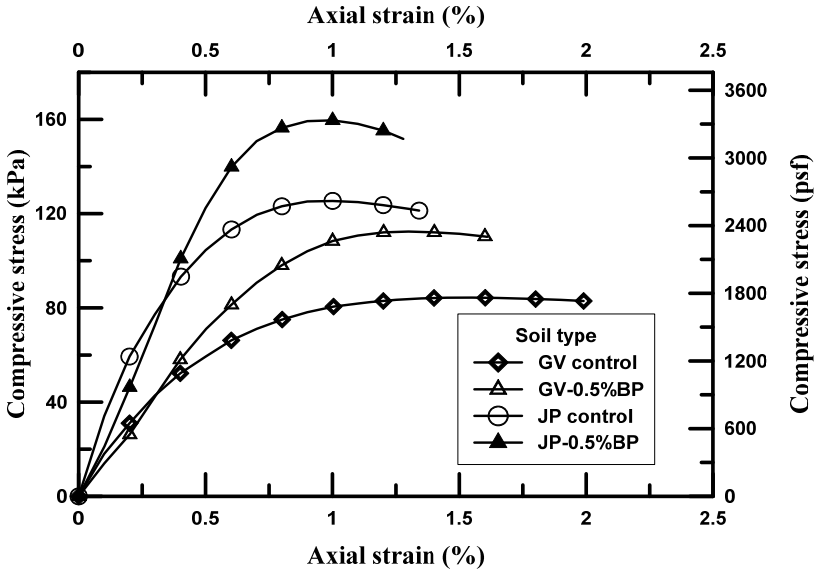

Figure 5-23 UCS test results of the control and treated soils

5.5 Direct Shear Test Results

The direct shear tests presented in section 5.2.1 did not involve the soils compacted at the optimum moisture contents of the biopolymer treated soils. Instead the biopolymer treated soils were compacted at the optimum moisture contents of the control soils. Once the maximum dry density and optimum moisture contents of the biopolymer treated soils were determined, the direct shear tests were conducted on the 0.5% biopolymer treated specimens compacted at 95% of MDD and OMC conditions. Figure 5-24 and Figure 5-25 show the results from the direct shear tests and failure envelope of the 0.5% biopolymer treated Grapevine soil. Resulting cohesion intercept and friction angles were 13.8

kPa and 33.8º respectively. Similarly, Figure 5-26 and Figure 5-27 show the results from the direct shear tests and failure envelope of the 0.5% biopolymer treated Joe Pool soil. Resulting cohesion intercept and friction angles were 16.9 kPa and 28.2º respectively.

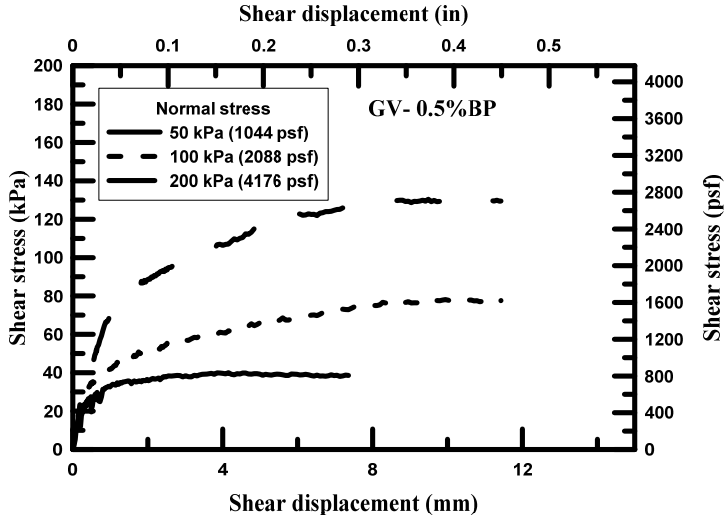

Figure 5-24 DS test results for biopolymer treated Grapevine soil

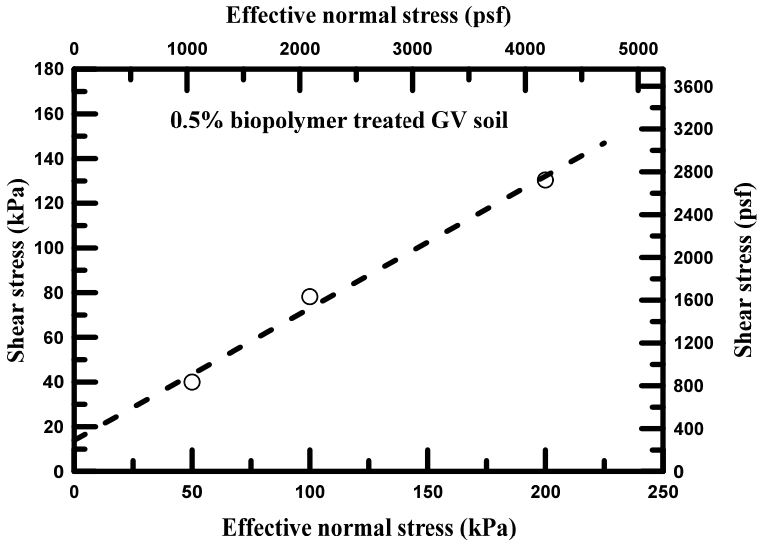

Figure 5-25 Failure envelope for the biopolymer treated Grapevine soil

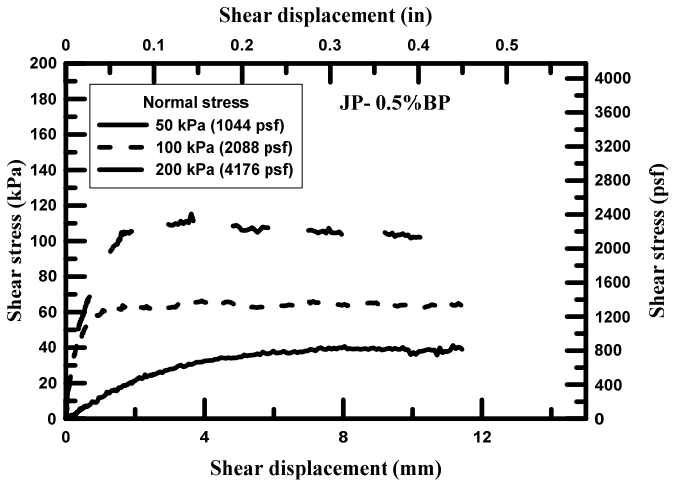

Figure 5-26 DS test results for biopolymer treated Joe Pool soil

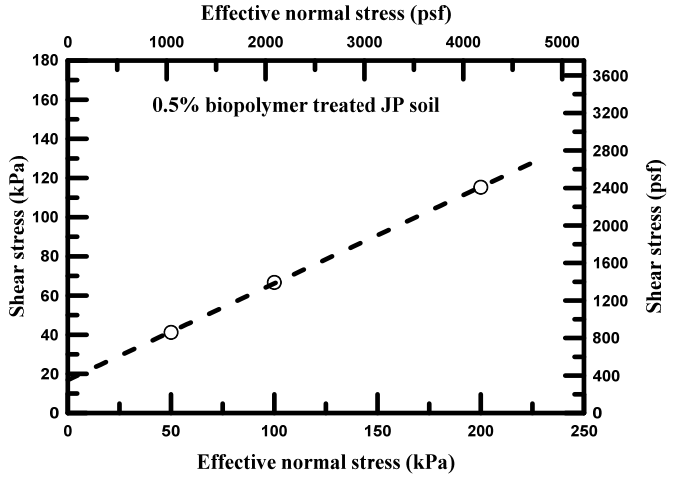

Figure 5-27 Failure envelope for the biopolymer treated Joe Pool soil

5.6 Torsional Ring Shear Test

The fully softened and residual shear strengths of the biopolymer treated specimens were determined using the TRS equipment. The procedure for the test is explained in Chapter 3. The tests were conducted at three effective normal stresses of 50, 100, and 200 kPa. The slurry soils were consolidated up to required

stress level using a stress increment ratio of unity. Then the soil was sheared at a displacement rate of 0.02 mm/min. The test was continued for a longer period of time to allow the soil to reach its residual strength. Thus, the fully softened and residual shear strengths were determined from the same sets of tests. The peak shear stresses give the fully softened shear strength. The residual shear strength envelope is determined from the shear stresses at the end of the experiments. Figure 5-28 and Figure 5-29 shows the TRS results for Grapevine and Joe Pool soils respectively.

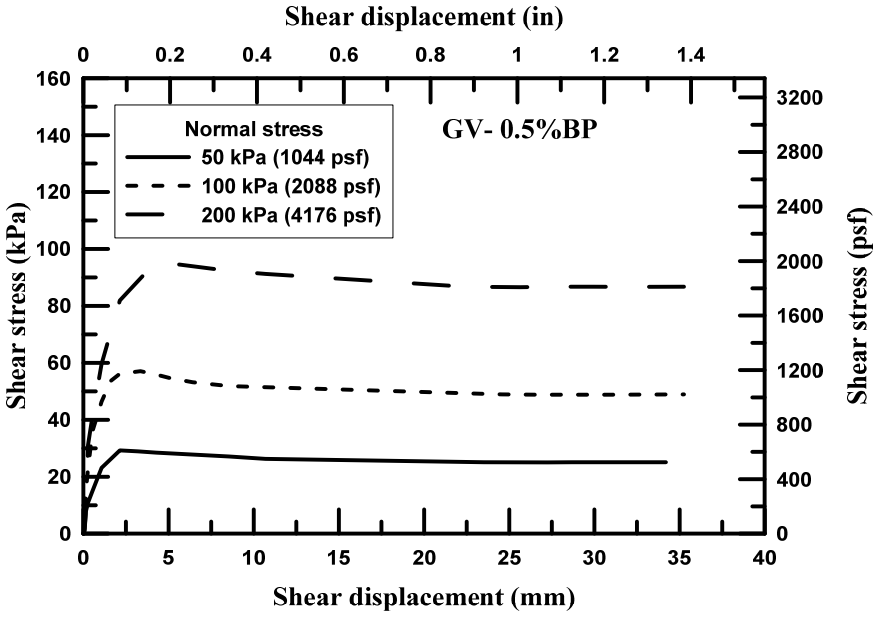

Figure 5-28 TRS results for biopolymer treated Grapevine soil

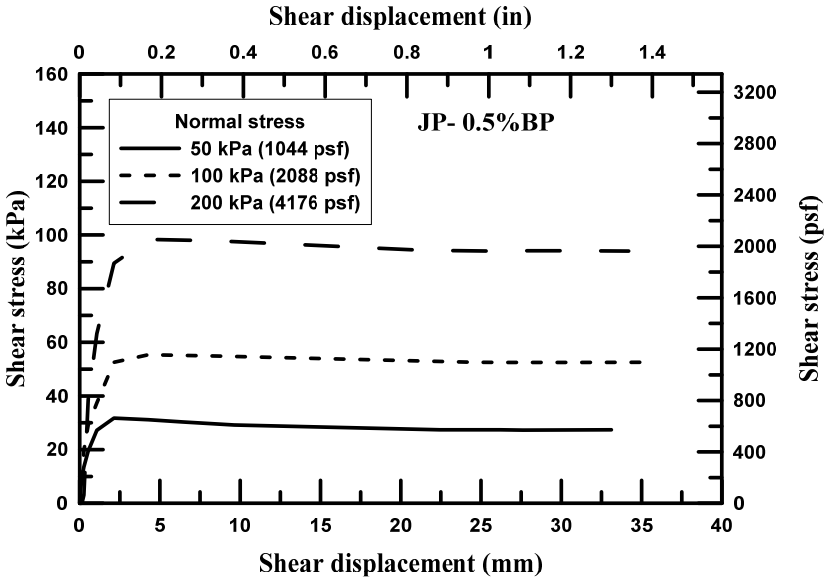

Figure 5-29 TRS results for biopolymer treated Joe Pool soil

It is evident from Figure 5-28 and Figure 5-29 that the shear stress abruptly increased with the increase in the displacement at the early stages of the shearing. The peak shear resistance was occurred before reaching 5 mm of displacement in each case. Then the shear resistance gradually decreased as the test continued. The shear resistance of the soils came to a fairly constant level for larger shear displacement. The shear resistance at this state is marked as the residual shear stress. The fully softened and residual shear strength envelopes are presented in Figure 5-30 and Figure 5-31 for Grapevine and Joe Pool soils respectively. The summary of the TRS test results are presented in Table 5-1.

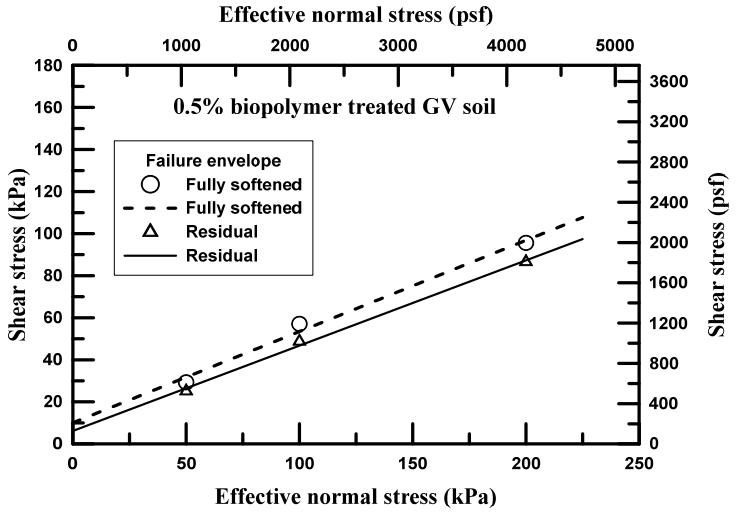

Figure 5-30 FSS and residual shear strength envelopes for biopolymer treated Grapevine soil

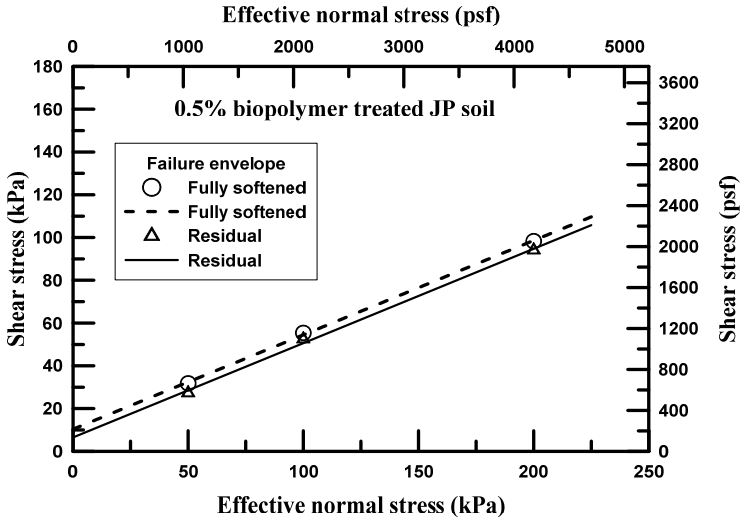

Figure 5-31 FSS and residual shear strength envelopes for biopolymer treated Joe Pool soil

Table 5-1 Summary of TRS test results on biopolymer treated soils

Soil	Fully softened		Residual	
	c'_{fs} (kPa)	φ'_{fs} (degrees)	c'_r (kPa)	φ'_r (degrees)
GV BP	10.0	23.4	6.2	22.0
JP BP	10.3	23.8	6.5	23.8

5.7 Direct Shear Test for Fully Softened Shear Strength

The fully softened shear strength is generally determined using torsional ring shear device. However, the current state of the art for FSS testing involves using either direct shear equipment or torsional ring shear equipment (Le, 2013). Le (2013) conducted a total of 120 fully softened shear strength tests. Out of that, 80 tests were conducted using direct shear machine and only 40 were conducted in TRS machine. In the current study, the fully softened shear strength of the biopolymer treated soils were also determined using the direct shear tests. Similar to the TRS test, the tests were conducted at the effective normal stresses of 50, 100 and 200 kPa. The biopolymer and soil mix was first brought to liquid consistency by adding deionized water. Then the soil was transferred into the shear mold. The specimen was tapped gently to remove any entrapped air bubbles. Then the normal stress was applied starting form 12.5 kPa then increased to required level by using a stress increment ratio of unity. After the consolidation was completed for the final normal stress shearing of the soil was started. The shearing rate was kept similar to that used in the TRS test (i.e. 0.02 mm/min). The

results from the tests are presented in Figure 5-32 and Figure 5-33 for Grapevine and Joe Pool soils respectively. Similarly, the failure envelopes for the soils are presented in Figure 5-34 and Figure 5-35 respectively. The fully softened cohesion and friction angle of the biopolymer treated Grapevine soil were 11.9 kPa and 30.9^0 respectively. Similarly, the fully softened cohesion and friction angle of the biopolymer treated Joe Pool soil were 12.6 kPa and 26.6^0 respectively.

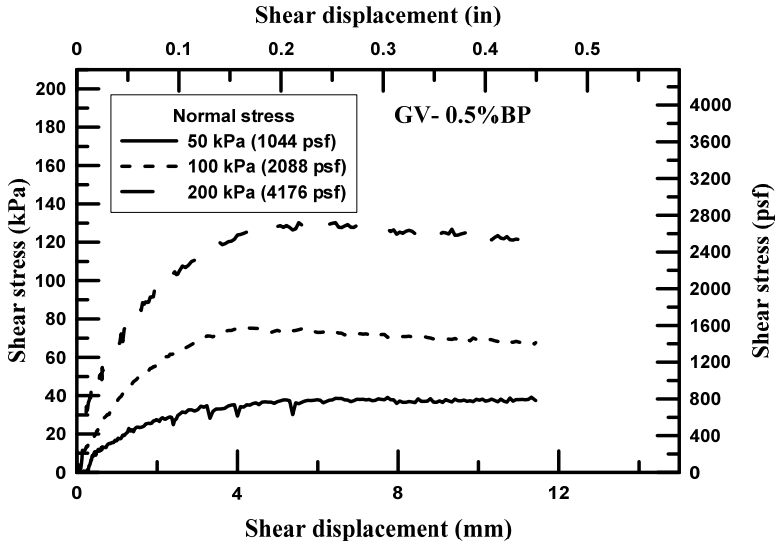

Figure 5-32 DS test results on Biopolymer treated Grapevine soil for fully softened shear strength

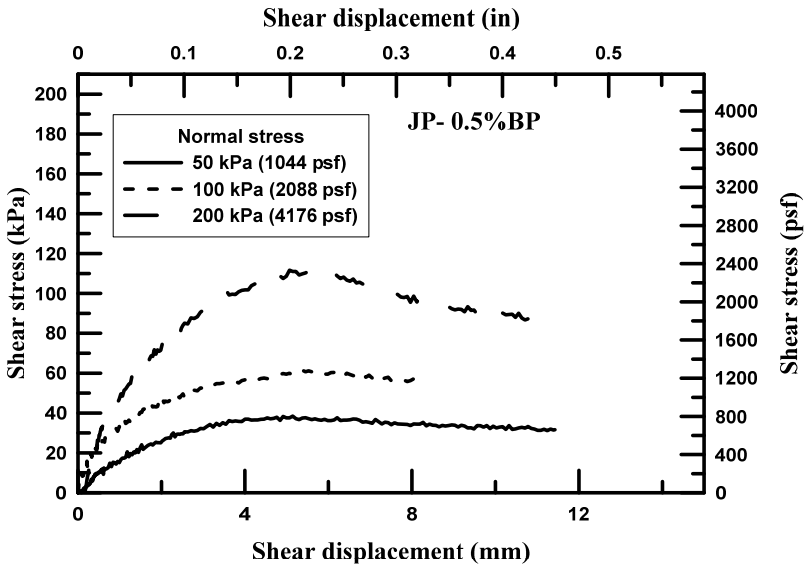

Figure 5-33 DS test results on Biopolymer treated Joe Pool soil for fully softened shear strength

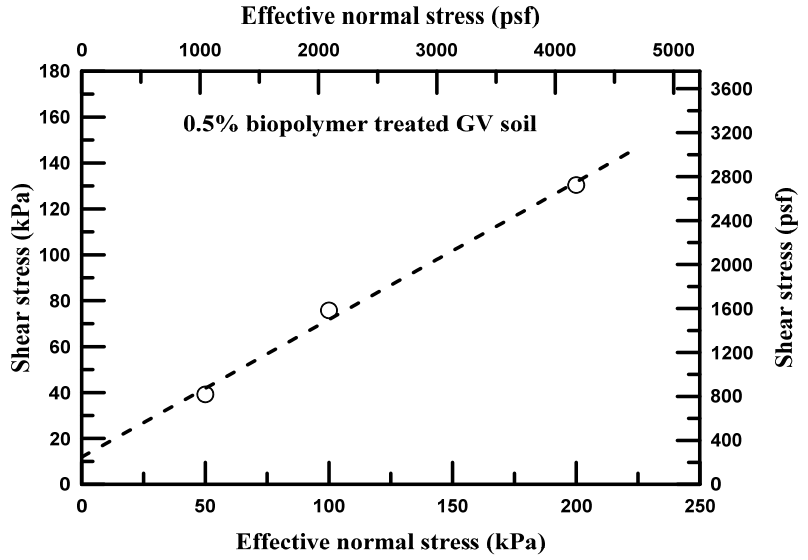

Figure 5-34 Fully softened shear strength envelope for biopolymer treated Grapevine soil from DS test

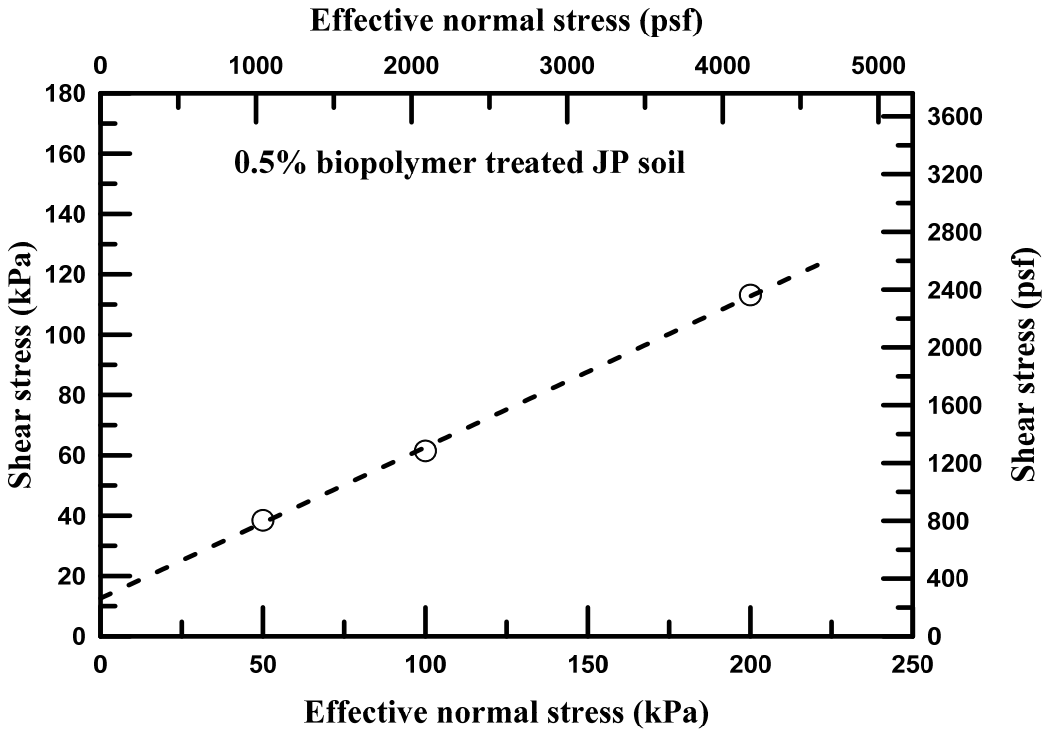

Figure 5-35 Fully softened shear strength envelope for biopolymer treated Joe Pool soil from DS test

5.8 Comparison of Biopolymer Treatment with Other Treatment Methods

5.8.1 Comparison of Shear Strength

The shear strengths of the biopolymer treated soils were compared with the same of untreated, 8%lime treated and 8%lime plus 0.15%fiber treated soils. Last two treated soils were determined by previous researchers; McCleskey (2005), Dronamraju (2008), and Le (2013). The 8%lime treatment is termed 'lime' treatment and 8%lime plus 0.15%fiber treatment is termed as 'lime+fiber' treatment in the subsequent discussion unless otherwise noted. Table 5-2 shows

the comparison between the shear strengths between different treatments for Grapevine soil. Similarly, Table 5-3 shows the same for the Joe Pool soil. The comparisons of the undrained, fully softened, and residual cohesions of different treatments for Grapevine and Joe Pool soils are shown in Figure 5-36 and Figure 5-37. Also, the comparisons of the fully softened and residual friction angles of different treatments for Grapevine and Joe Pool soils are shown in Figure 5-38 and Figure 5-39.

The undrained shear strength of the biopolymer treatment was observed to be slightly higher than the control and lime+fiber treatment for both soils. However, it was considerably smaller compared to the lime treatment. Similarly, the fully softened and residual cohesions of the biopolymer treatment were higher than the control but smaller than both lime treatment and lime+fiber treatment for both Grapevine and Joe Pool soils. In terms of friction angle, the biopolymer treatment did not show a sizeable improvement. Instead, the friction angles for the fully softened cases were smaller than the control soils. Only small increase in residual friction angle was observed. On the other hand, the friction angles of the lime and lime+fiber treatments were significantly higher than the control as well as biopolymer treatment. This is attributed to lime treatment modification of cohesive soils into aggregated cemented specimens that exhibit higher friction angles.

Thus, from the shear strength point of view, biopolymer treatment showed moderate improvements when compared to the control soil. The increase in shear strength can be helpful in solving the surficial slope failure problems in the dam slopes. It can be useful in places where chemical treatments are not suitable due to environmental concerns. However, since the dam slopes often experience surficial slope failure triggered due to desiccation cracking, it is important to study the shrinkage characteristics of the biopolymer treatment before coming to a strong conclusion.

Table 5-2 Comparison of shear strengths of different treatment methods for Grapevine soil

Soil treatment method	Peak Shear strength			Fully Softened		Residual	
	c_u (kPa)	c' (kPa)	φ' (degrees)	c'_{fs} (kPa)	φ'_{fs} (degrees)	c'_r (kPa)	φ'_r (degrees)
Control	42.2	2.4	29	0	34.8	0	18
Biopolymer	56.2	13.8	33.8	10	23.4	6.2	22
Lime	94.5	-	-	10	38.9	12.9	38
Lime+fiber	46.9	-	-	27.2	40	16.3	40

Table 5-3 Comparison of shear strengths of different treatment methods for Joe Pool soil

Soil treatment method	Peak Shear strength			Fully Softened		Residual	
	c_u (kPa)	c' (kPa)	φ' (degrees)	c'_{fs} (kPa)	φ'_{fs} (degrees)	c'_r (kPa)	φ'_r (degrees)
Control	62.7	2.4	29	0	27	0	20
Biopolymer	79.8	16.9	28.2	10.3	23.8	6.5	23.8
Lime	140.5	-	-	21.9	36.6	12.5	36
Lime+fiber	55.4	-	-	29	35.4	16.8	39

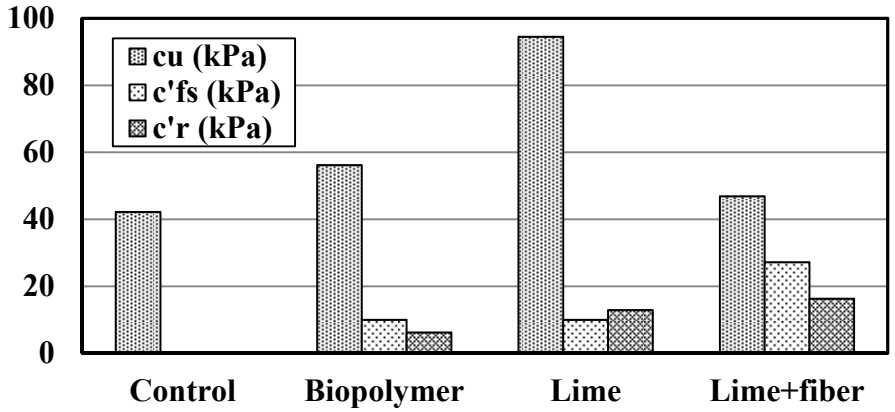

Figure 5-36 Comparisons of the undrained, fully softened, and residual cohesions of different treatments for Grapevine soil

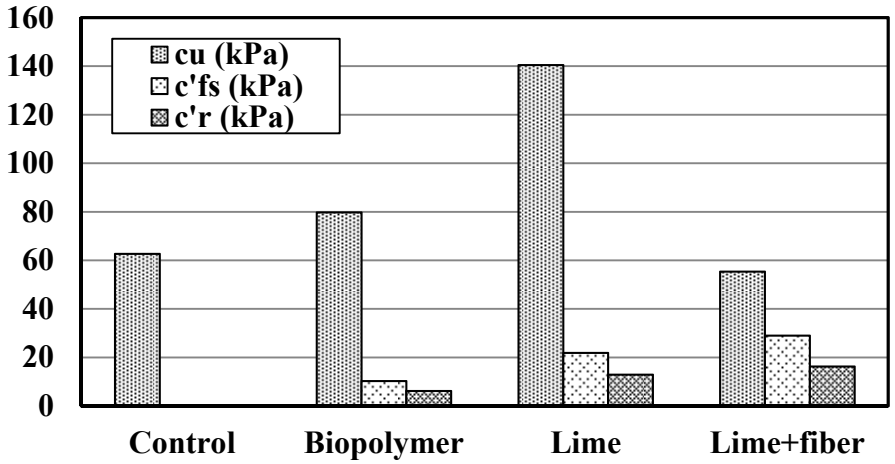

Figure 5-37 Comparisons of the undrained, fully softened, and residual cohesions of different treatments for Joe Pool soil

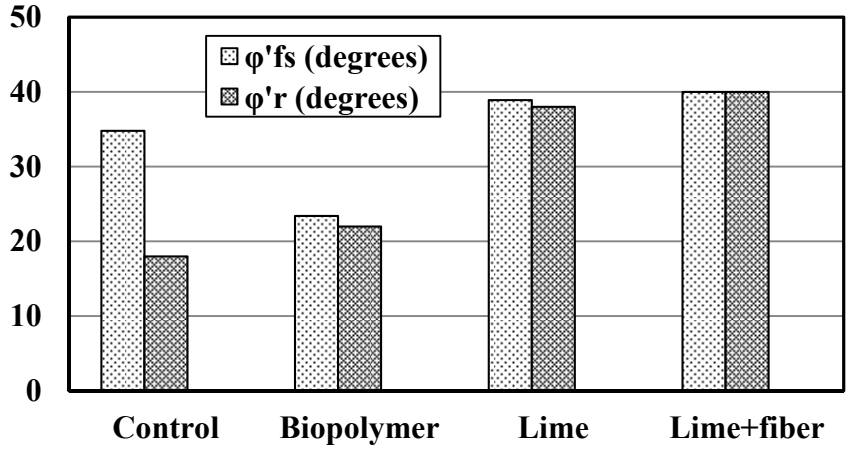

Figure 5-38 Comparisons of the fully softened and residual friction angles of different treatments for Grapevine soil

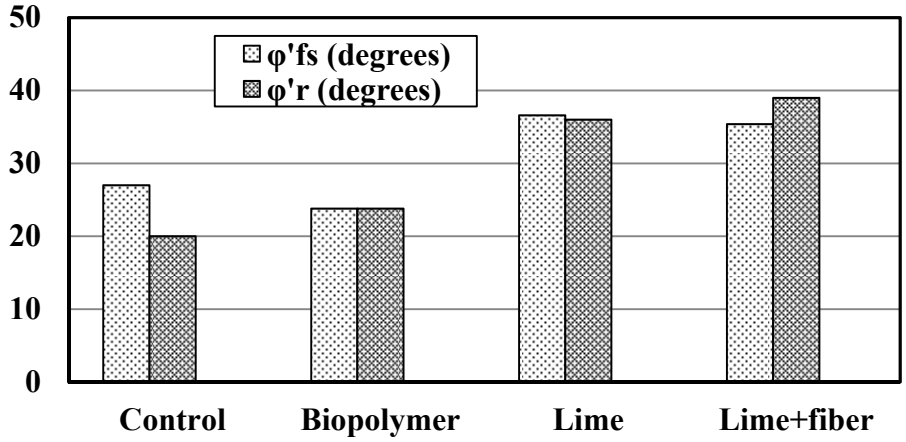

Figure 5-39 Comparisons of the fully softened and residual friction angles of different treatments for Joe Pool soil

5.8.2 Comparison of Linear Shrinkage Strain

Linear shrinkage bar tests were conducted on the biopolymer treated as well as lime treated, and lime+fiber treated Grapevine and Joe Pool soils. The

tests were conducted similar to the procedures described in Chapter 3. Figure 5-40 shows the biopolymer treated Grapevine and Joe Pool soil specimens at the end of the test. The soils exhibited a considerable amount of shrinkage and cracking. On the other hand, Figure 5-41 and Figure 5-42 show the lime treated and lime+fiber treated soil specimens respectively that experienced small shrinkage and no cracking. The linear shrinkage strains results are presented in Table 5-4. Similarly, comparisons of the shrinkage strains are presented graphically in Figure 5-43 and Figure 5-44 for Grapevine and Joe Pool soils respectively.

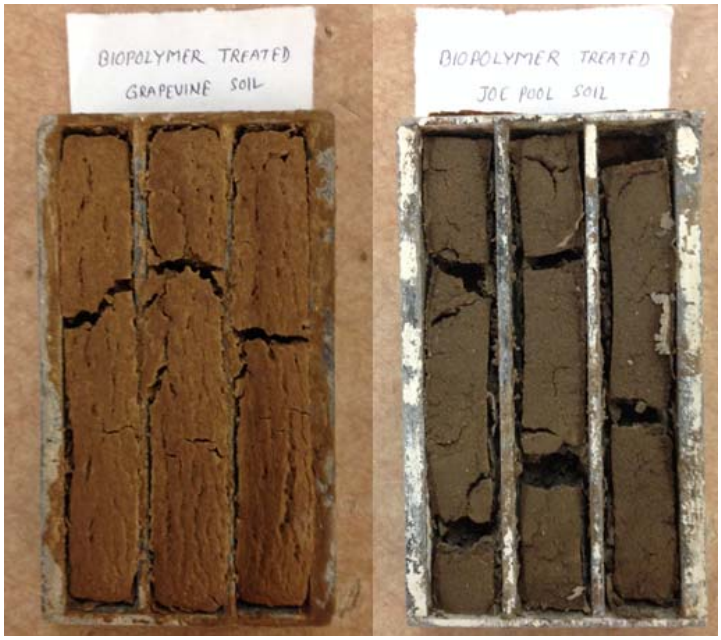

Figure 5-40 Linear shrinkage bar test on the biopolymer treated soils

Figure 5-41 Linear shrinkage bar test on lime treated soils

Figure 5-42 Linear shrinkage bar test on the lime+fiber treated soils

Table 5-4 Linear shrinkage strains of control and treated soils

Treatment type	Avg. linear shrinkage strain (%)	
	Grapevine soil	Joe Pool Soil
Control	9.1	12.8
Biopolymer	7.1	10.1
Lime	2.8	5.2
Lime+fiber	1.9	2.3

The control soil, biopolymer treated soil, lime treated soil, and lime+fiber treated soils had exhibited the larger to smaller shrinkage strains in that order. The shrinkage strains for the lime and lime treated soils were very small when compared to the control soils. Biopolymer treated soils showed a higher shrinkage potential compared to other treatments.

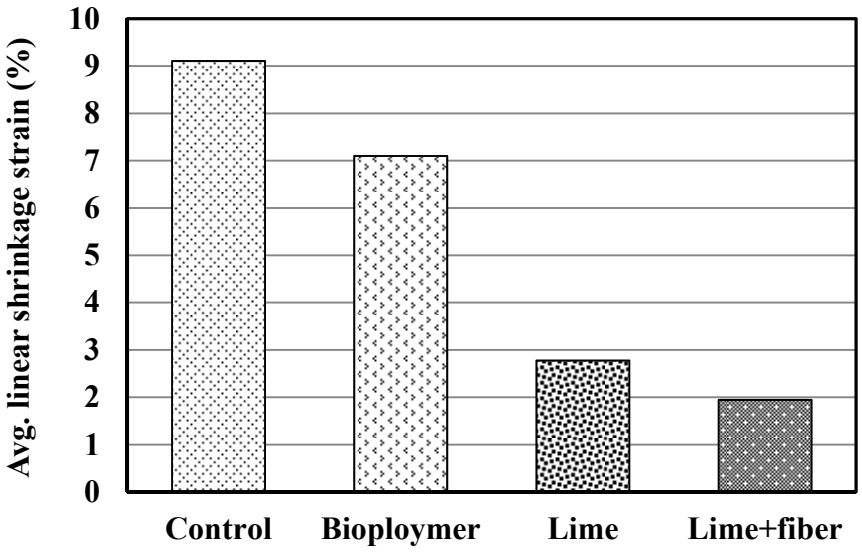

Figure 5-43 Comparison of linear shrinkage strains of different treatments for Grapevine soil

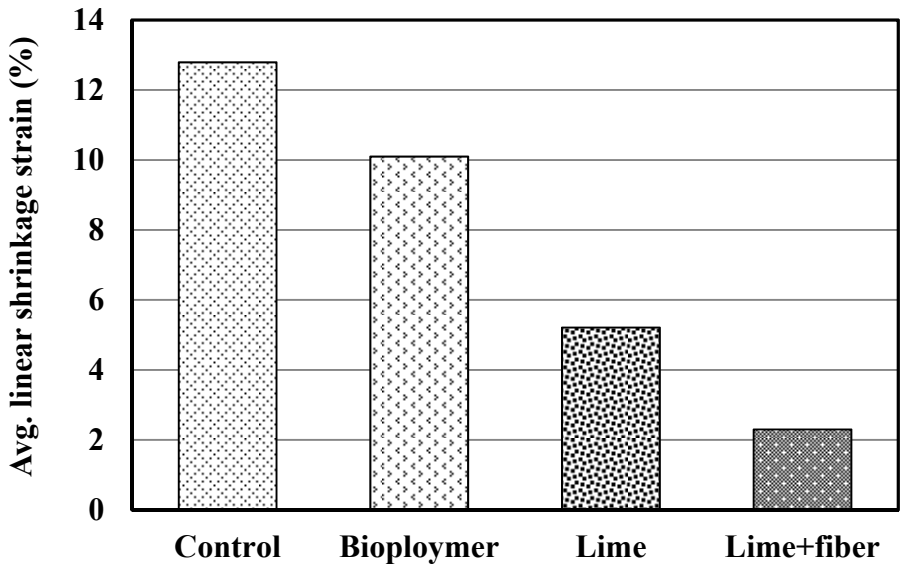

Figure 5-44 Comparison of linear shrinkage strains of different treatments for Joe Pool soil

5.8.3 Comparison of Indirect Tensile Strengths

Indirect tensile strengths tests were conducted following the procedures outlines in Chapter 3. The tests were conducted on the dry specimens initially molded at slurry state. The summary of the IDT test results of the slurry soil specimens are presented in the Table 5-5 and Table 5-6 respectively for Grapevine and Joe Pool soils. It can be observed that the control soils exhibited the highest tensile strength. The tensile strengths of biopolymer treated, lime treated, and lime+fiber treated soils were larger to smaller in the order. Soils treated with lime and lime+fiber lost the tensile strength dramatically compared to control soil. The lime+fiber treated soils had less than 5% of respective control

soils' shear strengths. Similarly, the lime treated Grapevine and Joe pool soils showed only 28% and 25% tensile strength of respective control soils.

Table 5-5 Tensile strengths of Grapevine soil with different treatments

Soil treatment type	Moisture content range (%)	No. of specimens	Mean IDT (kPa)	Standard deviation (kPa)
Control	3.9 - 5.0	10	381.8	32.3
Biopolymer	2.3 - 3.4	6	307.0	40.1
Lime	3.7 - 5.3	3	107.8	7.9
Lime+fiber	2.9 - 3.1	4	16.8	4.1

Table 5-6 Tensile strengths of Joe Pool soil with different treatments

Soil treatment type	Moisture content range (%)	No. of specimens	Mean IDT (kPa)	Standard deviation (kPa)
Control	4.4 - 5.8	10	877.6	107.14
Biopolymer	3.7 - 4.5	5	732.1	91.9
Lime	3.3 - 3.9	3	218.9	4.6
Lime+fiber	4.8 - 5.0	5	20.4	1.9

Additional IDT tests were conducted on the treated soils in order to study the tensile strengths of compacted specimens. The specimens were compacted at 95% of maximum dry density and optimum moisture content conditions. Compacted specimens were prepared using static compression method. The tests were conducted similar to that of slurry specimens. The summary of the IDT test results of the compacted specimens are presented in Table 5-7 and Table 5-8 for Grapevine and Joe Pool soils respectively. Unlike the slurry soils, the compacted soils showed increase in tensile strengths when the soils were treated with the

modifiers. The lime+fiber treatment showed the maximum increase in the tensile strength. Lime treated soils showed tensile strengths similar to the lime+fiber treated soils. The biopolymer treated specimens also showed considerable improvement, however, the tensile strengths were smaller than the treatments using lime. Thus, the slurry and compacted soils demonstrated completely different tensile strengths characteristics. Slurry soils showed reduction and compacted soils showed increment in the tensile strengths.

Table 5-7 Tensile strengths of compacted specimens for Grapevine soil

Soil treatment type	Moisture content range (%)	No. of specimens	Mean IDT (kPa)	Standard deviation (kPa)
Control	18.9 - 20.0	10	19.0	1.3
Biopolymer	14.5 - 15.1	6	30.0	5.1
Lime	17.8 - 18.8	3	30.4	2.7
Lime+fiber	16.7 - 17.8	4	33.3	2.2

Table 5-8 Tensile strengths of compacted specimens for Joe Pool soil

Soil treatment type	Moisture content range (%)	No. of specimens	Mean IDT (kPa)	Standard deviation (kPa)
Control	11.6 - 13.7	10	21.2	1.3
Biopolymer	21.1 - 23.4	6	37.6	3.7
Lime	23.6 - 25.1	3	44.7	5.0
Lime+fiber	23.0 - 24.4	4	47.8	3.0

5.8.4 Comparison of Shrinkage Induced Pressure

The shrinkage characterization of the treated soils was also obtained by performing the shrinkage induced pressure tests that are described in the previous chapter. SIP tests were conducted on the biopolymer, lime, and lime+fiber treated soils from both Grapevine and Joe Pool dam sites to determine their shrinkage potential and internal stress evolution during drying. The procedure similar to the one presented in Chapter 3 was followed in the tests. Three replicate tests were conducted on each type of treated soil for both of the dam soils.

The variations in moisture content as well as radial, vertical, and volumetric shrinkage strains with time of the biopolymer treated Grapevine soil are shown in Figure 5-45. Similarly, the evolution of SIPs with time is presented in Figure 5-46. Since the soil remains fairly saturated at the beginning of the experiment, no SIP was recorded at the early stages. The SIP started building up nearly after 30 hours of the beginning of the tests. In test 1, the SIP increased continuously and reached the peak at the end of the test. The SIP increased in the similar fashion for tests 2 and 3 also, but the peak is reached few hours before the end of the tests. The peak SIPs are 38.4, 41.3 and 40.4 kPa for tests 1, 2 and, 3, respectively. The final radial, vertical, and volumetric strains are, 12.5, 16.2, and 41.2%, respectively. Similarly, the moisture content of the soil was 5.8% at the end of the test.

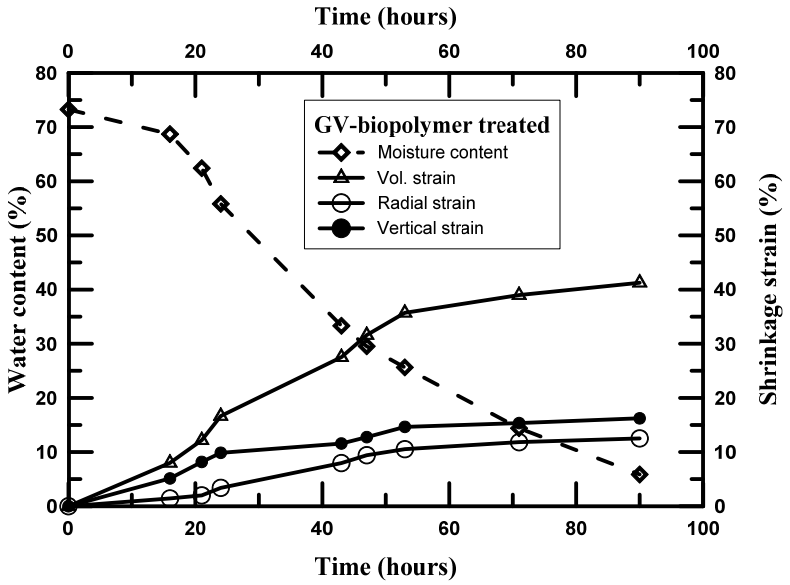

Figure 5-45 Time vs. moisture content and shrinkage strains plot of biopolymer treated Grapevine soil

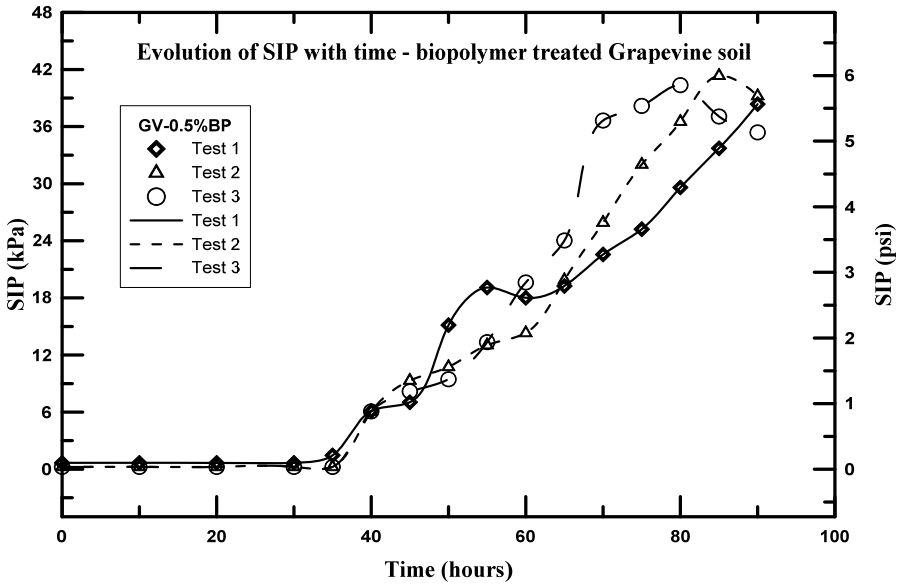

Figure 5-46 SIP test results for biopolymer treated Grapevine soil

The variations in moisture content as well as radial, vertical, and volumetric shrinkage strains with time of the biopolymer treated Joe Pool soil are shown in Figure 5-47. Similarly, the evolution of SIPs with time is presented in Figure 5-48. The SIP started building up nearly after 15 hours in tests 1 and 3, and 25 hours in test 2. The SIP increased gradually with time and reached the peak few hours before the end of the test. In tests 1 and 3 SIP remained fairly constant after attaining the peak. Whereas, there was a sudden drop in SIP after the peak was reached in test 2 due to formation of a crack. The peak SIPs are 61.7, 73.7 and 61.4 kPa for tests 1, 2 and, 3, respectively. The final radial, vertical, and volumetric strains are, 16.8, 19.6, and 53.3%, respectively. Similarly, the moisture content of the soil was 4.5% at the end of the test.

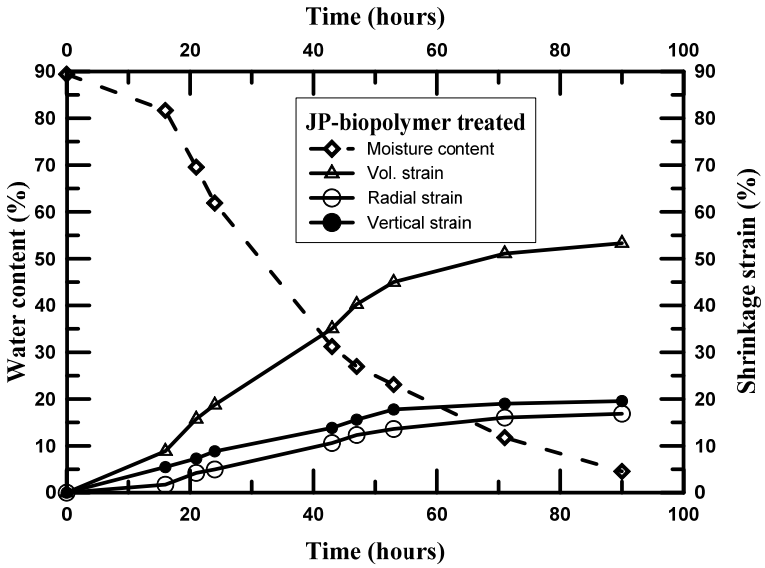

Figure 5-47 Time vs. moisture content and shrinkage strains plot of biopolymer treated Joe Pool soil

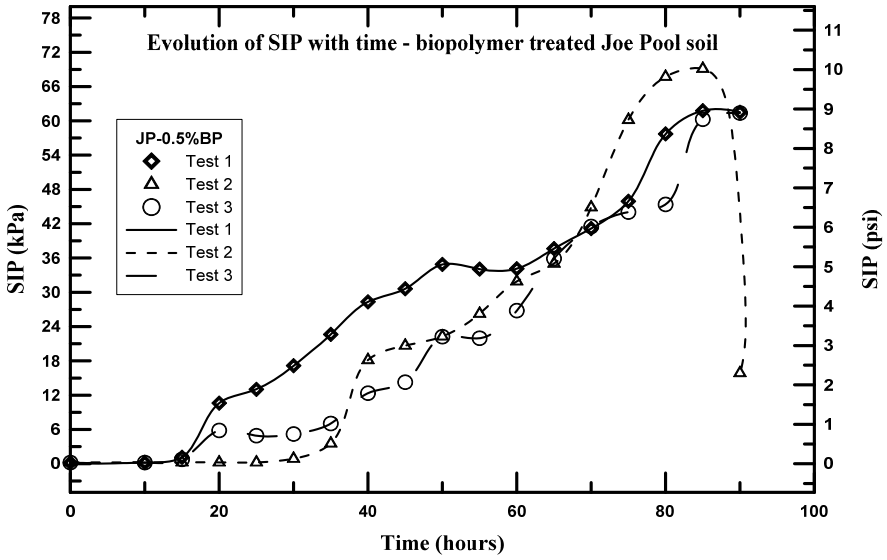

Figure 5-48 SIP test results for biopolymer treated Joe Pool soil

The variations in moisture content as well as radial, vertical, and volumetric shrinkage strains with time of the lime treated Grapevine soil are shown in Figure 5-49. Similarly, the evolution of SIPs with time is presented in Figure 5-50. Only test 1 could show a very small SIP and tests 2 and 3 did not show any increase in the SIP throughout the test. The peak SIP from the test 1 was 1.9 kPa. The final radial, vertical, and volumetric strains are, 7.2, 10.7, and 25.0%, respectively. Similarly, the moisture content of the soil was 2.6% at the end of the test.

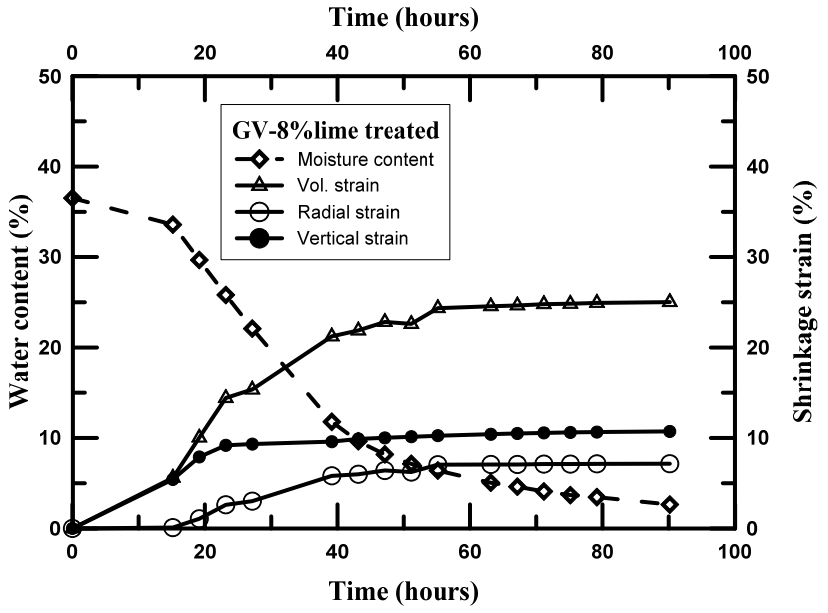

Figure 5-49 Time vs. moisture content and shrinkage strains plot of lime treated Grapevine soil

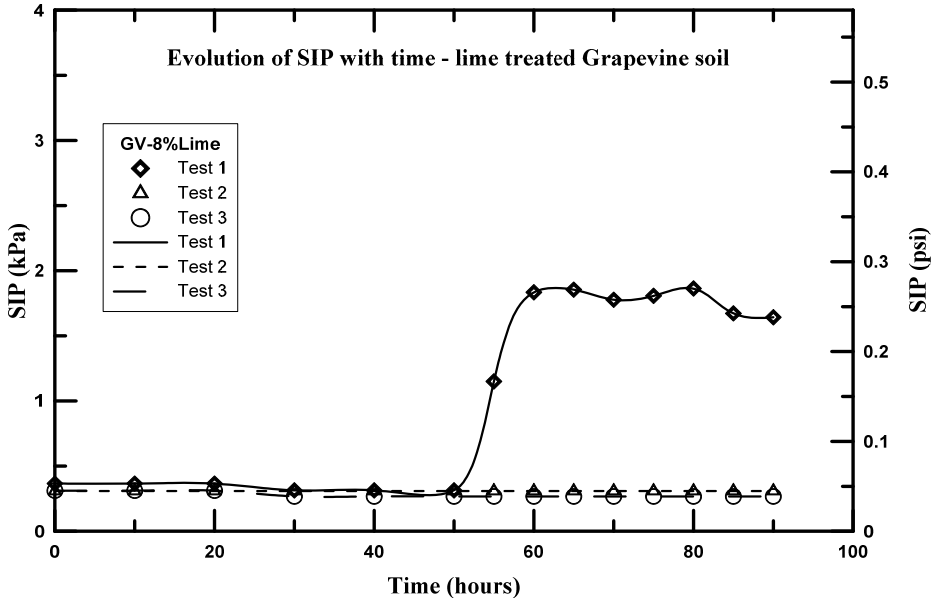

Figure 5-50 SIP test results for lime treated Grapevine soil

The variations in moisture content as well as radial, vertical, and volumetric shrinkage strains with time of the lime treated Joe Pool soil are shown in Figure 5-51. Similarly, the evolution of SIPs with time is presented in Figure 5-52. SIP start increasing after 10 hours in test 1 and after 25 hours in tests 2 and 3. Peak SIPs for the tests 1, 2, and 3 were 14.4, 12.4 and 13.8 kPa respectively. The final radial, vertical, and volumetric strains were, 7.9, 12.9, and 28.7% respectively. Similarly, the moisture content of the soil was 8.0% at the end of the test.

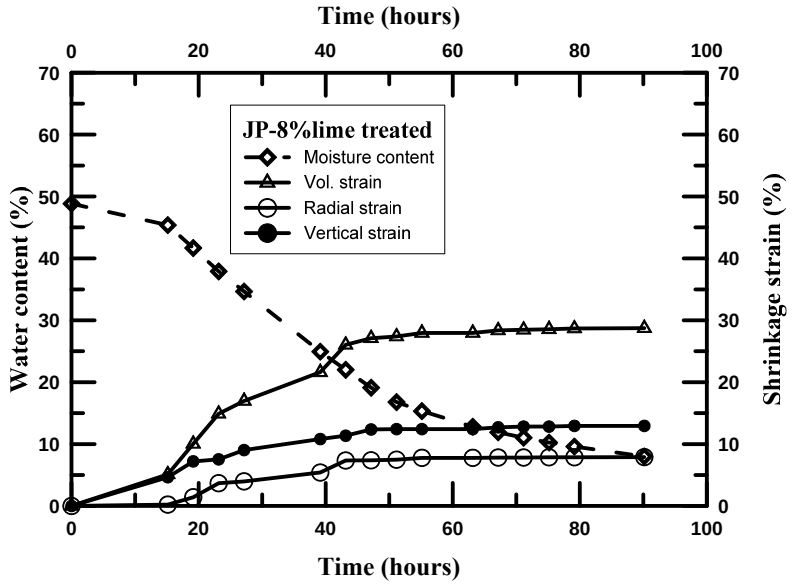

Figure 5-51 Time vs. moisture content and shrinkage strains plot of lime treated Joe Pool soil

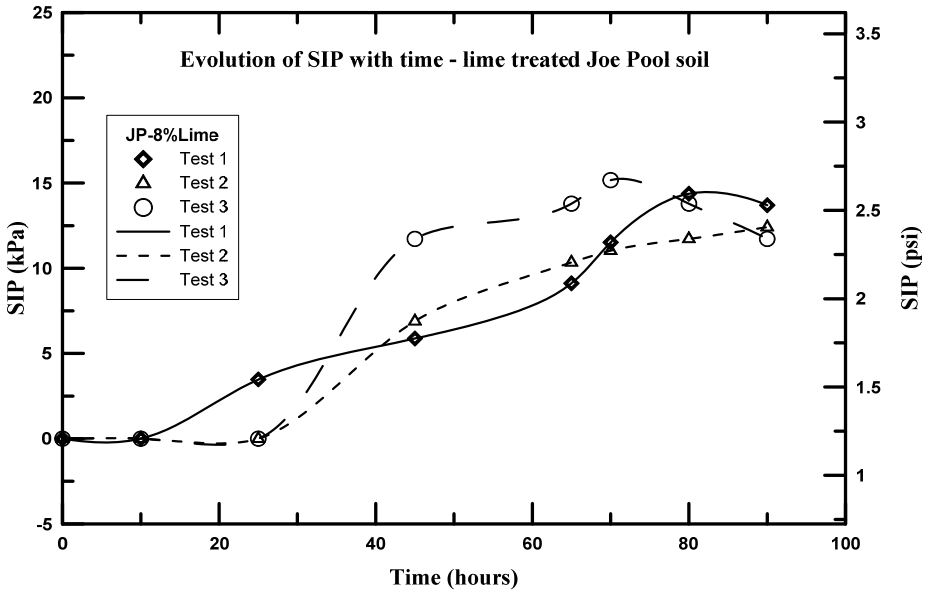

Figure 5-52 SIP test results for lime treated Joe Pool soil

SIP tests were also conducted on the lime+fiber treated Grapevine and Joe Pool soils. However, the specimens did not develop any SIP throughout the test. Figure 5-53(a) and (b) respectively show the lime+fiber treated Grapevine and Joe Pool soils at the end of the SIP test. The variations in moisture content as well as radial, vertical, and volumetric shrinkage strains with time of the lime+fiber treated Grapevine and Joe Pool soils are shown in Figure 5-54 and Figure 5-55. As it can be observed from the figures, the shrinkage strains of the soils were very small. That can be one of the reasons for the absence of SIP for the soils. The final radial, vertical, and volumetric strains for lime+fiber treated Grapevine soils were, 7.1, 9.3, and 23.5% respectively. The moisture content was 3.0% at the end of the test. For the lime+fiber treated Joe Pool soil, the final radial, vertical, and

volumetric strains were, 7.9, 12.8, and 28.7% respectively. And, the moisture content was 6.1% at the end of the test.

Figure 5-53 Lime+fiber treated specimens at the end of the SIP test

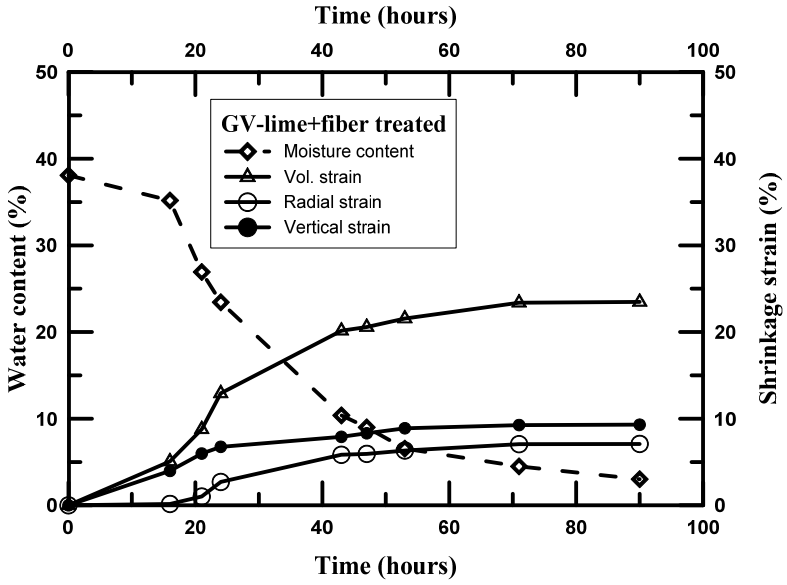

Figure 5-54 Time vs. moisture content and shrinkage strains plot of lime+fiber treated Grapevine soil

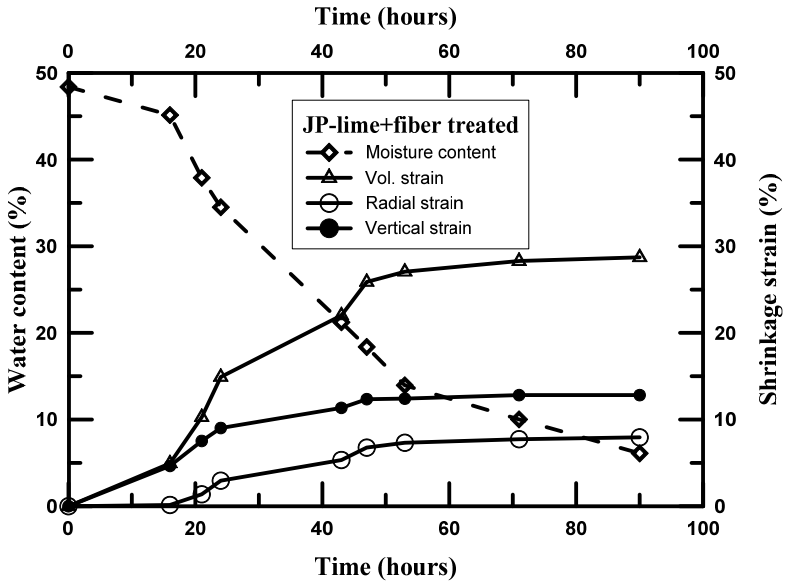

Figure 5-55 Time vs. moisture content and shrinkage strains plot of lime+fiber treated Joe Pool soil

Table 5-9 and Table 5-10 present the summary of the SIP results for Grapevine and Joe Pool soils respectively. The comparisons among the peak SIPs of different treatments of Grapevine soils are shown in Figure 5-56 and Figure 5-57 respectively. It is evident from the figures that the soil treatments reduced the SIP of the soil, meaning, the internal stresses developed within the soil during drying were small for the treated soils. Lime treated soils showed very negligible SIP compared to control and biopolymer treated soils. Biopolymer treated Grapevine and Joe Pool soils exhibited 60.1 % and 40.3% reduction in the peak SIP compared to the control respectively. It suggests that the biopolymer treatment can also be effective, if not equally effective as lime treatment, in

controlling the internal stresses during drying. The reduction in internal stress eventually reduces the desiccation cracking of the soil.

Table 5-9 Summary of SIP test results for Grapevine soils

Treatment type	Peak SIP (kPa)				
	Test 1	Test 2	Test 3	Mean	Standard deviation
Control	77.9	55.8	63.4	65.7	11.2
Biopolymer	38.4	41.3	40.4	40.0	1.5
Lime	1.9	0.0	0.0	0.6	1.1

Table 5-10 Summary of SIP test results for Joe Pool soil

Treatment type	Peak SIP (kPa)				
	Test 1	Test 2	Test 3	Mean	Standard deviation
Control	151	169.6	163.4	161.3	9.5
Biopolymer	61.7	73.7	61.4	65.6	7.0
Lime	14.4	12.4	13.8	13.5	1.0

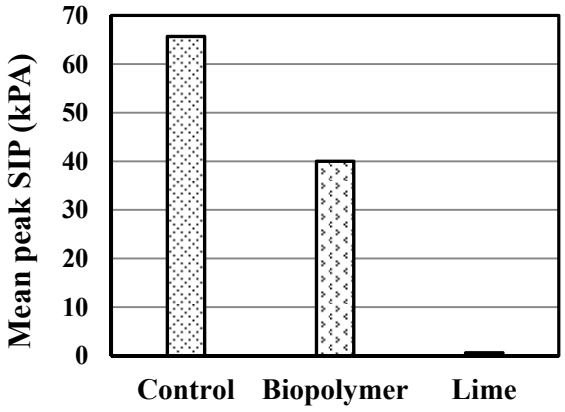

Figure 5-56 Comparison of mean SIPs of different treatments of Grapevine soil

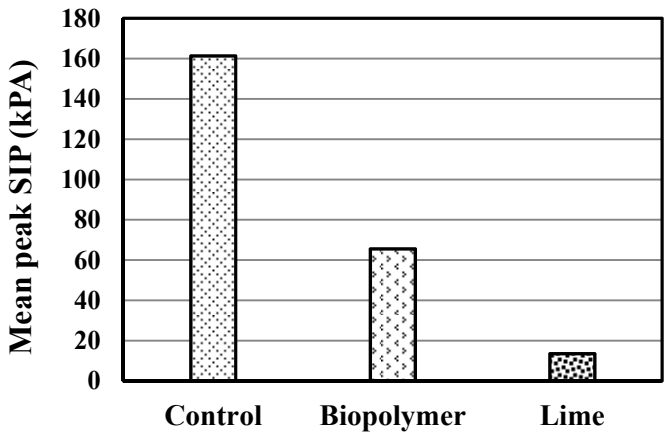

Figure 5-57 Comparison of mean SIPs of different treatments of Joe Pool soil

5.8.5 Comparison of Soil Water Characteristics Curve

Soil water characteristics curves were determined for the control and treated soils from both dam sites. Tempe cell and filter paper methods were used to find the SWCCs of the compacted specimens at lower and higher suction levels respectively. The test procedure outlined in Chapter 3 was followed to determine the curves. The experimental results for the Grapevine and Joe Pool soils are presented in Figure 5-58 and Figure 5-59 respectively.

The models developed by Brooks and Corey (1964), Van Genuchten (1980), and Fredlund and Xing (1994) were adopted to fit experimental data. The fitted curves are presented in Appendix A. SWCC parameters obtained from the experimental data are presented in the Table 5-11. Similarly, the model fitting parameters are presented in Table 5-12.

It can be observed form the Figure 5-58 that the Grapevine control and biopolymer treated soils show similar behavior at lower suction level. At higher suction lever, however, the treated soils show similar behavior. The saturated volumetric moisture content of the biopolymer treated soil was higher than the lime treated and lime and fiber treated soils. The air entry values range from 13 to 17 kPa and do not show a great variability.

In the case of Joe Pool soils, control and biopolymer treated soils showed highest and lowest volumetric moisture content at saturation. Below 200 kPa suction level, the biopolymer treated soil exhibited smallest suction for a given volumetric moisture content. However at higher suction levels all the treated soils exhibit similar moisture contents.

The results from the SWCC tests were used in the slope stability analysis of unsaturated slopes as presented in Chapter 6.

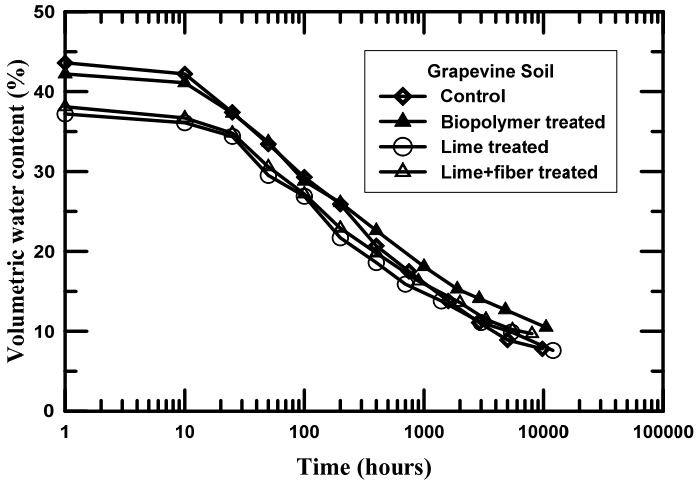

Figure 5-58 SWCC curves for control and treated Grapevine soils

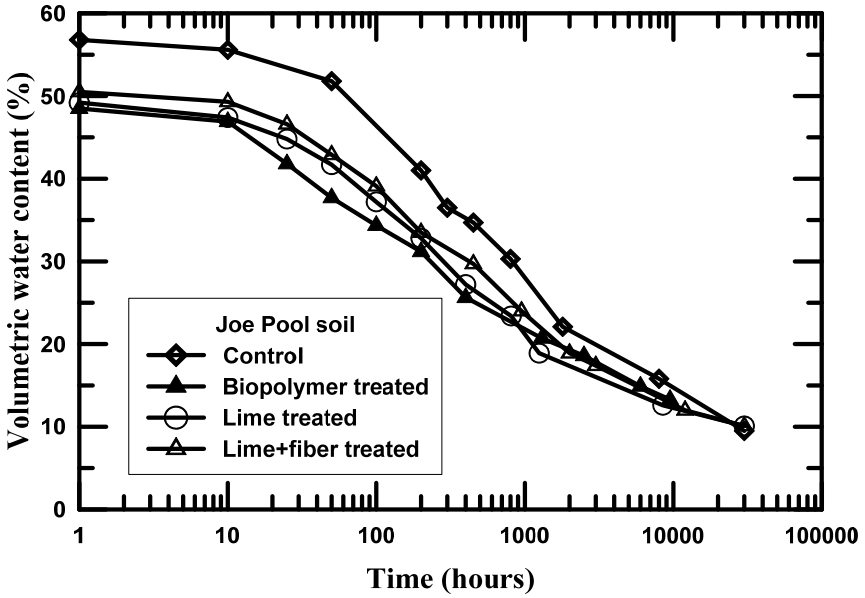

Figure 5-59 SWCC curves for control and treated Joe Pool soils

Table 5-11 SWCC parameters of the test soils

Soil	SWCC parameters		
	θ_s	Ψ_a (kPa)	θ_r
GV control	43.6	15	2
GV biopolymer treated	42.2	15	2
GV lime treated	37.2	17	1
GV lime+fiber treated	38.1	13	1
JP control	56.8	38	2.5
JP biopolymer treated	48.5	13	2.5
JP lime treated	49.2	19	2.5
JP lime+fiber treated	48.5	13	2.5

Table 5-12 SWCC model fitting parameters for the soils

Soil Treatment	Brooks and Corey (1964)		Van Genuchten -1990			Fredlund and Xing (1994)		
	λ	Ψ_b (kPa)	a (kPa^{-1})	n	m	a_1 (kPa)	n_1	m_1
GV control	0.27	15	0.025	1.35	0.259	70	1.1	1
GV biopolymer treated	0.22	15	0.024	1.3	0.23	80	0.85	0.95
GV lime treated	0.24	17	0.023	1.3	0.23	70	1.1	0.85
GV lime+fiber treated	0.21	13	0.025	1.3	0.231	90	0.9	1.05
JP control	0.25	38	0.015	1.3	0.231	170	1	1
JP biopolymer treated	0.2	13	0.034	1.25	0.2	100	0.8	1.05
JP lime treated	0.22	19	0.032	1.25	0.2	70	1	0.8
JP lime+fiber treated	0.2	13	0.034	1.25	0.2	100	0.8	1.05

5.9 Summary

This chapter presented the studies conducted on biopolymer treated Grapevine and Joe Pool soils. The optimum dosage of the biopolymer treatment was determined based on shear strength and swelling characteristics of the soil. This chapter also presented the results of the different tests conducted on the soils treated with biopolymer, lime and lime plus fiber. Various comparisons were made among the different treatment methods by indicating the pros and cons of each treatment method. The biopolymer treated soils showed moderate improvement in the shear strength and shrinkage studies when compared to control soils while both the lime treated and lime+fiber treated soils exhibited superior strength and shrinkage properties. Though Biopolymer treatments yielded moderate improvements, it can still be used for soil stabilization works as it has other tangible benefits including less carbon foot print compared to lime and lime+fiber treatments.

Chapter 6

Surficial Slope Stability Analyses

6.1 Introduction and Background

Dronamraju (2008) studied the effects of rainfall on surficial slope failures of the Joe Pool Dam Site. The study considered three different scenarios: no rainfall, short-term rainfall, and long-term rainfall conditions and analyzed the surficial slope failure of the slope. Le (2013) conducted additional research on the Grapevine and Joe Pool Dam slopes by introducing fully softened shear strength of the soils. Limit equilibrium approach was used in the slope stability analysis in either case.

In the current study, a finite difference program called Fast Lagrangian Analysis of Continua in 3 Dimensions (FLAC3D) has been used to investigate the surficial slope stability of the Grapevine and Joe Pool dams. FLAC3D uses the strength reduction factor approach to analyze the slope stability. Unlike in the GSTABLE and SLOPE/W, the programs used by the previous researchers Dronamraju (2008) and Le (2013) respectively, FLAC3D does not need input for possible failure surfaces. The strength reduction technique is generally applied in factor of safety (FOS) calculations by progressively reducing the shear strength of the material to bring the slope to a state of limiting equilibrium. The method is widely applied with the Mohr-Coulomb failure criterion. The cohesion and friction ($\tan \phi$) are divided by a factor which is called the safety factor.

A series of simulations are run with different values of trial safety factors to reduce the cohesion and friction until slope failure occurs. The factor of safety can also be found by reducing the strengths in small increments until a failure state is found. FLAC3D uses a bracketing approach similar to that proposed by Dawson et al. (1999). With this technique, stable and failure bracketing states are found first. Then, the bracket between stable and unstable conditions is gradually reduced until the difference between them becomes very small (Itasca, 2012).

Geometries of the dam slopes as used by Le (2013) have been used in this research. The slope geometries used by Le (2013) are presented in Figure 6-1 and Figure 6-2.

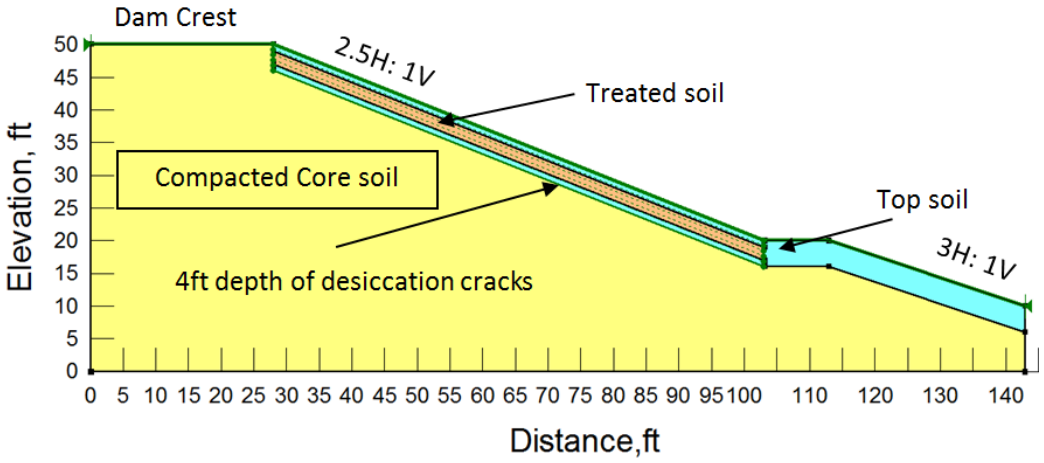

Figure 6-1 Cross-section of Grapevine Dam modeled in SLOPE/W (Le, 2013)

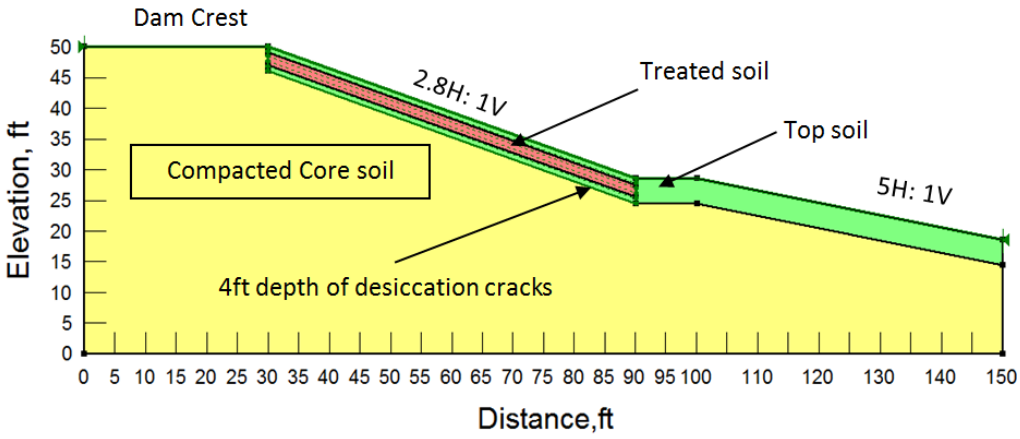

Figure 6-2 Cross-section of Joe Pool Dam modeled in SLOPE/W (Le, 2013)

6.2 Soil Properties

Both models of the Joe Pool and Grapevine Dams consisted of two soil regions: compacted core soil and treated soil. The control and treated soil properties were changed accordingly to represent their respective strength parameters, i.e. peak, fully softened or residual strengths. Since it was not required to input the possible failure surfaces, the program itself determined the failure mode of the slope. The factor of the safety of the slope can be smaller for global failure than the surficial failure. In such condition, the program gives the FOS for the global failure instead of surficial failure. The focus of this study was surficial slope failure.

Mohr-Coulomb material model was adopted for the analysis. The basic soil parameters such as density, cohesion, and friction angle were used as inputs. McCleskey (2005) conducted the compaction tests on the control and treated

soils. The maximum dry densities are adopted from his research as shown in Table 6-1 and Table 6-2.

Table 6-1 The maximum dry densities of the Grapevine Dam soils (McCleskey, 2005)

Description	Density (kg/m^3)
Control soil	1730
8% lime treated soil	1658
8%lime+0.15%fiber treated soil	1634

Table 6-2 The Maximum dry densities of the Joe Pool Dam soils (McCleskey, 2005)

Description	Density (kg/m^3)
Control soil	1498
8% lime treated soil	1562
8%lime+0.15%fiber treated soil	1522

As explained in Chapter 5, biopolymer treatment method was analyzed in this study. The maximum dry densities of the biopolymer treated Grapevine and Joe Pool soils presented in Table 6-3 were used in the stability analysis of biopolymer treated slopes.

Table 6-3 Maximum dry densities of biopolymer treated soils

Description	Density (kg/m3)
Biopolymer treated GV soil	1644
Biopolymer treated JP soil	1474

A separate analysis was carried out to study the effects of the soil's elastic modulus on the FOS of the slopes. The outcome of the analysis is presented in Table 6-4. It becomes evident from the Table 6-4 that the FOS remained unchanged when the elastic modulus of the soil was varied from 6 to 200 MPa. However, as expected the maximum displacement of the slope at failure decreased significantly as the elastic modulus of the soil increased from 6 to 200 MPa due to stiffening of the soil mass due to high modulus value. The maximum displacement contours of the slope at failure for soil elastic modulus of 6 and 200 MPa are shown in Figure 6-3 and Figure 6-4. This analysis shows that the FOS of a slope is independent of the elastic modulus of the soil. Therefore, a typical elastic modulus of 14 MPa was used in the present analysis along with a Poisson's ratio of 0.3. Although there were some changes in the maximum displacements at failure of the slope due to changes in elastic modulus, this subject matter was not within the scope in the current study and hence not included here.

Table 6-4 Effect of elastic modulus on FOS of the slope

Elastic modulus (MPa)	Factor of safety	Maximum displacement (m)
6	7.47	1.802
14	7.47	0.761
22	7.47	0.482
72	7.47	0.216
200	7.47	0.14

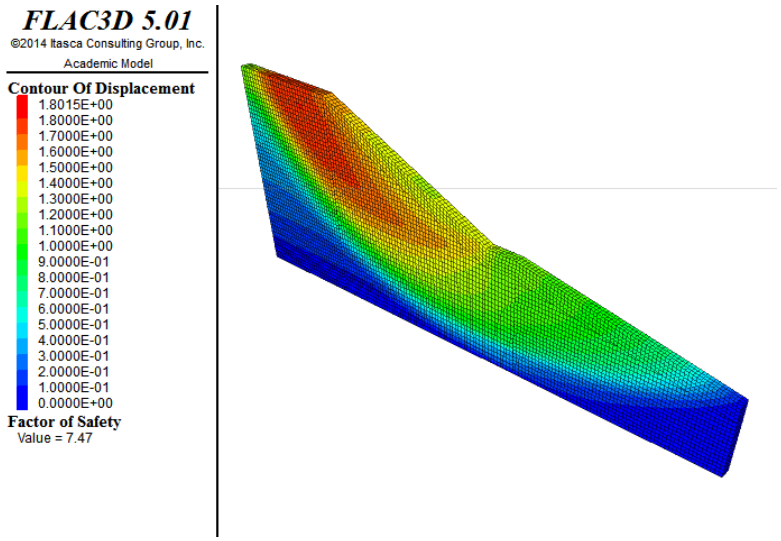

Figure 6-3 Displacement contour for soil elastic modulus of 6 MPa

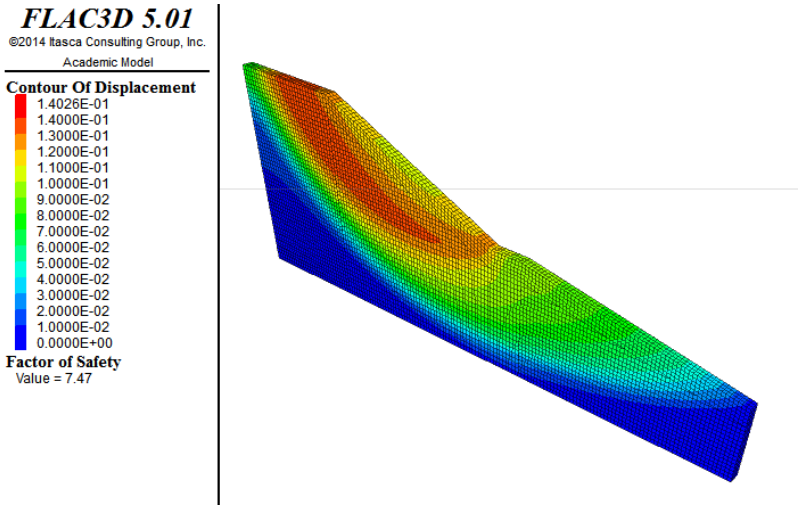

Figure 6-4 Displacement contour for soil elastic modulus of 200 MPa

The shear strengths of the control, lime treated and lime+fiber treated soils for both dam slopes used by Le (2013) were also used in the current analysis and are presented in Table 6-5. Similarly, the shear strength parameters of biopolymer treated soils used in the slope stability analysis are presented in Table 6-6.

Table 6-5 Shear strength properties of control, lime treated and lime+fiber treated soils used in the slope stability analyses (Le, 2013)

Soil	Treatment type	Peak shear strength parameters		Fully softened shear strength parameters		Residual shear strength parameters	
		Cohesion (kPa)	Friction angle (degrees)	Cohesion (kPa)	Friction angle (degrees)	Cohesion (kPa)	Friction angle (degrees)
GV	Control	2.4	29.1	0	34.8	0	18
	Lime treated	94.5	32.8	10	38.9	12.9	38
	lime+fiber treated	46.9	42.3	27.2	40	16.3	40
JP	Control	4.8	26.2	0	27	0	20
	Lime treated	140.6	23.5	21.9	36.6	12.5	36
	lime+fiber treated	55.4	34.3	29	35.4	16.8	39

Table 6-6 Shear strength properties of biopolymer treated soils used in the slope stability analyses

Soil	Peak shear strength parameters		Fully softened shear strength parameters		Residual shear strength parameters	
	Cohesion (kPa)	Friction angle (degrees)	Cohesion (kPa)	Friction angle (degrees)	Cohesion (kPa)	Friction angle (degrees)
Grapevine	13.8	33.8	10	23.4	6.2	22
Joe Pool	16.9	28.2	10.3	23.8	6.5	23.8

6.3 Effect of Width of Model in Factor of Safety

In FLAC3D, the smallest unit representing a material is called a zone. A zone in FLAC3D is similar to the element in the finite element method. The computation time of a model increases significantly with increase in the number of the zones of the model. Therefore, an additional analysis was also conducted to find the effect of the width of the model. Two different simulations were run with similar soil properties, zone sizes, length and steepness of the slope but with different width of the model; one with 20 m and the other with 1 m width. The geometry of the slopes modeled for the simulations are shown in Figure 6-5 and Figure 6-6, respectively for 20 and 1 m wide models. It can be seen that the FOS of the slope remains unchanged for varying width of the slope. However, it can be noticed that the magnitude of the maximum displacements are higher for the wider model and smaller for the narrower model. It can be the effect of the boundary condition because the sides of the slopes at both ends are restricted against lateral movement.

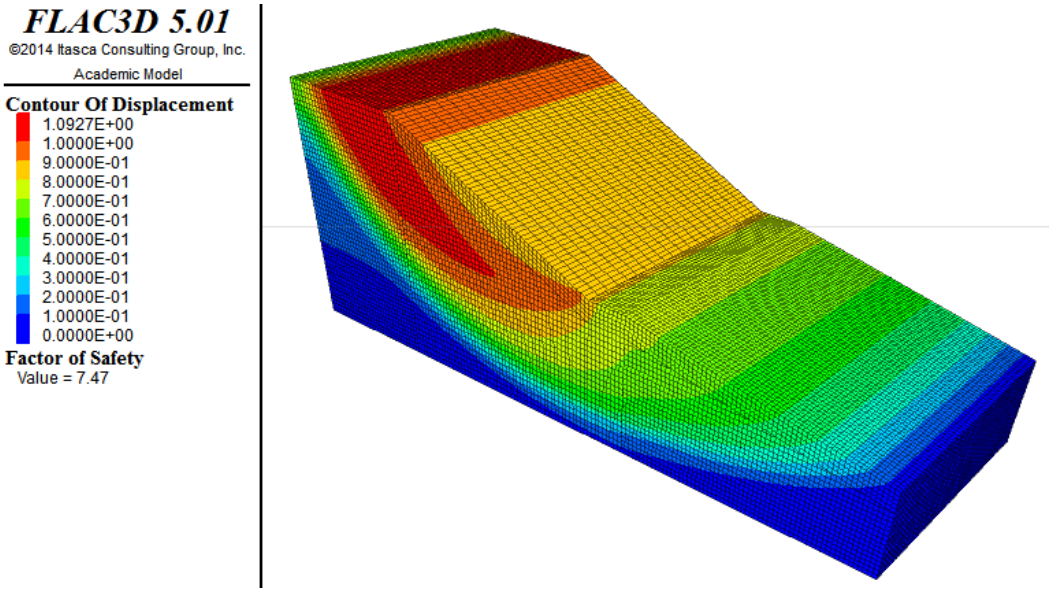

Figure 6-5 Geometry, FOS and displacement contours for 20 m wide model

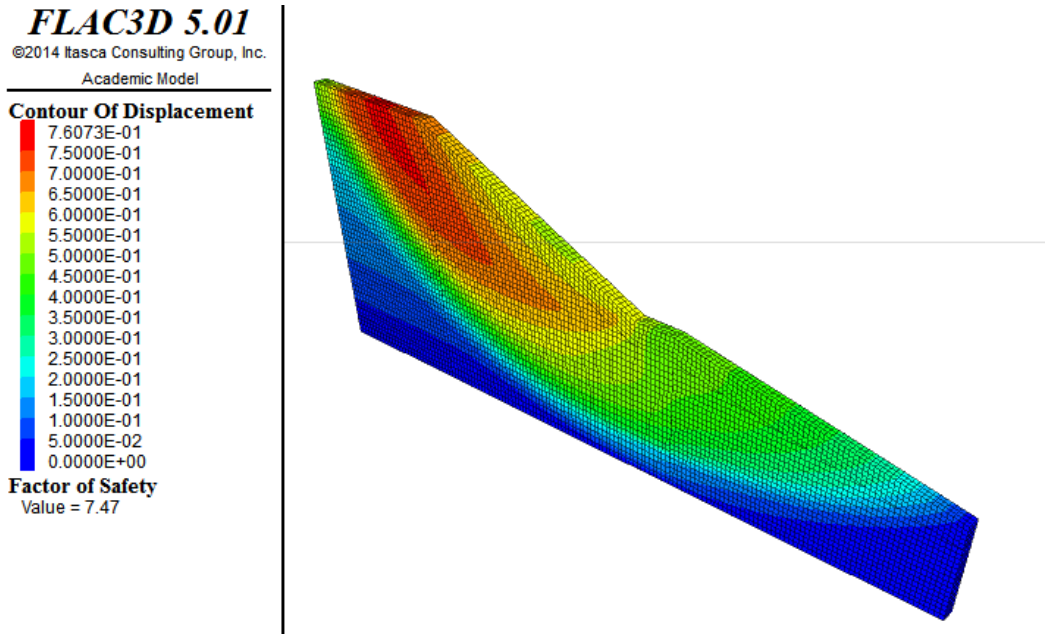

Figure 6-6 Geometry, FOS and displacement contours for 1 m wide model

6.4 Surficial Slope Stability Analysis for Peak, Fully Softened and Residual Shear Strength Conditions

The slope stability analyses were conducted on both Joe Pool and Grapevine dam slopes for four different top soils namely, control soil, biopolymer treated soil, lime treated soil, and lime+fiber treated soil. For each soil, the analysis was conducted for peak, fully softened and residual shear strength conditions.

Although, the focus of this research study is to determine the FOS against surficial slope failure of the dam slopes, the slope may not necessarily have the smallest FOS in surficial failure. Instead, it can have a smallest FOS in global (or deep seated) failure for a given geometry and soil strength conditions. If such condition occurs in any analysis, the strength of the core soil is increased significantly to make the slope to have the smallest FOS in surficial slope failure. The distinction between the surficial and global slope failure is made by observing the location of the maximum displacement contours of the slope at failure.

If the maximum displacement contours are located in the top soil (i.e., within 4 ft. from the top surface), it is considered surficial failure. Otherwise, it is considered global failure in the current study. Figure 6-7 and Figure 6-8 present examples of global and surficial slope failures, respectively of the Joe Pool Dam slope for control soil with peak shear strength parameters. The surficial slope

stability analysis results for Grapevine Dam slope are presented in Figure 6-9 through Figure 6-20. The same for the Joe Pool Dam slope is presented in Figure 6-21 through Figure 6-32. Table 6-7 shows the FOS of the Grapevine Dam slope for different treatment and shear strength conditions. Similarly, Table 6-8 shows the same for the Joe Pool Dam slope.

It was found that the Grapevine Dam control section with residual shear strength condition and Joe Pool Dam control section with both fully softened and residual shear strength conditions yielded the FOS values lower than the acceptable FOS limit of 1.5 for the slopes. All other combinations of soil strength and treatment conditions yielded FOS higher than 1.5. The results were compared with the ones obtained from Slope/W program by Le (2013) as shown in Figure 6-33. The comparison showed a good agreement between the results from the two methods with few exceptions.

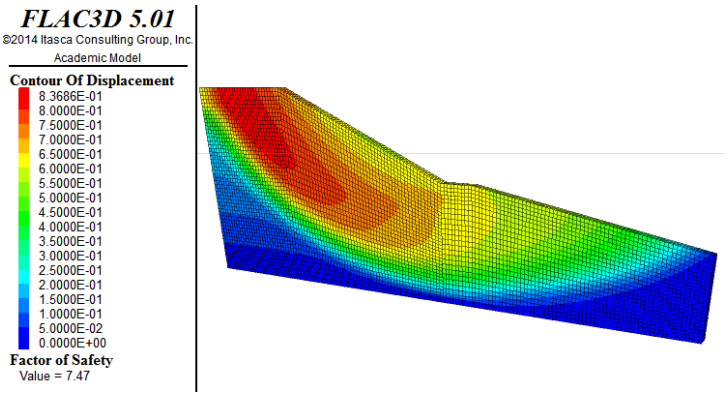

Figure 6-7 Minimum FOS for global slope failure of the Joe Pool dam slope with lime treated soil and peak shear strength parameters

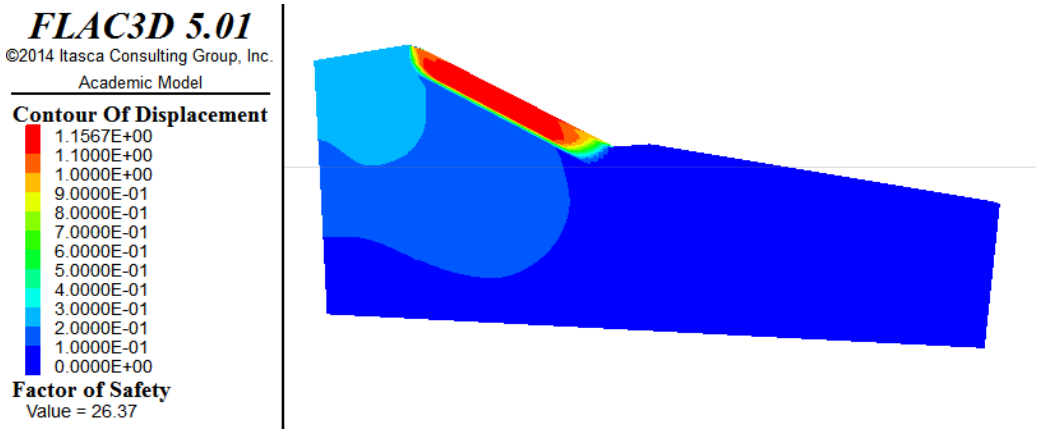

Figure 6-8 Minimum FOS for surficial slope failure of the Joe Pool dam slope with lime treated soil and peak shear strength parameters

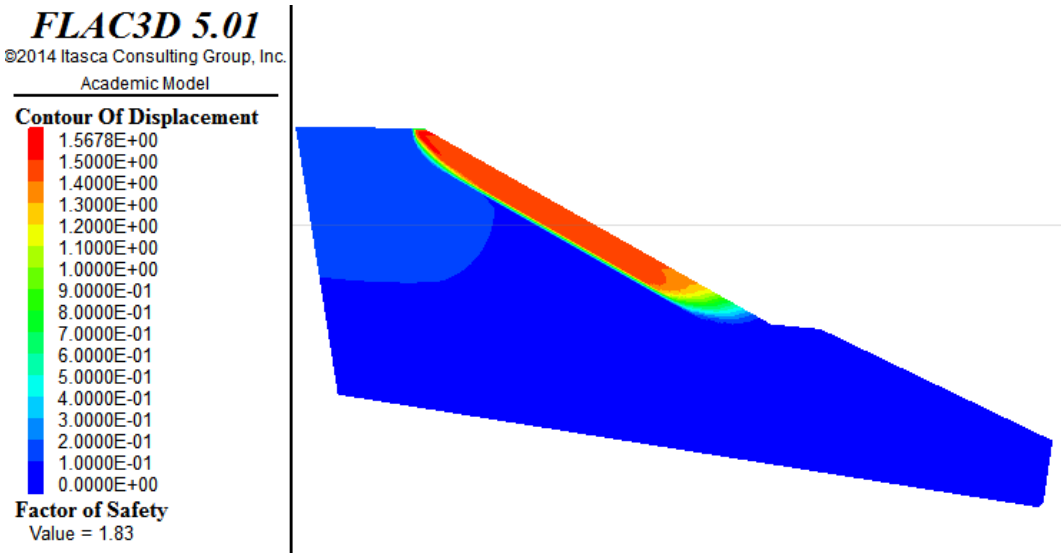

Figure 6-9 FOS of Grapevine Dam control section with peak shear strength parameters

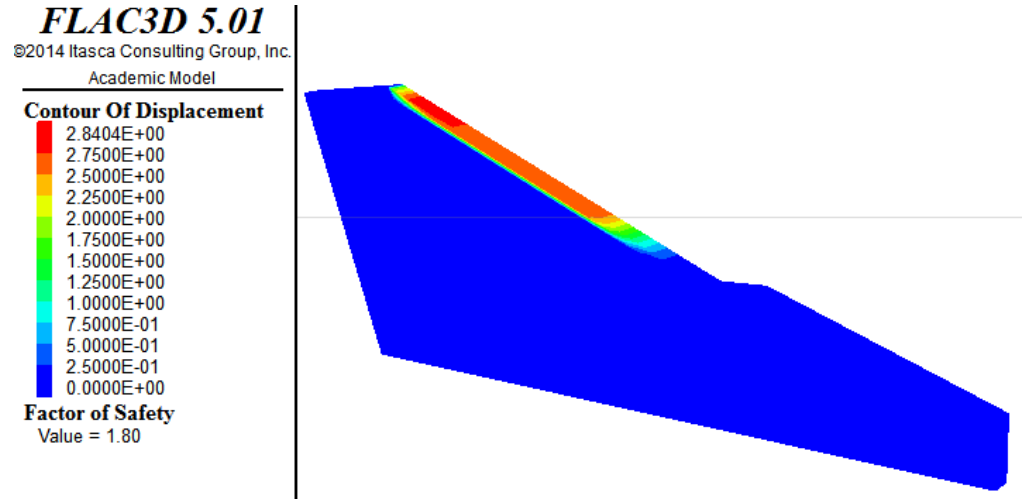

Figure 6-10 FOS of Grapevine Dam control section with fully softened shear strength parameters

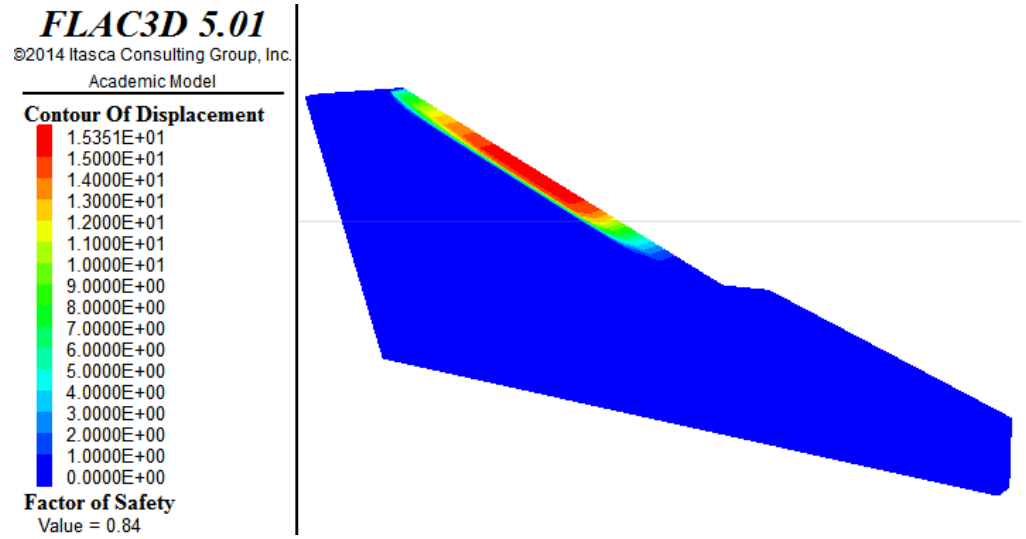

Figure 6-11 FOS of Grapevine Dam control section with residual shear strength parameters

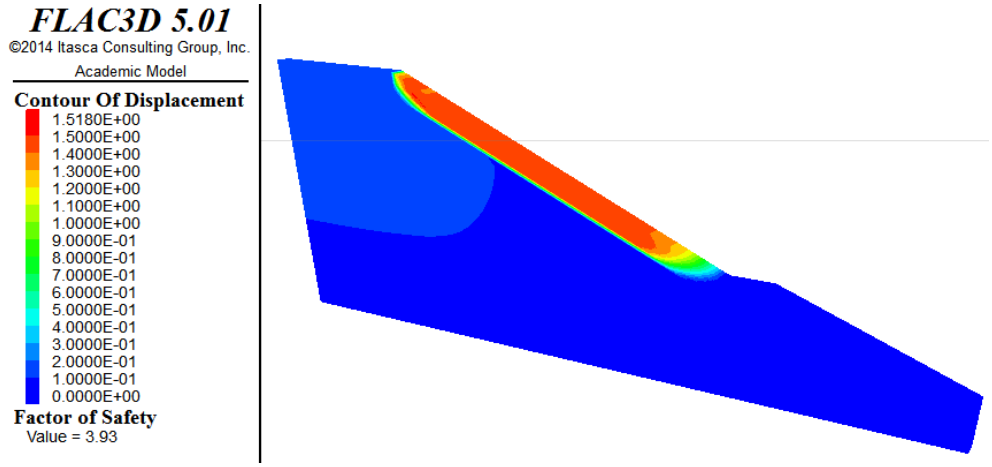

Figure 6-12 FOS of Grapevine Dam biopolymer treated section with peak shear strength parameters

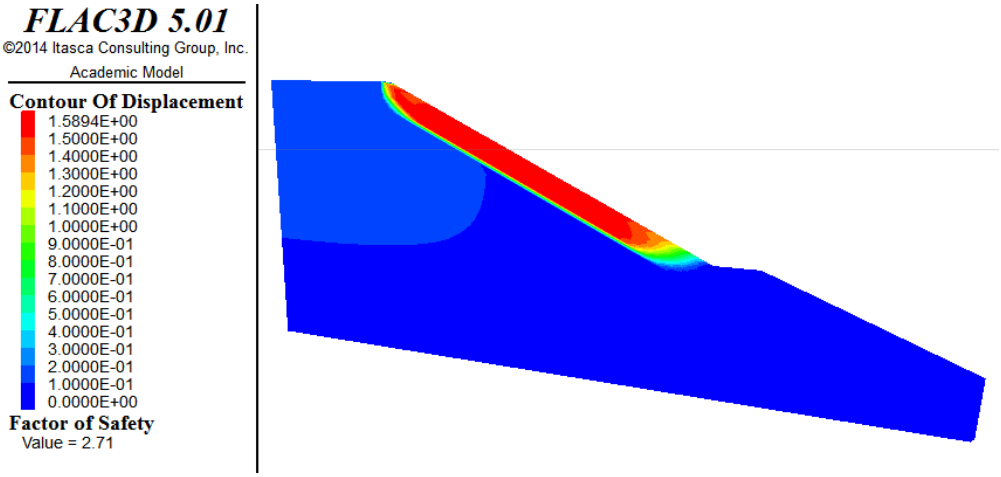

Figure 6-13 FOS of Grapevine Dam biopolymer treated section with fully softened shear strength parameters

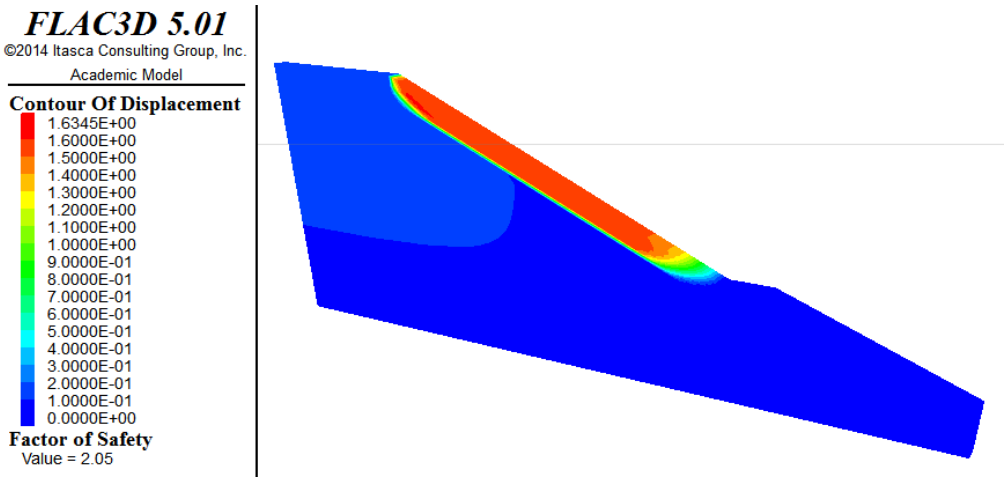

Figure 6-14 FOS of Grapevine Dam biopolymer treated section with residual shear strength parameters

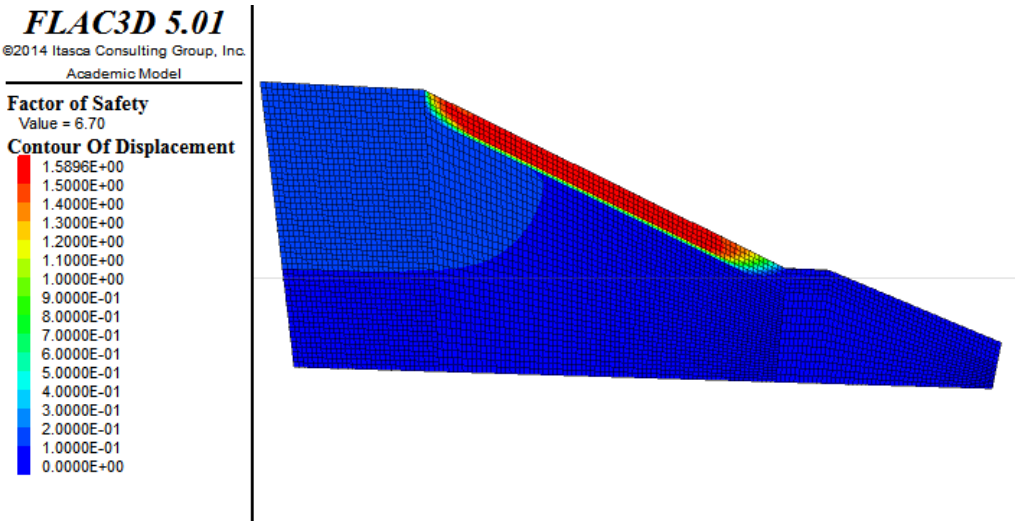

Figure 6-15 FOS of Grapevine Dam lime treated section with peak shear strength parameters

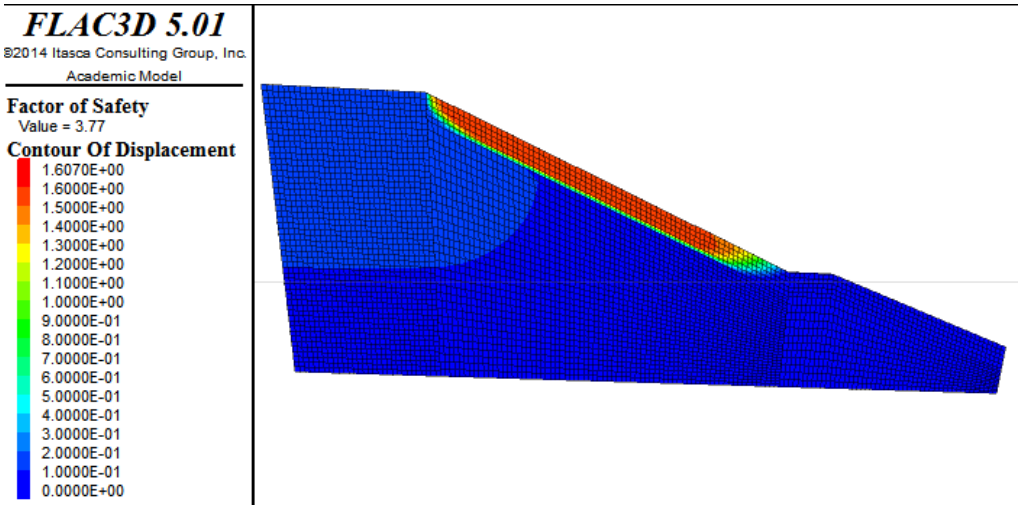

Figure 6-16 FOS of Grapevine Dam lime treated section with fully softened shear strength parameters

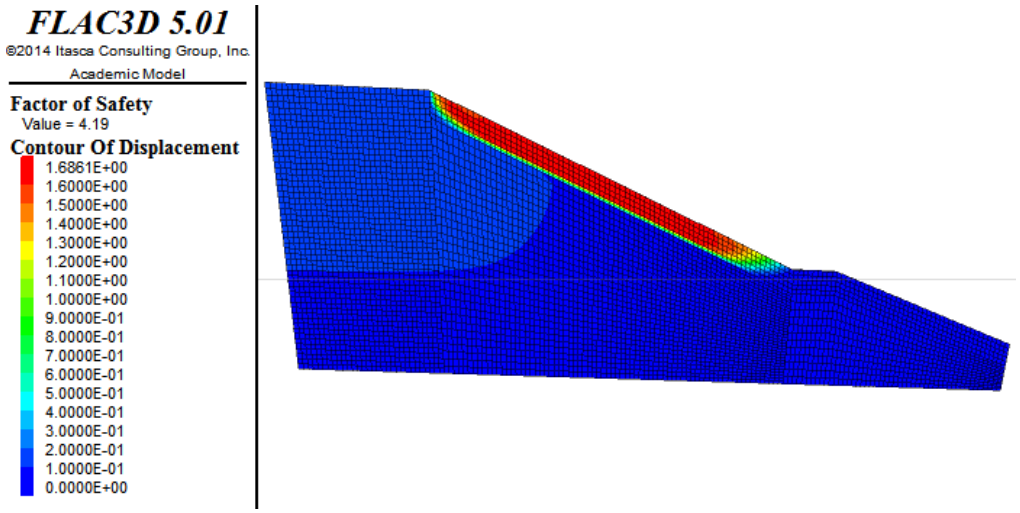

Figure 6-17 FOS of Grapevine Dam lime treated section with residual shear strength parameters

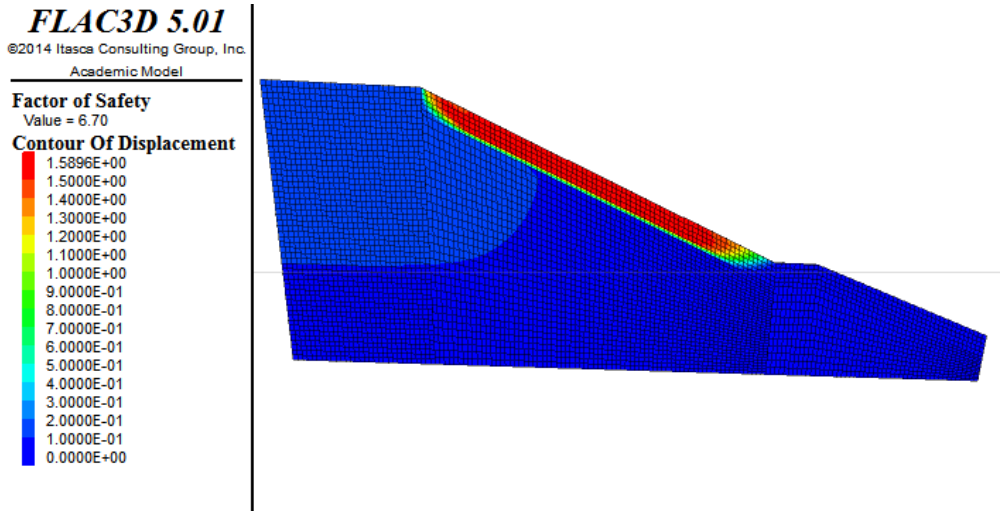

Figure 6-18 FOS of Grapevine Dam lime+fiber treated section with peak shear strength parameters

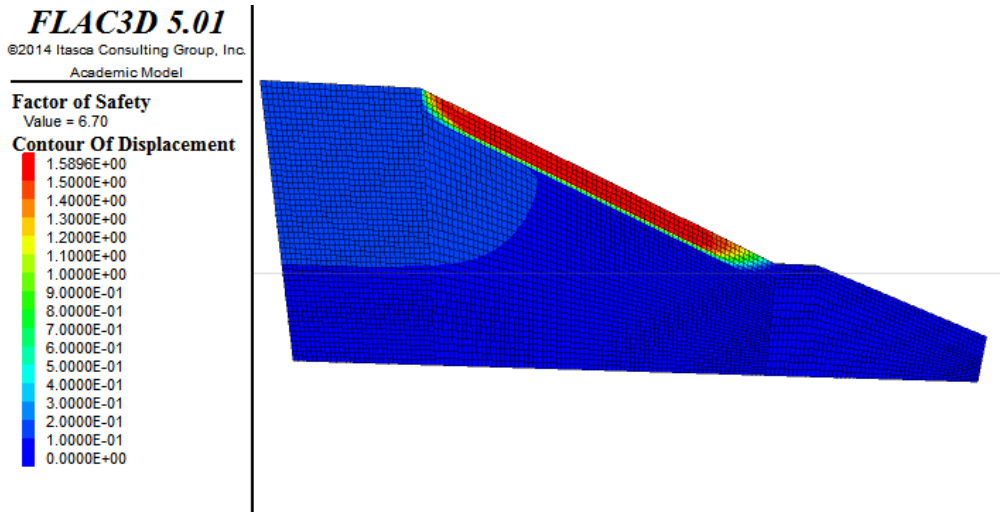

Figure 6-19 FOS of Grapevine Dam lime+fiber treated section with fully softened shear strength parameters

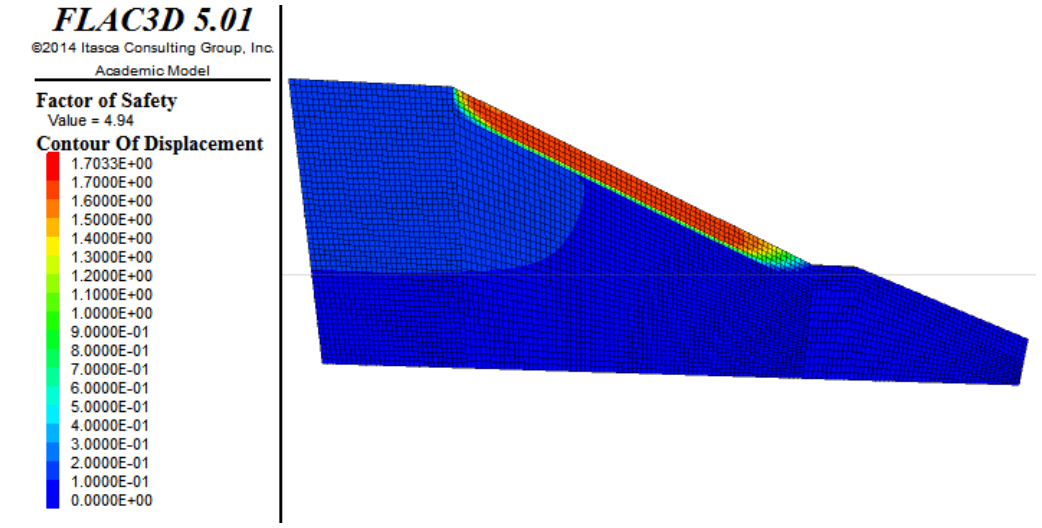

Figure 6-20 FOS of Grapevine Dam lime+fiber treated section with residual shear strength parameters

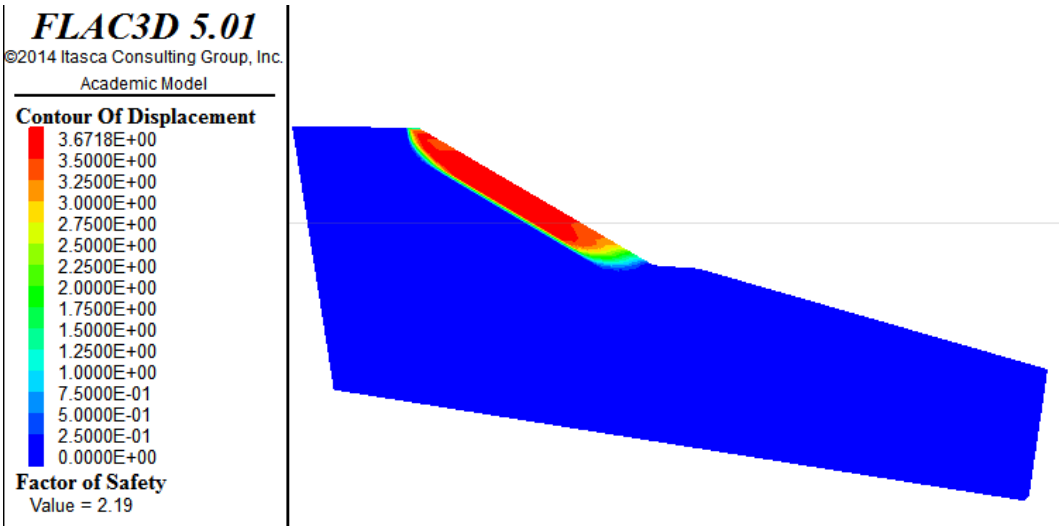

Figure 6-21 FOS of Joe Pool Dam control section with peak shear strength parameters

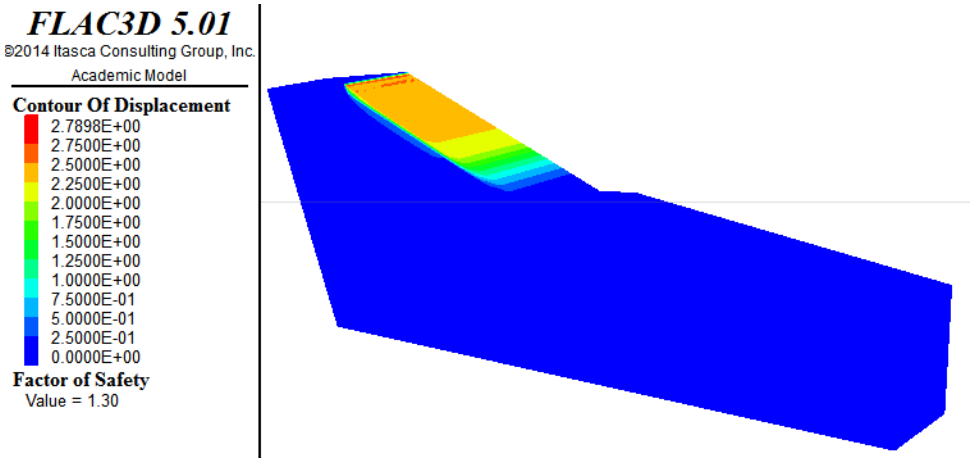

Figure 6-22 FOS of Joe Pool Dam control section with fully softened shear strength parameters

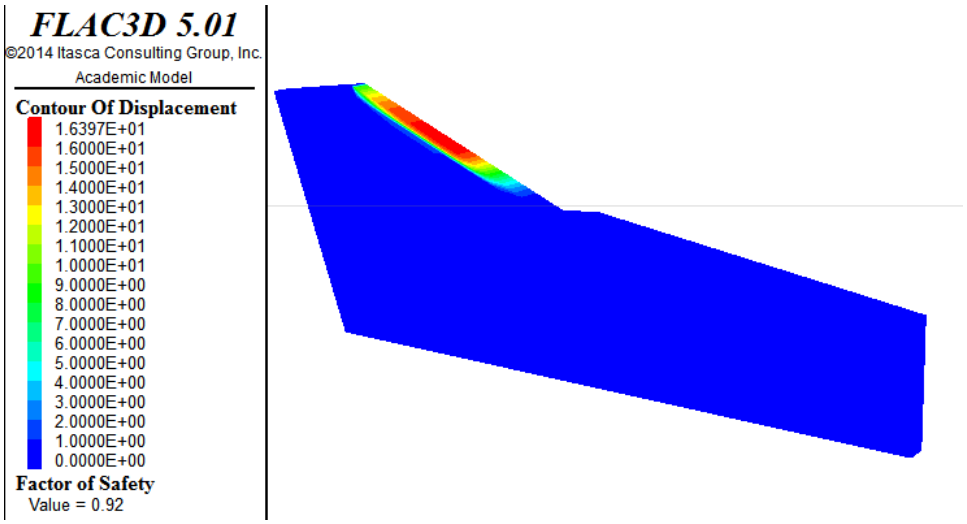

Figure 6-23 FOS of Joe Pool Dam control section with residual shear strength parameters

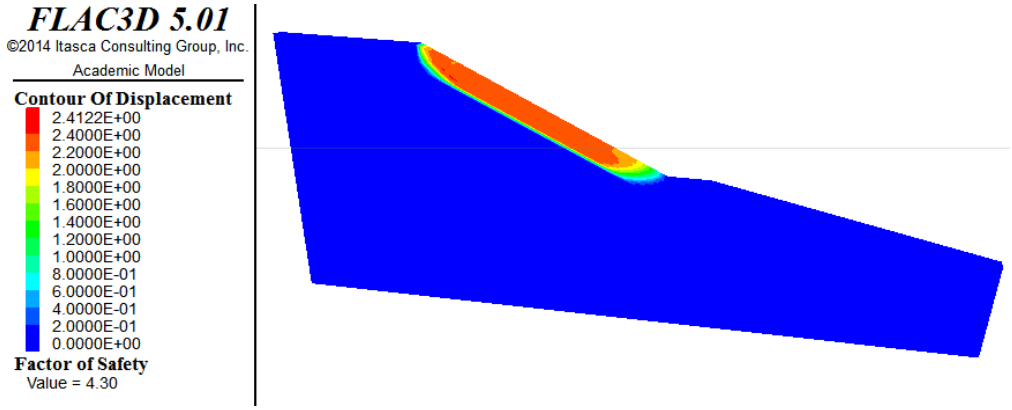

Figure 6-24 FOS of Joe Pool Dam biopolymer treated section with peak shear strength parameters

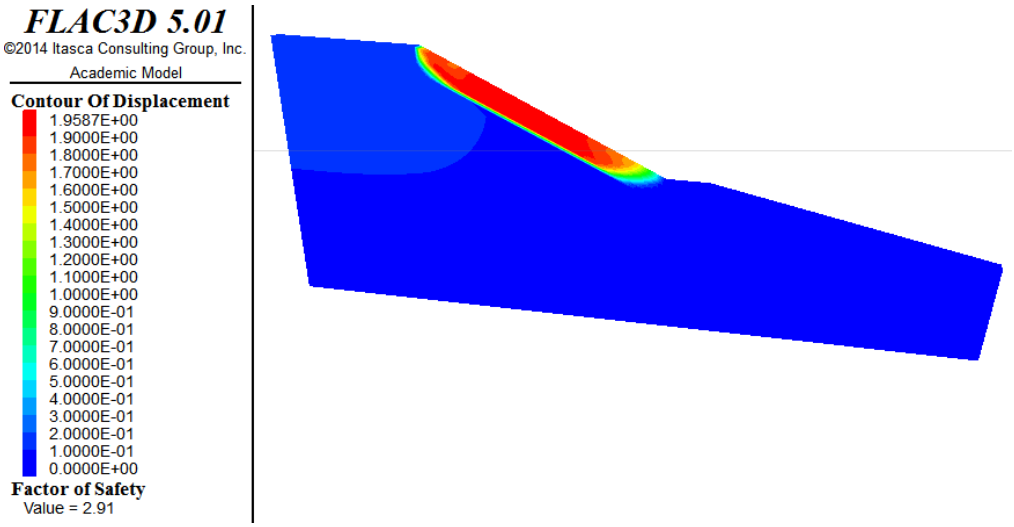

Figure 6-25 FOS of Joe Pool Dam biopolymer treated section with fully softened shear strength parameters

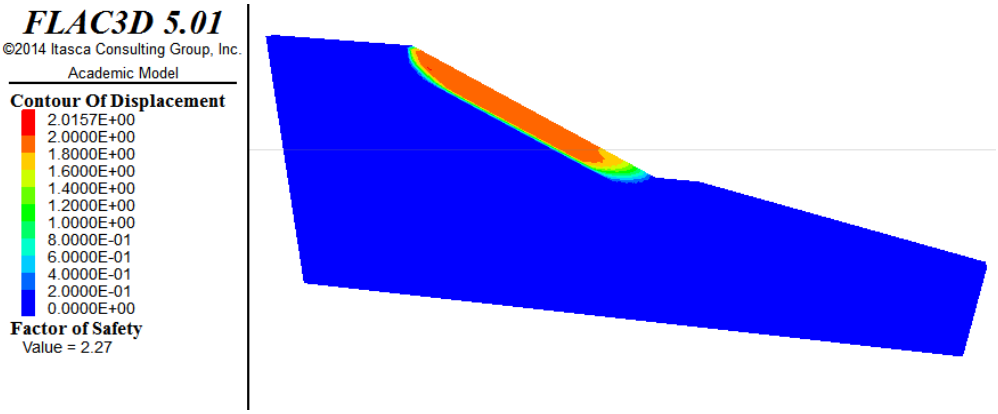

Figure 6-26 FOS of Joe Pool Dam biopolymer treated section with residual shear strength parameters

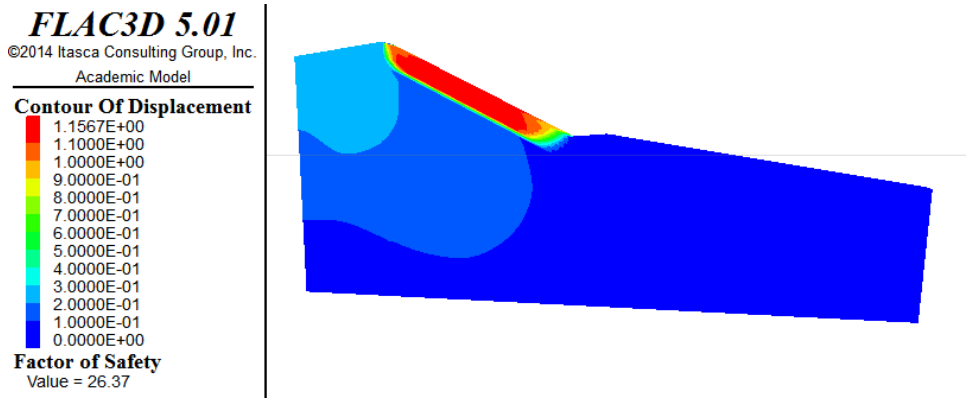

Figure 6-27 FOS of Joe Pool Dam lime treated section with peak shear strength parameters

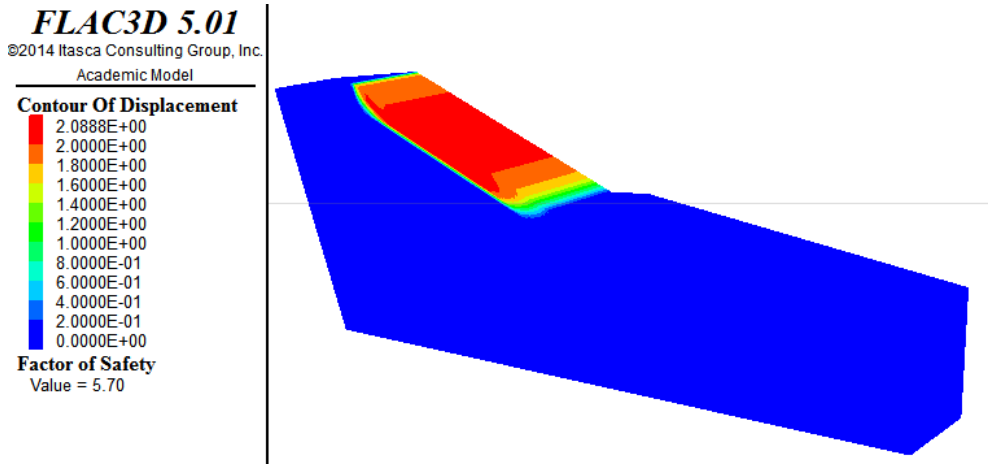

Figure 6-28 FOS of Joe Pool Dam lime treated section with fully softened shear strength parameters

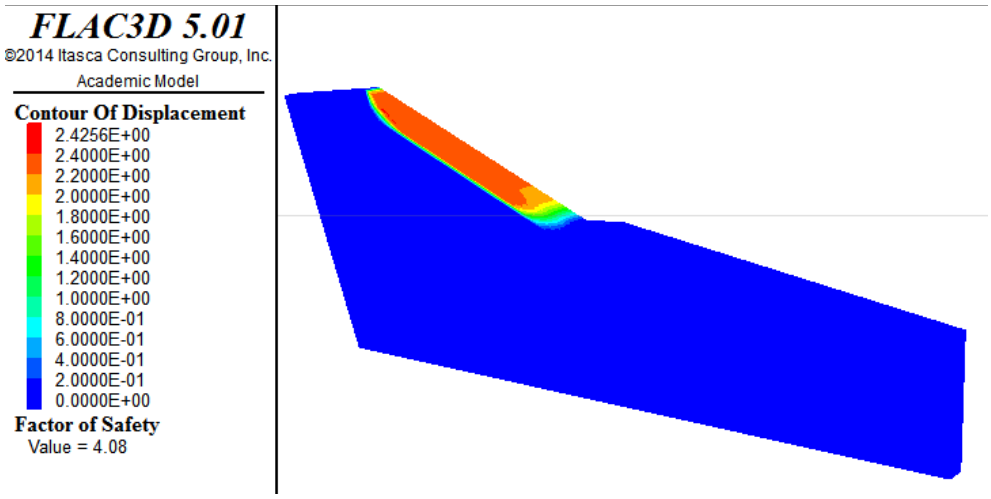

Figure 6-29 FOS of Joe Pool Dam lime treated section with residual shear strength parameters

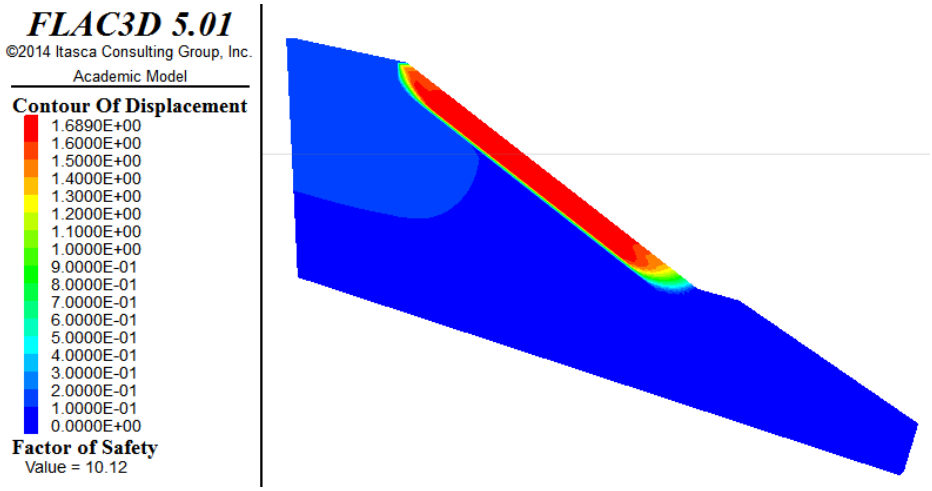

Figure 6-30 FOS of Joe Pool Dam lime+fiber treated section with peak shear strength parameters

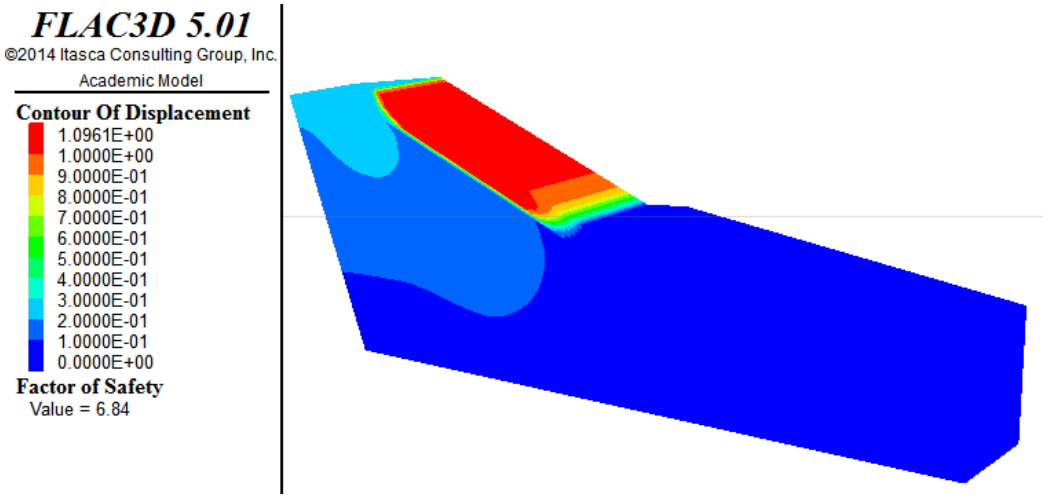

Figure 6-31 FOS of Joe Pool Dam lime+fiber treated section with fully softened shear strength parameters

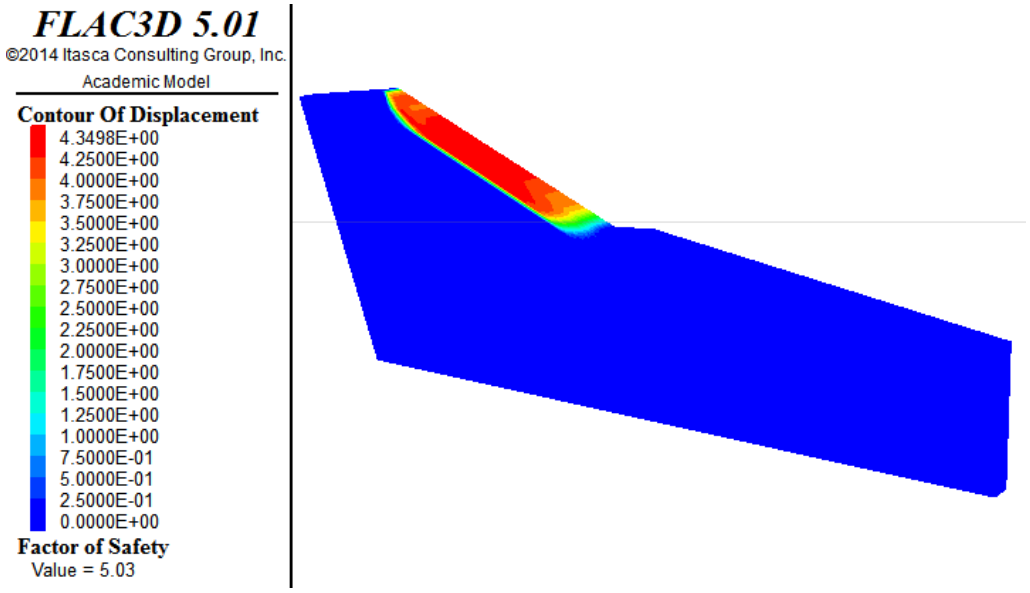

Figure 6-32 FOS of Joe Pool Dam lime+fiber treated section with residual shear strength parameters

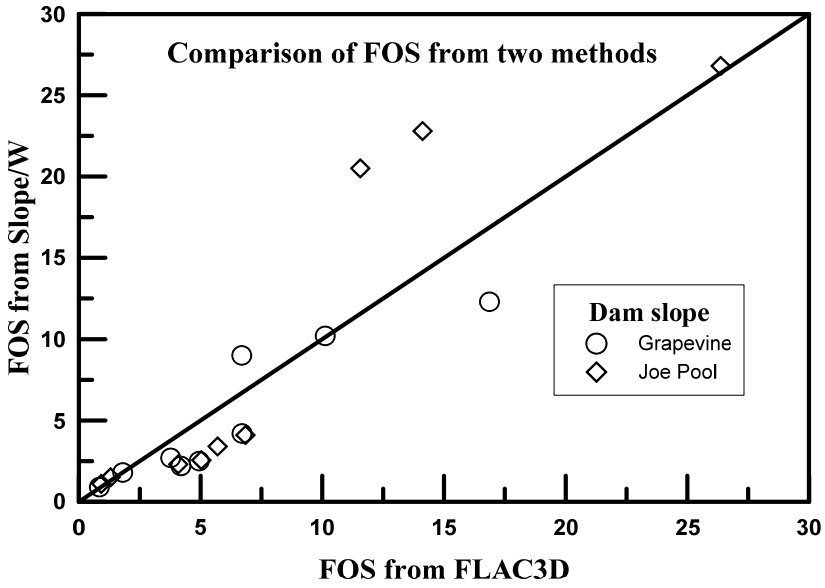

Figure 6-33 Comparison of FOS determined from Slope/W (Le, 2013) and FLAC3D

Table 6-7 The FOS of the Grapevine Dam slope at different soil and strength conditions

Soil	Peak		Fully softened		Residual	
	Minimum	Surficial	Minimum	Surficial	Minimum	Surficial
Control	1.83	1.83	1.80	1.80	0.84	0.84
Biopolymer treated	2.57	3.93	2.57	2.71	2.05	2.05
Lime treated	2.57	16.87	2.56	3.77	2.58	4.19
Lime+fiber treated	2.57	10.12	2.58	6.7	2.58	4.94

Table 6-8 The FOS of the Joe Pool Dam slope at different soil and strength conditions

Soil	Peak		Fully softened		Residual	
	Minimum	Surficial	Minimum	Surficial	Minimum	Surficial
Control	2.19	2.19	1.30	1.30	0.92	0.92
Biopolymer treated	4.30	4.30	2.91	2.91	2.27	2.27
Lime treated	7.45	26.37	5.7	5.7	4.08	4.08
Lime+fiber treated	7.45	11.56	6.84	6.84	5.03	5.03

6.5 Effects of Desiccation Cracks on Surficial Slope Stability of Dam Slopes

6.5.1 Two Cracks Parallel to the Dam Alignment

Desiccation cracks are very common in natural and engineered clay slopes. Most of the major cracks run near parallel to the alignment direction of the dams. Sometimes these crack locations can be very long. Le (2013) reported a desiccation crack almost 8 m long in the Joe Pool dam slope. The crack was along the alignment direction of the dam. To analyze the effect of such cracks, simulations were run with manually created cracks on the models. The cracks were considered long enough that a part of it can be modeled considering plane strain condition. The cracks were created by introducing interface elements at the intended locations of the cracks. And the cracks were represented by using very low shear strength and stiffness of the interface elements (friction angle = 0.1º, cohesion = 0.1 Pa, normal stiffness = 0.1 Pa, Shear stiffness of 0.1 Pa, and tensile strength =0 Pa).

The locations of the crack in the slope can be observed in the Figure 6-34 where the zones are made transparent enough to clearly visualize the interface elements (or the manually created cracks). One crack was on the crest and another crack was on the slope. The failure modes and FOS of the Grapevine Dam slope are presented in Figure 6-35 through Figure 6-46. The same for Joe Pool Dam slope is presented in Figure 6-47 through Figure 6-58. Table 6-9 and Table 6-10 present the FOS values of the Grapevine and Joe Pool Dam slopes with cracks,

respectively. The results showed that the crack in the crest does not have big impact in the stability of slope against surficial failure. The crack in the slope, on the other hand, showed moderate reduction in the FOS of the slopes.

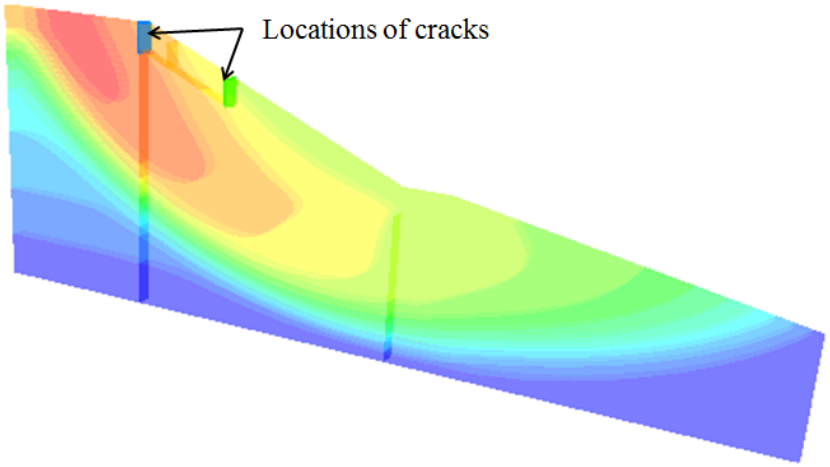

Figure 6-34 The locations of two parallel cracks created in the models

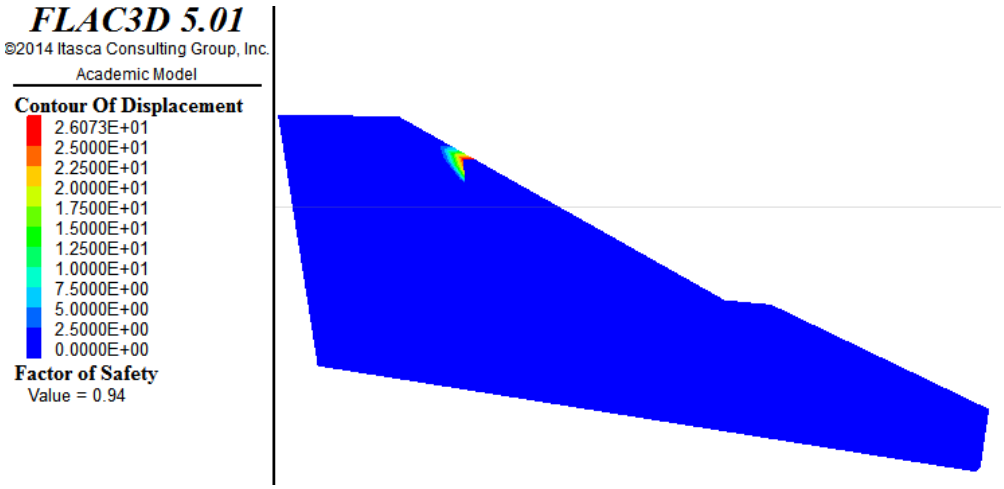

Figure 6-35 FOS of Grapevine Dam control section having two parallel cracks with peak shear strength parameters

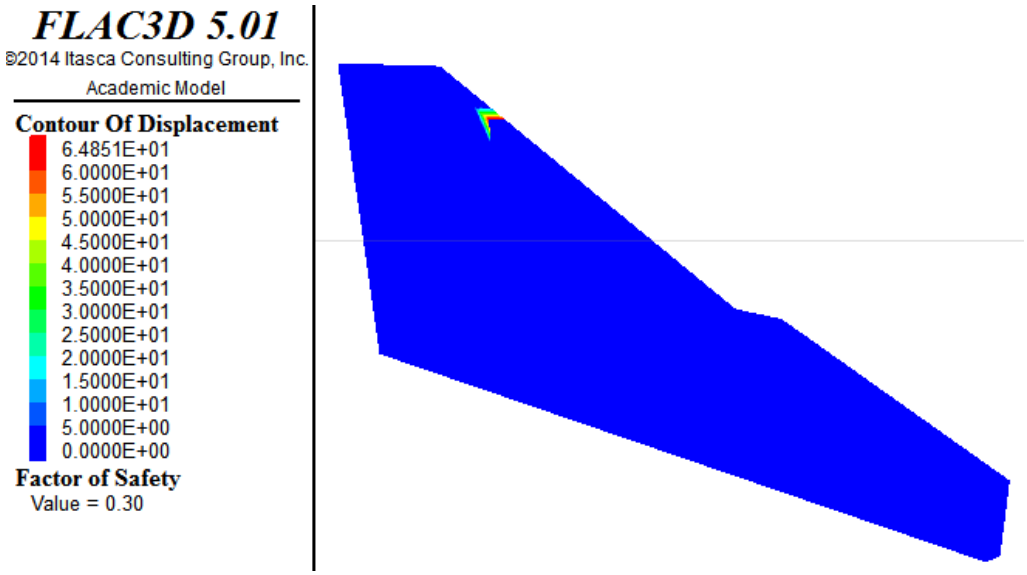

Figure 6-36 FOS of Grapevine Dam control section having two parallel cracks with fully softened shear strength parameters

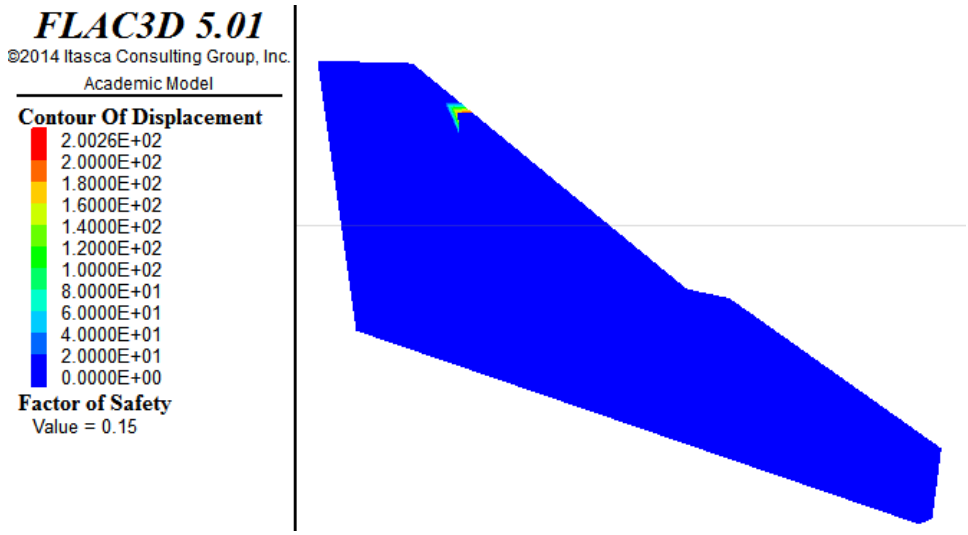

Figure 6-37 FOS of Grapevine Dam control section having two parallel cracks with residual shear strength parameters

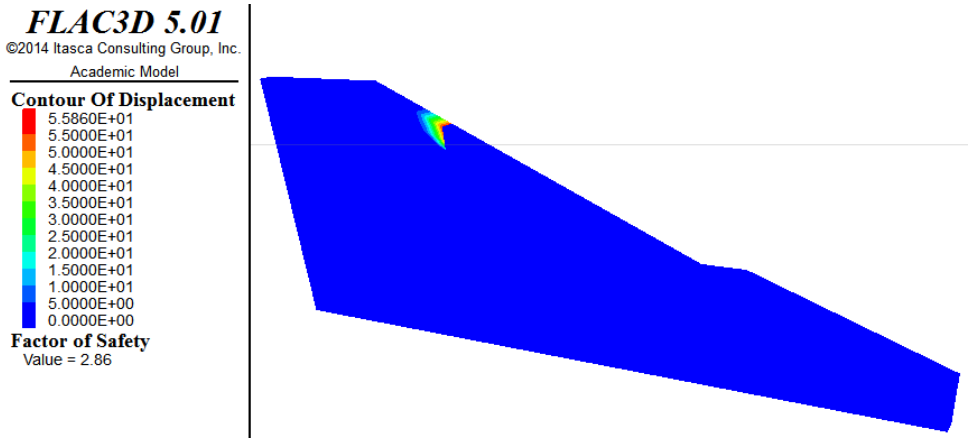

Figure 6-38 FOS of Grapevine Dam biopolymer treated section having two parallel cracks with peak shear strength parameters

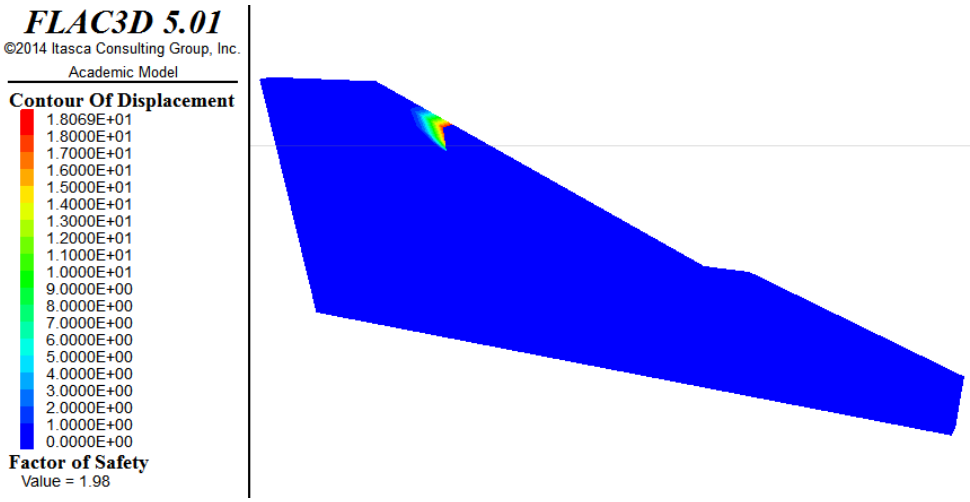

Figure 6-39 FOS of Grapevine Dam biopolymer treated section having two parallel cracks with fully softened shear strength parameters

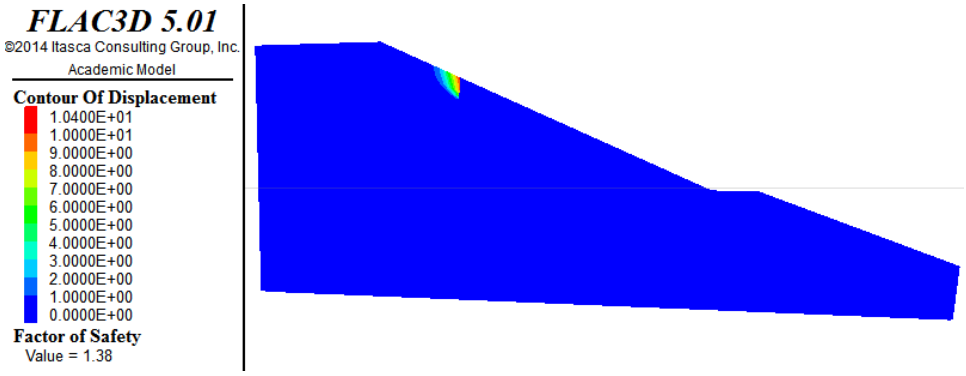

Figure 6-40 FOS of Grapevine Dam biopolymer treated section having two parallel cracks with residual shear strength parameters

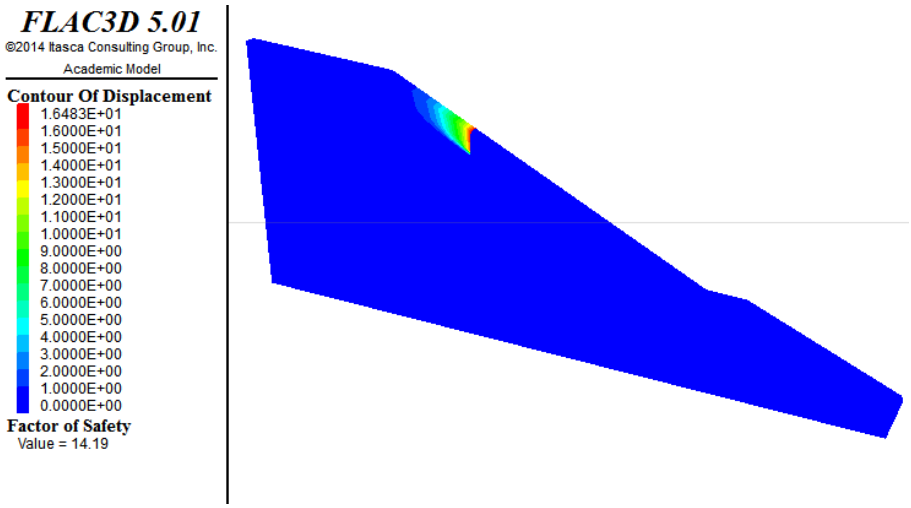

Figure 6-41 FOS of Grapevine Dam lime treated section having two parallel cracks with peak shear strength parameters

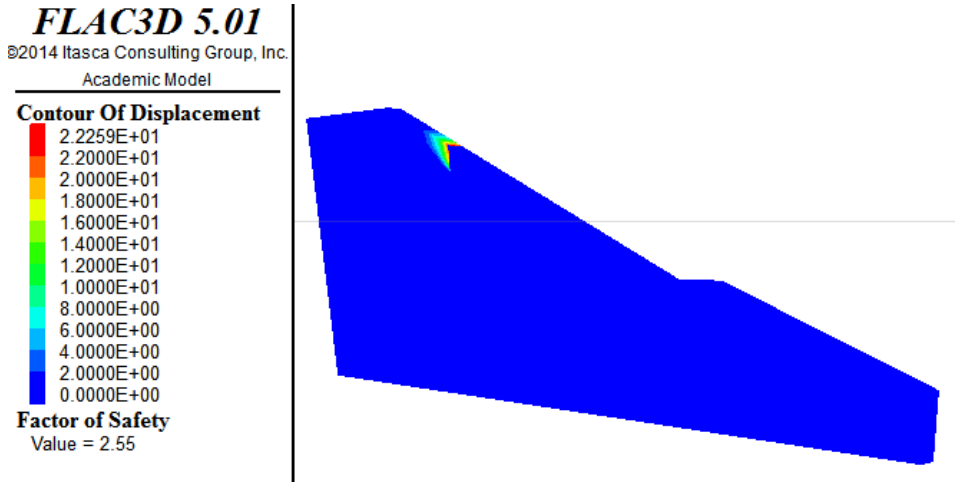

Figure 6-42 FOS of Grapevine Dam lime treated section having two parallel cracks with fully softened shear strength parameters

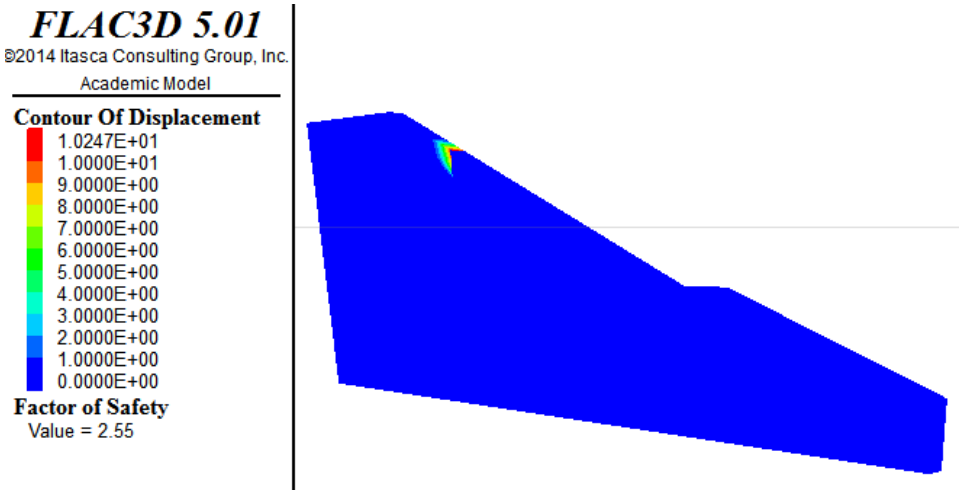

Figure 6-43 FOS of Grapevine Dam lime treated section having two parallel cracks with residual shear strength parameters

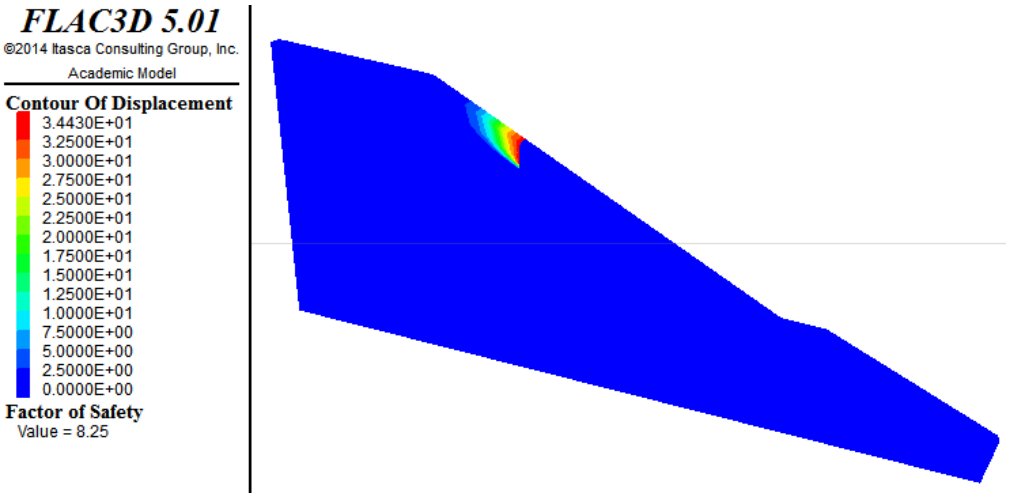

Figure 6-44 FOS of Grapevine Dam lime+fiber treated section having two parallel cracks with peak shear strength parameters

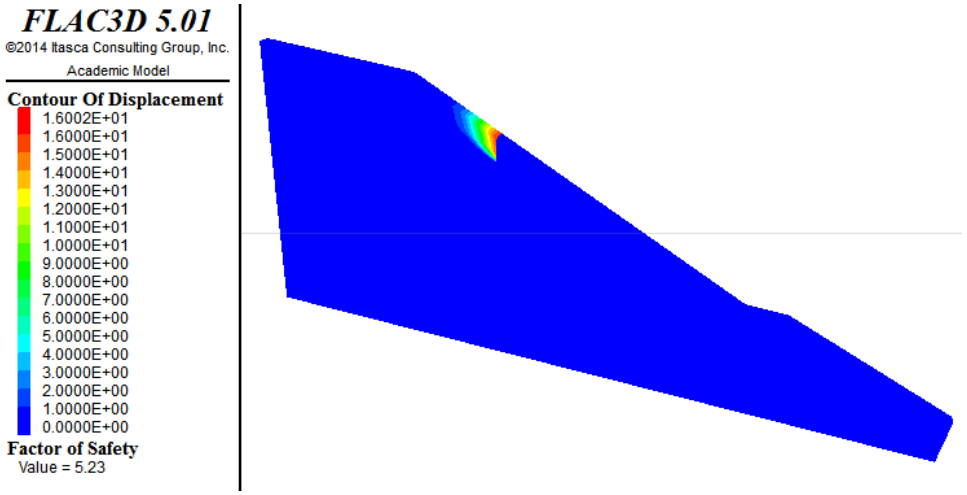

Figure 6-45 FOS of Grapevine Dam lime+fiber treated section having two parallel cracks with fully softened shear strength parameters

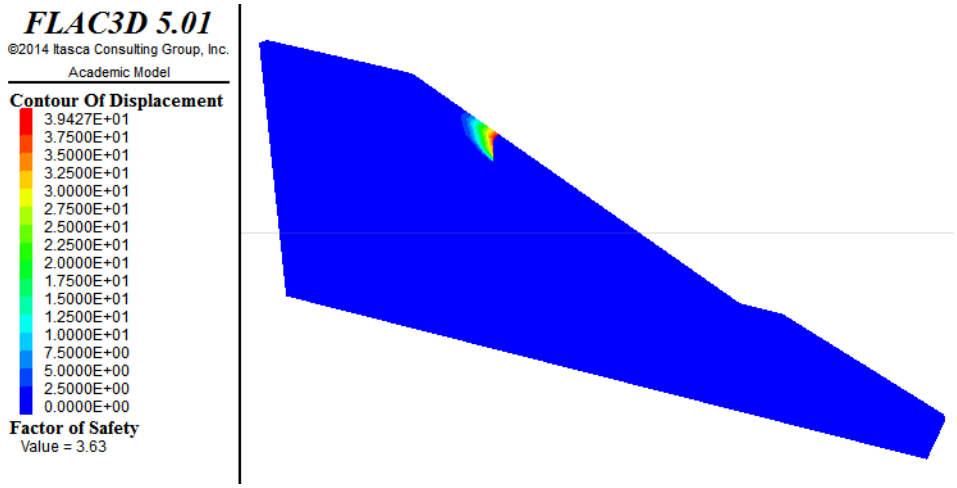

Figure 6-46 FOS of Grapevine Dam lime+fiber treated section having two parallel cracks with residual shear strength parameters

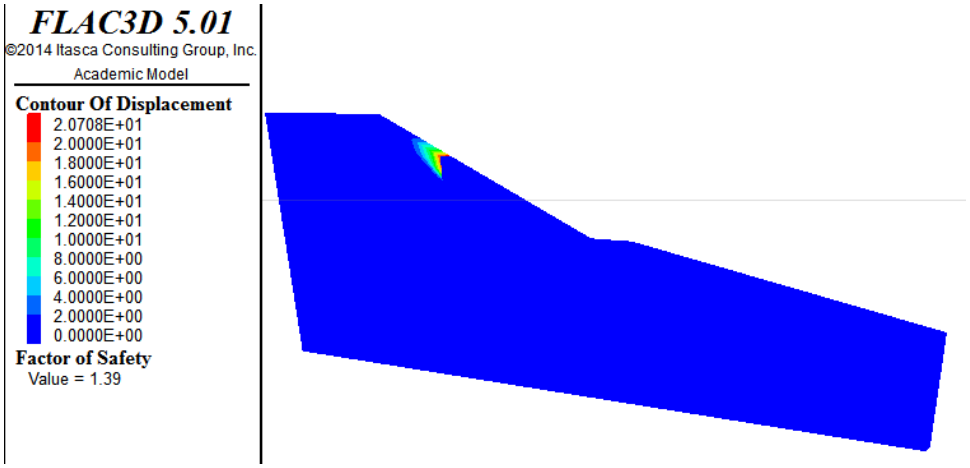

Figure 6-47 FOS of Joe Pool Dam control section having two parallel cracks with peak shear strength parameters

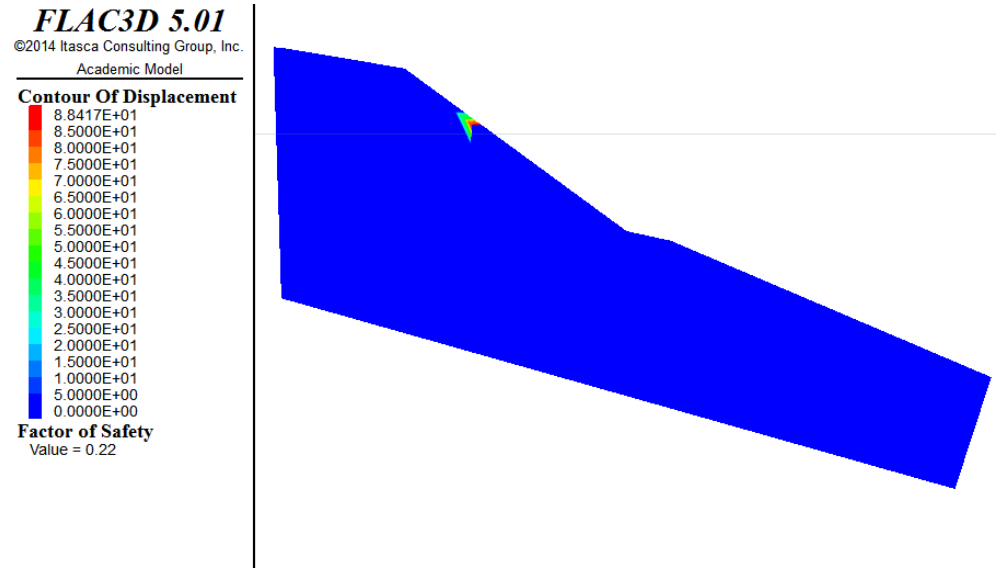

Figure 6-48 FOS of Joe Pool Dam control section having two parallel cracks with fully softened shear strength parameters

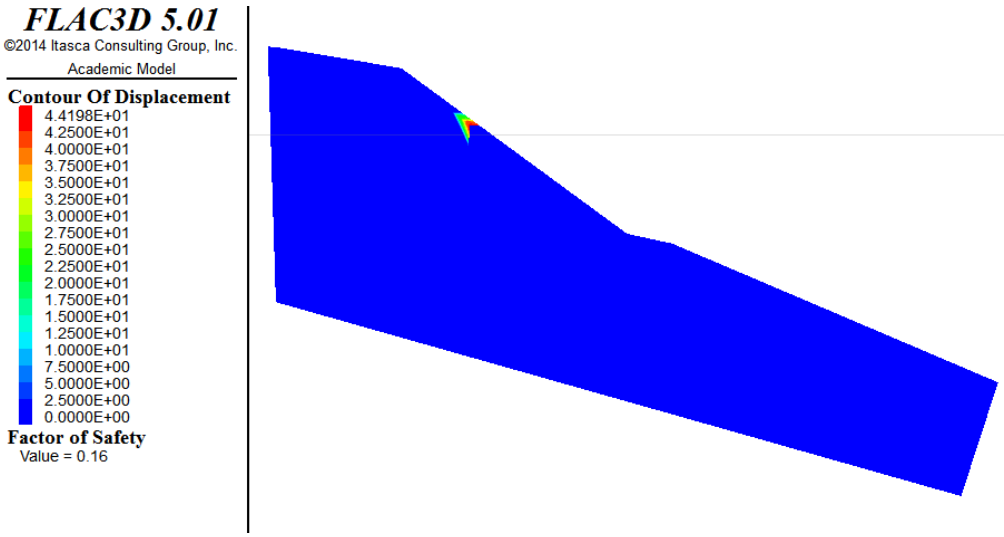

Figure 6-49 FOS of Joe Pool Dam control section having two parallel cracks with residual shear strength parameters

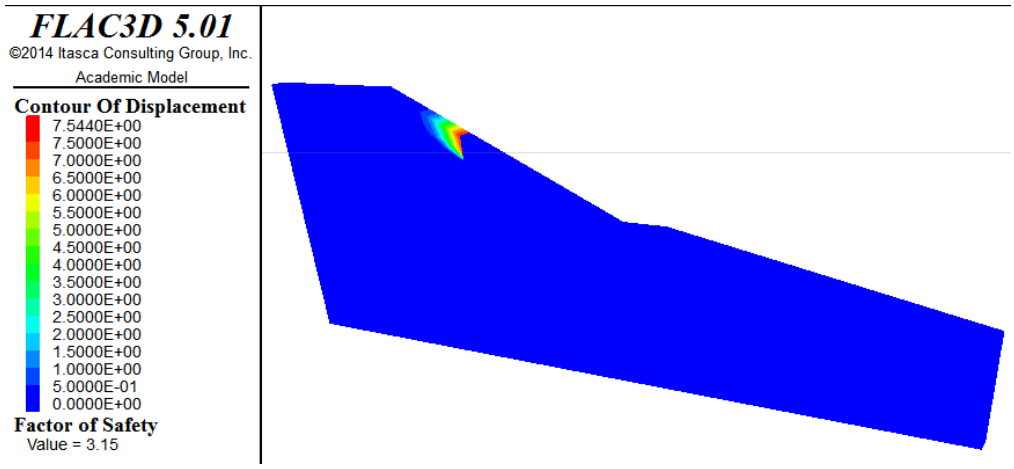

Figure 6-50 FOS of Joe Pool Dam biopolymer treated section having two parallel cracks with peak shear strength parameters

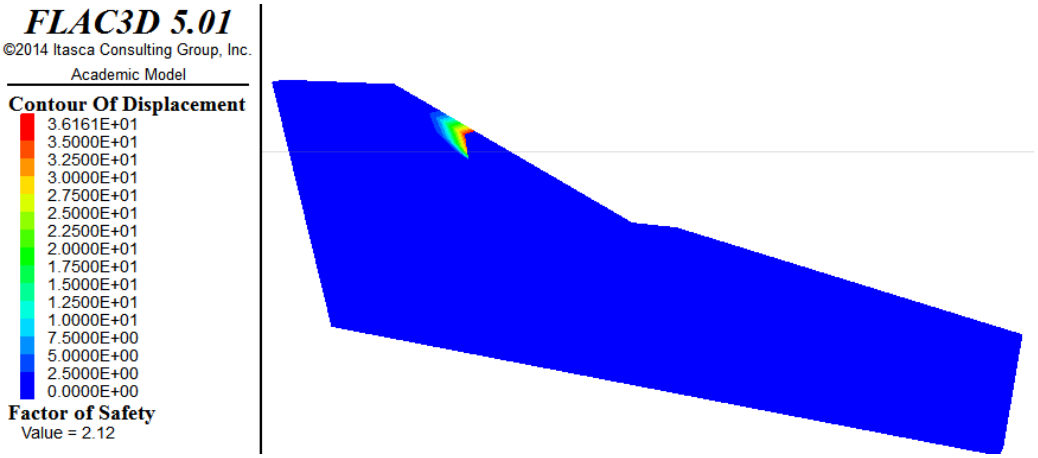

Figure 6-51 FOS of Joe Pool Dam biopolymer treated section having two parallel cracks with fully softened shear strength parameters

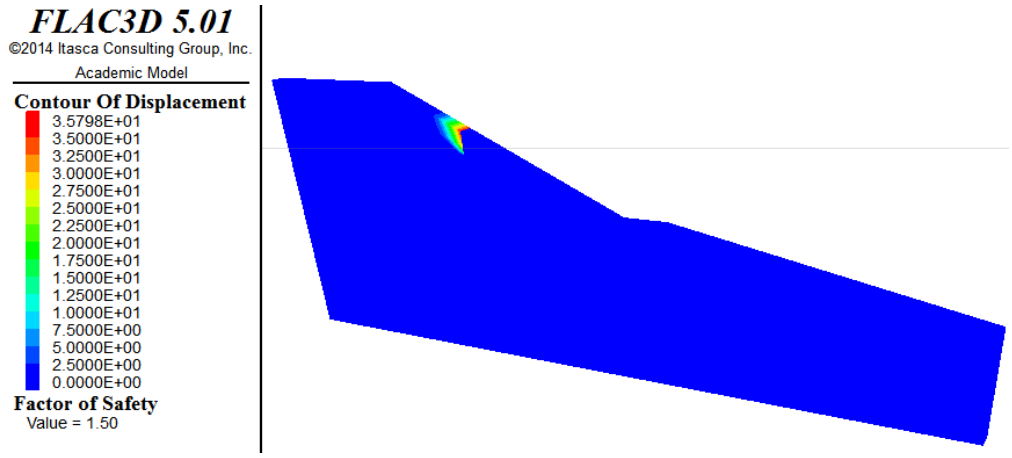

Figure 6-52 FOS of Joe Pool Dam biopolymer treated section having two parallel cracks with residual shear strength parameters

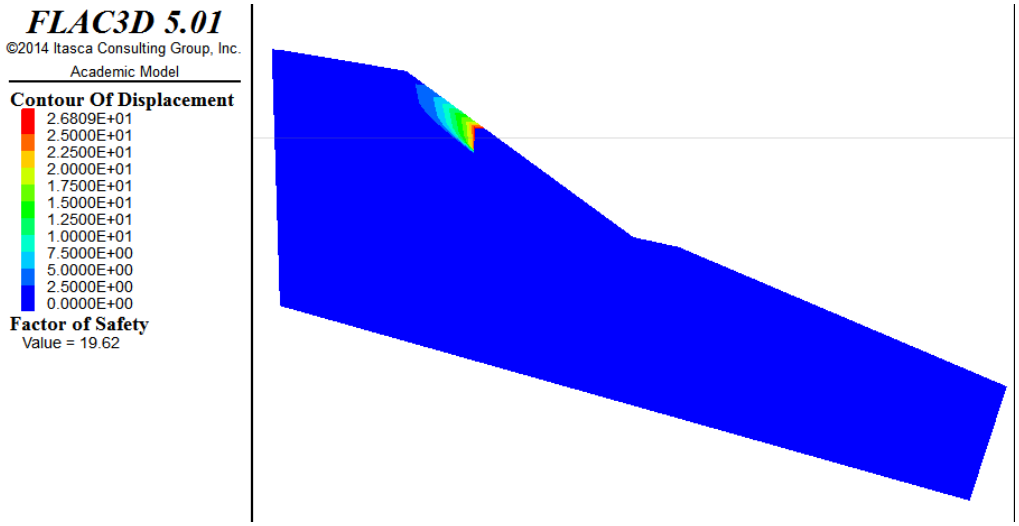

Figure 6-53 FOS of Joe Pool Dam lime treated section having two parallel cracks with peak shear strength parameters

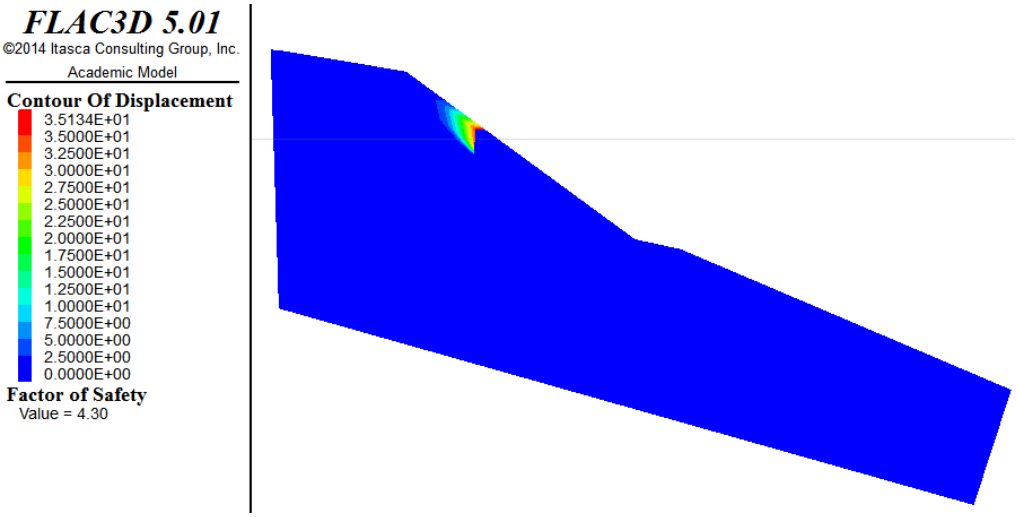

Figure 6-54 FOS of Joe Pool Dam lime treated section having two parallel cracks with fully softened shear strength parameters

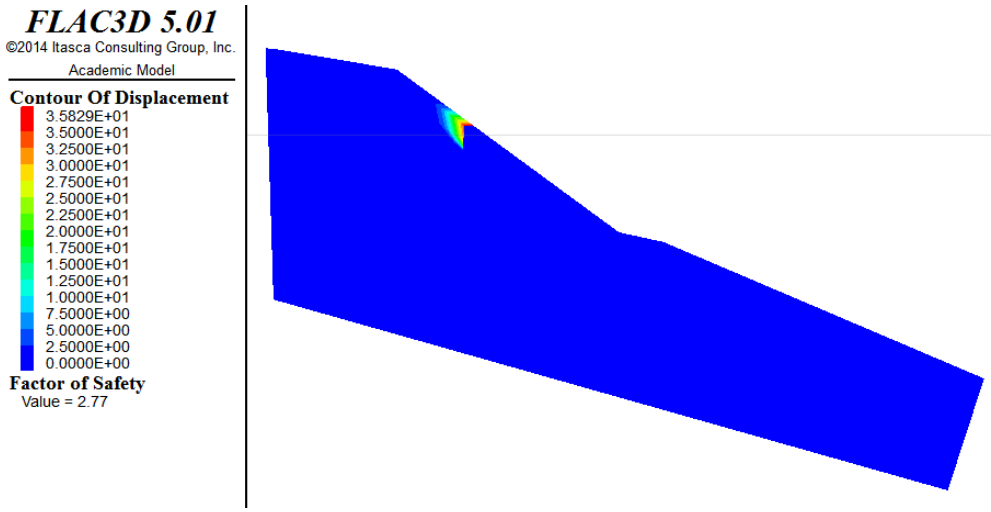

Figure 6-55 FOS of Joe Pool Dam lime treated section having two parallel cracks with residual shear strength parameters

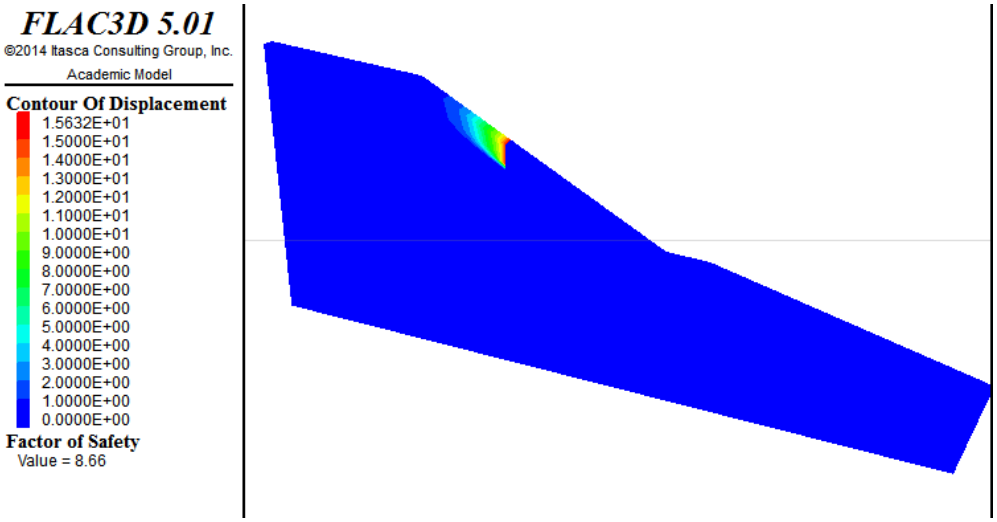

Figure 6-56 FOS of Joe Pool Dam lime+fiber treated section having two parallel cracks with peak shear strength parameters

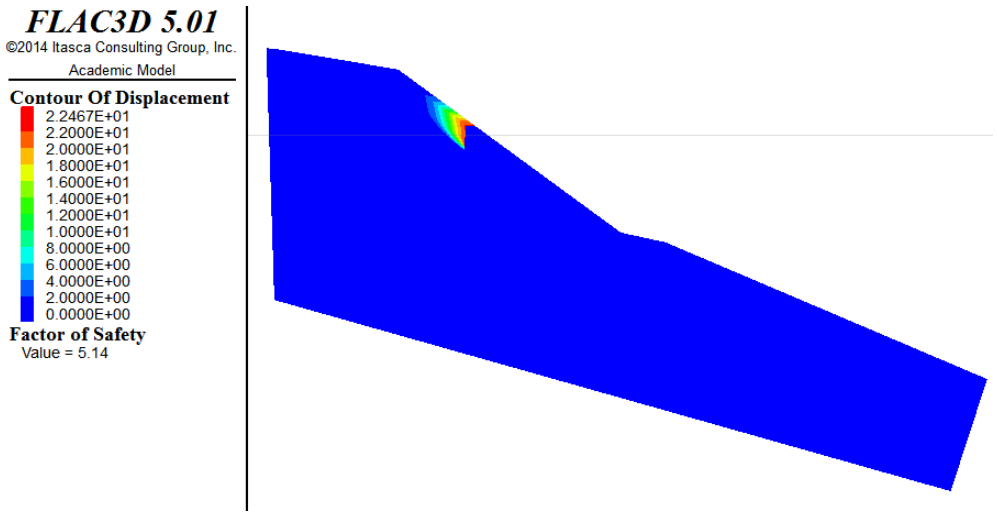

Figure 6-57 FOS of Joe Pool Dam lime+fiber treated section having two parallel cracks with fully softened shear strength parameters

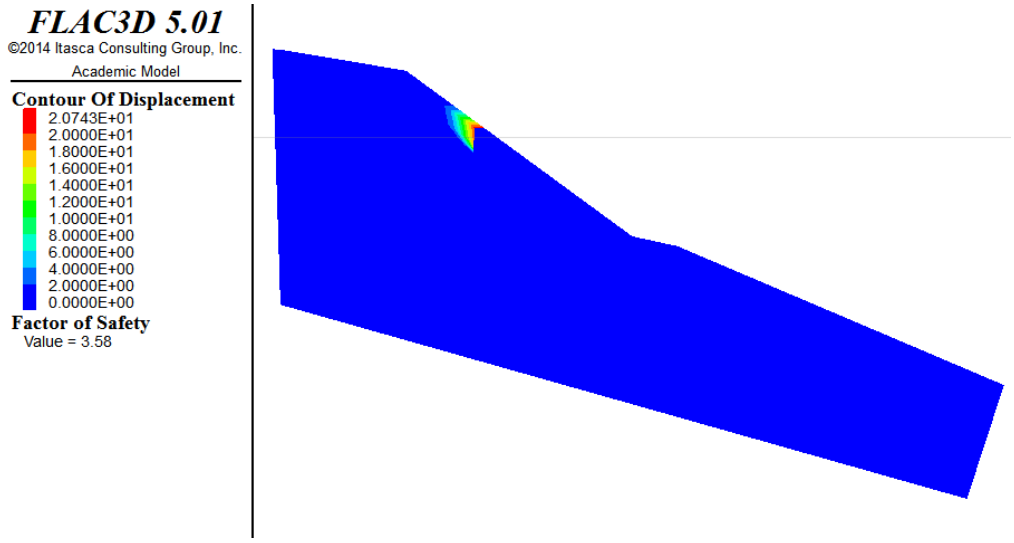

Figure 6-58 FOS of Joe Pool Dam lime+fiber treated section having two parallel cracks with residual shear strength parameters

Table 6-9 The FOS of the Grapevine Dam slope with two cracks

Soil	Peak		Fully softened		Residual	
	w/o cracks	w/ cracks	w/o cracks	w/ cracks	w/o cracks	w/ cracks
Control	1.83	0.94	1.30	0.3	0.84	0.15
Biopolymer treated	3.93	2.86	2.71	1.98	2.05	1.38
Lime treated	16.87	14.19	6.84	2.55	4.94	2.55
Lime+fiber treated	10.12	8.25	5.7	5.23	4.19	3.63

Table 6-10 The FOS of the Joe Pool Dam slope with two cracks

Soil	Peak		Fully softened		Residual	
	w/o cracks	w/ cracks	w/o cracks	w/ cracks	w/o cracks	w/ cracks
Control	2.19	1.39	1.30	0.22	0.92	0.16
Biopolymer treated	4.30	3.15	2.91	2.12	2.27	1.5
Lime treated	26.37	19.62	6.84	4.30	5.01	2.77
Lime+fiber treated	22.56	8.66	5.7	5.14	4.08	3.58

6.5.2 A Network of Intersecting Cracks

It was observed that the introduction of the two parallel cracks on the slopes generally reduced the FOS of the slopes. However, the FOS of the most of the sections was still higher than the minimum safe FOS limit of 1.5. One reason for this can be the locations of the cracks. The cracks may not be located in the places where their presence would have reduced the FOS significantly. The other reason may be that the presence of cracks in the alignment direction may not have great effect in the FOS of the slope. To further investigate the effect of cracks, a network of cracks was created with cracks running in two perpendicular directions. The manually created crack network in the slope is as shown in Figure 6-59. The failure modes and FOS of the Grapevine Dam slope with crack network are presented in Figure 6-60 through Figure 6-69. The same for Joe Pool Dam slope is presented in Figure 6-70 to Figure 6-79. Table 6-11 shows the FOS of the Grapevine Dam slope with and without the network of cracks. Similarly, Table 6-12 shows the same for Joe Pool soil.

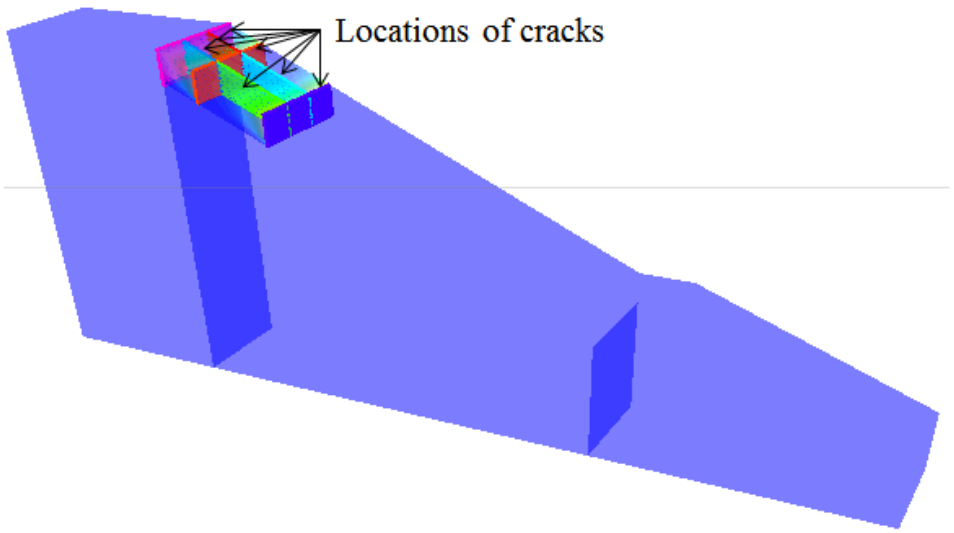

Figure 6-59 Network of the cracks intersecting orthogonally

It can be observed from Table 6-11 and Table 6-12 that the presence of a network of cracks can reduce the FOS of a slope significantly. The FOS decreased from 2.27 to 0.82 for the biopolymer treated section in Joe Pool dam. A FOS of 2.27 is considered safe in slope stability analysis. A FOS of less than 1 is considered a failure. Thus a network of crack can cause the surficial failure of otherwise stable slope. It is also to be noted that the presence of cracks in the crest only in the alignment direction is not very problematic as evidenced from the earlier analysis.

Comparison of the FOS for Grapevine and Joe Pool dam slopes with and without the cracks are shown in Figure 6-80 and Figure 6-81 respectively. As

expected, the network of orthogonally intersecting cracks showed higher reduction in the FOS of the slopes.

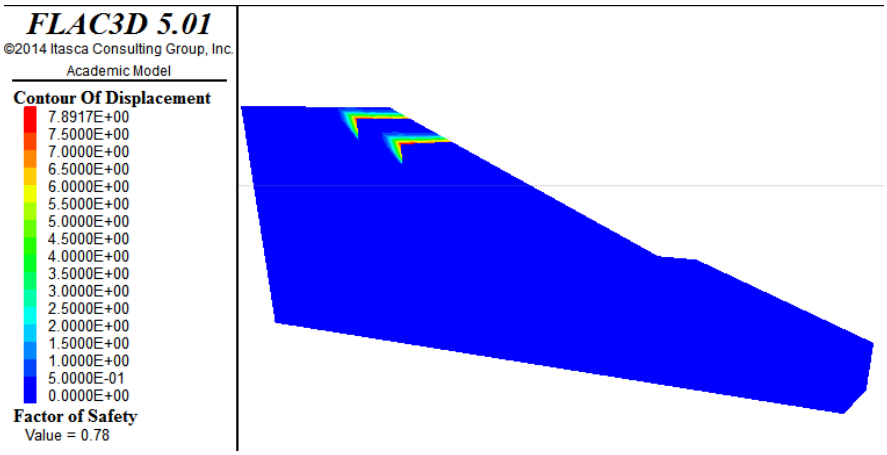

Figure 6-60 FOS of Grapevine Dam control section having a network of intersecting cracks with peak shear strength parameters

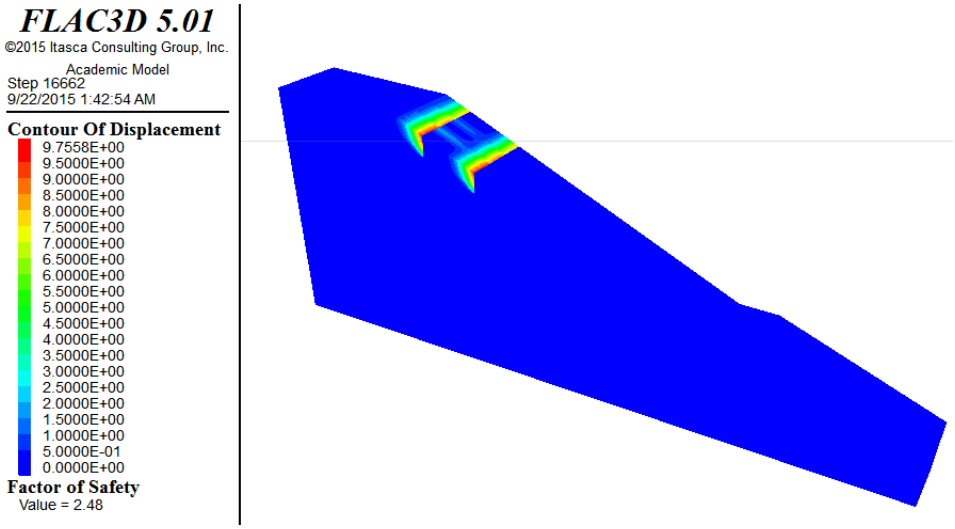

Figure 6-61 FOS of Grapevine Dam biopolymer treated section having a network of intersecting cracks with peak shear strength parameters

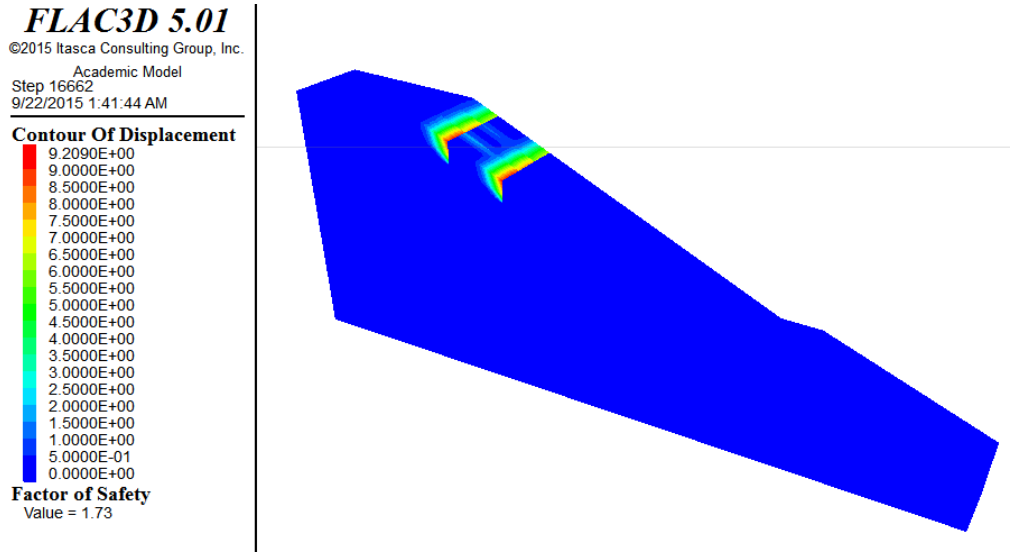

Figure 6-62 FOS of Grapevine Dam biopolymer treated section having a network of intersecting cracks with fully softened shear strength parameters

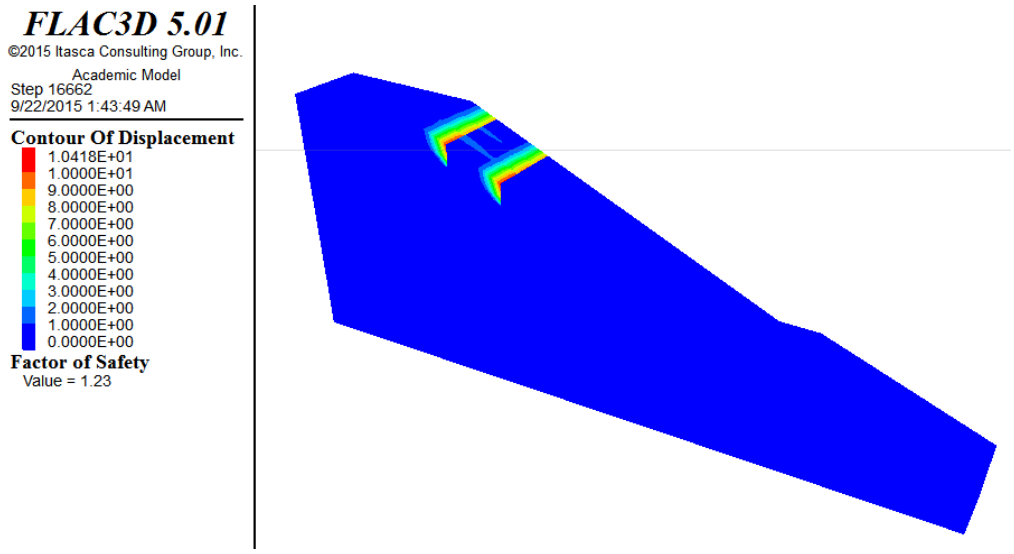

Figure 6-63 FOS of Grapevine Dam biopolymer treated section having a network of intersecting cracks with residual shear strength parameters

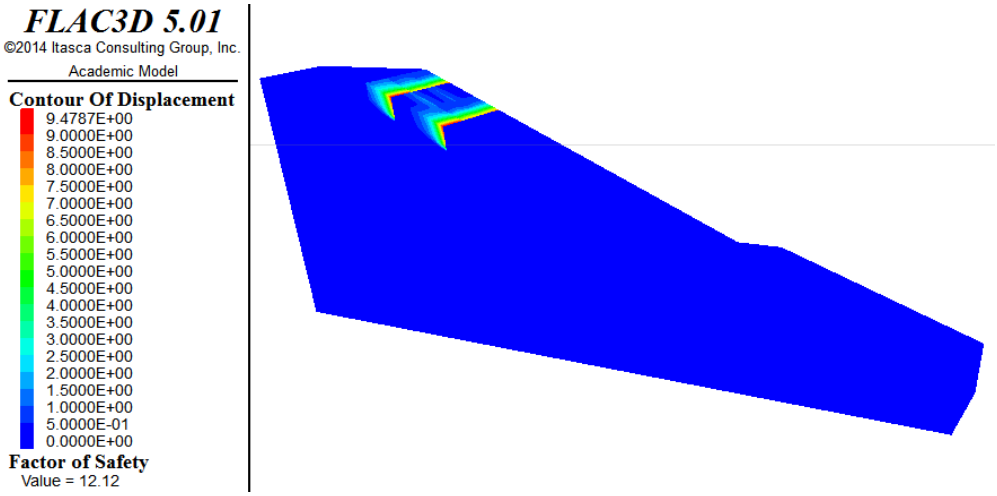

Figure 6-64 FOS of Grapevine Dam lime treated section having a network of intersecting cracks with peak shear strength parameters

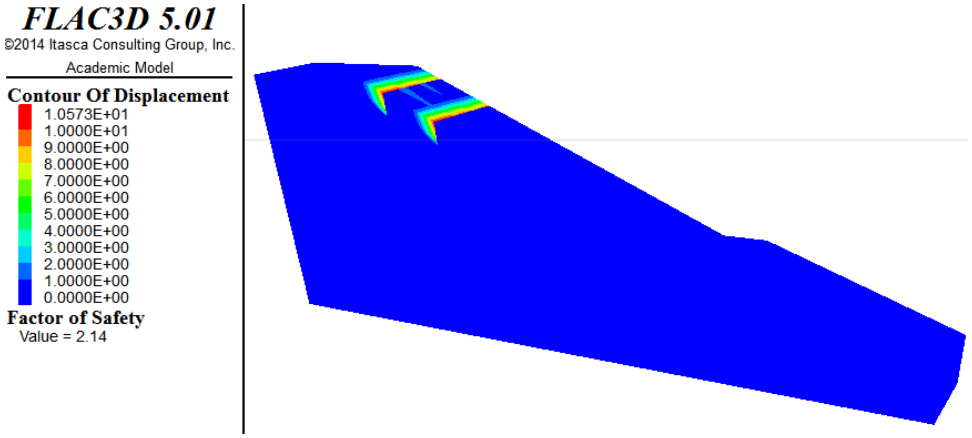

Figure 6-65 FOS of Grapevine Dam lime treated section having a network of intersecting cracks with fully softened shear strength parameters

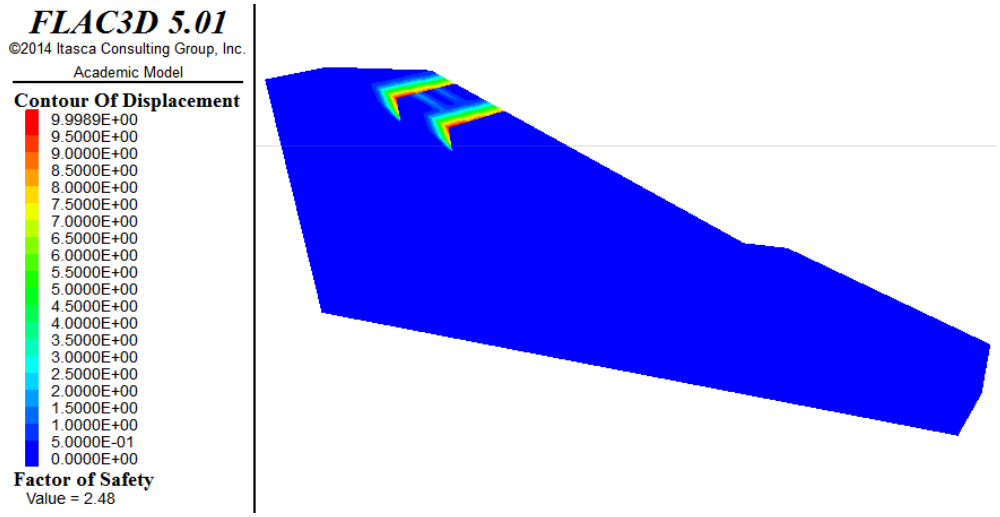

Figure 6-66 FOS of Grapevine Dam lime treated section having a network of intersecting cracks with residual shear strength parameters

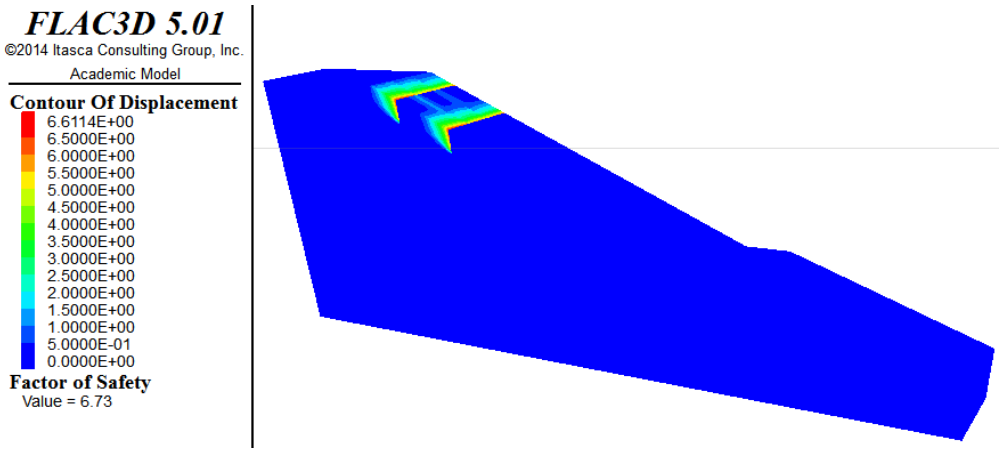

Figure 6-67 FOS of Grapevine Dam lime+fiber treated section having a network of intersecting cracks with peak shear strength parameters

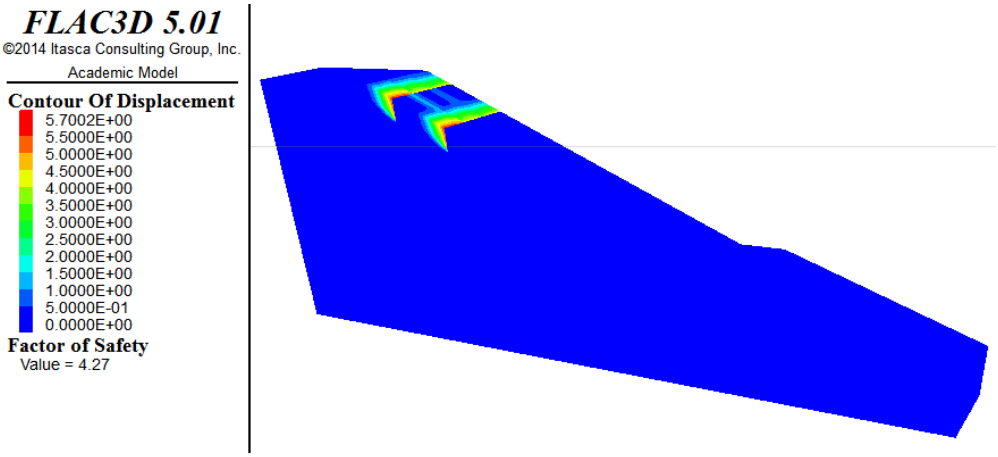

Figure 6-68 FOS of Grapevine Dam lime+fiber treated section having a network of intersecting cracks with fully softened shear strength parameters

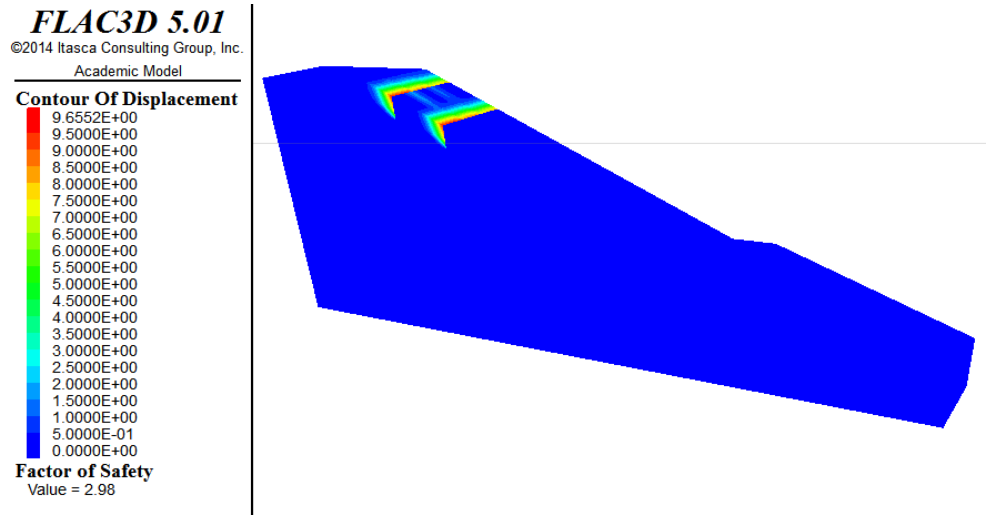

Figure 6-69 FOS of Grapevine Dam lime+fiber treated section having a network of intersecting cracks with residual shear strength parameters

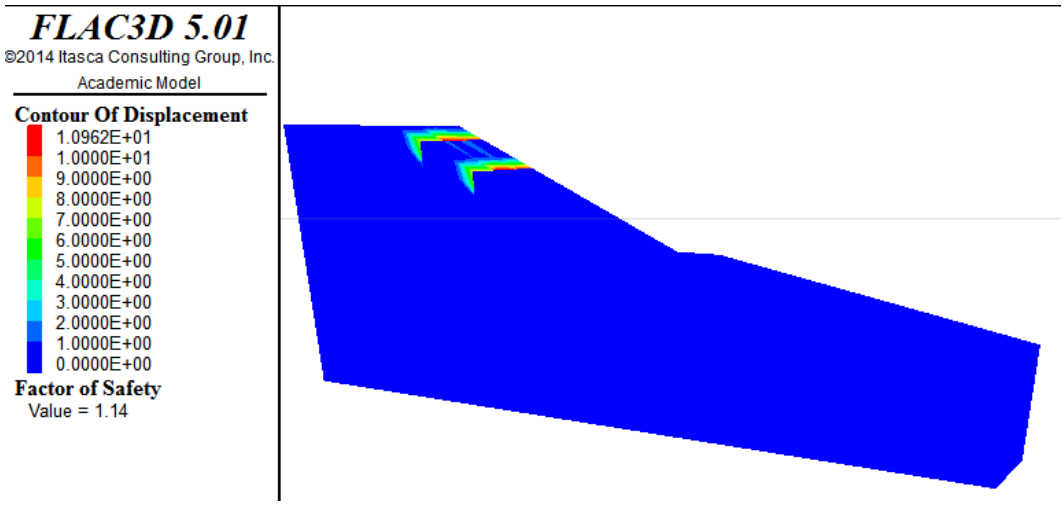

Figure 6-70 FOS of Joe Pool Dam control section having a network of intersecting cracks with peak shear strength parameters

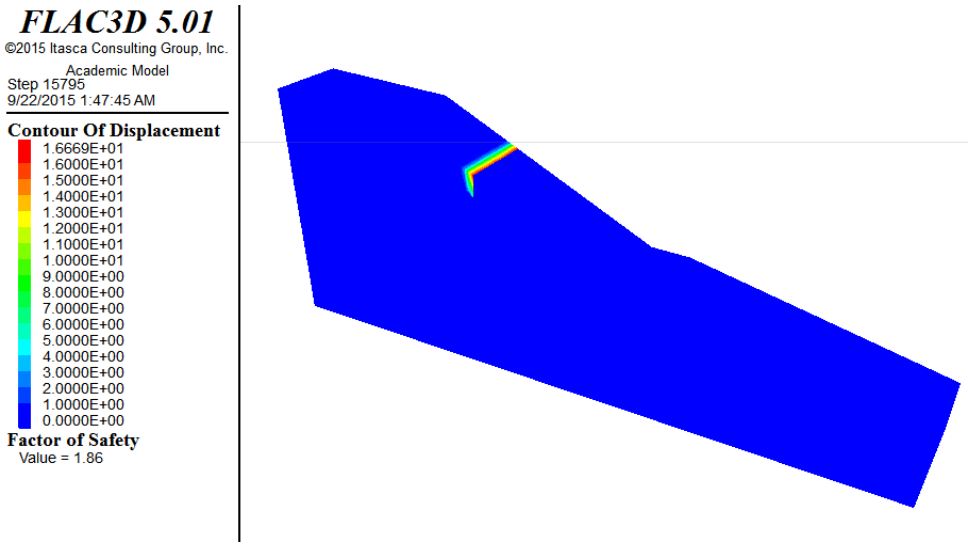

Figure 6-71 FOS of Joe Pool Dam biopolymer treated section having a network of intersecting cracks with peak shear strength parameters

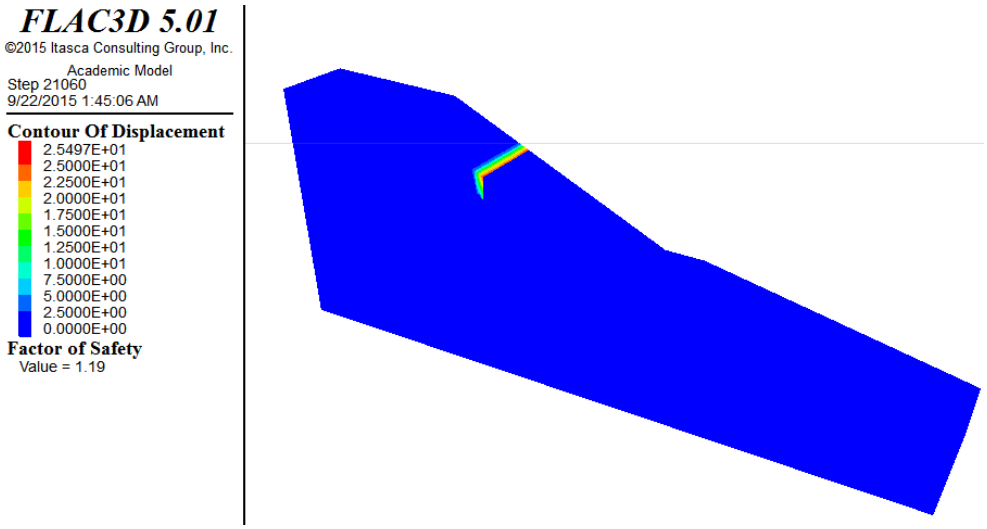

Figure 6-72 FOS of Joe Pool Dam biopolymer treated section having a network of intersecting cracks with fully softened shear strength parameters

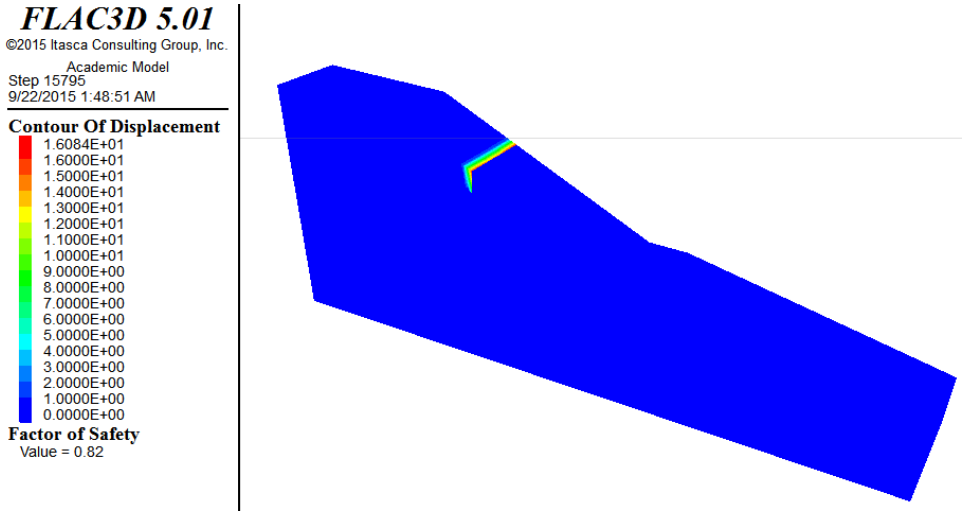

Figure 6-73 FOS of Joe Pool Dam biopolymer treated section having a network of intersecting cracks with residual shear strength parameters

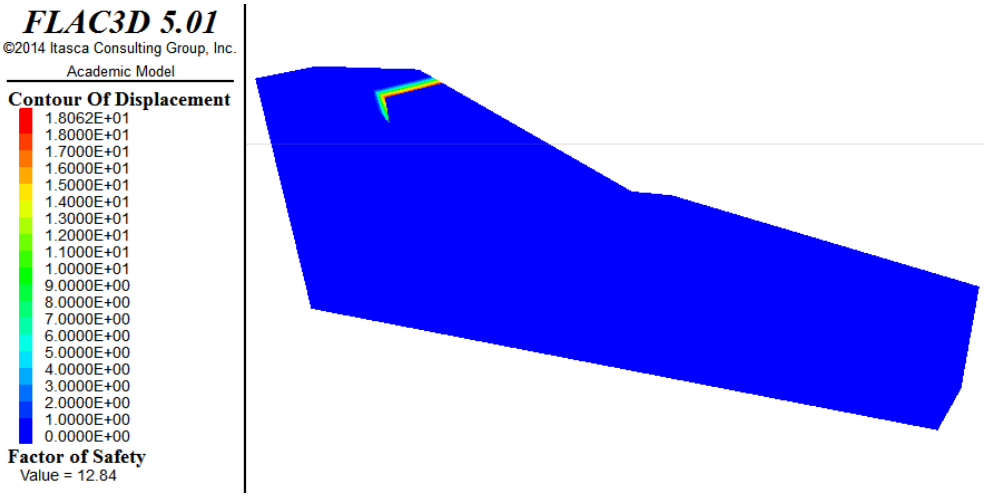

Figure 6-74 FOS of Joe Pool Dam lime treated section having a network of intersecting cracks with peak shear strength parameters

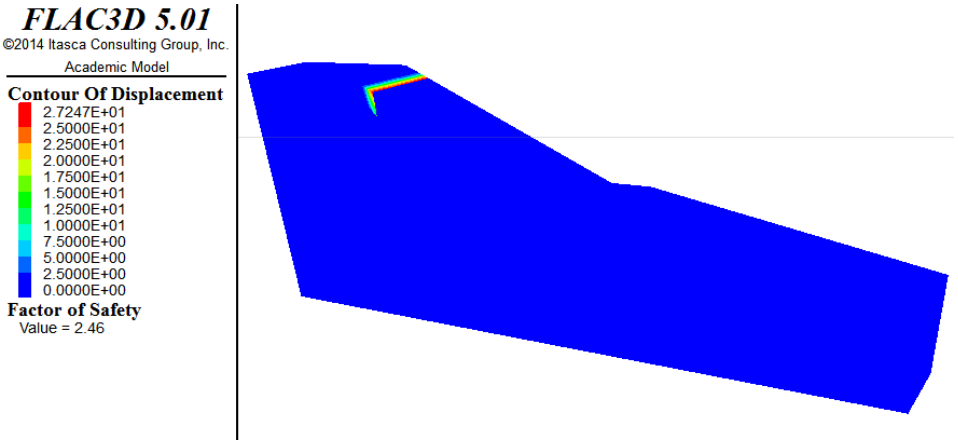

Figure 6-75 FOS of Joe Pool Dam lime treated section having a network of intersecting cracks with fully softened shear strength parameters

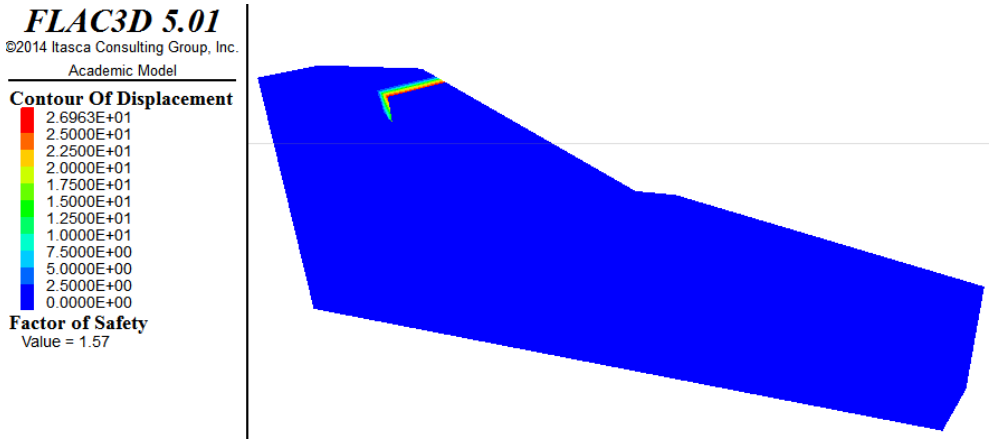

Figure 6-76 FOS of Joe Pool Dam lime treated section having a network of intersecting cracks with residual shear strength parameters

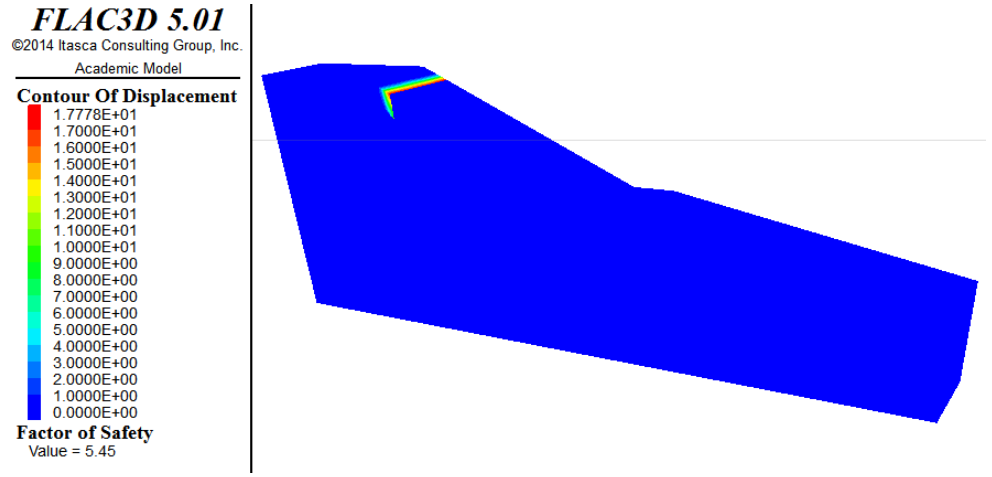

Figure 6-77 FOS of Joe Pool Dam lime+fiber treated section having a network of intersecting cracks with peak shear strength parameters

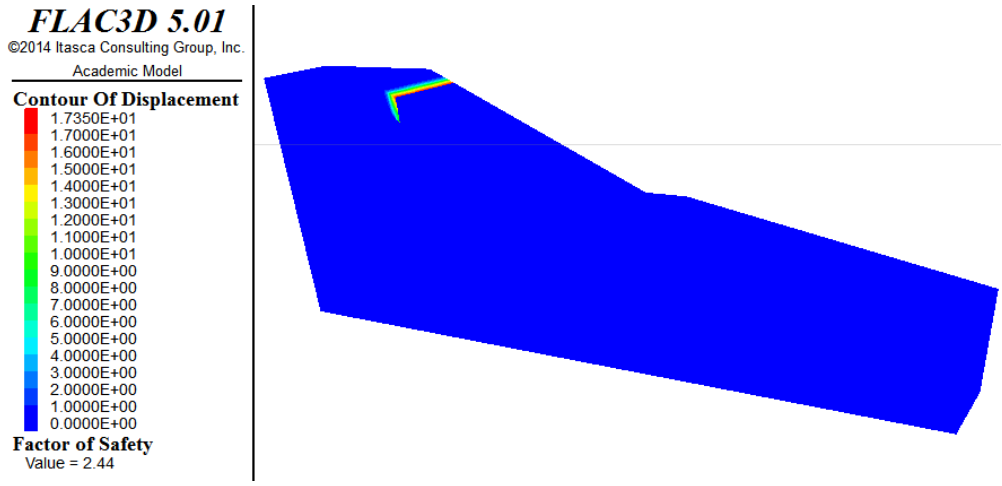

Figure 6-78 FOS of Joe Pool Dam lime+fiber treated section having a network of intersecting cracks with fully softened shear strength parameters

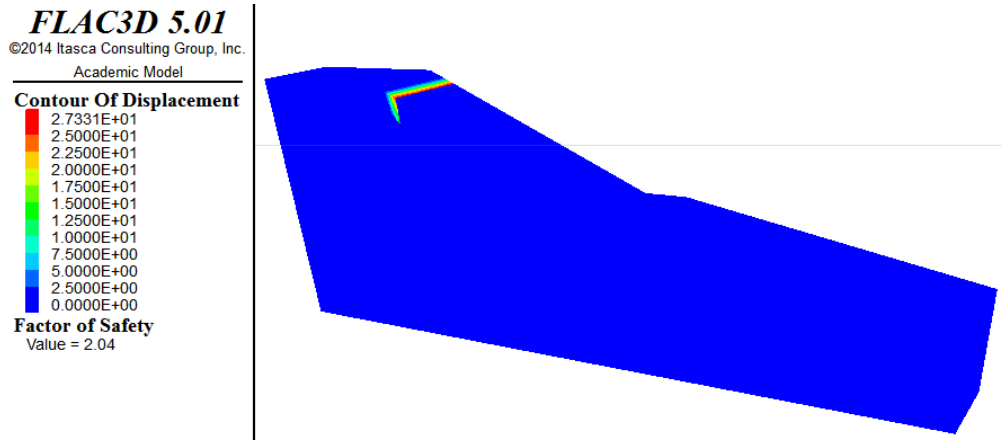

Figure 6-79 FOS of Joe Pool Dam lime+fiber treated section having a network of intersecting cracks with residual shear strength parameters

Table 6-11 The FOS of the Grapevine Dam slope with a network of orthogonal cracks

Soil	Peak		Fully softened		Residual	
	w/o cracks	w/ cracks	w/o cracks	w/ cracks	w/o cracks	w/ cracks
Control	1.83	0.78	1.30	-	0.84	-
Biopolymer treated	3.93	2.48	2.71	1.73	2.05	1.23
Lime treated	16.87	12.09	6.84	2.13	4.94	2.48
Lime+fiber treated	10.12	6.73	5.7	4.27	4.19	2.98

Table 6-12 The FOS of the Joe Pool dam slope with a network of orthogonal cracks

Soil	Peak		Fully softened		Residual	
	w/o cracks	w/ cracks	w/o cracks	w/ cracks	w/o cracks	w/ cracks
Control	2.19	1.14	1.30	-	0.92	-
Biopolymer treated	4.30	1.86	2.91	1.19	2.27	0.82
Lime treated	26.37	12.84	6.84	2.46	5.01	1.57
Lime+fiber treated	22.56	5.45	5.7	2.43	4.08	2.04

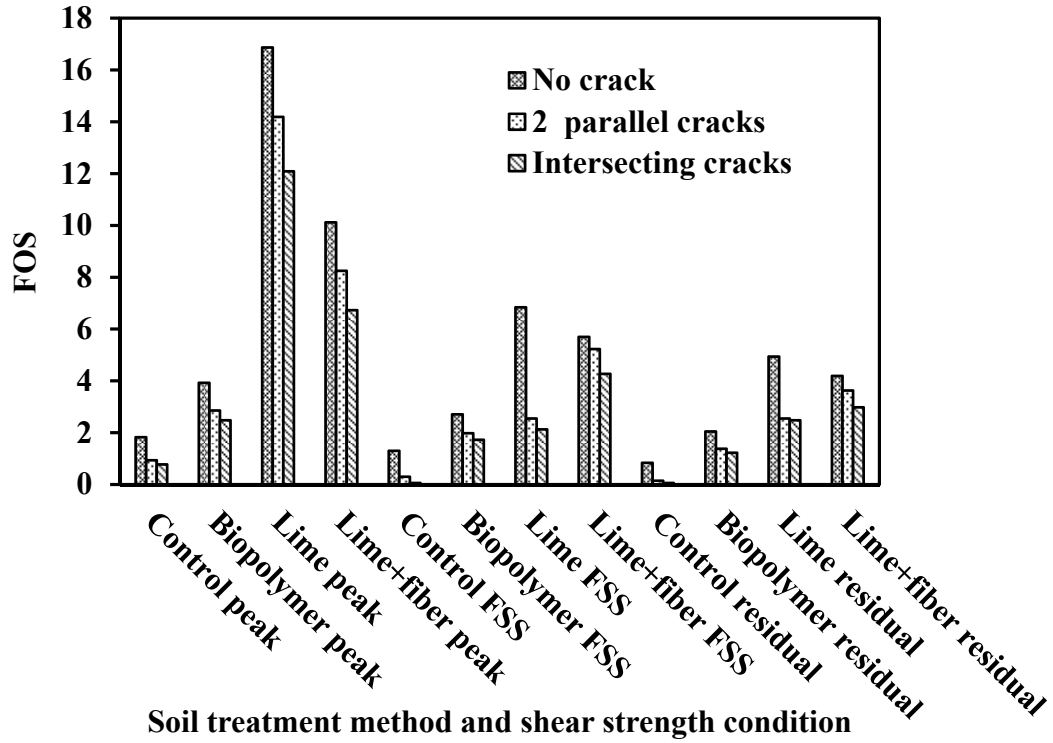

Figure 6-80 Comparison of FOS of the different sections of Grapevine Dam slope with different shear strength and cracking conditions

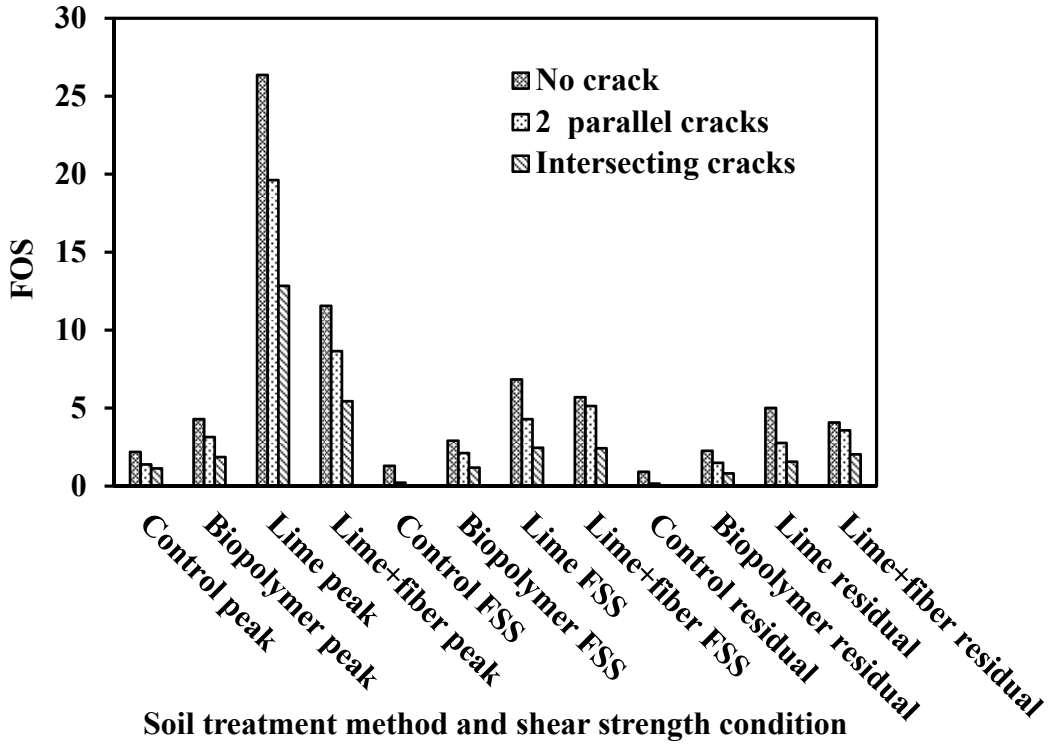

Figure 6-81 Comparison of FOS of the different sections of Joe Pool Dam slope with different shear strength and cracking conditions

A separate parametric study was conducted to analyze the stability of the dam slopes with the crack network by varying shear strengths. First, the friction angle was varied from 0 to 30 degrees while keeping the cohesion intercept constant at 20 kPa. Then, the cohesion intercept was varied from 10 to 40 kPa while keeping the friction angle constant at 20 degrees. The results of the parametric study are presented in Table 6-13. Similarly, the sensitivity of the parameters in the reduction of FOS due to presence of crack network in both of the dam slopes was assessed using the plot as shown in Figure 6-82. The failure

modes and failure modes for the analyses are presented in Figure 6-83 through Figure 6-110. There was a constant rate of reduction in the FOS when friction angle was reduced from 30 to 0 degrees. On the other hand, the rate of reduction in FOS decreased with decrease in cohesion from 40 to 10 kPa for Grapevine Dam slope. The opposite trend was observed for the Joe Pool dam slope while varying the cohesion from 40 to 10 kPa. It indicated that a slope well above the FOS margin of 1.5 can become vulnerable to surficial slope failure due to presence of networks of cracks.

Table 6-13 Results of the parametric study with and without network of cracks

Soil	Friction angle (degrees)	FOS		Cohesion (kPa)	FOS	
		w/o crack	w/ crack		w/o crack	w/ crack
GV	0	3.02	2.35	10	2.52	1.65
	10	3.52	2.59	20	4.05	2.83
	20	4.05	2.83	30	5.59	4.02
	30	4.64	3.09	40	7.33	5.23
JP	0	3.27	2.38	10	2.65	1.66
	10	3.78	2.62	20	4.33	2.84
	20	4.33	2.84	30	5.97	4.06
	30	4.92	3.11	40	7.45	5.3

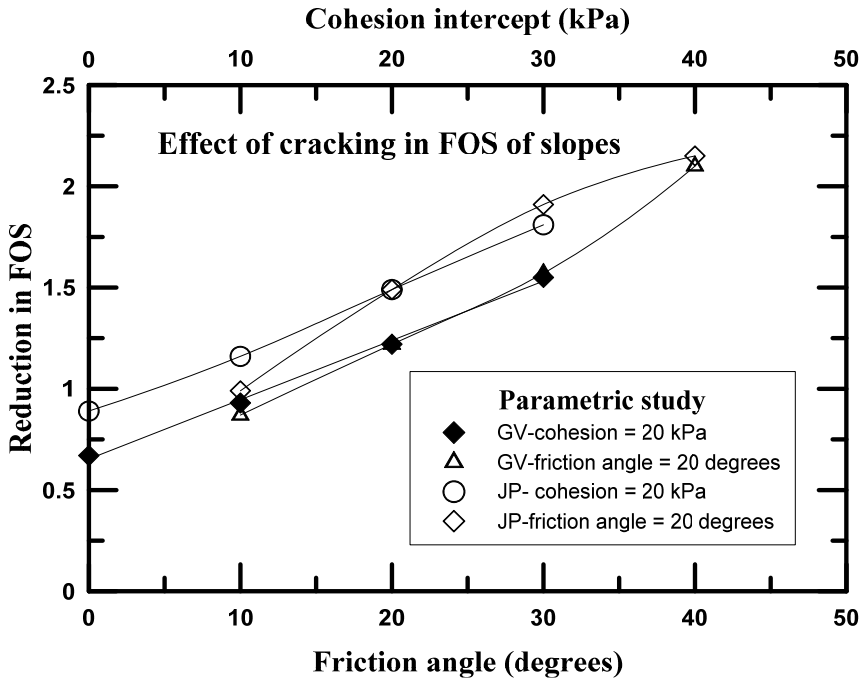

Figure 6-82 The difference in FOS with and without cracks at different friction and cohesion levels

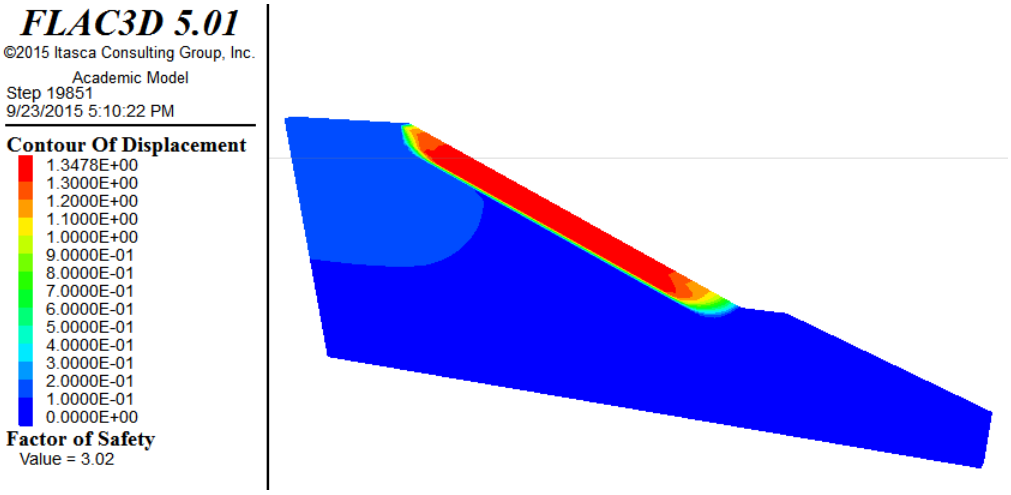

Figure 6-83 FOS of Grapevine Dam slope with top soil cohesion of 20 kPa and friction angle of 0 degree

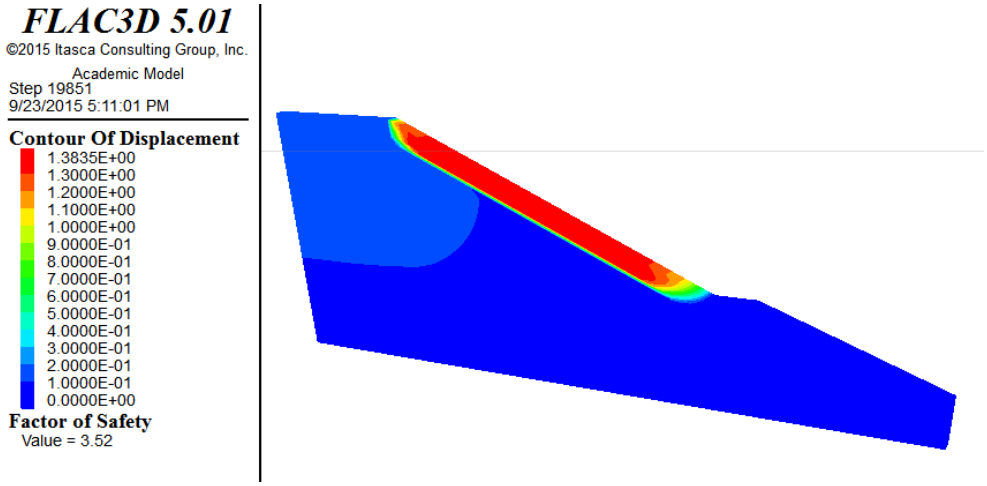

Figure 6-84 FOS of Grapevine Dam slope with top soil cohesion of 20 kPa and friction angle of 10 degrees

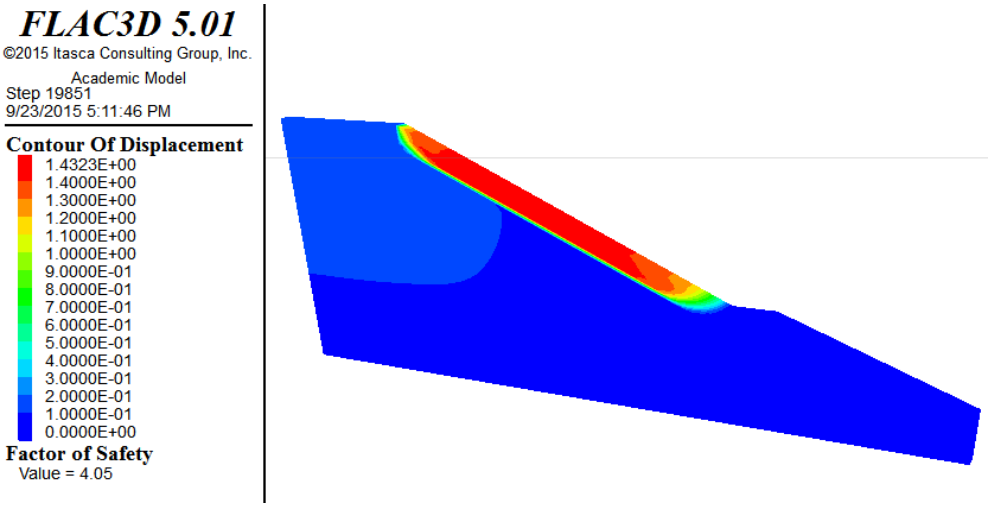

Figure 6-85 FOS of Grapevine Dam slope with top soil cohesion of 20 kPa and friction angle of 20 degrees

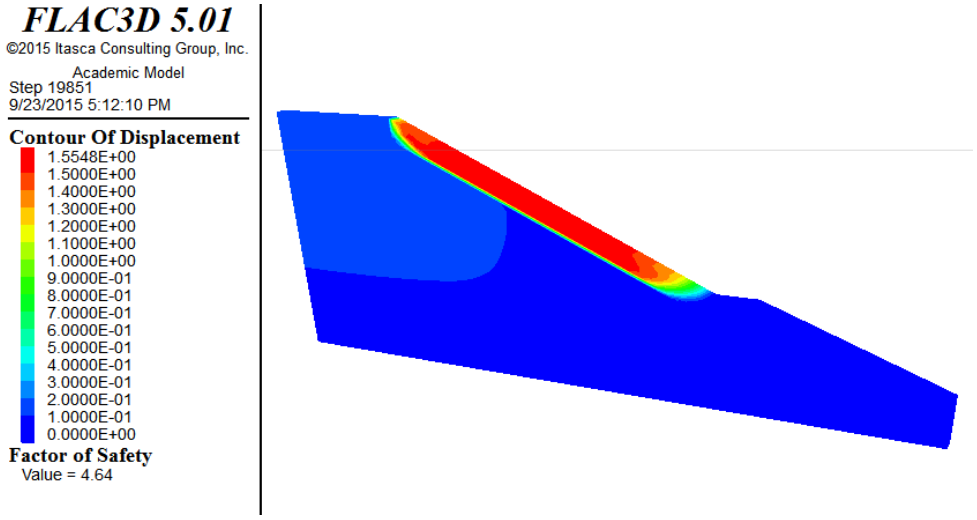

Figure 6-86 FOS of Grapevine Dam slope with top soil cohesion of 20 kPa and friction angle of 30 degrees

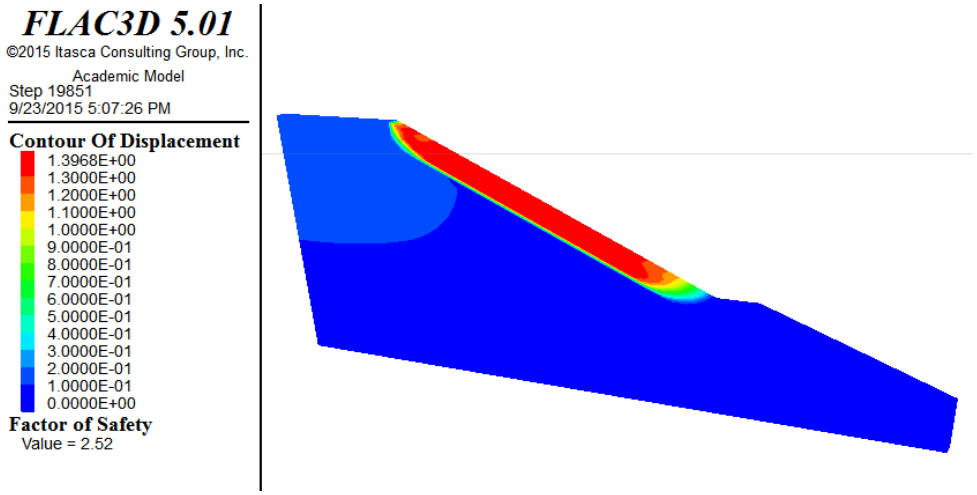

Figure 6-87 FOS of Grapevine Dam slope with top soil cohesion of 10 kPa and friction angle of 20 degrees

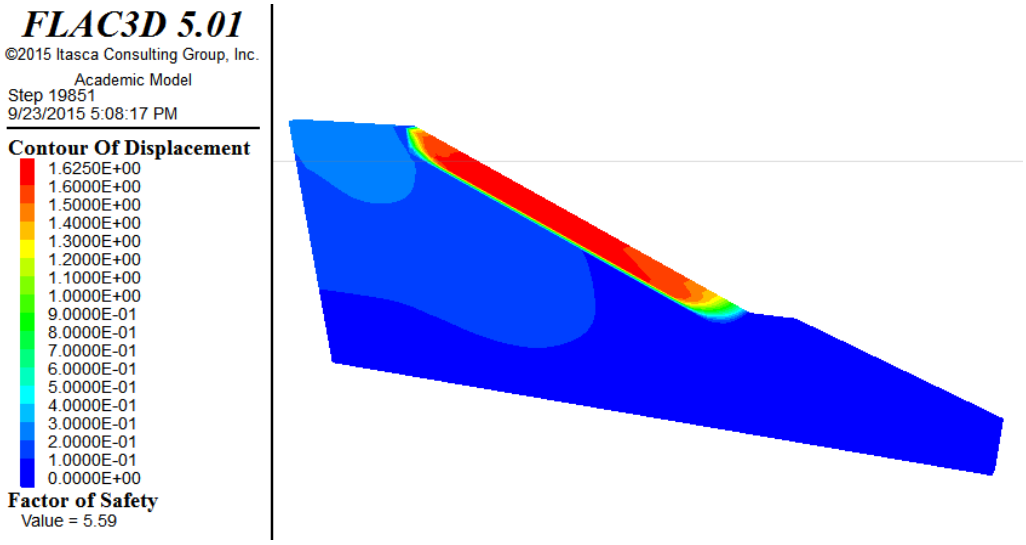

Figure 6-88 FOS of Grapevine Dam slope with top soil cohesion of 30 kPa and friction angle of 20 degrees

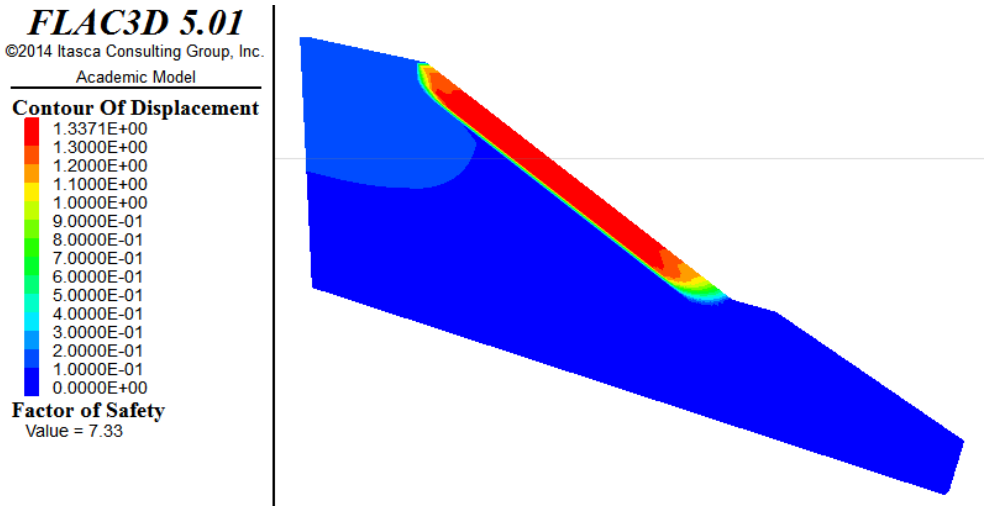

Figure 6-89 FOS of Grapevine Dam slope with top soil cohesion of 40 kPa and friction angle of 20 degrees

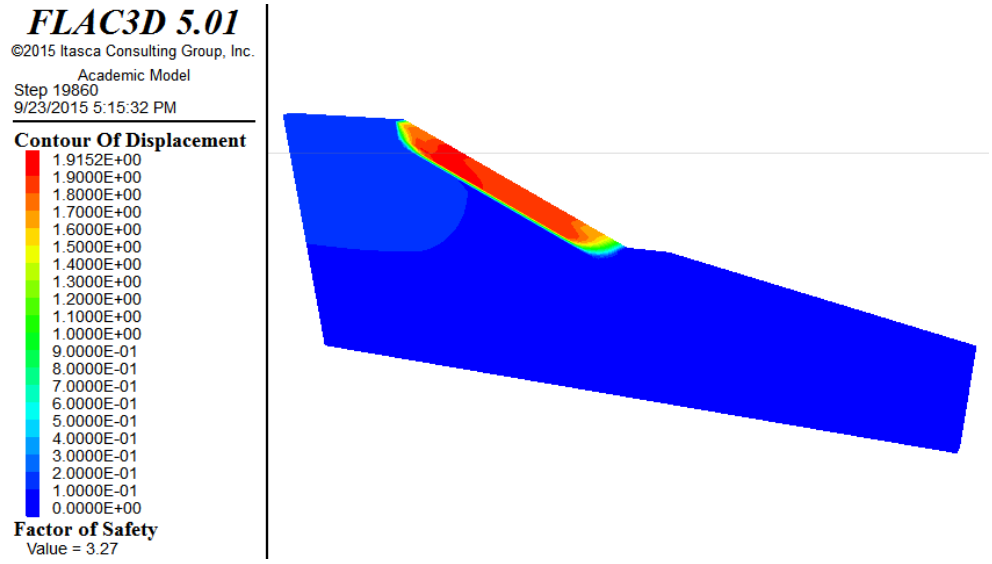

Figure 6-90 FOS of Joe Pool Dam slope with top soil cohesion of 20 kPa and friction angle of 0 degrees

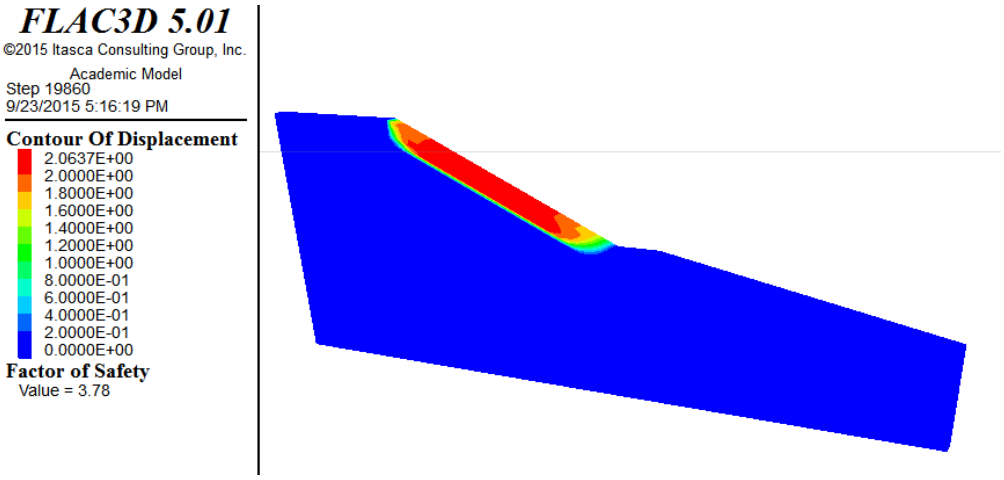

Figure 6-91 FOS of Joe Pool Dam slope with top soil cohesion of 20 kPa and friction angle of 10 degrees

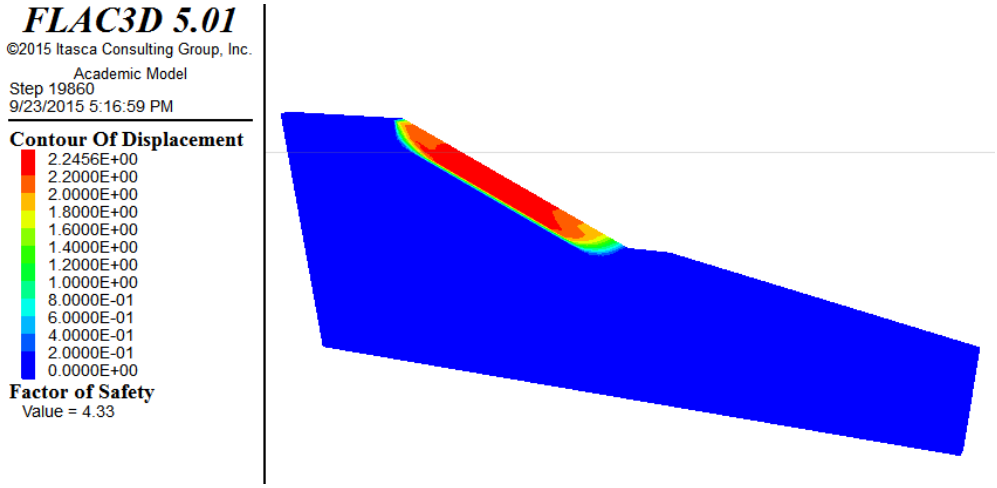

Figure 6-92 FOS of Joe Pool Dam slope with top soil cohesion of 20 kPa and friction angle of 20 degrees

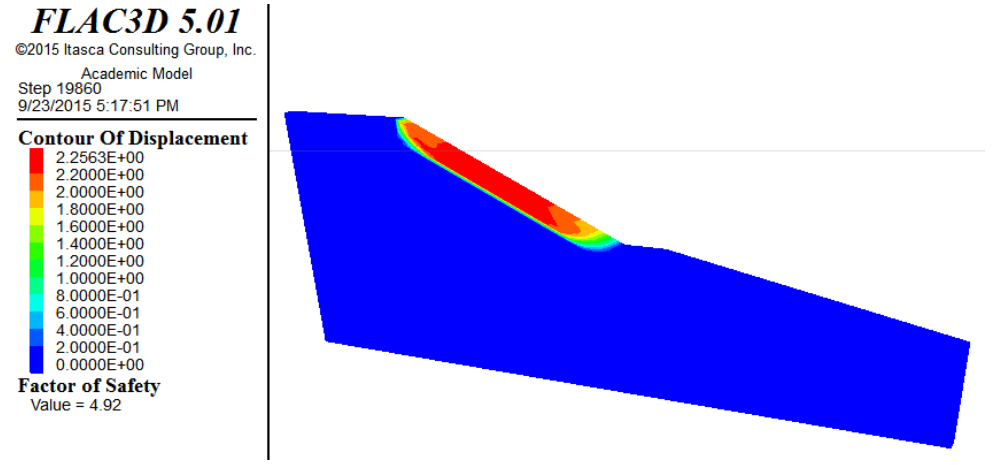

Figure 6-93 FOS of Joe Pool Dam slope with top soil cohesion of 20 kPa and friction angle of 30 degrees

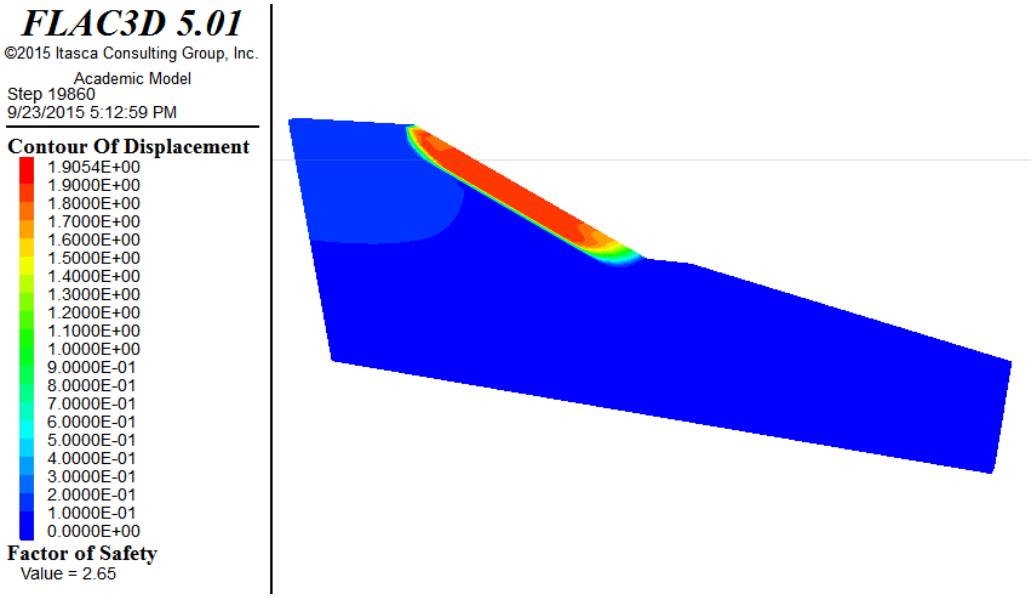

Figure 6-94 FOS of Joe Pool Dam slope with top soil cohesion of 10 kPa and friction angle of 20 degrees

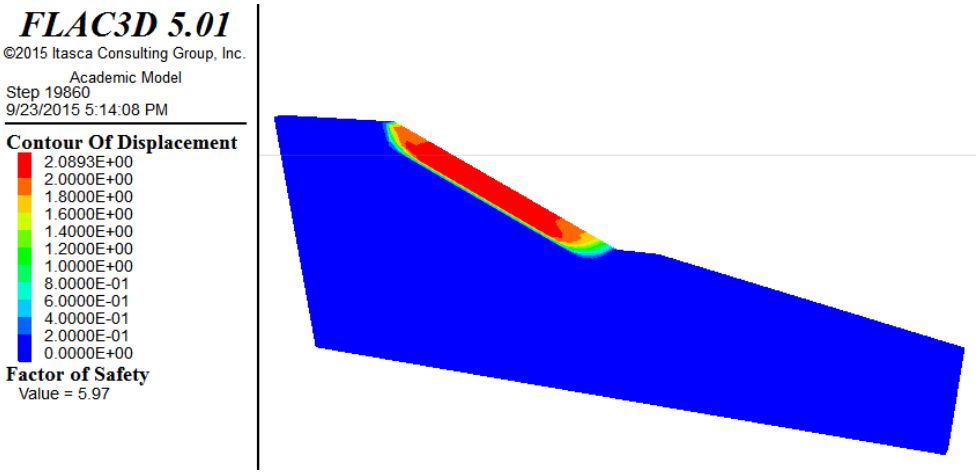

Figure 6-95 FOS of Joe Pool Dam slope with top soil cohesion of 30 kPa and friction angle of 20 degrees

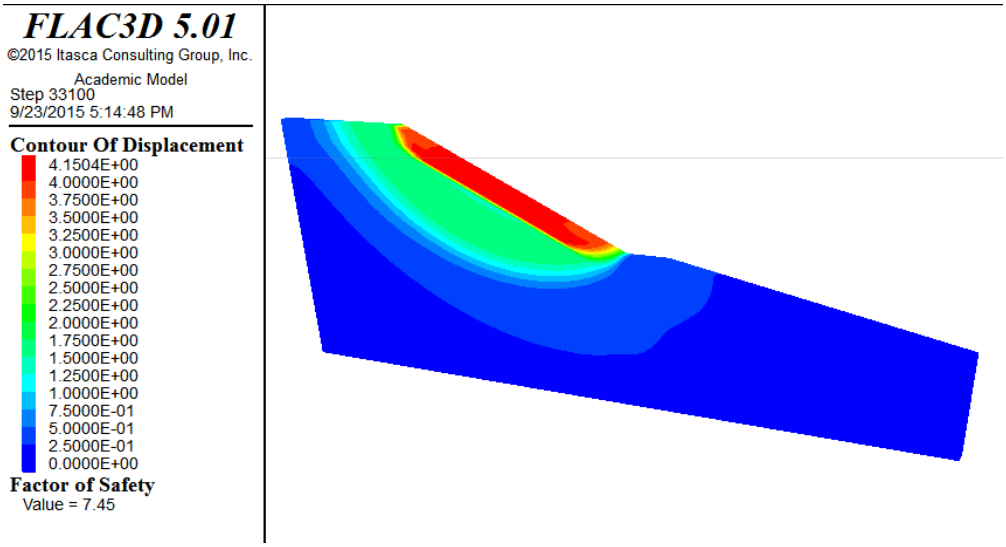

Figure 6-96 FOS of Joe Pool Dam slope with top soil cohesion of 40 kPa and friction angle of 20 degrees

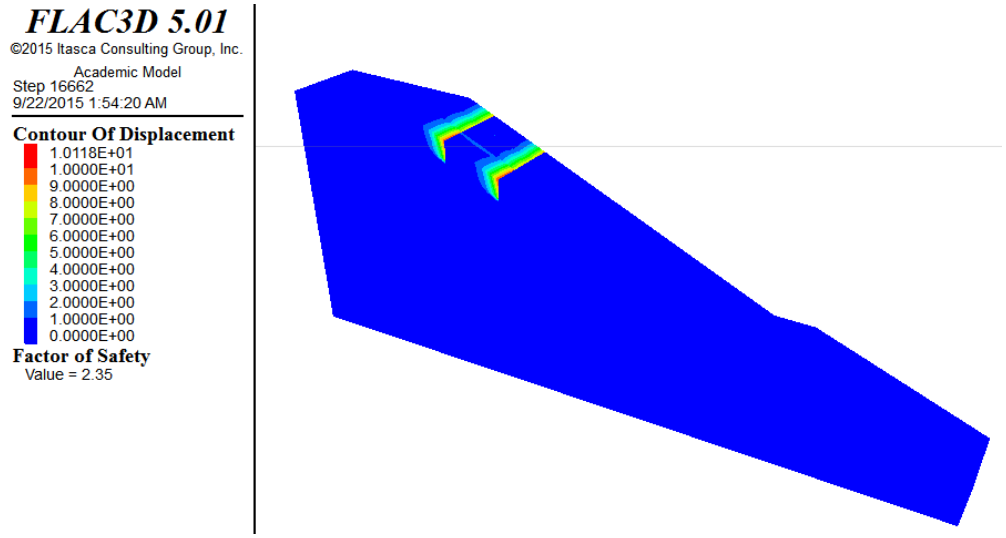

Figure 6-97 FOS of Grapevine Dam slope having a intersecting network of cracks with top soil cohesion of 20 kPa and friction angle of 0 degree

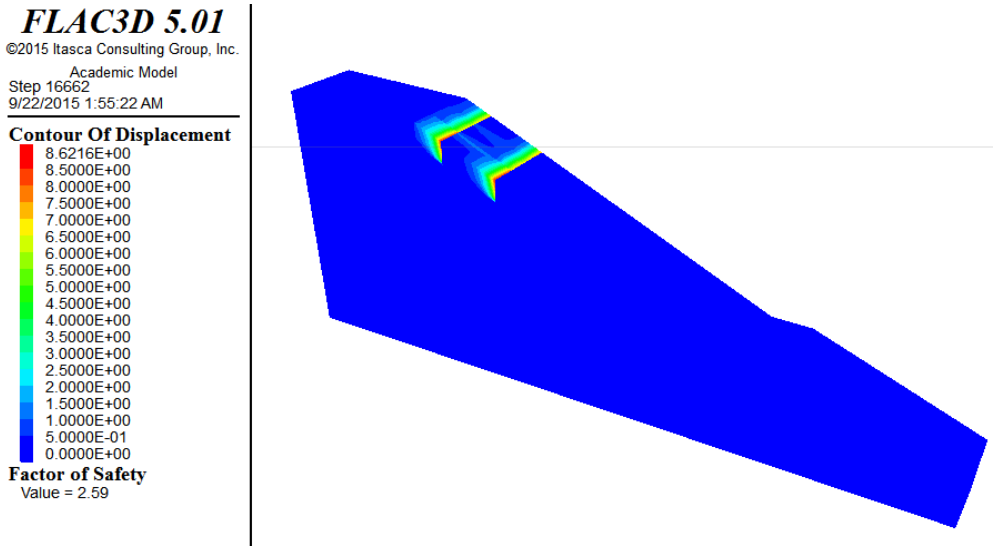

Figure 6-98 FOS of Grapevine Dam slope having a intersecting network of cracks with top soil cohesion of 20 kPa and friction angle of 10 degrees

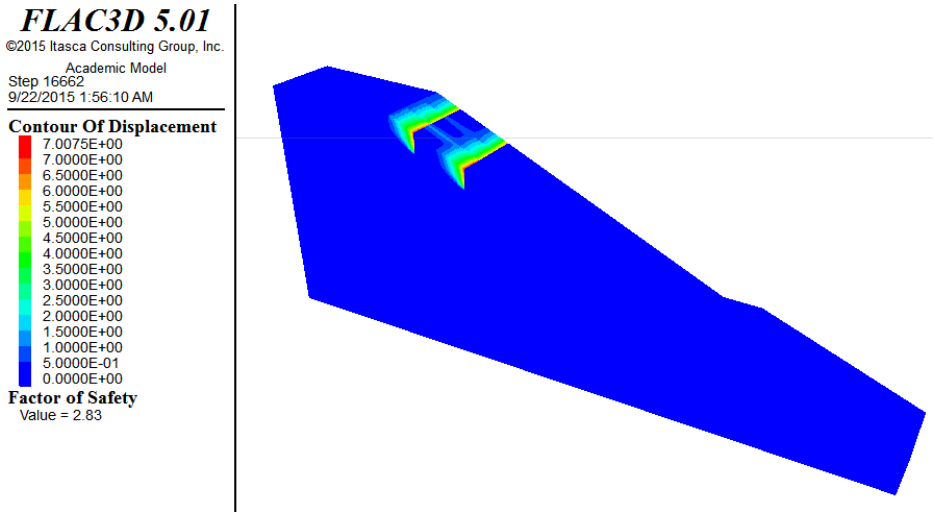

Figure 6-99 FOS of Grapevine Dam slope having a intersecting network of cracks with top soil cohesion of 20 kPa and friction angle of 20 degrees

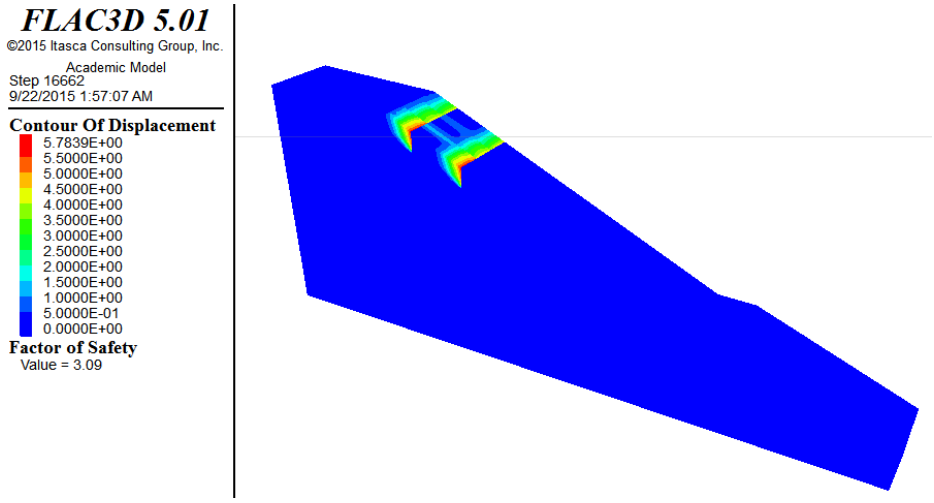

Figure 6-100 FOS of Grapevine Dam slope having a intersecting network of cracks with top soil cohesion of 20 kPa and friction angle of 30 degrees

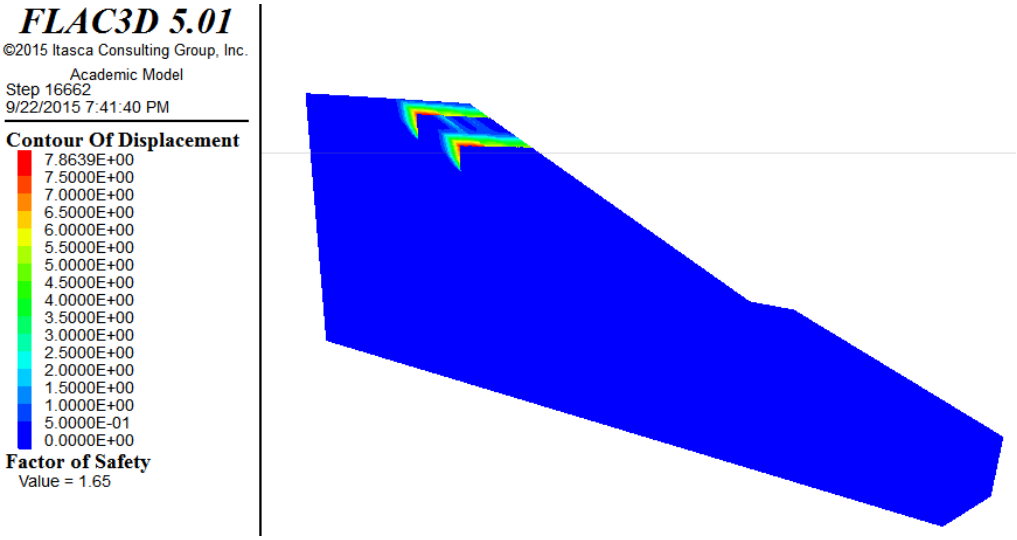

Figure 6-101 FOS of Grapevine Dam slope having a intersecting network of cracks with top soil cohesion of 10 kPa and friction angle of 20 degrees

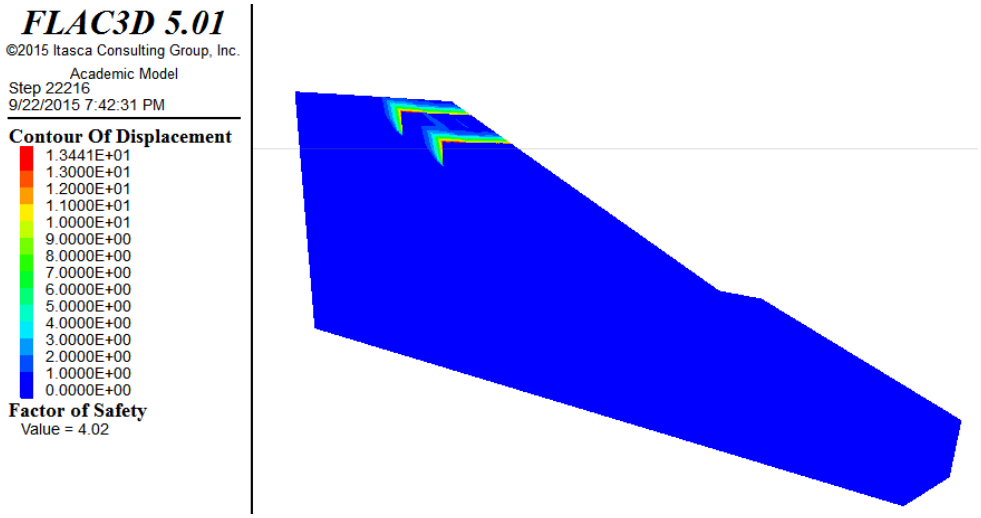

Figure 6-102 FOS of Grapevine Dam slope having a intersecting network of cracks with top soil cohesion of 30 kPa and friction angle of 20 degrees

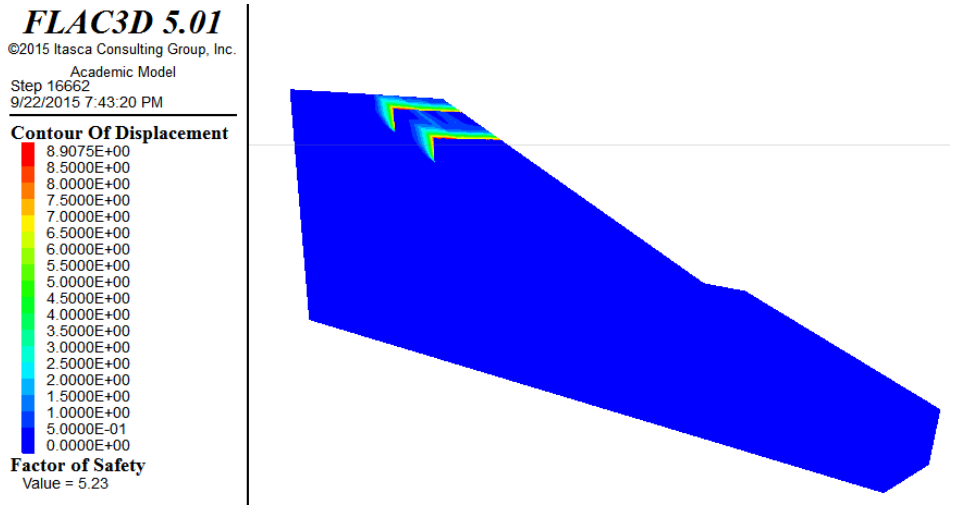

Figure 6-103 FOS of Grapevine Dam slope having a intersecting network of cracks with top soil cohesion of 40 kPa and friction angle of 20 degrees

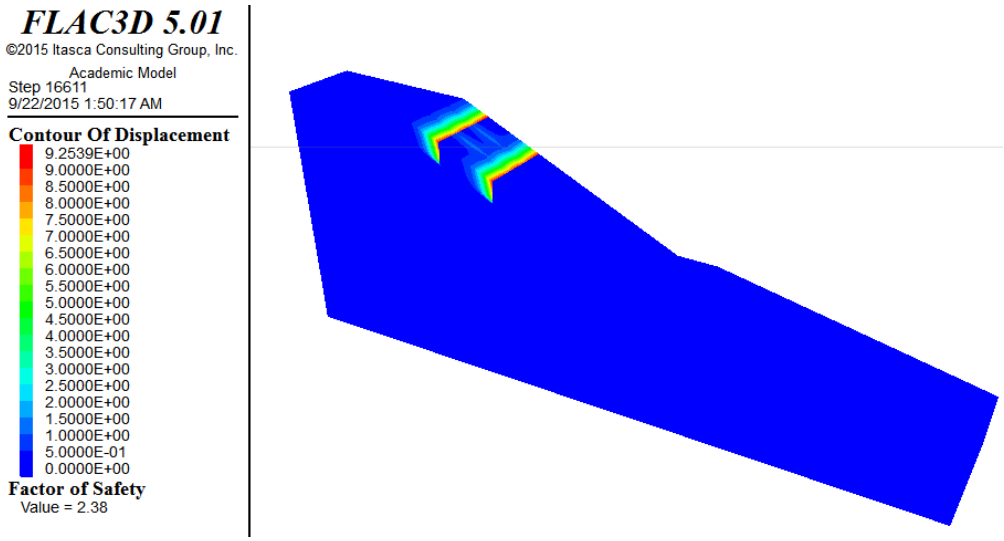

Figure 6-104 FOS of Joe Pool Dam slope having a intersecting network of cracks with top soil cohesion of 20 kPa and friction angle of 0 degree

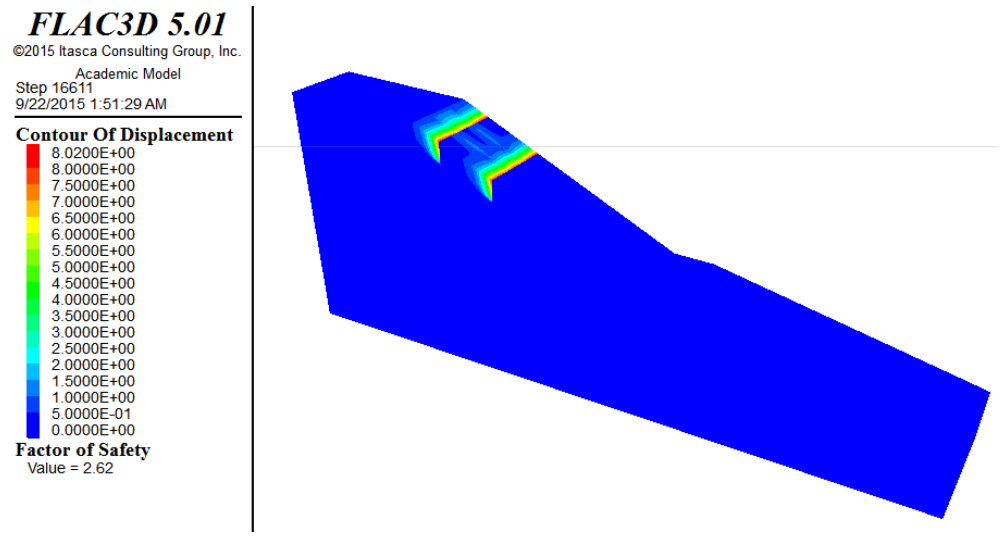

Figure 6-105 FOS of Joe Pool Dam slope having a intersecting network of cracks with top soil cohesion of 20 kPa and friction angle of 10 degrees

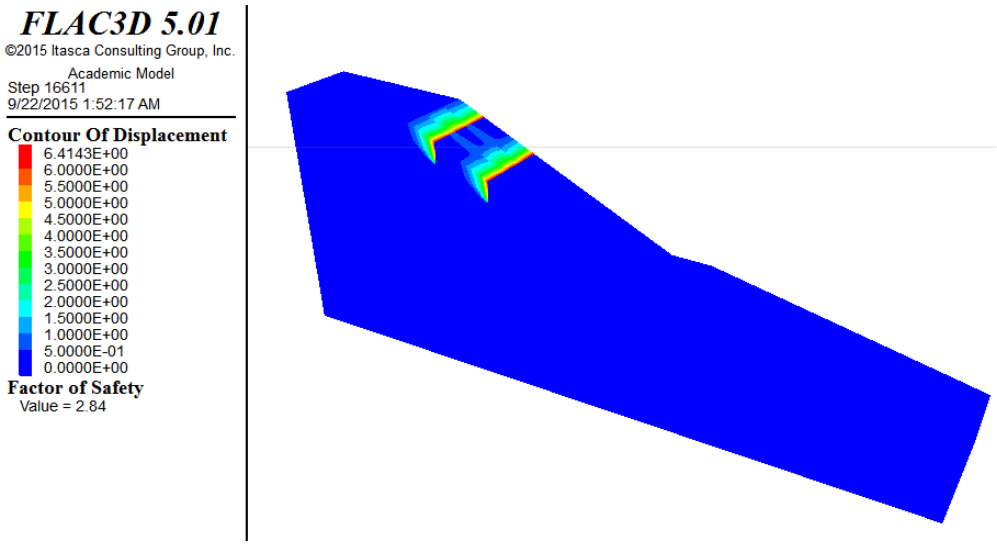

Figure 6-106 FOS of Joe Pool Dam slope having a intersecting network of cracks with top soil cohesion of 20 kPa and friction angle of 20 degrees

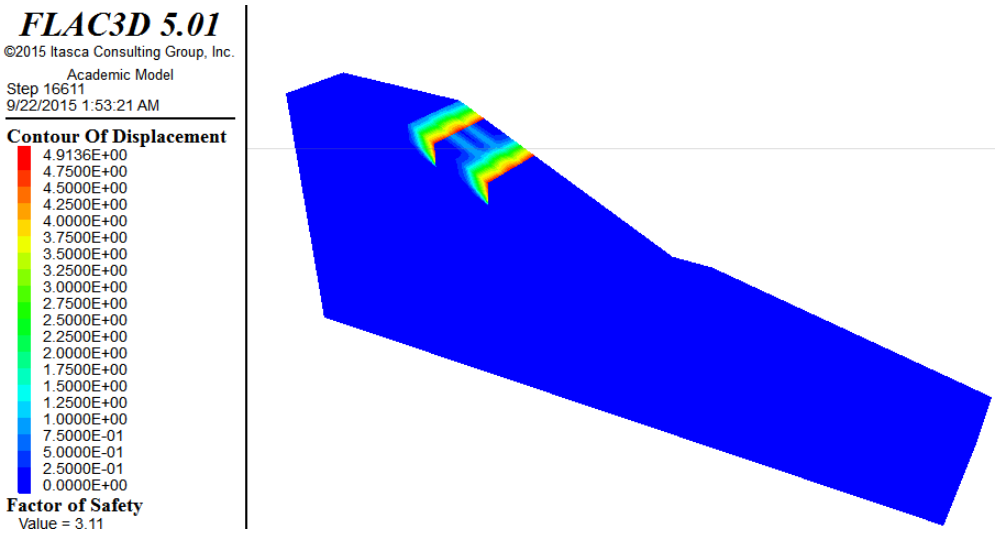

Figure 6-107 FOS of Joe Pool Dam slope having a intersecting network of cracks with top soil cohesion of 20 kPa and friction angle of 30 degrees

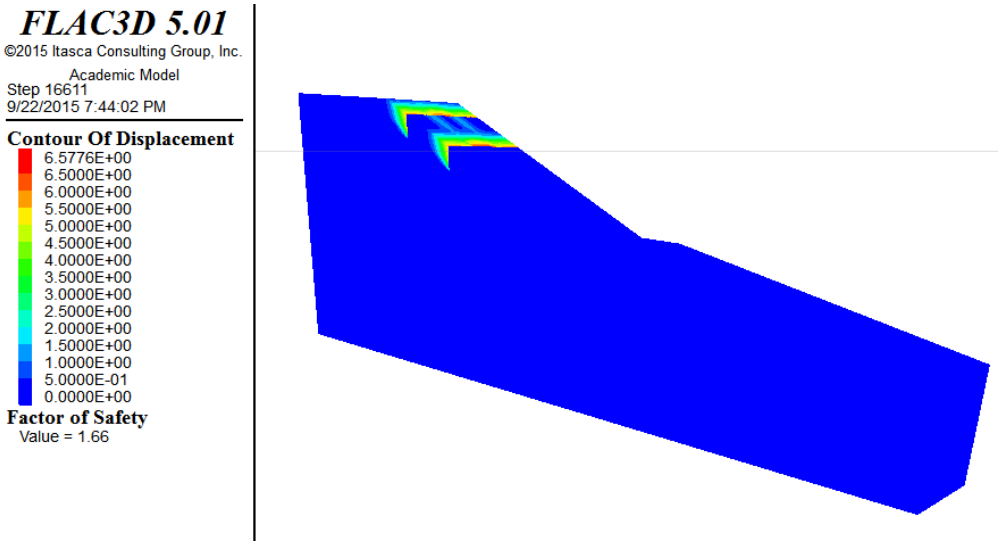

Figure 6-108 FOS of Joe Pool Dam slope having a intersecting network of cracks with top soil cohesion of 10 kPa and friction angle of 20 degrees

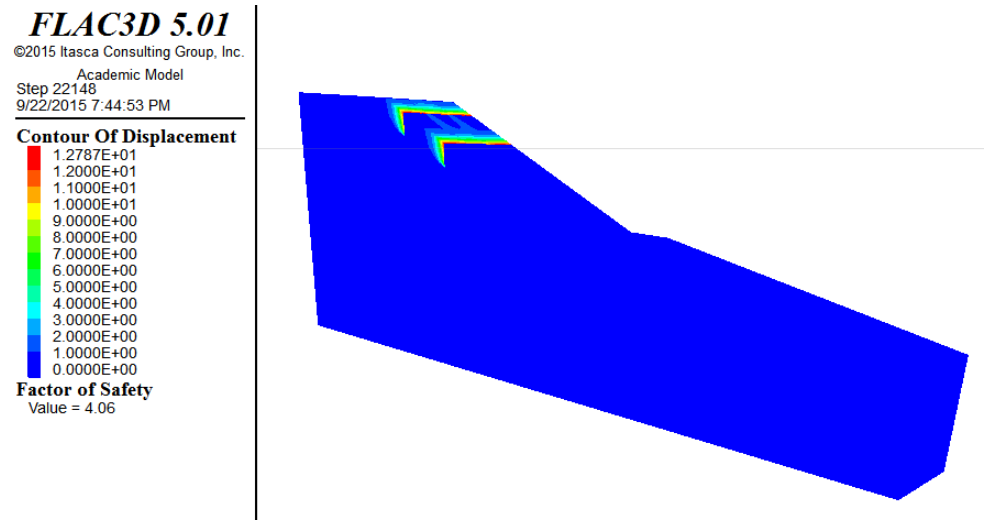

Figure 6-109 FOS of Joe Pool Dam slope having a intersecting network of cracks with top soil cohesion of 30 kPa and friction angle of 20 degrees

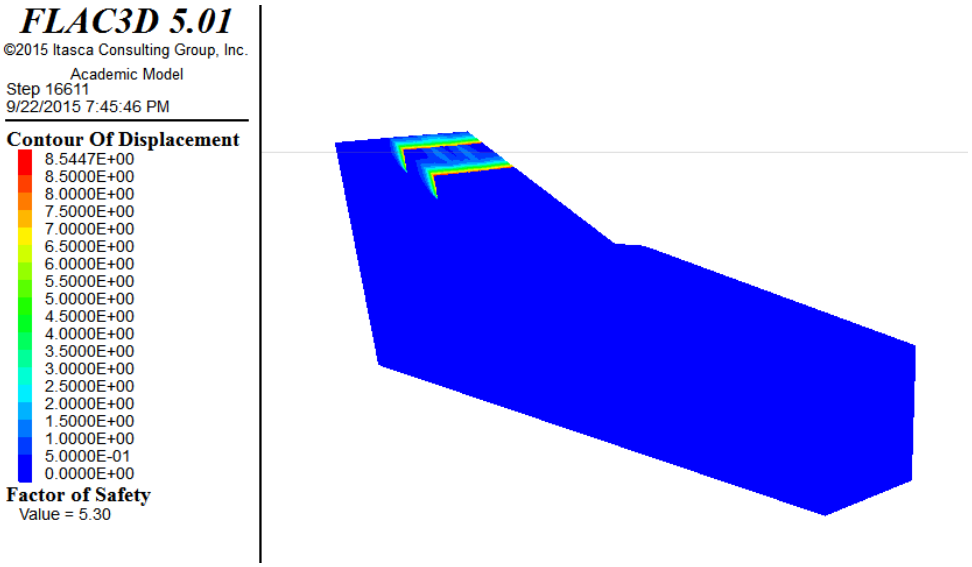

Figure 6-110 FOS of Joe Pool Dam slope having a intersecting network of cracks with top soil cohesion of 40 kPa and friction angle of 20 degrees

6.6 Effect of Suction on the Surficial Slope Stability of Dam Slopes

Dronamraju (2008) and Le (2013) monitored the seasonal moisture content variations on both Grapevine and Joe Pool Dam slopes over a period of 4 years. Moisture content probes were installed within the top 0.5 m depth from the top of the surface. The sensors were installed at two different depths. The top and bottom probes were installed at 0.25 m and 0.5 m depths from the surface, respectively. In each dam, the moisture content variation was monitored for five different top soil conditions namely, untreated (or control), 20%compost treated, 4%lime+0.30%fiber treated, 8%lime+0.15%fiber treated, and 8%lime treated. However, only the untreated top soil condition is addressed in this current

research. Table 6-14 and Table 6-15 show the volumetric moisture contents of the untreated section in Grapevine and Joe Pool Dam control sections respectively in driest and wettest conditions.

Table 6-14 Volumetric moisture contents of the untreated section in the Grapevine Dam slope in driest and wettest conditions (Le, 2013)

Year	2009		2010		2011		2012	
	High	Low	High	Low	High	Low	High	Low
Top	38	35	30	15	35	14	35	26
Bottom	36	33	30	11	37	14	35	24
Average	37	34	30	13	36	14	35	25

Table 6-15 Volumetric moisture contents of the untreated section in the Joe Pool Dam slope in driest and wettest conditions (Le, 2013)

Year	2009		2010		2011		2012	
	High	Low	High	Low	High	Low	High	Low
Top	46	24	49	24	49	23	51	25
Bottom	36	22	38	22	40	25	38	23
Average	41	23	43.5	23	44.5	24	44.5	24

The four years average volumetric moisture content of the Grapevine dam untreated soil for wet and dry seasons were 34.5 and 21.5%, respectively. The same for the Joe Pool dam untreated soil were 43.4 and 23.5%, respectively. The average of the wet and dry season moisture content was calculated and referred to as the moisture content of the moderate season. The moisture contents of the

Grapevine and Joe Pool Dam soils in the moderate seasons were determined to be 28 and 33.4%, respectively.

The SWCC model of parameters of the Grapevine and Joe Pool Dam untreated and treated soils were presented in Chapter 5. The matric suction corresponding to the volumetric moisture content of each season was calculated using the Brooks and Corey (1964), Van Genuchten (1980), and Fredlund and Xing (1994) model fitting parameters. Then, the average of the three suction values was calculated and presented as shown in Table 6-16.

The shear strength of an unsaturated soil given by Fredlund (1978) was presented in Equation 2-14. The equation can be modified as follows to determine the angle of internal friction with respect to suction ($\emptyset^b$):

$$\emptyset^b = tan^{-1}\left[\frac{\tau - c' - (\sigma - u_a)tan\emptyset'}{(u_a - u_w)}\right] \quad 6\text{-}1$$

Or,

$$\emptyset^b = tan^{-1}\left[\frac{\tau_{unsat} - \tau_{sat}}{(u_a - u_w)}\right] \quad 6\text{-}2$$

To determine the friction angle $\emptyset^b$, additional direct shear tests were conducted on both Grapevine and Joe Pool soil specimens at suction levels of 100 and 150 kPa. The soil specimens were brought to the desired matric suction levels using the axis translation technique in Tempe Cell. Once the equilibrium was obtained, the specimens were taken out sheared in the direct shear machine using

a sharing rate of 0.005 mm/min. The direct shear tests on saturated specimens were explained in chapter 5. The test results were used to find the friction angle $\emptyset^b$ for each test. The average of $\emptyset^b$ was obtained for each soil as shown in Table 6-17. The apparent cohesions of the soils to be used in the slope stability analyses were then calculated by multiplying the matric suction with tan($\emptyset^b$). The apparent cohesions of the soils at different seasons are presented in Table 6-18.

Table 6-16 Matric suction of the Grapevine and Joe Pool Dam untreated soils in different seasons

Soil	Season	Volumetric moisture content (%)	Matric suction (kPa)
GV	Wet	34.5	50
	Dry	21.5	215.7
	Moderate	28	72.3
JP	Wet	43.4	138
	Dry	23.5	1560
	Moderate	33.4	410

Table 6-17 Determination of friction angle $\emptyset^b$

Soil	Normal stress (kPa)	Matric suction (kPa)	Shear stress at failure (kPa)	$\emptyset^b$ (degrees)	Average $\emptyset^b$ (degrees)
GV	50	0	30.8	-	10.7
		100	50.6	11.19	
		150	57.7	10.16	
JP	50	0	31.1	-	9.9
		100	49.9	10.64	
		150	55.4	9.2	

Once the apparent cohesion of the soils was determined, total cohesion intercept for a given season was determined by adding the apparent cohesion with the cohesion of the soils at saturation. The total cohesion intercepts used in the surficial slope stability analysis of the unsaturated slopes are shown in Table 6-18. The corresponding FOSs are presented in Table 6-19. The Results are also shown in Figure 6-111 through Figure 6-116.

Table 6-18 Apparent cohesion and total cohesion intercept of the soils at different season

Soil	Season	Apparent cohesion (kPa)	Total cohesion (kPa)
GV	Wet	9.4	47.9
	Dry	40.6	79.1
	Moderate	13.5	52
JP	Wet	6.7	82.15
	Dry	272.3	347.75
	Moderate	71.5	146.95

Table 6-19 The FOS of the slopes at different seasons

Soil	Season	FOS
GV	Dry	8.06
	Moderate	3.94
	Wet	3.3
	Saturated	1.83
JP	Dry	50.09
	Moderate	14.79
	Wet	3.39
	Saturated	2.19

As expected, the FOS of the slopes against surficial failure was higher in dry season and lower in wet season. Even lower FOS was observed in the case of saturated soil. It should be noted that there was substantial reduction in the FOS from dry to wet season in case of Joe Pool Dam slope. The reductions were smaller in the case of Grapevine Dam slope. The reduction in the FOS is related directly to the increase in the moisture content of the soil. The presence of desiccation cracks provides a more direct flow path to the rainwater into the slope. Consequently, the moisture content of the soil increases and the matric suction decreases. The decrease in the suction causes the loss of the apparent cohesion and the factor of the safety of the slope can decrease significantly as observed in the case of Joe Pool soil. Therefore, controlling the desiccation cracking of the slopes using the soil treatment methods helps in maintaining the safety of the slope against surficial failure.

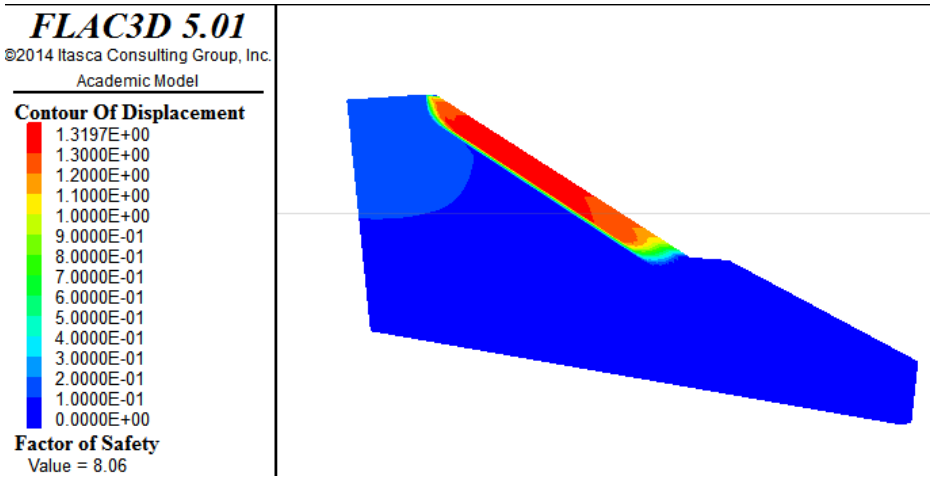

Figure 6-111 FOS of Grapevine Dam control section in dry season

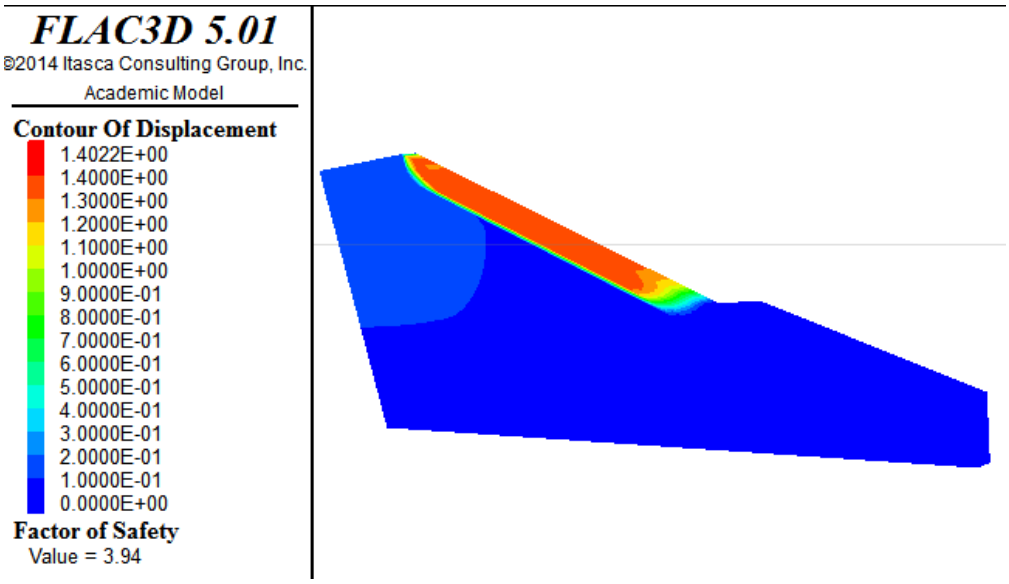

Figure 6-112 FOS of Grapevine Dam control section in moderate season

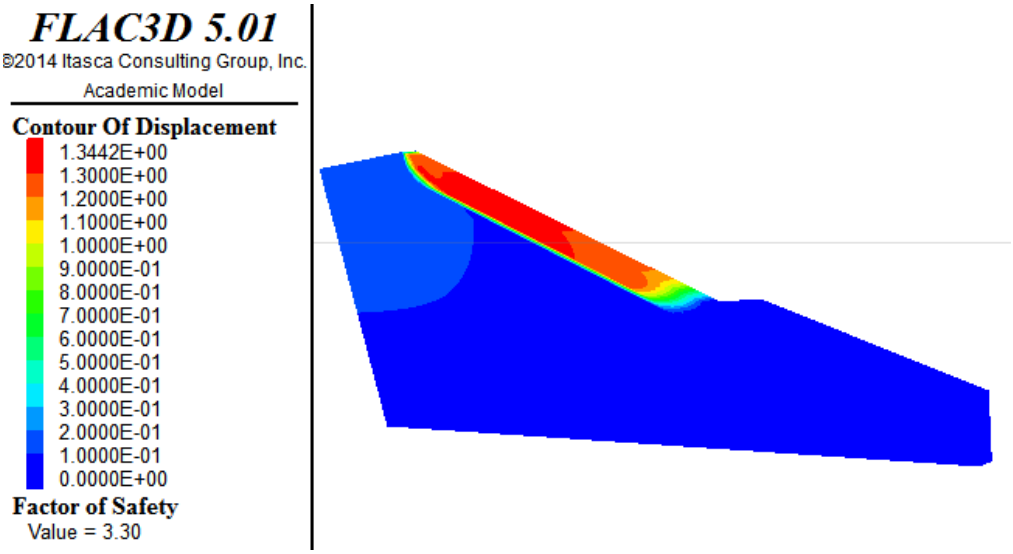

Figure 6-113 FOS of Grapevine Dam control section in wet season

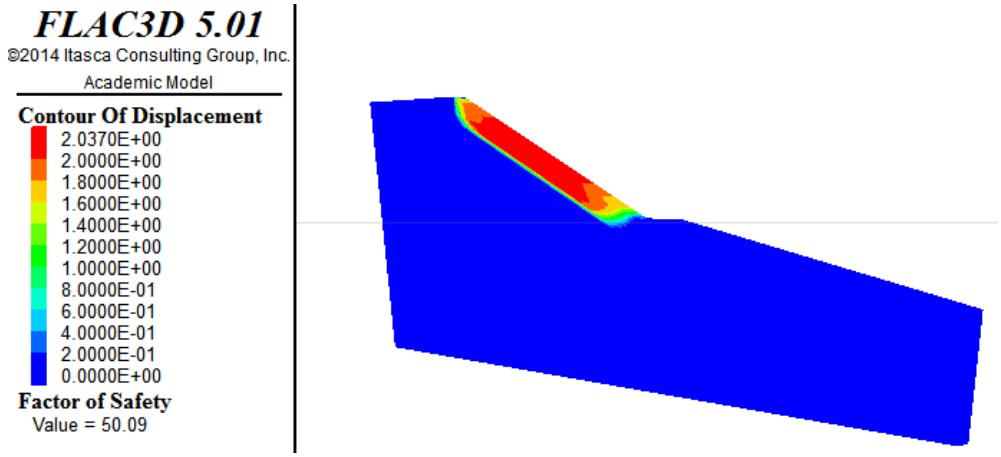

Figure 6-114 FOS of Joe Pool Dam control section in dry season

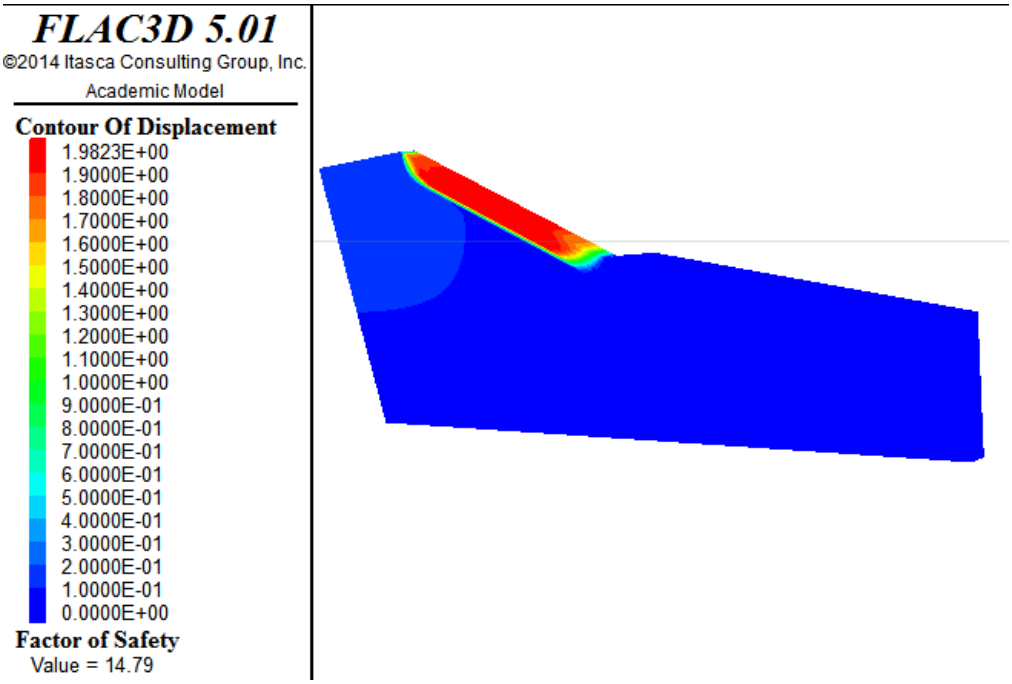

Figure 6-115 FOS of Joe Pool Dam control section in moderate season

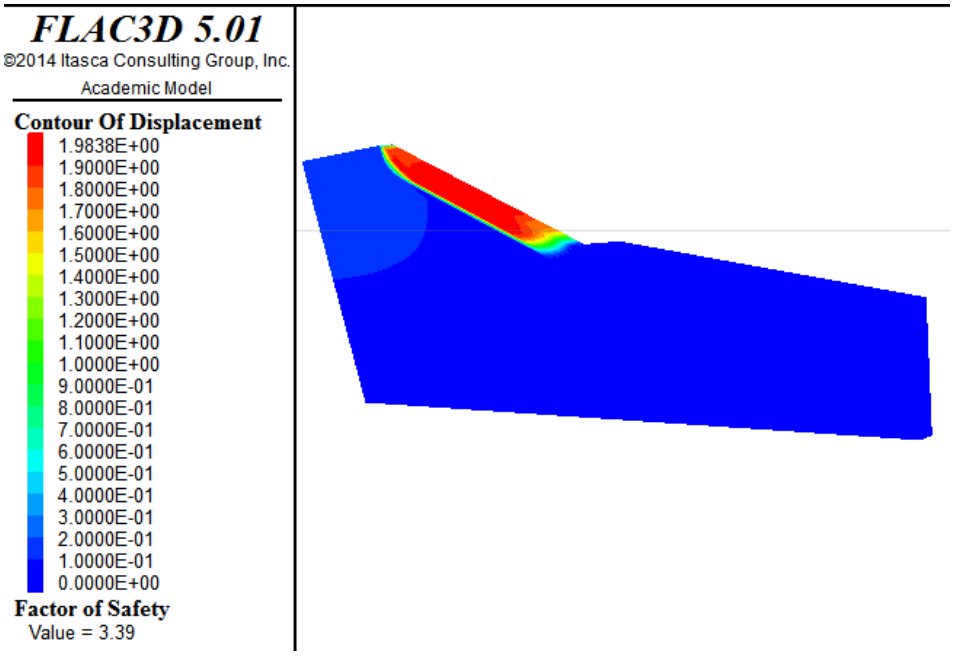

Figure 6-116 FOS of Joe Pool Dam control section in wet season

6.7 Summary

A finite difference program called Fast Lagrangian Analysis of Continua in 3 Dimensions (FLAC3D) was used to investigate the surficial slope stability of the Grapevine and Joe Pool dams. In addition, the effects of seasonal moisture content fluctuations and extent of desiccation cracks on slope stability issues were also focused. The summary of findings from this chapter is as follows:

1. The slope stability analysis using finite difference program showed that the Grapevine Dam control section with residual shear strength condition and Joe Pool Dam control section with both fully softened and residual shear strength conditions yielded the FOS values lower than the acceptable FOS limit of 1.5. All other combinations of soil strength and treatment conditions yielded FOS higher than 1.5. The results when compared with the ones obtained from Slope/W program by Le (2013) were in good agreement with exceptions in few cases.
2. Stability analysis of the slope with two cracks parallel to the dam alignment showed that the crack in the crest does not have big impact in the stability of slope against surficial failure. The crack in the slope, on the other hand, showed moderate reduction in the FOS of the slopes. In case of the analysis using a network of orthogonally intersecting cracks, it was found that presence of

such cracks can reduce the FOS of a slope significantly causing an otherwise stable slope to have a skin failure.

3. A parametric study on both of the dam slopes to assess the reduction in FOS due to the crack network showed that the rate of FOS reduction remained constant when the friction angle was reduced from 40 to 0 degree keeping the cohesion constant at 20 kPa. On the other hand, keeping the friction angle constant at 20 degrees, the rate of reduction in FOS decreased with decrease in cohesion from 40 to 10 kPa in Grapevine Dam slope. The opposite trend was observed in the Joe Pool dam slope while varying the cohesion from 40 to 10 kPa.
4. The slope stability analysis of unsaturated slopes showed higher FOS in dry season and lower FOS in wet season. Even lower FOS was observed in the case of saturated condition. There was substantial reduction in the FOS from dry to wet season in case of Joe Pool Dam slope. The reduction in the FOS was related to the increase in the moisture contents of the soil. Desiccation cracks can exacerbate the moisture condition in the slope. Controlling the desiccation cracks using soil treatment methods can preserve the dam slope safety against surficial failure.

Chapter 7

Summary and Conclusions

7.1 Introduction

The main objective of this dissertation research was to refine and develop the shrinkage induced pressure (SIP) test for improved shrinkage characterization of different soils. Another objective was to use this methodology to address biopolymer treatment to reduce shrinkage cracking thereby control surficial slope failures. In addition, this research also aimed at investigating three dimensional (3D) slope stability analyses of two dams namely, Grapevine and Joe Pool Dam embankment slopes.

As a part of the first objective, this research aimed at establishing a relationship between the SIP measurements and tensile strengths of the soil determined from indirect tensile strength tests. The objectives were assessed based on comprehensive laboratory studies on a total of ten (10) natural expansive soils and two soils treated with biopolymer and lime. Digital image correlation technique was also focused in understanding the shrinkage cracking patterns and mechanism of natural and stabilized soils. In addition, statistical regression modeling and numerical modeling studies were conducted to further address the research objectives in understanding the impact of shrinkage characterization on the slope stability studies.

A literature review of the research works relevant to this study was presented in Chapter 2. The mechanism of desiccation cracking, effects of desiccation cracking on tensile strength, soil suction, and slope stability analysis were discussed. Furthermore, the literature review also covered soil treatment methods, expansive soils, clay mineralogy, SWCC, two and three dimensional slope stability analyses, and unsaturated slope stability analysis.

Shrinkage induced pressure (SIP) test, indirect tensile strength (IDT) test, linear shrinkage bar tests, determination of soil water characteristics curve, and digital image correlation technique were included as the main components of research methodology to study the soil behavior during dying, shrinkage, and cracking. In addition, laboratory tests were also conducted to determine the basic soil properties, engineering properties, and chemical and mineralogical composition of the soils. All the experiments conducted in this dissertation research study were detailed in Chapter 3. A statistical linear regression model was developed to predict the peak SIP from clay and Montmorillonite contents of soils as presented in chapter 4.

Three different treatments methods namely, biopolymer treatment, lime treatment, and lime+fiber treatment were analyzed to study changes in shrinkage behavior of the soil and their influence in reducing the desiccation cracking problem. The findings of the soil treatment studies were presented in Chapter 5. The test methods used in the shrinkage characterization of the untreated soils were

also repeated to compare the changes brought in by the introduction of the soil additives.

Finally, 3D slope stability analysis of the dam slope was conducted to study the effects of desiccation cracking and seasonal moisture content variation on the stability of the dam slopes. The slope stability analyses and their findings were outlined in Chapter 6.

7.2 Summary of Findings

The summary of the findings of this dissertation research are as follows:

1. Linear shrinkage bar test showed that the shrinkage strain of these soils is dependent on the Montmorillonite content of the soils. Higher Montmorillonite content generally yielded higher shrinkage strain. Furthermore, the indirect tensile strengths of the soils were higher for the soil specimens prepared from slurry state when compared to the ones compacted at OMC and 95% of MDD conditions. The scatter plot between the IDTs of slurry and compacted soil specimens exhibited a general upward trend. This indicates that the soils showing higher tensile strength at compacted state have a tendency to have higher tensile strength at slurry state.
2. In the SIP tests, the suction and the SIP remained small during the initial shrinkage phase called structural shrinkage phase. The

second phase of the drying, also called proportional shrinkage phase, was characterized by higher drying and shrinkage strain rates. Both the suction and SIP increased rapidly in the proportional shrinkage phase. In the final stage of drying, also called residual shrinkage phase, the soils exhibited small changes in shrinkage strains even if the moisture content was decreasing. The SIP remained almost constant or decreased if any cracks were developed in the specimen.

3. The average of peak SIPs of the soils when plotted against corresponding volumetric shrinkage strains exhibited an overall upward trend; an increase in shrinkage strain was associated with an increase in SIP. The linear regression between the parameters yielded a coefficient of determination of 0.77. It demonstrated that the SIP can be used as an estimator for the volumetric shrinkage potential of the soils.
4. The comparison of SIP and IDT of slurry soil specimens showed that the SIPs were only between 17.2 to 24.9% of their respective IDTs. It indicated that the actual SIP value is very smaller than the indirect tensile strength of the slurry soil. On the other hand, the comparison between SIP and IDT of the compacted soil specimens showed that the IDTs were only between 11.9 to 18.8%

of their corresponding SIPs except for the Grapevine Dam soil. Thus the SIPs of the soils were very higher than the IDTs of the compacted specimens.

5. The 3D digital image correlation (3D DIC) technique was effective in determining the tensile strain of the soils at the time of cracking, cracking moisture content, crack width and length, and total area of cracks. This novel technique was also successful in monitoring the evolution of crack width with time, time of crack formation, vertical displacement profile along a given section, and vertical and horizontal displacements of crack edges. In addition, the curling up (or lifting off) of the crack edges were also successfully monitored. Based on this technique, lime treated soils showed superior shrinkage and cracking resistance compared to the untreated soils.
6. Considering shear strength and swell pressure as two key properties, 0.5% biopolymer was determined as the efficient dosage for both Grapevine and Joe Pool Dam soils. From the shear strength point of view, biopolymer treatment showed moderate improvements when compared to the control soil. The increase in shear strength can be helpful in solving the surficial slope failure problems in the dam slopes. It can be useful in places

where chemical treatments are not suitable due to environmental concerns.

7. The linear shrinkage strains of the biopolymer treated soils were lower than the control soil but higher than the lime and lime+fiber treated soil. On the other hand, the IDTs of the biopolymer treated soils were smaller than the control soils and greater than the lime based treatment methods in the case of slurry soils. However, the opposite was observed in case of the IDTs of compacted soil specimens. In addition, all the treatment methods reduced the SIP of the soils. The lime based treatments showed very small SIPs compared to control and biopolymer treated soils. Thus, the biopolymer treated soils showed moderate improvement in the shear strength and shrinkage studies when compared to control soils while both the lime treated and lime+fiber treated soils exhibited superior strength and shrinkage properties.
8. A statistical regression model was developed to predict the peak SIP of clayey soils from clay and Montmorillonite contents as the predictor variables based on results from ten soils. The model showed good agreement between the measured and predicted SIPs of four new sets of soils.

9. The slope stability analysis results obtained using finite difference program FLAC3D when compared with the ones obtained from Slope/W program by Le (2013) were in good agreement with exceptions in few cases. Stability analysis of the slopes with two cracks parallel to the dam alignment showed that the crack in the crest does not have big impact in the stability of slope against surficial failure. The crack in the slope, on the other hand, showed moderate reduction in the FOS of the slopes. In case of the analysis using a network of orthogonally intersecting cracks, it was found that presence of such cracks can reduce the FOS of a slope significantly causing an otherwise stable slope to have a skin failure.
10. A parametric study conducted to assess the reduction in FOS due to the crack network showed that the rate of FOS reduction remained constant when the friction angle was reduced from 40 to 0 degree. On the other hand, the rate of reduction in FOS decreased with decrease in cohesion from 40 to 10 kPa in Grapevine Dam slope. The opposite trend was observed in the Joe Pool Dam slope. Furthermore, the slope stability analysis of unsaturated slopes showed higher FOS in dry season and lower FOS in wet season. Even lower FOS was observed in the case of

saturated condition. There was substantial reduction in the FOS from dry to wet season in case of Joe Pool Dam slope. The reduction in the FOS was related to the increase in the moisture contents of the soil. Desiccation cracks can exacerbate the moisture condition in the slope. Controlling the desiccation cracks using soil treatment methods can preserve the dam slope safety against surficial failure.

7.3 Recommendations for Future Research

It is recommended for the future research that the shrinkage induced pressure test be extended for field applications by measuring the change in resistance of the sensors using electronic multimeters. In addition, the indirect tensile strength tests should also cover wider moisture content ranges to relate the IDT and SIP at different moisture contents. The weathering resistance of biopolymer treated soils should be assessed using durability tests. In addition, the performance of the biopolymer treated soils should be assessed by constructing test sections in field.

Appendix A

SWCC Models of Treated Soils

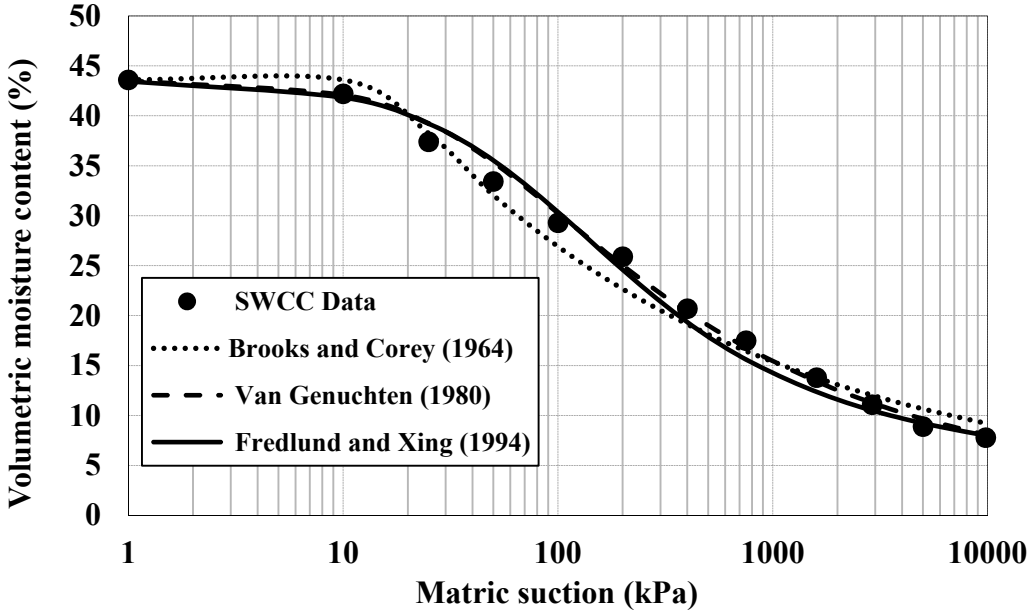

Figure A-1 SWCC models fitting of Grapevine Dam control soil

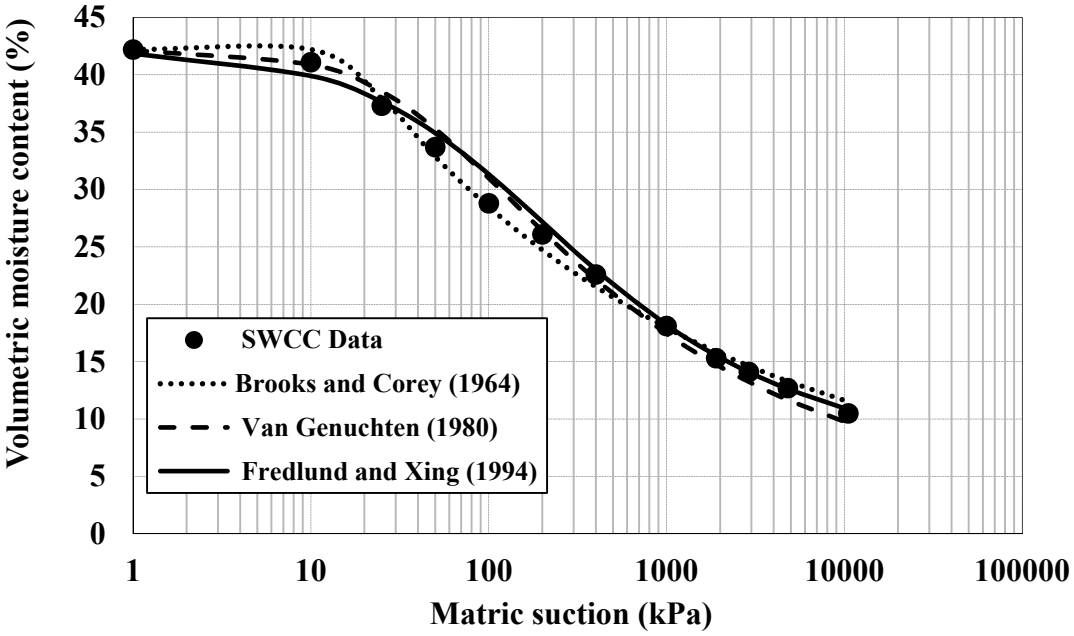

Figure A-2 SWCC models fitting of Grapevine Dam biopolymer treated soil

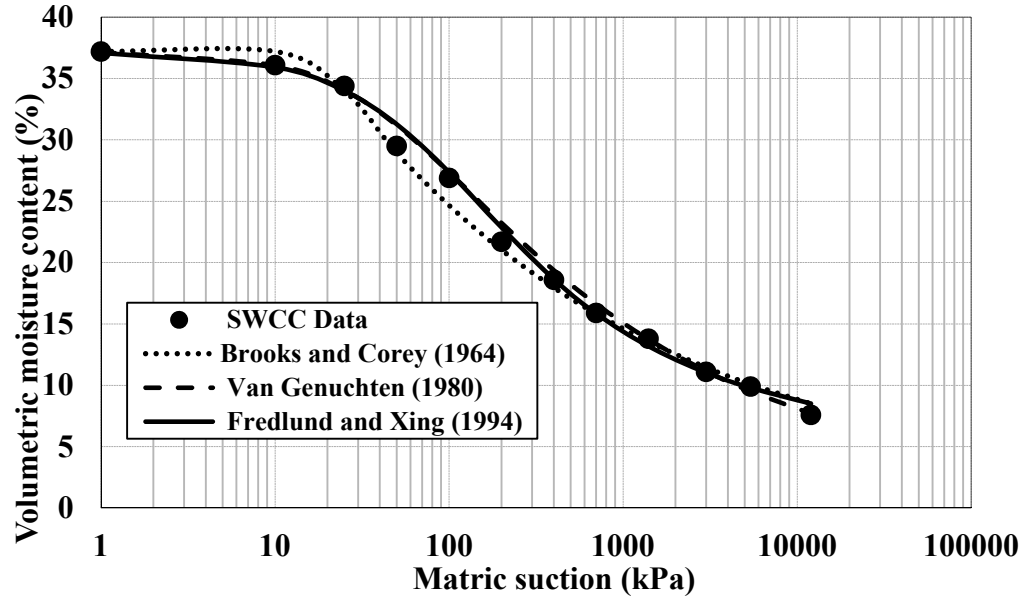

Figure A-3 SWCC models fitting of Grapevine Dam lime treated soil

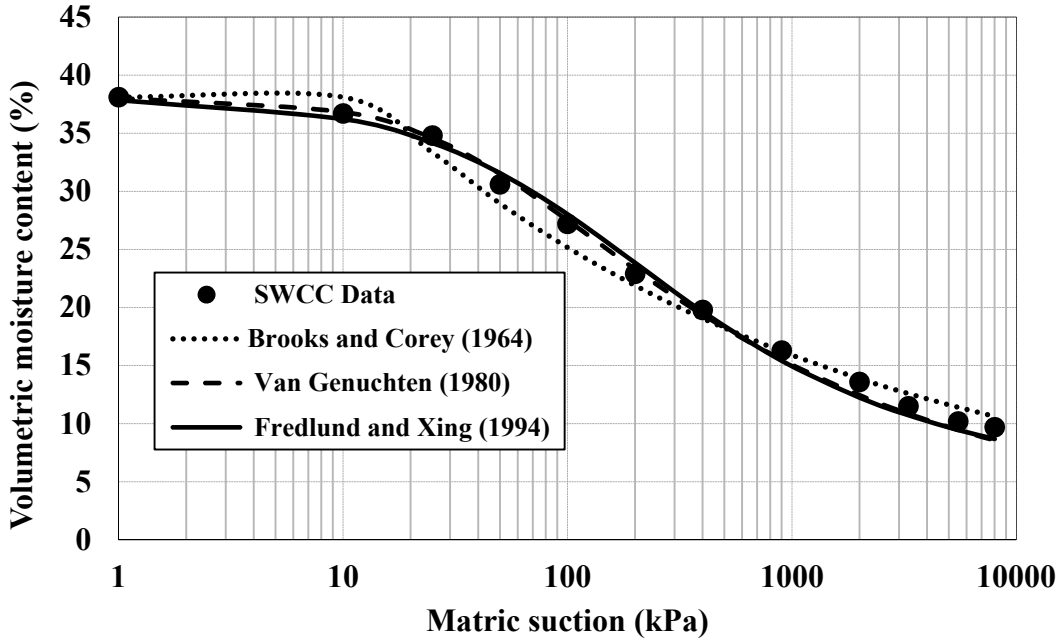

Figure A-4 SWCC models fitting of Grapevine Dam lime+fiber treated soil

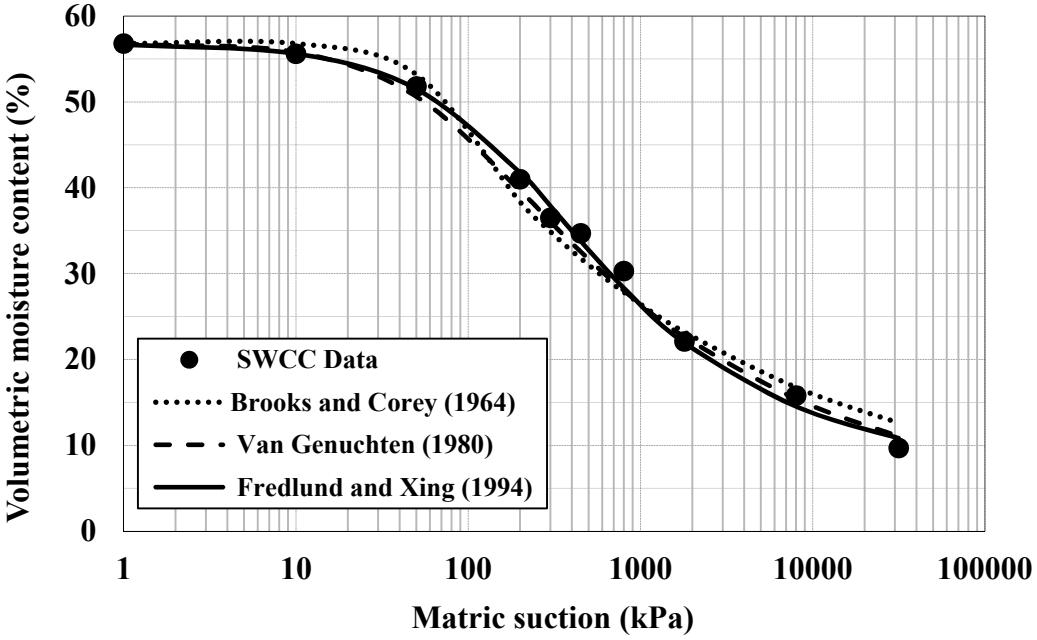

Figure A-5 SWCC models fitting of Joe Pool Dam control soil

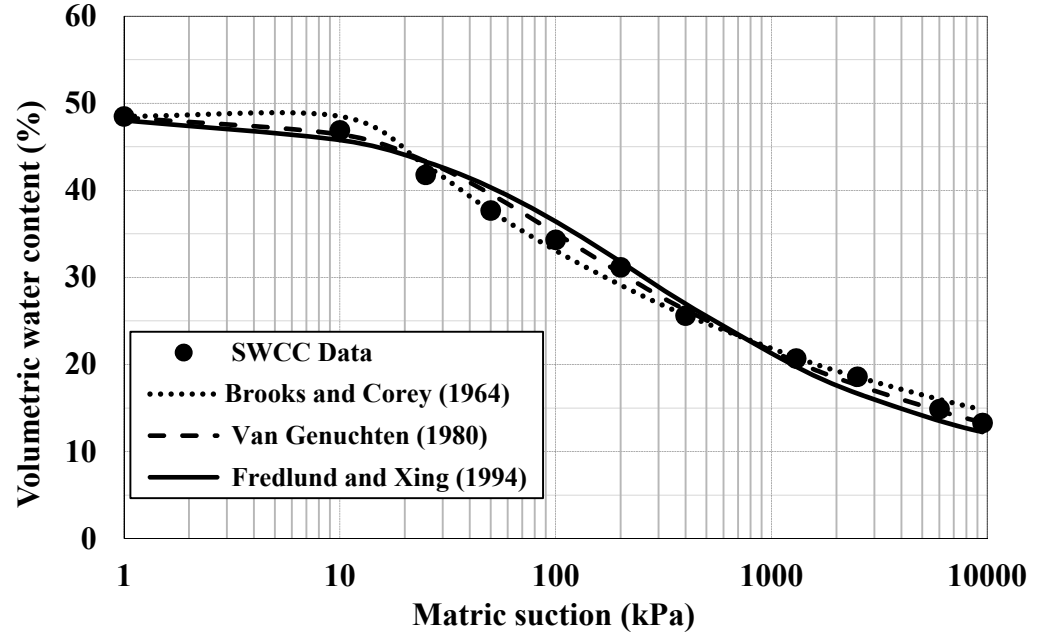

Figure A-6 SWCC models fitting of Joe Pool Dam biopolymer treated soil

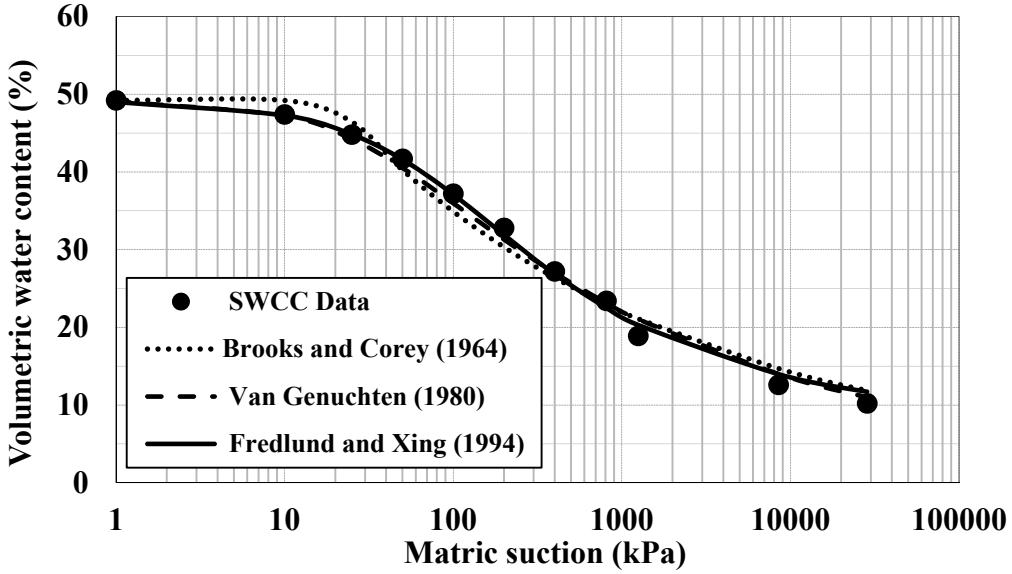

Figure A-7 SWCC models fitting of Joe Pool Dam lime treated soil

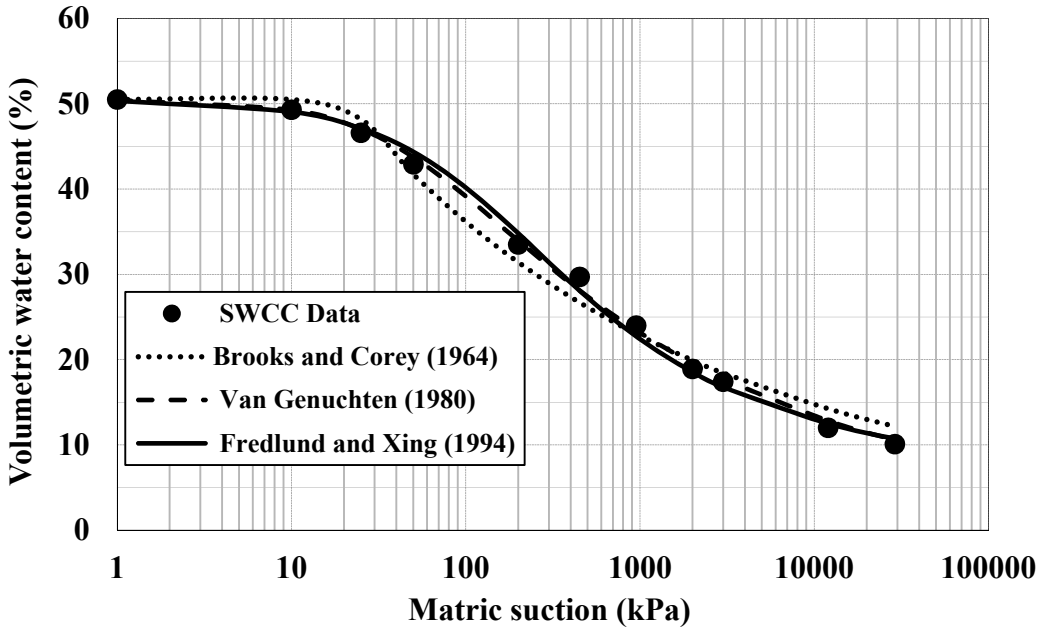

Figure A-8 SWCC models fitting of Joe Pool Dam lime+fiber treated soil

References

Abou Najm, M., Mohtar, R. H., Weiss, J., and Braudeu, E. (2009). "Assessing internal stress evolution in unsaturated soils." *Water Resources Research,* 45, W00C11, doi:10.1029/2007WR006484.

Abramson, L.W., Lee, T. S., Sharma, S., and Boyce, G. M. (2002). Slope stability and stabilization methods, second edition, *John Wiley & Sons Inc*., New York.

Aitchison, G. (1957). "The strength of quasi-saturated and unsaturated soils in relation to the pressure deficiency in the pore water," *paper presented at 4th International Conference on Soil Mechanics and Foundation Engineering*, London.

Albrecht, B. and Benson, C. (2001). "Effect of desiccation on compacted natural clays." *Journal of Geotechnical and Geoenvironmental Engineering*, 127(1), pp. 67-76.

Albataineh, N. (2006). "Slope stability analysis using 2D and 3D methods," Master's Thesis, The University of Akron.

Al-Rawas, A. A., Hago, A. W., and Al-Sarmi, H. (2005). "A comparative evaluation of various additives used in the stabilization of expansive soils from Oman*," Building and Environment*, 40(5), pp. 681-687.

Amarasiri, A. L. and Kodikara, J.K. (2011). "Use of material interfaces in DEM to simulate soil fracture propagation in mode I cracking." *International Journal of Geomechanics,* 11(4), pp. 314-322.

Abedine, Z., E., and Robinson, G. H. (1971). "A study on cracking in some vertisols of Sudan." *Geoderman*, 5, pp. 229-241

Amarasiri, A. L., Kodikara, J., Costa, S. (2011). "Numerical Modelling of Desiccation Cracking." *International Journal for Numerical and Analytical Methods in Geomechanics,* 35, pp. 82–96.

Amarasiri, A., Kodikara, J. (2013). "Numerical modelling of desiccation cracking using the cohesive crack method." International Journal of Geomechanics 13(3), pp. 213-221.

American Society for Testing and Materials (ASTM D136). (2001). *Standard test method for sieve analysis of fine and coarse aggregates.*

American Society for Testing and Materials (ASTM D7608). (2010). *Standard test method for torsional ring shear test to determine drained fully softened shear strength and nonlinear strength envelope of cohesive soils (using normally consolidated specimen) for slopes with no preexisting shear surfaces.*

American Society for Testing and Materials (ASTM D6467). (2013). *Standard test method for torsional ring shear test to determine drained residual shear strength of cohesive soils.*

American Society for Testing and Materials (ASTM D422). (2007). *Standard test method for particle size analysis of soils.*

American Society for Testing and Materials (ASTM D4318). (2005). *Standard test methods for liquid limit, plastic limit, and plasticity index of soils*.

American Society for Testing and Materials (ASTM D854). (2014). *Standard test methods for specific gravity of soil solids by water pycnometer*.

American Society for Testing and Materials (ASTM D698). (2012). *Standard test methods for compaction characteristics of soil using standard effort (12400 ft-lbf/ft^3 (600kN-m/m^3))*.

American Society for Testing and Materials (ASTM D5298). (2010). *Standard test methods for measurement of soi potential (suction) using filter paper*.

American Society for Testing and Materials (ASTM D3967). (2008). *Standard test methods for splitting tensile strength of intact rock core specimens*.

Anagnosti, P. (1969). "Three dimensional stability of fill dams." *Proceedings of the 7th International Conference on Soil Mechanics and Foundation Engineering*, Mexico, 2, pp. 275-280.

Ayad, R., Konrad, J. M., Soulié, M. (1997). "Desiccation of a sensitive clay: application of the model CRACK." *Canadian Geotechnical Journal* 34, pp. 943–951.

Bishop, A. W. (1955). "The use of the slip circle in the stability analysis of slopes", *Geotehnique*, 5(1), pp.7-17.

Bishop, A. (1959), The principle of effective stress, *Teknisk Ukeblad*, 106(39), pp. 859– 863.

Borchardt, G. (1989), "*Smectites*", In J.B. Dixon and S.B. Weed, eds., Minerals in Soil Environments, 2nd ed., Madison, WI: Soil Science Society of America.

Braudeau, E., Frangi, J. P., and Mohtar, R. H. (2004). "Characterizing nonrigid aggregated soil-water medium using its shrinkage curve," *Soil Science Society of America Journal*, 68, pp. 359–370.

Brown, K. W., and Anderson, D. C. (1983). "Effects of organic solvents on the permeability of compacted clay liners," USEOA Rep. EPA-600/w-83-016.

Carter, D. L., Mortland, M. M., and Kemper, W. D., (1986), "Specific Surface" In *Methods of Soil Analysis* (Edited by Klute, A.), Part 1, second edition *Agronomy* 9:413-423.

Cerato, A. B., and Lutenegger, A. J. (2002) "Determination of surface area of fine-grained soils by the ethylene glycol monoethyl ether (EGME) method", *Geotechnical Testing Journal*, 25(3), pp. 315-321.

Chang, I., and Cho, G.C.(2012). "Strengthening of Korean residual soil with beta-1,3/1,6-glucan biopolymer," *Construction and Building Materials*, 30, pp. 30-35.

Chapman, H . D. (1965). Cation exchange capacity. In: *Methods of soil analysis* (Edited by Black, C. A.) 2, pp. 891-901. Number 9 in the series *Agronomy*.

Chen, R. H. (1981): "Three-dimensional slope stability analysis," Joint Highway Research Project, Eng. Experiment station, Purdue University, Report JHRP-81-17.

Chen, R. H. and Chameau, J. L. (1983). "Three-dimensional limit equilibrium analysis of slopes," *Geotechnique,* 32(1) pp. 31-40.

Chen, F. H. (1988). Foundations on expansive soils, 2nd Edition, *Elsevier Science Publications*, New York.

Chen, R., Zhang, L., and Budhu, M. (2013). "Biopolymer stabilization of mine tailings." *Journal of Geotechnical and Geoenvironmental Engineering*, 139(10), pp. 1802-1807.

Chittoori, B. C. S. (2008). "Clay mineralogy effects on long-term performance of chemically treated expansive clays." PhD Dissertation, The University of Texas at Arlington.

Chittoori, B. C. S, and Puppala, A. J. (2011). "Quantitative estimation of clay mineralogy in fine-grained soils." *Journal of Geotechnical and Geoenvironmental Engineering*, 137(11), pp. 997-1008.

Cho, S. E. and Lee, S. R. (2002), "Evaluation of surficial stability for homogeneous slopes considering rainfall characteristics", *Journal of Geotechnical and Geoenvironmental Engineering*, 128(9), 756-763.

Chowdhury, R., Flentje, P., Bhattacharya, G. (2010). Geotechnical slope analysis, *CRC Press*, London.

Cole, D.M., Ringelberg, D.B., and Reyynolds, C.M. (2012). "Small scale mechanical properties of biopolymer," *Journal of Geotechnical and Geoenvironmental Engineering,* 138(9), pp. 1063-1074.

Corte, A., and Higashi A. (1960). Experimental research on desiccation cracks in soil. U.S. Army Snow Ice and Permafrost Research Establishment. Research Report No. 66, Corps of Engineers, Wilmette, Illinois, U.S.A.

Costa, S., Kodikara, J., Thusyanthan, N. I. (2008). "Modelling of desiccation crack development in clay soils." *Proceedings of the 12th international conference of IACMAG*, Goa, India, pp. 1099-1107.

Costa, S. (2009). "Study of desiccation cracking and fracture properties of clay soils," PhD Dissertation, Monash University.

Costa, S., Kodikara, J., Shannon, B. (2013). "Salient factors controlling desiccation cracking of clay in laboratory experiments." *Geotechnique,* 63(1), pp. 18-29.

Cyrus, S. (2008). "Studies on the development and control of desiccation cracks in compacted clay liner soils." PhD dissertation, Cochin University of Science and Technology.

Dade, W., Davis, J.D., Nicholos, P.D., Nowell, A.R.M., Thistle, D., and Trexler, M.B., White, D.C., (1990). "Effects of bacterial exopolymer adhesion on the entrainment of sand," *Geomicrobiology Journal*, 8(1), 1-16.

Day, R. W. (1996). "Design and repair for surficial failures." *Practice Periodical on Structural design and Construction*, 1, pp. 83-87.

Dawson, E. M., Roth, W. H., and Drescher, A. (1999). "slope stability analysis by strength reduction," *Geotechnique*, 49(6), pp. 835-840.

Theory and background, FLAC3D Version 5.0. manual (2012). *Itasca Consulting Group Inc.,* Minneapolis, Minnesota.

D'Cunha, N. J., Misra, D., and Thompson, A.M. (2009). "Experimental investigation of the applications of natural freezing and curdlan biopolymer for permeability modification to remediate DNAPL contaminated aquifers in Alaska." *Cold Region Science and Technology*, 59(1), 42-50*Cold Region Science and Technology*, 59(1), pp. 42-50.

DeJong, J. T., Mortensen, B. M., Martinez, B. C., and Nelson, D. C. (2008). "Bio-mediated soil improvement." *Ecological engineering*, 36(2), pp. 197-210.

DeJong, J.D., Martinez, B.C., Ginn, T.R., and Nelson, D.C. (2013). "Bio-geo-chemical processes for improvement of soil engineering properties with focus on microbially induced calcite precipitation**."** *ISSMGE TC 215.*

Dronamraju, V. S. (2008). "Studies on Field Stabilization Methods to Prevent Surficial Slope Failures of Earth Fill Dams." PhD dissertation, University of Texas at Arlington.

Duncan, J. M. (1992). "State-of-the-art static stability and deformation analysis," *Stability and Performance of Slopes and Embankments: II*, Geotechnical Special Publication 31, ASCE, Reston, VA, pp. 222–266.

Duncan, J. M. (1996). "State of the art: limit equilibrium and finite element analysis of slopes," *Journal of Geotechnical Engineering*, 122(7), pp. 577–596.

Duncan, J. M., and Wright, G. S. (2005). Soil Strength and Slope Stability, *John Wiley & Sons*, Hoboken, N.J.

Escario, V., and Saez, J. (1986). "The shear strength of partly saturated soils," *Geotechnique,* 36(3), pp. 453– 456.

United States Army Corps of Engineers. (2003). Slope stability, *Engineering Manual EM 1110-2-1902*.

Fang, H. Y. (1994). "Cracking and fracture behavior of soil." *Fracture Mechanics Applied to Geotechnical Engineering. ASCE, Geotechnical Special Publication* 43, 102-117.

Fang, H. Y., and Chen, W. F. (1972). "Further study of double-punch test for tensile strength of soils,". Fritz Laboratory Reports.

Fredlund, D. G., and Morgernstern, N. R. (1977). "Stress state variables for unsaturated soils," *Journal of Geotechnical Engineering Division*, 103(5) pp. 447-466.

Fredlund, D. G. (1987). "The stress state for expansive soils," *Proceedings of the sixth international conference on expansive soils*, New Delhi, pp. 524-534.

Fredlund, D., Rahardjo, H., and Gan, J. (1987). "Non linearity of strength envelope for unsaturated soils," *Proceedings of the Sixth International Conference on Expansive Soils*, pp. 49– 54.

Fredlund, D. G., and Rahardjo, H. (1993). Soil Mechanics for Unsaturated Soils, *John Wiley and Sons*, New York.

Fredlund, D.G., and Houston, A.L. (2009). "Protocol for the assement of unsaturated soil properties in geotechnical engineering practice." *Canadian Geotechnical Journal*, 46, pp. 694-707.

Fredlund, D. G., Rahardjo, H., and Fredlund, M. D. (2012). Unsaturated soil mechanics in engineering practice, John Wiley and Sons, Hoboken, New Jersey.

George, K. P. (1969). "Cracking in pavements influenced by viscoelastic properties of soil cement." *Highway research record No.263*, Highway research board, Washington DC.

Greaves, H. M. (1996). "An introduction to lime stabilization," *Lime stabilization, Proceedings of the Seminar Held at Loughborough University,* Thomas Telford Ltd., London, pp.5-12.

Groisman, A., Kaplan, E. (1994). "An experimental study of cracking induced by desiccation," *Europhysics Letters* 25(6), pp. 415–420.

Guney, Y., Sari, D., Cetin, M., Tuncan, M. (2007). "Impact of cyclic wetting-drying on swelling behavior of lime-stabilized soil," *Building and Environment*, 42(2), pp.681-688.

Hovland, H. J. (1977). "Three-dimensional slope stability analysis method," *Journal of the Geotechnical Engineering Division*, 103(9), pp. 971-986.

Hoyos, L. R., Puppala A. J., and Chainuwat, P. (2004). "Dynamic properties of chemically stabilized sulfate rich soils," *Journal of Geotechnical and Geoenvironmental Engineering*, 130(2), pp.153-162.

Hu, L. B., Peron, H., Hueckel, T., and Laloui, L. (2013). "Mechanisms and critical properties in drying shrinkage of soils: experimental and numerical parametric studies." Canadian Geotechnical Journal, 50, pp. 536-549.

Intharasombat, N. (2005). "Laboratory and field investigations to address erosion, volume change and desiccation cracking of compost amended expansive subsoils.", Ph.D. Dissertation, The University of Texas at Arlington.

Ivanov, V., and Chu, J. (2008). "Applications of microorganisms to geotechnical engineering for bioclogging and biocementation of soil in situ." *Rev. Environ. Sci. Biotechnol.*, 7(2), pp. 139-153.

Jackson, M. L., (1958), "Soil chemical analysis", *Prentice Hall Inc*., Englewood Cliffs, N.J.

Jones, D. E., and Holtz, W. J. (1973). "Expansive soils: The hidden disaster." *Civil Engineering*, 430(8), pp. 49-51.

Kavazanjian, E. Jr, Iglesias, E. & Karatas, I. (2009). "Biopolymer soil stabilization for wind erosion control." *Proc. 17th Int. Conf. Soil Mech. Geotech. Engng*, Alexandria 2, 881–884.

Khatami, H.R., and O'Kelly, B.C. (2013). "Improving mechanical properties of sand using biopolymers," *Journal of Geotechnical and Geoenvironmental Engineering*, 139(8), pp. 1402-1406.

Khattab, A. A. S., and Al-Taie, Kh. I. L. (2006). "Soil-Water Characteristic Curves (SWCC) for Lime Treated Expansive Soil from Mosul City", *Unsaturated Soils*, pp. 1671-1682.

Khattab, A. A. S, Al-Muhtar, M., and Fleureau, M. J. (2007). "Long term stability characteristics of a lime-treated plastic soil," *Journal of Materials in Civil Engineering*, 19(4), pp.358-366.

Kindle, E. M. (1917). "Some factors affecting the development of mud cracks," *The Journal of Geology* 25(2), pp. 135–144.

Knudsen D., Peterson, G. A., and Pratt P. F. (1982). "Lithium, sodium and potassium" In: *Methods of Soil Analysis* (Edited by Page, A. L.), Part 2. American Society of Agronomy, Madison, WI, pp. 229–231.

Kodikara, J., and Choi, X. (2006). "A simplified analytical model for desiccation cracking of clay layers in laboratory tests," *Unsaturated Soils,* pp. 2558-2569.

Kodikara, J., and Costa, S. (2013). "Desiccation cracking in clay soils: Mechanism and modeling," *Multiphysical Testing of Soils and Shales*, Springer Berlin Heidelberg, pp. 21-32.

Kodikara, J., Barbaour, S. L., Fredlund, D. G. (2000). "Desiccation cracking of soil layers." *Proceedings of the Asian conference in unsaturated soils, UNSAT ASIA,* Singapore, pp. 693-698.

Konrad, J. M., Ayad, R. (1997). "An idealized framework for the analysis of cohesive soils undergoing desiccation," *Canadian Geotechnical Journal*, 34, pp. 477–488.

Kutner, M. H., Nachtscheim, C. J., Neter, J., and Li, W. (2005). "Applied linear statistical model." 5th edition, *McGraw Hill Inc.*, NY.

Lachenbruch, A. H. (1961). "Depth and spacing of tension cracks." *Journal of Geophysical Research* 66(12), pp. 4273–4292.

Lai, H.T., Kim, D., Park, J.S., and Yen, T.F. (2013). "Studies of crosslinked biopolymer structure for environmental tools in terms of rate of swelling ratio, viscosity, and biodegradability:Part A." *J. Environmental Earth Sciences*, 70(5), pp. 2405-2413.

Larson, S. L., Newman, J. K., Griggs, C. S., Beverly, M., and Nestler, C. C. (2012). "Biopolymers as an alternative to petroleum based polymers for soil modification," ERDC TR-12-8, U.S. Army Corps of Engineer, Washington DC.

Larson, S. L., Newman, K., and O'Connor, G. (2013). "Biopolymer as an Alternative to Petroleum-based Polymers to Control Soil Erosion: Iowa Army

Ammunition Plant". *Report no. ER-0920*, USACE ERDC, Vicksburg, Mississippi.

Lau, J. T. K. (1987). "Desiccation cracking of clay soils." M.Sc. thesis, Department of Civil Engineering, University of Saskatchewan, Saskatoon, Canada.

Lakshmikantha, M. R., Prat, P. C., Ladesma, A. (2006). "An experimental study of cracking mechanisms in drying soils," *Proceedings of the 5th International Conference on Environmental Geotechnics*, Thomas Telford, London pp. 533–540.

Le, M. (2013). "Investigations to develop field stabilization methods to mitigate surficial slope failures." PhD dissertation, University of Texas at Arlington.

Lecocq, N., and Vandewalle, N. (2003). "Dynamics of crack opening in a 1-dimensional desiccation experiment." *Physica* A 321, pp.431-441.

Little, D. N. (1995). Handbook for stabilization of pavement subgrades and base courses with lime, Kendall/Hunt, Iowa.

Lu, N., and Likos, W. (2004). Unsaturated soil mechanics, *John Wiley and Sons*.

Lu, N., and Likos, W. (2006). "Suction stress characteristic curve for unsaturated soils," *Journal of Geotechnical and Geoenvironmental Engineering*, 132(2), pp. 131–142.

Maghchiche, A., Haouam, A., and Immirzi, B. (2010). "Use of polymers and biopolymers for water retaining and soil stabilization in arid and semiarid regions." *J. of Taibah University for Science Journal*, 4, pp. 9-16.

Maher, H. M., and Ho, C. Y. (1994). "Mechanical Properties of Kaolinite/fiber Soil Composite," *Journal of Geotechnical Engineering*, 120(8), pp. 1381-1393.

Maier, R. M., Pepper, I. L., Gerba, C. P. (2000). *Environmental microbiology*, Second edition, *Academic Press*, Burlington, MA, USA.

Martinez, B. C., Barkouki, T. H., DeJong, J. T. & Ginn, T. R. (2011). "Upscaling of microbial induced calcite precipitation in 0.5 m columns: experimental and modeling results." *Proc. Geo-Frontiers 2011: Advances in Geotechnical Engineering*, Dallas, TX, ASCE Geotechnical Special Publication 211, pp. 4049–4059.

McCarthy, F. D., (2002). *Essentials of soil mechanics and Foundation*, Sixth edition, Prentice Hall, Upper Saddle River, New Jersey, USA.

McClesky, L. K Jr. (2005). "Experimental Investigations to Select Stabilization Methods to Mitigate Embankment Desiccation Cracks in order to Reduce Slope Failures." Master's thesis, The University of Texas at Arlington.

McCleskey, L. K., Puppala, A. J., Dronamraju, S. V., and Perrin, L. (2008). "Remedial Measures Planned to Prevent Surficial Failures." *GeoEdmonton*, Canadian Geotechnical Society.

Miller, J. C., and Rifai, S. (2004). “Fiber Reinforcement for Waste Containment of Soil Liners.” *Journal of Environmental Engineering*, 130(8), pp. 891-895.

Mitchell, J.K., and Santamarina, J.C. (2005). “Biological considerations in geotechnical engineering.” *Journal of Geotechnical and Geoenvironmental Engineering*, 131(10), pp. 1222-1233.

Mitchel, J. K., and Soga, K. (2005). *Fundamentals of soil behavior*, Third edition, John Wiley and Sons, Hoboken, New Jersey.

Morgenstern, N. R., and Price, V. E. (1965). “The analysis of the stability of general slip surfaces.” *Geotechnique*, 15(1), pp. 79-93.

Morgenstern, N. R., and Price, V. E. (1967). “A numerical method for solving the equations of stability of general slip surfaces.” *Computer Journal*, 9(4), pp. 388–393.

Morris, P. H., Graham, J., and Williams, D. J. (1992). “Cracking in drying soils.” *Canadian Geotechnical Journal*, 29, pp. 263-277.

Nahlawi, H., and Kodikara, J. (2006). “Laboratory experiments on desiccation cracking of thin soil layers.” *Geotechnical and Geological Engineering,* 24, pp. 1641-1664.

Nataraj, M. S., and McMains, K. L. (1997). “Strength and deformation properties of soils reinforced with fibrillated fibers.” *Geosynthetics International*, 4, pp. 65-79.

Nelson, D., and Miller, D. J. (1992). *Expansive Soils Problems and practice in Foundation and Pavement Engineering,* John Wiley & Sons, pp. 40-80.

Nugent, R.A., Zhang, G., and Gambrell, R.P. (2009). "Effect of exopolymers on the liquid limit of clays and its engineering implications." *Transportation Research Record* 2101, Transportation Research Board, Washington, DC, pp. 34-43.

Nugent, R. A., Zhang, G. and Gambrell, R. P. (2010). "The effect of exopolymers on the erosional resistance of cohesive sediments." *Proc. 5th Int. Conf. on Scour and Erosion*, San Francisco, CA, pp. 162–171.

Nugent, R. A., Zhang, G., and Gambrell, R. P. (2011). "The effect of exopolymers on the compressibility of clays." *ASCE Geo-Frontiers,* pp. 3935-3944.

Nugent, R.A., Zhang, G., and Gambrell, R.P. (2011). "The effect of exopolymers and void ratio on the erosional resistance of cohesive sediments." *ASCE Geo Frontiers,* pp. 1493-1502.

Oh, S., Lu, N. (2015). "Slope stability analysis under unsaturated conditions: case studies of rainfall induced failure of cut slopes." *Engineering Geology*, 184, pp. 96-103.

Omidi, G. H., Thomas, J. C., and Brown, K. W. (1996). "Effect of desiccation cracking on the hydraulic conductivity of a compacted clay liner." *Water, Air and Soil Pollution* 89, pp. 91-103.

Orts, J.W., et al. (2007). "Use of synthetic polymers and biopolymers for soil stabilization in agricultural, construction and military applications." *Journal of Materials in Civil Engineering*, 19(1), pp. 58-66.

Pan, B., Xie, H., Xu, B., and Dai, F. (2006). "Performance of sub-pixel registration algorithms in digital image correlation." *Measurement Science and Technology*, 17(6), pp. 1615 -1621.

Pan, B., Qian, K., Xie, H., and Asundi, A. (2009). "Two-dimensional digital image correlation for in-plane displacement and strain measurement: a review." *Measurement Science and Technology*, 20, 17pp.

Pedarla, A. (2013). "SWCC and clay mineralogy based models for realistic simulation of swell behavior of expansive soils." PhD Dissertation, The University of Texas at Arlington.

Puljan, V. (2010). "Experimental studies on shrinkage induced pressure measurements of four expansive clays." Master's Thesis, The university of Texas at Arlington.

Puppala, A. J., Banavathu, N., Qasim, R. S., Williammee, R., and Intharasombat, N. (2004). "Laboratory investigations to address the use of compost amendments to enhance expansive subsoils." *Recycled Materials in Geotechnics*, pp. 91-104.

Puppala, A. J., Punthutaecha, K., and Vanapalli, S. K. (2006). "Soil-water characteristics curves of stabilized expansive soils." *Journal of Geotechnical and Geoenvironmental Engineering*, 132(6), pp. 736-751.

Puppala, A. J., Wejrungsikul, T., and Puljan, V. (2011). "Shrinkage induced pressure measurements in unsaturated expansive soils." *Proceedings of Unsaturated Soils: Theory and Practices*, Kasetsart University, Thailand.

Puppala, A. J., Wejrungsikul, T., Puljan, V., and Manosuthkij, T. (2012) "Measurements of Shrinkage Induced Pressure (SIP) in Unsaturated Expansive Clays." *Geotechnical Engineering Journal of the SEAGS & AGSSEA*, Vol. 43(1).

Puppala, A. J., Saride, S. Williammee, R. (2012) "Sustainable reuse of limestone quarry fines and RAP in pavement base/subbase layers." *Journal of Materials*, 24, pp. 418-429.

Peron, H., Delenne, J. Y., Laloui, L., and El Youssoufi, M. S. (2009). "Discrete element modeling of drying shrinkage and cracking of soils." *Computers and Geotechnics*, 36, pp. 61-69.

Peng, X., and Horn, R. (2005). "Modeling soil shrinkage curve across wide range of soil types." *Soil Science Society of America Journal*, 69(3), pp. 584-592.

Peng, X., Zhang, Z. B., Wang, L. L., and Gan, L. (2012). "Does soil compaction change soil shrinkage behavior?" *Soil & Tillage Research* 125, 89-95.

Rahardjo, H., Lim, T. T., Chang, M. F., and Fredlund, D. G. (1995). "Shear strength characteristics of a residual soil." *Canadian Geotechnical Journal*, 32, pp. 60-67.

Raj, P. P. (2008). *Soil mechanics and foundation engineering*, Dorling Kinderssley (India) Pvt. Ltd. Patparganj, Delhi.

Ranjan, G. and Rao, A. S. R. (2005). *Basic and applied soil mechanics,* Revised second edition, New Age International Publishers, Dayarganj, New Delhi.

Ritchie, J. T., and Adams, J. E. (1974). "Field measurement of evaporation from soil shrinkage cracks." *Proceedings of the Soil Science Society of America*, 38(1) pp. 131-134.

Skempton, A. W., and LaRochelle, P. (1965). "The Bradwell slip: a short-term failure in London clay." *Geotechnique*, 15(3) pp. 221-242.

Spencer, E. (1967). "A method of analysis of the stability of embankments assuming parallel inter-slice forces." *Geotechnique*, 17(1), pp. 11–26.

Spencer, E. (1968). "Effect of tension on stability of embankments." *Journal of Soil Mechanics and Foundation Division*, 94(5), pp. 1159-1173.

Spencer, E. (1973). "The thrust line criterion in embankment stability analysis." *Geotechnique*, 23 pp. 85-101.

Stevens, J. (1996). *Applied multivariate statistics for the social sciences*, Lawrence Erlbaum Associates, Inc., New Jersey.

Sutherland, I. W. (2001). “Biofilm exopolysaccharides: a strong and sticky framework.” *Microbiology*, 147, pp. 3-9.

Tekscan Inc. homepage. FlexiForce® Force Sensors. http://www.tekscan.com /flexiforce /flexiforce. html. Accessed Oct. 6, 2015.

Terzaghi, K. (1936). “The shear resistance of unsaturated soils.” *Proceedings of the 1st International Conference on Soil Mechanics and Foundation Engineering*, Harvard University, Cambridge, Massachusetts.

Terzaghi, K., Peck, R. B., and Mesri, G. (1996). *Soil Mechanics in Engineering Practice*, Third Edition, John Wily and Sons Inc. New York.

Texas Department of Transportation (TEX-107-E). (1999). *Test procedure for determining the bar linear shrinkage of soils.*

Thompson, M. L., and Ukrainczyk, L. (2002). “Micas.” Edited by Dixon, J. B., and Schulze, D. G. *Soil mineralogy with environmental applications, SSSA*, Madison, WI, pp. 431-466.

Toramaru, A., Matsumoto, T. (2004). “Columnar joint morphology and cooling rate: A starch-water mixture experiment.” *Journal of Geophysical Research* 109, B02205.

Towner, G. D. (1987). “The mechanics of cracking of drying clay.” Journal of Agricultural Engineering Research, 36, pp. 115-124.

Vipulanandan, C., and Leung, M. (1990)."Seepage Control in Contaminated and Permeable Houston Clay: A Laboratory Study." *Hazardous Waste and Hazardous Materials*, 8(1), pp. 17-32.

Walker, P., J. (1995). "Strength, durability and shrinkage characteristics of cement stabilized soil blocks." *Cement and concrete composites*, 17(4), pp. 301-310.

Westergaard, H. M. (1926). "Stresses in concrete pavements computed by theoretical analysis." *Public Roads* 7(2).

Williams, H. F. L. (2003). "Urbanization pressure increases potential for soils-related hazards Denton County, Texas." *Environmental Geology*, 44(8), pp. 933-938.

Xiao, M., Reddi, N. L., Howard, J., Devine, A., and Scott, R. R. (2006). "Rainfall erosion control on roadside embankment using compost soils." *Unsaturated Soil, Seepage, and Environmental Geotechnics*, GSP 148, pp. 226-231.

Yesiller, N., Miller, C. J., Inci, G., Yaldo, K. (2000). "Desiccation and cracking behaviour of three compacted landfill liner soils." *Engineering Geology*, 57, pp. 105–121.

Biographical Information

Raju Acharya was born in December 1984, in Devbhumi Baluwa, Kavre, Nepal. He graduated from Tribhuvan University, Kathmandu, Nepal in 2010 with Bachelor's degree in Civil Engineering. He then joined the University of Kansas in August 2011. He completed his Masters of Science in Civil Engineering from KU in December 2012. He then joined doctoral program in the Department of Civil Engineering at the University of Texas at Arlington in January 2013. He worked under supervision of Distinguished Professor Anand J. Puppala with research focus on shrinkage characterization of clayey soils. In his dissertation research, he conducted comprehensive shrinkage characterization tests on a total of ten natural expansive soils and various soil treatment methods. He also developed a statistical regression model to predict shrinkage induced pressure, and performed three dimensional slope stability analyses to study the effect of desiccation cracking and soil suction. He successfully defended his dissertation in October 2015. During his stay at UTA, he captained UTA's geowall competition team in 2014. In 2015, he represented UTA in national geoprediction competition and won prestigious Mohr Circle Award by presenting the best solution to the prediction problem. He also published technical papers in national and international journals and conferences.